

Design of a High-speed-force-stroke Thermomechanical Micro-actuator via Geometric  
Contouring and Mechanical Frequency Multiplication

by

Shih-Chi Chen

B.S. National Tsing Hua University (Taiwan), 1999

S.M. Massachusetts Institute of Technology, 2003

Submitted to the Department of Mechanical Engineering  
in Partial Fulfillment of the Requirements for the Degree of

Doctor of Philosophy

at the

Massachusetts Institute of Technology

September 2007

© 2007 Massachusetts Institute of Technology  
All Rights Reserved

Signature of Author.....  
Department of Mechanical Engineering  
August 24, 2007

Certified by.....  
Martin L. Culpepper  
Associate Professor of Mechanical Engineering  
Thesis Supervisor

Accepted by.....  
Lallit Anand  
Chairman, Department Committee on Graduate Students

*This page is intentionally left blank*

Design of a High-speed-force-stroke Thermomechanical Micro-actuator via Geometric Contouring and Mechanical Frequency Multiplication

by

Shih-Chi Chen

Submitted to the Department of Mechanical Engineering on August 24, 2007  
in partial fulfillment of the requirements for the Degree of  
Doctor of Philosophy in Mechanical Engineering

ABSTRACT

The aims of this research were to understand (1) why marked performance improvements are observed when one contours the geometry of micro-thermomechanical actuators ( $\mu$ TMAs), (2) how to parametrically model and optimize these improvements, (3) how to use transient electrical command signals to augment these improvements, and (4) how to design arrayed pairs of actuator teams that enable the realization of these improvements within small-scale precision machines.

This work has extended the performance envelope of small-scale electromechanical systems to cover the needs of emerging positioning applications that were previously impractical. The results are important to, for example, small-scale machines that are increasingly needed within biological imaging equipment, equipment for nanomanufacturing, and instruments for nano-scale research. These positioning systems must be of small geometric scale in order to achieve viable bandwidth (kHz), resolution (nanometers), cost (\$10s/device) and stability ( $\text{\AA}/\text{min}$ ) levels. Miniaturized machines require small-scale actuators, but unfortunately, state-of-the-art actuators are not capable of simultaneously satisfying the force ( $\sim 10\text{mN}$ ), stroke ( $\sim 100\mu\text{m}$ ) and bandwidth ( $\sim 1\text{kHz}$ ) requirements of the preceding applications. In the absence of a practical actuation technology, many small-scale devices were relegated to “demo” status, and they never realized the full promise that small-scale machines could deliver for the preceding applications.

This work has generated two concepts – geometric contouring and mechanical frequency multiplication – that make  $\mu$ TMAs behave in a manner that is very different from how they have acted in the past:

- (1) Geometric contouring: The variation of a beam’s cross-sectional area along its length to achieve more favorable thermal characteristics, *i.e.* temperature profile, while simultaneously reducing the elastic energy storage within the beam, and
- (2) Mechanical frequency multiplication: The use of  $\mu$ TMAs pairs that cooperate to reduce their combined cycle time below their individual cycle times, thereby increasing their operating frequency.

The utility and practical implementation of these techniques were illustrated via a case study on a three-axis optical scanner for a two-photon endomicroscope. The device consisted of three sub-systems: (i) an optical system (prism, graded index lens, and optical fiber) that was used to deliver/collect photons during imaging, (ii) a small-scale electromechanical scanner that could raster scan the focal point of the optics through a specimen and (iii) a silicon optical bench that connects the electromechanical and optical systems. The scanner was required to fit within a 7mm  $\text{\O}$  endoscope port and scan at 1kHz throughout a  $100 \times 100 \times 100 \mu\text{m}^3$  volume. The results of this thesis were used to engineer a scanner that was capable of 3.5kHz x 100Hz x 30Hz scanning throughout a  $125 \times 200 \times 200 \mu\text{m}^3$  volume. Preceding  $\mu$ TMA technology could only scan over 12.5% of the required volume at 10% of the required frequency.

This work forms a body of knowledge – design rules, principles and best practices – that may be used to realize similar benefits in other small-scale devices.

Thesis Supervisor: Martin L. Culpepper  
Title: Associate Professor of Mechanical Engineering

*This page is intentionally left blank*

# Acknowledgements

---

Without the following people's contribution, this work would not have been completed.

First I thank my adviser Professor Martin Culpepper for giving me the freedom to explore my own ideas, and at the same time providing valuable guidance when needed. Marty has been an excellent advisor to work with. From him, I obtained not only the scientific knowledge but more importantly the ability to identify and solve problems.

I would also like to thank my thesis committee members: Professor Peter So for his support throughout my Ph.D. and his constant availability for discussions and guidance; Professor Steven Hall for his insightful comments and constructive criticisms that held me to a high research standard; Professor Dennis Freeman for providing his time and laboratory facilities to conduct my research experiments; Professor Carol Livermore for the discussions with her, ranging from personal issues to career planning.

I thank the MTL staff: Dave Terry, Dennis Ward, Kurt Broderick, and Vicky Diadiuk, just to name a few. Without their valuable experience and patience, I would not have been able to design and fabricate my device.

I also thank my fellow graduate students and colleagues at MIT, past and present: Dariusz Golda, Chris DiBiasio, Jonathan Hopkins, Michael Cullinan, Michael Whitson, Kartik Varadarajan, Fernando Tubilla Kuri, Bob Panas, Heejin Choi, and Daekeun Kim for helping me to stay sane throughout these difficult years. Also, my special thanks to all who carefully read and commented on countless revisions of my dissertation.

To my family: Mou, Polly, Mufan, and Qing I thank you for your unbounded love and support.

*This page is intentionally left blank*

# Table of Contents

<b>CHAPTER 1 INTRODUCTION</b> .....	<b>15</b>
1.1 SYNOPSIS .....	15
1.2 SCOPE.....	16
1.3 REVIEW OF MICRO-ACTUATORS FOR POSITIONING .....	19
1.3.1 <i>Electrostatic</i> .....	19
1.3.2 <i>Electromagnetic</i> .....	20
1.3.3 <i>Piezoelectric</i> .....	21
1.3.4 <i>Thermomechanical</i> .....	22
1.3.5 <i>Micro-actuators comparison</i> .....	23
1.4 FLEXURE SYSTEM AND PRECISION MOTION GUIDANCE .....	23
1.5 OPTICAL MICROSCOPY FOR HIGH RESOLUTION BIOMEDICAL IMAGING .....	24
1.5.1 <i>Two-photon excitation microscopy</i> .....	25
1.5.2 <i>Confocal microscopy</i> .....	27
1.5.3 <i>Optical coherence tomography (OCT)</i> .....	28
1.6 CASE STUDY: SCANNER FOR A TWO-PHOTON ENDOMICROSCOPE .....	29
1.6.1 <i>Overview of device function and prior art</i> .....	29
1.6.2 <i>Functional requirements and constraints</i> .....	30
1.6.3 <i>Proposed solutions and technologies</i> .....	30
1.6.4 <i>Potential impact of the case study</i> .....	30
<b>CHAPTER 2 GEOMETRIC CONTOURING OF TMAS</b> .....	<b>33</b>
2.1 INTRODUCTION: CONCEPTS AND DESIGN PARAMETERS .....	33
2.2 THERMAL MODELING .....	35
2.2.1 <i>Modeling assumptions</i> .....	35
2.2.2 <i>1D thermal modeling</i> .....	36
2.2.3 <i>Effect of contouring on quasi-static thermal performance</i> .....	38
2.3 STIFFNESS AND DEFORMATION MODELING .....	40
2.4 DISPLACEMENT, STIFFNESS AND FORCE CHARACTERISTICS .....	45
2.4.1 <i>Summary of actuator-level modeling</i> .....	45
2.4.2 <i>The effect of contouring on a chevron TMA</i> .....	47
2.4.3 <i>The effect of contouring on the performance of a parallel TMA</i> .....	51
2.5 IMPLICATIONS OF QUASI-STATIC RESULTS FOR DEVICE DESIGN .....	51
2.5.1 <i>Effect of contouring on performance with equal displacement constraint</i> .....	51
2.5.2 <i>Enhancement in stroke and maximum force output</i> .....	53
2.6 DYNAMIC CHARACTERISTICS OF CONTOURED TMAS.....	54
2.6.1 <i>Effects of contouring on transient thermal behavior of a beam</i> .....	55
2.6.2 <i>Effects of contouring on a specific contoured chevron TMA performance</i> .....	57
2.6.3 <i>Step responses and velocity characteristics of contoured chevron TMAs</i> .....	61
2.7 CHARACTERIZATION OF CONTOURING ENHANCED PERFORMANCE .....	63
2.8 A PULSING TECHNIQUE FOR HIGH-BANDWIDTH POSITIONING.....	67
2.8.1 <i>Concept of pulsing</i> .....	67
2.8.2 <i>The effects of high-bandwidth pulsing on a contoured chevron TMA</i> .....	68
2.8.3 <i>Determination of driving signal</i> .....	73
2.8.4 <i>The reason for increased heat transfer rate at beam ends during pulsing</i> .....	74
2.8.5 <i>Mechanical failure limits</i> .....	75
2.9 SUMMARY .....	77
<b>CHAPTER 3 MECHANICAL FREQUENCY MULTIPLIER</b> .....	<b>79</b>
3.1 INTRODUCTION.....	79
3.2 CONCEPTS AND DESIGN .....	80

3.3	PULSE GENERATION.....	81
3.4	MFM FIBER RESONATOR.....	83
3.4.1	<i>Functional requirements and constraints</i> .....	83
3.4.2	<i>Fiber resonator concept</i> .....	83
3.4.3	<i>Design concerns</i> .....	84
3.4.4	<i>Driving signal for system level model</i> .....	90
3.4.5	<i>Simulation results</i> .....	92
3.5	SUMMARY.....	95
<b>CHAPTER 4 DEVICE FABRICATION.....</b>		<b>97</b>
4.1	OVERVIEW OF MICRO-FABRICATION AND PACKAGING.....	97
4.1.1	<i>Wafers</i> .....	98
4.1.2	<i>Lithography</i> .....	99
4.1.3	<i>Metal Evaporation</i> .....	101
4.1.4	<i>Etching</i> .....	101
4.2	DESIGN OF MICRO-FABRICATION PROCESSES.....	103
4.2.1	<i>Micro-fabrication platform</i> .....	103
4.2.2	<i>Cursory inspection</i> .....	104
4.3	FAB CONSIDERATIONS.....	109
4.3.1	<i>Stiction effect</i> .....	109
4.3.2	<i>Variations</i> .....	109
4.4	SUMMARY.....	113
<b>CHAPTER 5 CASE STUDY: A THREE-AXIS MICROSCALE SCANNING SYSTEM.....</b>		<b>115</b>
5.1	OVERVIEW.....	115
5.2	MICRO-OPTICAL SYSTEM.....	116
5.2.1	<i>Performance criteria for a two-photon endomicroscope</i> .....	116
5.2.2	<i>Functional requirements and constraints</i> .....	117
5.2.3	<i>Concepts for the optical system</i> .....	117
5.2.4	<i>Sensitivity analysis of the optical assembly</i> .....	124
5.3	ENDOSCOPIC SCANNER DESIGN.....	138
5.3.1	<i>Actuation system design</i> .....	139
5.3.2	<i>Choice of bearings and concepts</i> .....	142
5.3.3	<i>Assembling and packaging</i> .....	151
5.3.4	<i>Device characterization</i> .....	152
5.4	FIBER RESONATOR DESIGN.....	160
5.4.1	<i>Characterization of double clad photonic crystal fiber (DCPCF)</i> .....	161
5.4.2	<i>Meso-scale endoscopic fiber resonator design and characterization</i> .....	162
5.4.3	<i>Characterization of MFM fiber resonator</i> .....	167
5.5	SCANNING SYSTEM INTEGRATION.....	173
5.6	SUMMARY.....	175
<b>CHAPTER 6 CONCLUSIONS.....</b>		<b>177</b>
6.1	SUMMARY OF RESEARCH.....	177
6.2	THESIS CONTRIBUTIONS.....	178
6.3	EXTENSIONS AND VISIONS FOR FUTURE RESEARCH.....	179
6.3.1	<i>Extension of geometric contouring and MFM to other applications</i> .....	179
6.3.2	<i>Miniaturization of next generation scanner</i> .....	180
6.3.3	<i>Confocal and two-photon endomicroscope</i> .....	181
<b>APPENDIX A NOMENCLATURE.....</b>		<b>183</b>
<b>APPENDIX B EFFICIENCY OF TMAS.....</b>		<b>185</b>
<b>REFERENCES.....</b>		<b>187</b>



# List of Figures

FIGURE 1–1 A CASE STUDY MICRO-FABRICATED THREE-AXIS OPTICAL SCANNER .....	16
FIGURE 1–2 COMMONLY USED MICRO-SCALE TMAS AND THE CONCEPT OF GEOMETRIC CONTOURING.....	17
FIGURE 1–3 SCHEMATICS FOR A MECHANICAL FREQUENCY MULTIPLIER .....	18
FIGURE 1–4 SCHEMATIC OF A TYPICAL TWO-PHOTON MICROSCOPE AND A 3D SAMPLE IMAGE OF HUMAN SKIN TISSUE (COURTESY OF PROFESSOR PETER SO) .....	26
FIGURE 1–5 SCHEMATIC AND WORKING PRINCIPLE OF A TYPICAL CONFOCAL MICROSCOPE .....	28
FIGURE 1–6 A COMPARISON OF A ONE-PHOTON CONFOCAL MICROSCOPE AND TPE MICROSCOPE EXCITATION PROFILES (COURTESY OF PROFESSOR PETER SO) .....	28
FIGURE 2–1 COMMONLY USED TMAS AND RELEVANT DESIGN PARAMETERS .....	34
FIGURE 2–2 DESIGN PARAMETERS THAT ARE USED TO DESCRIBE THE CONTOURED BEAM’S GEOMETRY .....	35
FIGURE 2–3 SCHEMATICS OF THERMAL MODELING FOR CONTOURED TMAS.....	37
FIGURE 2–4 COMPARISON OF THERMAL CHARACTERISTICS BETWEEN EXAMPLE 1 AND EXAMPLE 2.....	40
FIGURE 2–5 COMPARISON OF THERMAL CHARACTERISTICS BETWEEN EXAMPLE 1 AND EXAMPLE 3.....	40
FIGURE 2–6 ERROR OBSERVED WHEN CALCULATING (A) THE AXIAL STIFFNESS AND (B) LATERAL BENDING STIFFNESS OF A SINGLE CONTOURED BEAM USING EQUIVALENT INERTIAL AND AREA.....	44
FIGURE 2–7 RELATIONSHIP BETWEEN DESIGN PARAMETERS AND THE (A) AXIAL STIFFNESS REDUCTION AND (B) LATERAL BENDING STIFFNESS REDUCTION OF A SINGLE CONTOURED BEAM.....	45
FIGURE 2–8 NON-DIMENSIONAL PARAMETERS FOR A CHEVRON TMA VS. ENHANCEMENT RATIOS FOR (A) DISPLACEMENT PER UNIT POWER, (B) TRANSMISSION RATIO, AND (C) ACTUATOR STIFFNESS.....	49
FIGURE 2–9 NON-DIMENSIONAL DESIGN PARAMETERS FOR A PARALLEL TMA VS. ENHANCEMENT RATIOS FOR (A) DISPLACEMENT PER UNIT POWER, (B) TRANSMISSION RATIO, AND (C) ACTUATOR STIFFNESS.....	50
FIGURE 2–10 RELATIONSHIP BETWEEN DESIGN PARAMETER CHANGES AND DECREASE IN MAXIMUM TEMPERATURE FOR CHEVRON BEAM TMAS.....	52
FIGURE 2–11 RELATIONSHIP BETWEEN DESIGN PARAMETER CHANGES AND THE DECREASE IN ACTUATOR POWER CONSUMPTION FOR CHEVRON BEAM TMAS.....	52
FIGURE 2–12 RELATIONSHIP BETWEEN DESIGN PARAMETER CHANGES AND (A) ACTUATOR STROKE AND (B) POWER REDUCTION RATIO.....	54
FIGURE 2–13 COMPARISON OF TRANSIENT HEATING PROCESS BETWEEN A CONTOURED AND STRAIGHT BEAM.....	56
FIGURE 2–14 STEP RESPONSES OF EXAMPLE C AND D WITH CONSTANT INPUT CURRENT CONSTRAINT .....	59
FIGURE 2–15 SQUARE-WAVE RESPONSES OF EXAMPLE C AND WITH EQUAL DISPLACEMENT CONSTRAINT .....	61
FIGURE 2–16 RISE TIME AND FALL TIME FOR 24 CHEVRON BEAM TMAS .....	62
FIGURE 2–17 NORMALIZED FORWARD AND RETURN SPEED FOR 24 CHEVRON BEAM TMAS .....	63
FIGURE 2–18 SCHEMATICS OF COMPUTER MICROVISION SYSTEM.....	65
FIGURE 2–19 REPOSES TO A SQUARE WAVE INPUT OF THREE CHEVRON TMAS.....	66
FIGURE 2–20 FREQUENCY SPECTRUM OF THREE CHEVRON TMAS .....	67
FIGURE 2–21 CONCEPTS AND PRINCIPLES FOR PULSING TECHNIQUE FOR A CONTOURED JOULE HEATED BEAM.....	68
FIGURE 2–22 EXAMPLE F: HEATING/COOLING PROCESSES OF A CONTOURED BEAM IN RESPONSE TO A SINGLE SHORT PULSE.....	70
FIGURE 2–23 EXAMPLE G: HEATING/COOLING PROCESSES OF A CONTOURED BEAM IN RESPONSE TO A CONVENTIONAL SIGNAL.....	70
FIGURE 2–24 EXAMPLE H: HEATING/COOLING PROCESS OF A STRAIGHT BEAM IN RESPONSE TO A CONVENTIONAL SIGNAL.....	71
FIGURE 2–25 ELONGATION OF THE CONTOURED BEAM AND STRAIGHT BEAM UNDER DIFFERENT DRIVING CONDITIONS WITH MAXIMUM TEMPERATURE AT 1000 °K .....	72
FIGURE 2–26 DETERMINATION OF THE PROPER CURRENT ( $I_p$ ) AND PULSE WIDTH ( $T_p$ ) SO THAT $T(X_l, T_p)$ EQUALS TO $T(X_2, T_p)$ .....	73
FIGURE 2–27 TEMPERATURE GRADIENT AND PRODUCT OF TEMPERATURE GRADIENT AND CROSS-SECTION AREA AT THE END OF A BEAM AS A FUNCTION OF TIME FOR EXAMPLE F, G, AND H .....	75
FIGURE 2–28 LIMITING CONDITIONS FOR CONTOURED TMAS.....	76
FIGURE 3–1 : SCHEMATICS OF A MFM SYSTEM. A, B: PULSE GENERATOR TMA PAIR CONCEPT; C, D: IDEAL CASE FOR PULSE PAIRS TO RUN IN TIME-DELAYED FASHION .....	81

FIGURE 3–2 SCHEMATICS FOR A MECHANICAL FREQUENCY MULTIPLIER .....	81
FIGURE 3–3 A FEA (COMSOL) SIMULATED EXAMPLE OF PULSE–GENERATING PAIR DESIGN .....	82
FIGURE 3–4 CONCEPT OF RESONATOR STAGE.....	84
FIGURE 3–5 SCHEMATIC FOR A MFM FIBER RESONATOR SYSTEM.....	84
FIGURE 3–6 TEMPERATURE DISTRIBUTIONS ALONG THE CHEVRON TMAS OF THE MFM RESONATOR. THE DASHED LINES ARE POSSIBLE TEMPERATURE PROFILES WITH DIFFERENT DESIGN OBJECTIVES (CASE I, II AND III).....	85
FIGURE 3–7 FIBER RESONANT FREQUENCY AND FIBER LATERAL STIFFNESS VARIATION AS A FUNCTION OF $L_1$ AND $L_2$ .....	87
FIGURE 3–8 OFFSET LONGITUDINAL AND LATERAL MODES BY PARTIALLY REMOVING MATERIALS FROM FIBER.....	88
FIGURE 3–9 CURRENT PATHS AT THE MFM RESONATOR WITH DIFFERENT SOURCES .....	90
FIGURE 3–10 EXAMPLES OF THE PARAMETRIC SIGNAL MODEL WITH $n=0.001, 0.1, 3,$ AND $100; p=0, 1; m=2; f=1$ .....	91
FIGURE 3–11 A FOUR–CHANNEL ANALOG RC DELAY CIRCUIT THAT WAS USED TO DRIVE THE MFM FIBER RESONATOR .....	91
FIGURE 3–12 TIME–DELAYED SHORT PULSES FOR FOUR TMAS: A, B, C, AND D .....	92
FIGURE 3–13 TRANSIENT THERMAL MODELING OF THE MFM FIBER RESONATOR .....	93
FIGURE 3–14 SIMULATED MFM RESONATOR STAGE MOTION. THE MFM FIBER RESONATOR’S THERMAL SETTling TIME MAY BE NEGLECTED DUE TO THE SYMMETRIC DESIGN,.....	94
FIGURE 3–15 SIMULATED MFM RESONATOR DISPLACEMENT AND TEMPERATURE DISTRIBUTION AT 1.6 KHZ.....	95
FIGURE 4–1 MICRO–FABRICATION PLATFORM FOR ACTIVE SILICON OPTICAL BENCH.....	98
FIGURE 4–2 TYPICAL LITHOGRAPHY PROCEDURES.....	99
FIGURE 4–3 IMAGES FROM AN OPTICAL MICROSCOPE OF THE SILICON ENDOSCOPIC SCANNER .....	106
FIGURE 4–4 IMAGES FROM AN OPTICAL MICROSCOPE OF MFM FIBER RESONATOR .....	106
FIGURE 4–5 SEM IMAGES OF THE MICRO–FABRICATED ENDOSCOPIC SCANNER .....	107
FIGURE 4–6 SURFACE PROFILE OF THE SILICON ENDOSCOPIC SCANNER.....	108
FIGURE 4–7 COMPARISON OF DIFFERENT EXPOSURE TIME OF PHOTORESIST .....	110
FIGURE 4–8 DRIE SIDEWALLS OF THE SILICON ENDOSCOPIC SCANNER.....	112
FIGURE 4–9 SEM IMAGES OF THE SILICON ENDOSCOPIC SCANNER.....	113
FIGURE 5–1 SCHEMATICS OF THE CARTESIAN 3D RASTER SCANNING ROUTE FOR THE ENDOMICROSCOPE .....	117
FIGURE 5–2 OPTICAL CONFIGURATIONS FOR A MACRO–SCALE TWO–PHOTON MICROSCOPE (A), AND TWO MINIATURIZED TPE ENDOMICROSCOPY THAT UTILIZE GRIN LENSES (B AND C).....	118
FIGURE 5–3 (A) A CROSS–SECTION VIEW OF THE DCPCF, WHERE A SINGLE MODE CORE IS EMBEDDED IN A HIGH NA ( $\sim 0.6$ AT 600NM) MULTIMODE FIBER STRUCTURE, AND (B) ATTENUATION OF THE MULTIMODE GUIDE [106]...	119
FIGURE 5–4 FOUR DIFFERENT DECOUPLING SCANNING SCENARIOS, WHERE THREE OUT OF THE FOUR OPTICAL ELEMENTS (OBJECTIVE LENS, TUBE LENS, PRISM, OR FIBER) WERE CHOSEN TO RUN SIMULATION .....	120
FIGURE 5–5 SPOT DIAGRAM COMPARISON FOR TIP–AND–TILT AND TRANSLATIONAL SCANNING .....	121
FIGURE 5–6 FINALIZED OPTICAL DESIGN AND RELATIVE LOCATIONS/DIMENSIONS OF OPTICAL COMPONENTS .....	122
FIGURE 5–7 RESOLUTION AND NORMALIZED POINT SPREAD FUNCTION WITHOUT MISALIGNMENT AND ABERRATION, FWHM = 0.73 $\mu\text{m}$ . NOTE THE Y–AXIS REPRESENTS THE NORMALIZED INTENSITY OF THE PSF.....	123
FIGURE 5–8 GEOMETRIC RELATIONSHIP BETWEEN THE GRIN LENS AND SHUTTLE (FRONT VIEW) .....	125
FIGURE 5–9 EXAMPLE 1 AND 2 FOR INVESTIGATING THE EFFECTS OF (1) PARTIALLY BLOCKED BEAM, AND (2) MISALIGNMENTS THAT ARE CAUSED BY FABRICATION ERRORS IN GRIN LENS AND SHUTTLE GEOMETRIES.....	125
FIGURE 5–10 SPOT DIAGRAM AND PSF OF THE UNBLOCKED BEAM .....	127
FIGURE 5–11 SPOT DIAGRAM AND PSF OF THE BEAM BLOCKED BY 100 MICRONS .....	128
FIGURE 5–12 SPOT DIAGRAM AND PSF OF THE BEAM BLOCKED BY 200 MICRONS .....	129
FIGURE 5–13 EFFECTS OF MISALIGNMENT IN Y–AXIS FROM 0 TO 50 MICRONS.....	131
FIGURE 5–14 EFFECTS OF MISALIGNMENT IN X–AXIS FROM 0 TO 50 MICRONS.....	133
FIGURE 5–15 THE EFFECT ON SYSTEM RESOLUTION AS A FUNCTION OF (1) MISALIGNMENT OF THE OPTICAL COMPONENTS AND (2) THE BLOCKING OF LIGHT .....	133
FIGURE 5–16 SIMULATED EXCITATION/EMISSION RAY TRACING RESULTS OF CHROMATIC ABERRATION, WHERE IN SIMULATION EXCITATION WAVELENGTH = 720 NM AND EMISSION WAVELENGTH = 510 NM WERE USED.....	135
FIGURE 5–17 INTENSITY AND LASER PROFILE CHARACTERIZATION OF DCPCF (COURTESY OF MR. HEEJIN CHOI) ..	136
FIGURE 5–18 TWO–PHOTON EFFICIENCY MEASUREMENT FOR DIFFERENT SIGNAL PRE–CHIRPING LENGTHS.....	137
FIGURE 5–19 SCHEMATICS OF THE ENDOSCOPIC MICRO–SCANNER AND MICRO–OPTICAL BENCH DESIGN, WHERE THE FEMTOSECOND LASER BEAM IS GUIDED TO THE OPTICAL PLATFORM THROUGH THE RESONATING FIBER. ON THE OPTICAL PLATFORM, THE COLLIMATED LASER GOES TO THE OBJECTIVE GRIN LENS THROUGH THE REFLECTION OFF OF A MILLIMETER–SCALE PRISM. ....	139

FIGURE 5–20 A SOB WITH INTEGRATED TMAS AND FLEXURAL BEARINGS THAT GENERATE LINEAR AND ROTARY MOTIONS .....	140
FIGURE 5–21 A FLEXURAL ROTARY BEARING OPTIMIZATION. THE RESULTS SHOW THAT AT 70° THE BEARING WILL HAVE AN OPTIMAL TRANSMISSION RATIO (DEFINED AS PARASITIC DISPLACEMENT OVER ACTUATOR DISPLACEMENT) EQUAL TO $2.9 \times 10^{-3}$ [MM/MM]. .....	143
FIGURE 5–22 TRANSMISSION RATIO, AXIAL, LATERAL STIFFNESS OF A CHEVRON MECHANISM AS A FUNCTION OF ANGLE.....	145
FIGURE 5–23 A TWO–SPRING MODEL FOR THE CASCADED CHEVRON MECHANISM .....	145
FIGURE 5–24 OPTIMAL TRANSMISSION RATIO AND POWER EFFICIENCY AS A FUNCTION OF NUMBER OF ACTUATORS. ....	147
FIGURE 5–25 A TRANSMISSION RATIO SURFACE PLOT AS A FUNCTION OF $\theta_1$ , $\theta_2$ , AND $N$ .....	148
FIGURE 5–26 A TRANSMISSION RATIO PLOT FOR THE GRIN LENS SHUTTLE WITH THE LOW POWER OBJECTIVE .....	149
FIGURE 5–27 A TRANSMISSION RATIO PLOT FOR THE PRISM SHUTTLE WITH THE LOW POWER OBJECTIVE .....	149
FIGURE 5–28 A TRANSMISSION RATIO PLOT FOR THE GRIN LENS SHUTTLE FOR $N = 5$ .....	150
FIGURE 5–29 A TRANSMISSION RATIO PLOT FOR THE PRISM SHUTTLE FOR $N = 5$ .....	150
FIGURE 5–30 ASSEMBLING PROCEDURES FOR GRIN LENS AND PRISM .....	151
FIGURE 5–31 A PACKAGED SOB FOR EXPERIMENTATION AND A CONCEPT PACKAGE FOR PRODUCTION .....	152
FIGURE 5–32 MEASURED FREQUENCY SPECTRUM AND SIMULATED MODE SHAPES FOR GRIN LENS SHUTTLE .....	153
FIGURE 5–33 STEP RESPONSE OF GRIN LENS SHUTTLE .....	154
FIGURE 5–34 DISPLACEMENT VS. INPUT COMMAND PLOT FOR GRIN LENS SHUTTLE .....	156
FIGURE 5–35 DEMONSTRATION OF PULSING TECHNIQUE ON THE GRIN LENS SHUTTLE WITH CONTOUR CHEVRON TMAS.....	156
FIGURE 5–36 MEASURED FREQUENCY SPECTRUM AND SIMULATED MODE SHAPES OF PRISM SHUTTLE .....	158
FIGURE 5–37 STEP RESPONSE OF PRISM SHUTTLE .....	159
FIGURE 5–38 DISPLACEMENT VS. INPUT COMMAND PLOT OF PRISM SHUTTLE .....	160
FIGURE 5–39 SCHEMATICS OF THE FIBER RESONATOR DESIGN .....	161
FIGURE 5–40 COMPARISON OF PREDICTED AND MEASURED FIBER RESONANCE FREQUENCY .....	162
FIGURE 5–41 CONCEPTS FOR THE MESO–SCALE FIBER RESONATOR.....	164
FIGURE 5–42 DESIGN PARAMETERS FOR A FLEXURAL BEARING .....	165
FIGURE 5–43 IMAGE OF THE MESO–SCALE FIBER RESONATOR MADE BY WIRE–EDM.....	166
FIGURE 5–44 EXPERIMENTS FOR FIBER RESONATOR CHARACTERIZATION.....	167
FIGURE 5–45 WIRE–BONDED MFM RESONATOR PACKAGE .....	168
FIGURE 5–46 EXPERIMENTAL SETUP FOR MFM RESONATOR EXPERIMENT .....	168
FIGURE 5–47 FIBER ASSEMBLING PROCEDURES FOR MFM FIBER RESONATOR.....	169
FIGURE 5–48 ASSEMBLED MFM STAGE WITH THE MULTI–MODE FIBER .....	170
FIGURE 5–49 RESULTS OF THE FREQUENCY SWEEP PERFORMED BY THE MESO–SCALE FIBER RESONATOR .....	171
FIGURE 5–50 FIBER IN RESONANCE ACTUATED BY MFM RESONATOR .....	172
FIGURE 5–51 CCD IMAGES OF MFM RESONATOR OPERATED AT 965 HZ.....	172
FIGURE 5–52 EXPERIMENTAL SETUP FOR TWO–PHOTON IMAGING .....	174
FIGURE 5–53 SCREENSHOTS OF X–Y SCAN, WHERE X AND Y–AXIS SCAN AT 730HZ AND 1HZ RESPECTIVELY.....	174
FIGURE 5–54 SCREENSHOTS OF TWO–PHOTON EMISSION AT THE FOCAL PLANE DURING Z–AXIS SCANNING AT 2 HZ FOR 100 $\mu$ M.....	175

*This page is intentionally left blank*

# List of Tables

TABLE 1–1 : MICRO–ACTUATOR PERFORMANCE IN COMPARISON TO FUNCTIONAL REQUIREMENTS (FRS) OF A THREE– AXIS ENDOSCOPIC SCANNER.....	19
TABLE 1–2 FUNCTIONAL REQUIREMENTS FOR THE ENDOSCOPIC SCANNER GENERATED BASED ON THE OPTICAL DESIGN .....	30
TABLE 1–3 INTERNAL CANCERS THAT WOULD BE IMPACTED VIA TPE ENDOMICROSCOPY [93] .....	31
TABLE 2–1 DESIGN PARAMETERS THAT WERE USED FOR WITH THE THERMOMECHANICAL MODELING OF A SINGLE BEAM .....	38
TABLE 2–2 DESIGN PARAMETERS THAT WERE USED IN EXAMPLES 1, 2, AND 3 .....	39
TABLE 2–3 VALUES THAT WERE USED IN COMPARISON OF STIFFNESS RESULTS FROM THE THEORY AND FEA .....	43
TABLE 2–4 PARAMETERS THAT WERE USED FOR MODELING OF THE EXAMPLE TMAS .....	47
TABLE 2–5 PARAMETERS THAT WERE USED FOR THE DESIGNS SHOWN IN FIGURE 2–10 TO FIGURE 2–12.....	53
TABLE 2–6 DESIGN PARAMETERS THAT WERE USED IN EXAMPLES A AND B .....	55
TABLE 2–7 DESIGN PARAMETERS THAT WERE USED IN EXAMPLES C, D AND E .....	58
TABLE 2–8 SUMMARY OF PERFORMANCE OF EXAMPLE C, D, AND E .....	59
TABLE 2–9 STATIC RESULTS OF THREE CHEVRON TMAS WITH CONSTANT CURRENT INPUT.....	64
TABLE 2–10 DESIGN PARAMETERS THAT WERE USED IN EXAMPLES F, G AND H.....	69
TABLE 2–11 SUMMARY OF PERFORMANCE OF EXAMPLE F, G, AND H .....	72
TABLE 3–1 FUNCTIONAL REQUIREMENTS AND DESIGN CONSTRAINTS FOR THE RESONATOR .....	83
TABLE 3–2 ADJUSTING LONGITUDINAL AND LATERAL RESONANT FREQUENCIES OF THE DCPCF .....	88
TABLE 3–3 DESIGN PARAMETERS AND IMPROVED PERFORMANCES OF CONTOURED TMAS IN COMPARISON TO CONVENTIONAL CONSTANT CROSS–SECTION TMAS .....	89
TABLE 3–4 SUMMARY OF MFM FIBER RESONATOR MODELING AND DESIGN .....	92
TABLE 4–1 MICRO–FABRICATION PLATFORM FOR SILICON ENDOSCOPIC SCANNER .....	104
TABLE 5–1 PERFORMANCE CRITERIA OF A TWO–PHOTON ENDOMICROSCOPE.....	116
TABLE 5–2 FUNCTIONAL REQUIREMENTS FOR THE ENDOSCOPIC SCANNER GENERATED BASED ON THE OPTICAL DESIGN .....	117
TABLE 5–3 PUGH CHART OF THE OPTICAL CONFIGURATION FOR CONCEPT SELECTION .....	119
TABLE 5–4 PUGH CHART OF THE SCANNING SCENARIOS FOR CONCEPT SELECTION .....	121
TABLE 5–5 FUNCTIONAL REQUIREMENTS FOR EACH OPTICAL COMPONENTS GENERATED BASED ON THE OPTICAL SYSTEM CHARACTERISTICS .....	123
TABLE 5–6 SPECIFICATIONS OF THE SELECTED PRISM AND THREE FINAL CANDIDATES OF GRIN LENSES.....	124
TABLE 5–7 SUMMARY OF FABRICATION ERROR SENSITIVITY ANALYSIS AND ITS AFFECTS ON $\Delta H$ (X–AXIS) .....	126
TABLE 5–8 GRIN LENS AND PARAMETERS THAT WERE USED FOR RAY TRACING MODEL .....	126
TABLE 5–9 PUGH CHART OF THE GRIN LENS SHUTTLE FOR CONCEPT SELECTION.....	134
TABLE 5–10 EFFECTS OF PULSE WIDENING ON THE DCPCF .....	138
TABLE 5–11 FUNCTIONAL REQUIREMENTS FOR THE ENDOSCOPIC SCANNER .....	138
TABLE 5–12 FUNCTIONAL REQUIREMENTS AND CONSTRAINTS FOR THE TMAS THAT WERE USED IN THE SOB .....	141
TABLE 5–13 SIMULATED PERFORMANCE OF CONTOURED TMA FOR THE SOB .....	141
TABLE 5–14 DESIGN PARAMETERS AND PERFORMANCE ENHANCEMENTS OF CONTOURED TMAS THAT WERE USED IN GRIN LENS SHUTTLE AND PRISM SHUTTLE .....	142
TABLE 5–15 SIMULATED PERFORMANCE OF TRANSLATIONAL AND ROTARY BEARING WITH INTEGRATED TMA TRAIN .....	143
TABLE 5–16 SUMMARY OF THREE SCANNER DESIGNS FOR DIFFERENT OBJECTIVES.....	151
TABLE 5–17 SUMMARY OF GRIN LENS DYNAMIC TEST .....	154
TABLE 5–18 SUMMARY OF HIGH–SPEED PULSING TECHNIQUE APPLIED ON GRIN LENS SHUTTLE .....	157
TABLE 5–19 PERFORMANCE ENHANCEMENTS OF CONTOURED TMAS THAT WERE USED IN GRIN LENS SHUTTLE .....	157
TABLE 5–20 SUMMARY PRISM SHUTTLE DYNAMIC TEST .....	159
TABLE 5–21 PUGH CHART OF ACTUATOR SELECTION FOR THE MESO–SCALE FIBER RESONATOR.....	163
TABLE 5–22 SPECIFICATIONS OF THE SELECTED PIEZOELECTRIC ACTUATOR (PI, P–882.51).....	163
TABLE 5–23 SUMMARY OF SIMULATED PERFORMANCE FOR CONCEPTS A, B, AND C .....	164
TABLE 5–24 PUGH CHART OF THE FIBER RESONATOR FOR CONCEPT SELECTION .....	164

TABLE 5–25 NORMALIZED MATERIAL PROPERTY TABLE FOR MATERIAL SELECTION .....	165
TABLE 5–26 SUMMARY OF MESO–SCALE FIBER RESONATOR CHARACTERISTICS .....	166
TABLE 5–27 PARAMETERS THAT WERE USED FOR MFM RESONATOR EXPERIMENT .....	173
TABLE 5–28 SUMMARY OF MFM EXPERIMENTAL RESULTS .....	173

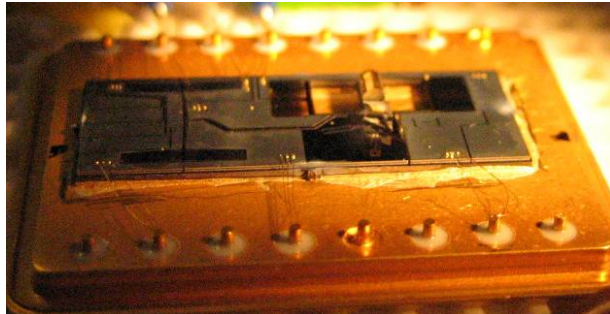
**Introduction**

---

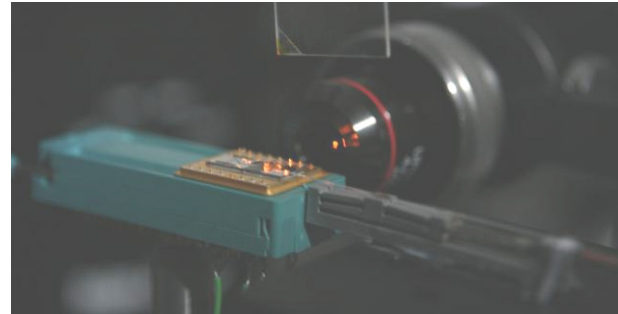
**1.1 Synopsis**

The purpose of this research was to understand and advance the physical limits of micro-scale thermomechanical actuators (TMAs) when (1) geometric contouring and (2) mechanical frequency multiplication (MFM) are used in their design and control. When combined, these techniques have been shown to simultaneously improve the force, speed, and stroke of a TMA by more than an order of magnitude. The results of this work are important because there are emerging applications that require small-scale actuators with performance characteristics that are far beyond the capabilities of state-of-the-art actuators. For example, the case study scanning device for this research requires 100s-micron stroke, kHz bandwidth, and 10s mN force from its micro-actuators. In the absence of new actuator technology, several emerging applications that require high performance actuators will never be realized. Many of these applications are related to “nano” and “bio” technologies. Improved actuator concepts, modeling/simulation tools, and control methods are therefore important to the broad and rapid adoption of new technologies and products in the nano and bio fields. The results of this research provide these concepts, tools, and methods. Given the actuator technology, the impact of this research is envisioned to be realized through new applications such as endoscopic imaging, micro-optics alignment and positioning, and probe-based nanomanufacturing.

The results of this work enable the design of a new type of TMA. The systematic approach created herein for the design and optimization of TMAs may also be used to improve the performance of other micro-actuators. The utility of the concepts, and the accuracy of the models for TMAs, were ascertained via experiment upon the three-axis, high-bandwidth micro-optical scanner that is shown in Figure 1-1. This device is intended for use in optical biopsy.



A: A packaged micro-optical scanner with GRIN lens and prism mounted



B: The packaged scanner aligned with the fiber and femto-second laser for two-photon imaging

**Figure 1-1 A case study micro-fabricated three-axis optical scanner**

## 1.2 Scope

This section presents a brief overview of the reasons why this research was undertaken and a synopsis of the research results. The discussion will start in the context of a practical application that requires a new type of actuator—a three-axis high-bandwidth micro-scanner—to enable optical raster scanning for endoscopic applications. The following bullet points provide a summary of the requirements for the endoscopic scanner:

- Force:  $\sim 10$ s mN
- Bandwidth:  $\sim 100$ s to 1000s Hz
- Stroke:  $\sim 100$ s  $\mu$ m
- Scanner envelope: less than 7 mm

At present, no micro-actuator technology satisfies these performance requirements. This level of performance is increasingly required in applications within emerging fields such as nanomanufacturing [1, 2], active alignment and manipulation of micro-optics [3, 4], data storage [5–7], instruments for nano-scale measurements [8], and the manipulation of samples for biomedical and biological experiments [5]. As will be explained later, TMAs were the most promising micro-actuator, but they were not good enough. This research will therefore focus upon new concepts and approaches that lead to TMAs with fundamentally different behaviors that allow them to achieve order of magnitude improvement in performance. The following provides background on the working principle of TMAs and then covers the concepts and methods that were generated in this thesis.

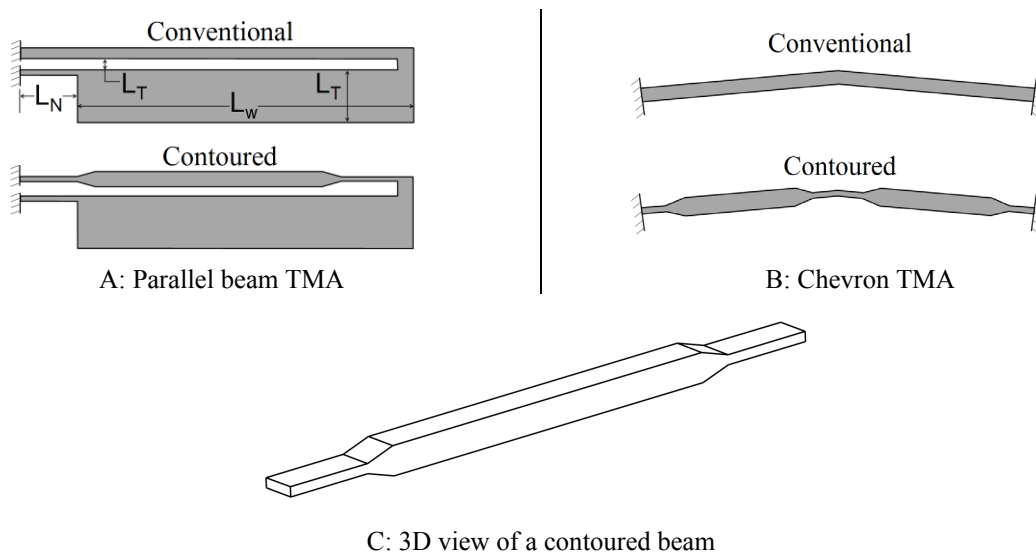
A TMA makes use of Joule heating and the thermal expansion of materials to generate displacements. Figure 1-2A and Figure 1-2B show two types of TMAs—parallel TMAs [9–11]



and chevron TMAs [12–14]. These TMAs contain at least one slender beam that acts as the transducing element. When a current is passed through these beams, the Joule heating causes the beams to strain in a way that enables the TMAs to exert forces and impose displacements. Although TMAs are well-known for their moderate force and stroke outputs, their bandwidth is limited by large thermal time constants. Through this work, it has been found that the limitations associated with thermal time constants may be overcome via the application of (1) geometric contouring, as shown in Figure 1–2 and (2) mechanical frequency multiplication, as shown in Figure 1–3.

**Geometric contouring**

The geometric contouring method refers to the variation of the cross-section of a TMA’s heated beam along its length, as illustrated in Figure 1–2. If designed properly, this technique simultaneously enhances a TMA’s thermal and mechanical behavior, thereby improving the TMA’s static and dynamic performance. In later sections, it will be shown that it is possible to simultaneously achieve large improvements in stroke ( $\uparrow 4x$ ), force ( $\uparrow 2x$ ), and bandwidth ( $\uparrow 20x$ ). It will also be shown that the power consumption ( $\downarrow 40\%$ ) and stored mechanical energy may be reduced.



**Figure 1–2 Commonly used micro-scale TMAs and the concept of geometric contouring**

### Mechanical frequency multiplication

MFM is an approach that enables a low-speed actuator to exhibit high-bandwidth/force/stroke when it is arrayed with other, similar actuators. As shown in Figure 1-3, a typical MFM system consists of many parallel, flexure-connected and opposed actuator pairs that are driven by properly delayed, *i.e.* phased, signals. The opposed actuators possess different forward and return stroke speeds. The concept of MFM is to use the high-speed portion of the one actuator to rapidly achieve half-cycle motion and then use the high-speed portion of an opposed actuator to rapidly return through the last half cycle. If  $N$  actuator pairs are placed in parallel, time delayed signals may be used to drive each set with a delay, thereby increasing the cycling frequency by  $N$ . A TMA is a good example of the implementation of the MFM concept because of the large difference between forward and return stroke speeds.

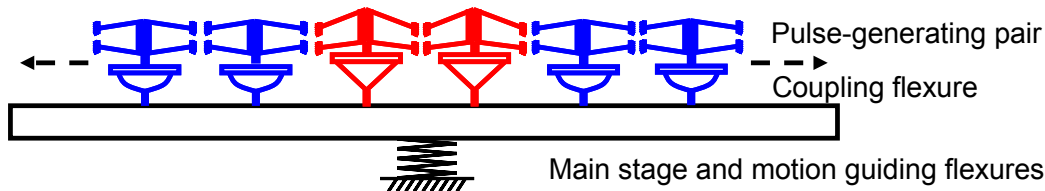


Figure 1-3 Schematics for a mechanical frequency multiplier

The principle of geometric contouring and MFM were implemented and the benefits were ascertained within the following case study on a high-bandwidth scanning system.

### Case study: Three-axis high-speed scanner

A scanner for a two-photon endomicroscope was selected as a case study for the micro-actuator technology. This implementation was chosen because of its demanding functional requirements and its potential for high impact on next-generation medical instrumentation. As will be explained in later sections, TMAs were used because they were the most suitable micro-actuation technology when considering the low voltage requirement for *in vivo* procedures. The creation of an *in vivo* two-photon endomicroscope opens the door to enabling optical biopsy—a minimally invasive procedure. In contrast, traditional excisional biopsy is invasive and typically takes weeks to receive results. As a two-photon endomicroscope acquires real-time tissue information, the optical biopsy may be used to expedite examination procedures, reduce personnel costs and reduce risks to the patient. Optical biopsies may therefore be performed

more frequently and this is envisioned to lead to the detection of more cancers at earlier stages. This would in turn save more lives.

The primary technologies that were used in this research are now reviewed with the aim of justifying their use, and providing context for discussion in subsequent sections.

### 1.3 Review of micro-actuators for positioning

Four micro-actuation technologies have been reviewed: (1) electrostatic, (2) electromagnetic, (3) piezoelectric, and (4) thermomechanical. The relative advantages and disadvantages of each are discussed. The case study provides a basis for comparing the characteristics of each actuator to practical needs. The results are summarized in Table 1–1. Note that in this research maximum force, maximum stroke, and maximum speed were used as the performance metrics for comparing micro-actuators. Although actuation stress and actuation strain are more commonly used metrics for macro-scale actuators, it was better to compare micro-scale actuators/devices with actuation force and displacement because of their limited scalability, which is caused by limited variation in sizes and fabrication processes [15].

**Table 1–1 : Micro-actuator performance in comparison to functional requirements (FRs) of a three-axis endoscopic scanner**

Parameters	Speed	Force	Stroke	Foot-print	Normalized energy density ratios [16, 17]	Ease of Fabrication	Ease of integration for multi-axis actuation
Endoscopic Scanner FRs	1–3 kHz	10 mN	100 $\mu\text{m}$	< 7 mm			
Actuation type							
Electrostatic	+	x	+	–	$\sim 10^{-4}$	+	x
Electromagnetic	o	+	+	–	$\sim 10^{-2}$	–	–
Piezoelectric	+	+	x	+	$\sim 10^{-1} - 10^{-2}$	–	–
Electrothermal	–	+	+	+	1 ( $10^{5-7} \text{ Jm}^{-3}$ )	+	+
Nomenclature	+: good (better than FRs) –: bad (needs extensive research work)				o: normal (satisfies FRs with proper design) x: hopeless (limited by fundamental principles)		

#### 1.3.1 Electrostatic

Electrostatic actuators generate force and motion by utilizing gradients in electrostatic fields. Such actuators have been used extensively in micro-devices because of their low power consumption [18]. Electrostatic actuators are, however, not suitable for high-force and multi-axis positioning applications because of their low force density and the tight space constraints

between the electrodes, *i.e.* the small gaps between the electrodes. The later was a problem as the gaps may be on the order of the fabrication errors.

Comb-drives are the most commonly used type of electrostatic actuators. They are able to provide  $\sim 10$ s of microns range [19] and bandwidths of 1–10s of kHz [20]. Although each comb-finger provides only a small force ( $\sim 1$ – $10$ nN), milli-Newton level of force may be achieved by stacking large-area fingers [21], or by reducing the gaps between moving fingers and stators [20]. It is difficult to generate milli-Newtons of force without adding a significant amount of mass to the system through added combs because of their low force and energy density. Comb-drive actuators may also be used to design long-stroke ( $\sim 100$   $\mu\text{m}$ ) X–Y positioners [22]. Interdigital comb structures limit the ability of comb-drive to perform combined in- and out-of-plane motions. Applications for comb-drive actuators range from positioning optical elements to data storage [7, 19, 23–28]. Comb-drives actuators may also be used to generate lateral motion, *i.e.* the parallel-plate actuators [29–37]. This configuration will increase the force output by sacrificing the maximum range of actuator displacement ( $\sim 2$   $\mu\text{m}$ ).

Advantages:

Ease of micro-fabrication  
Long stroke  
High-speed  
Low power consumption

Disadvantages:

Low force density/output  
Limited capability of generating multi-axis motions

### 1.3.2 Electromagnetic<sup>1</sup>

Electromagnetic micro-actuators have the advantages of relatively high force and large stroke for the size of the actuator. These advantages come at the cost of a large actuator footprint ( $\sim$ cm), the need for external field sources (permanent or electro-magnets), and the complexity of micro-scale manufacturing and assembly processes. Currently, the complex micro-fabrication processes for electromagnetic actuators prevent them from being used for practical applications.

There are several research efforts that aim to integrate the micro-fabrication of micro-coils or permanent magnets for micro-electromagnetic actuator designs. Despite fabrication difficulties, researchers have built prototype micro-electromagnetic actuators/manipulators that

---

<sup>1</sup> This section was written with consultation and advice from my colleague Dariusz Golda, who specializes in micro-scale electromagnetic actuator and piezoelectric actuator design.

use external magnets for data storage [8, 38] and fluid pumps [39]. Large strokes ( $50+\mu\text{m}$ ) in one or two axes have been obtained only for slow speeds (10s of Hz) and large sizes ( $\sim\text{cm}$ ). The use of permanent magnets, and new coil concept designs have enabled some devices to operate in five axes [8, 40], while others have been able to achieve high-speeds ( $\sim 1\text{ kHz}$ ) [8, 41, 42] and a relatively small device footprint ( $\sim 1.5\text{ mm}$ ) [43].

Advantages:  
 High force  
 Long stroke  
 Ability to attract and repel

Disadvantages:  
 Large actuator footprint  
 Need for external field source  
 Complex micro-fabrication/assembly processes

### 1.3.3 Piezoelectric

Piezoelectric actuators produce mechanical strain when a voltage is applied across a piezoelectric material. The advantages of piezoelectric actuators include high energy density, high bandwidth, and lower operating voltages in comparison to electrostatic actuators. Fabrication complexity and the poor reproducibility of the material make-up and the geometric characteristics of actuators combine to limit the practical application of piezoelectric actuators in small-scale positioning devices.

Micro-piezoelectric actuators provide limited strain and displacement (strain  $\sim 0.1\%$ ). In addition, they may only be fabricated/deposited as thin films ( $\sim 1\ \mu\text{m}$ ) and these films do not provide enough force to actuate bulk micro-mechanical structures ( $\sim 10\text{s to }100\text{s }\mu\text{m}$ ) that are encountered in precision positioning applications. The most common type of micro-scale piezoelectric actuator is the bimorph cantilever beam [44–47]. In addition to the bimorph beam, several devices have been created, including tunable optical gratings, linear drive systems, rotary motors, and 2D mirror scanners [48–53]. Piezoelectric actuated multi-axis micro-positioners have not been demonstrated because of the difficulties associated with generating in-plane motion.

Advantages:  
 High energy density  
 High bandwidth  
 Lower operating voltage compared to electrostatics

Disadvantages:  
 Complex micro-fabrication process  
 Poor reproducibility of actuator characteristics  
 Limited output displacement

### 1.3.4 Thermomechanical

TMAAs have been the most widely used actuators in Microelectromechanical Systems (MEMS). This class of actuator generates controlled mechanical motions via electrothermal transduction that provides relatively large energy/force density, typically 2–4 orders of magnitude higher than other micro-actuators, as shown in Table 1–1 [16, 17]. TMAAs possess the advantages that are enabled by the use of simple/elegant shapes/structures: manufacturability, small device envelopes, moderately high force/stroke, and low-voltages. Several micro-scale nanopositioners have been designed with integrated TMAAs [4, 54–57]. The disadvantages of TMAAs include low bandwidth, high/constant power consumption, and high operating temperature ( $\sim 1000$  °K) that may affect the accuracy and repeatability of a precision system. Important applications that have used TMAAs include thermal inkjet print heads [58, 59], micro-pumps/valves [60–62], bimorph beams [63, 64], and TMAAs that heat the bulk of a silicon structure to provide linear motion [9–14].

Parallel and chevron TMAAs are the two main types of TMAA that are used in MEMS nanopositioners [4, 54–57] and micro-motors [65–68]. These TMAAs may be designed to exert several mN of force [69], to possess bandwidth of thousands of Hz [4], and to provide nanometer-level resolution over several micrometers of range [4]. Note that each of the aforementioned state-of-the-art performance goals for force, speed, and stroke were achieved at the expense of one of the other two goals.

Previous work aimed to (i) model the dominant physical phenomena that govern the performance and (ii) optimize the beam geometry of a TMAA. For example, coupled-domain modeling work, *i.e.* the linking of the thermal and mechanical domains, has been conducted in order to better understand how the physics may be used to accurately predict actuator performance [70–72]. Numerous studies were undertaken in order to optimize the performance of TMAAs by adjusting the length and width of the TMAA's beams [73–76], or by incorporating flexural bearings into standard TMAAs so as to reduce stress concentration without considering thermal effects [77].

Advantages:  
High energy density  
Ease of fabrication

Disadvantages:  
High power consumption  
Low bandwidth

Small device envelope  
Low operation voltage  
Multi-axis actuation capability

High operating temperature

### 1.3.5 Micro-actuators comparison

At present, no micro-actuator technology satisfies the performance criteria for the emerging small-scale devices, as summarized in Table 1-1. TMAs were selected for this work because of their qualities in regards to designing/fabricating decoupled axes of motion. Also, the high force/energy density nature enables TMA-driven nanopositioners to possess a reduced device envelope ( $\sim$ mm) and a higher natural frequency (on the order of 1-10s kHz). Electrostatic actuators have been ruled out for the prototype because of their low force/energy density and high operating voltages. Piezoelectric actuators have not been considered because of their limited stroke and inconsistent material and geometric characteristics. Electromagnetic micro-actuators were the only alternative for which operating physics did not fundamentally limit their effectiveness. Unfortunately, the complex fabrication processes and larger footprint ( $\sim$ cm) for electromagnetic micro-actuators makes them less suitable for use in small-scale positioners. Provided that the low bandwidth ( $\sim$ 100s Hz) limitations of meso-scale TMAs may be resolved, TMAs would be the best candidate for miniaturized nanopositioners.

This research aims to enhance the overall performance of micro-scale TMAs, *i.e.* increase the bandwidth, reduce the power consumption and operating temperature while retaining their high energy density, ease of fabrication, and small envelope. This thesis will show that this may be achieved through the application of geometric contouring and MFM.

## 1.4 Flexure system and precision motion guidance

Flexure systems generate smooth and controlled motions via the compliance of their structure. They possess advantages over traditional mechanisms in precision motion application. Advantages include: no wear between joint members, no backlash, low hysteresis, and no assembly required [78]. The later is important as it is difficult to assemble conventional bearing types at the small-scale. Flexures are the only viable bearing technology. Micro-actuators may be fabricated and integrated with micro-scale flexure mechanisms. When actuated, the actuators cause the flexible members to deform, thereby producing controlled motions that may be used for positioning. Flexural bearings, however, usually operate with some parasitic error motions,

and they require a large device envelope to obtain the range that may be attained by other types of bearings. Recent advances in compliant mechanism synthesis tools [79] and modeling methods [78, 80, 81] have improved the modeling accuracy for micro-scale flexure mechanisms. These advances in modeling and designing flexure mechanisms has enabled the creation of micro-scale, nanometer resolution, multi-axis positioning stages [4] which are in need of new actuation technologies.

One distinctive drawback with flexures is that, during flexing, about 50% of the energy exerted by the actuator will not be available for producing work; instead this energy will be stored in the deformed flexures. The contouring of flexural elements has been extensively used to alleviate this problem. This approach, however, has not been properly used in the design of micro-scale TMAs. Designers in the past either did not consider the problem of energy storing in TMA flexures [73–76] or (2) did not consider contouring in thermal and mechanical energy domains [77]. The geometric contouring method that has come from this work tackles this issue by utilizing properly designed contoured beams to improve thermal and mechanical performance. Detailed modeling and design methods for this will be discussed in Chapter 2.

## **1.5 Optical microscopy for high resolution biomedical imaging**

The technology outlined in this research may be applied in a variety of applications that require precision positioning as discussed previously. This section covers applications that form the basis for the case study. In order to understand the case study, it is important to understand the field of application – optical scanning microscopy.

Many situations exist wherein it is necessary to “see” inside of the body. In macro-scale embodiments of these microscopy techniques, samples are placed upon a large scanning stage. For *in vivo* imaging, the optics/lenses must be manipulated within the body and the scanning accomplished therein. As such, optical microscopes with three-dimensional (3D) resolving capability are needed, but they must be miniaturized and incorporated within an endoscope that may be placed through relatively small ports that allow minimally invasive access to body cavities. Three-dimensional imaging of tissues in this way would be an important advance in minimally invasive surgery and could complement or supplant the need for excisional biopsies.



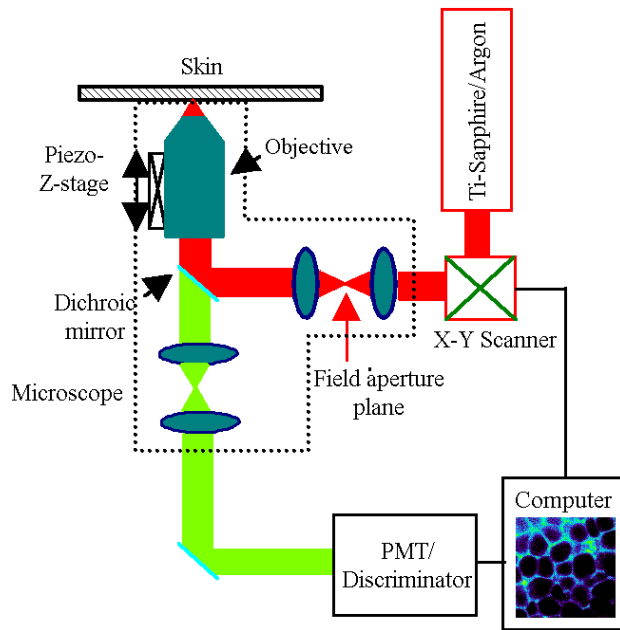
Small scale precision positioning technologies are needed to realize optical endomicroscopy when scanning of micro-optical components is necessary.

The following sections review the working principles of (1) two-photon excitation microscopy, (2) confocal microscopy, and (3) optical coherence tomography. These sections also explain why two-photon excitation (TPE) microscopy is more suitable for *in vivo* procedures than the other methods. The case-study is focused upon a scanner for a two-photon endomicroscope. Previous works on confocal and TPE endomicroscopes are also discussed.

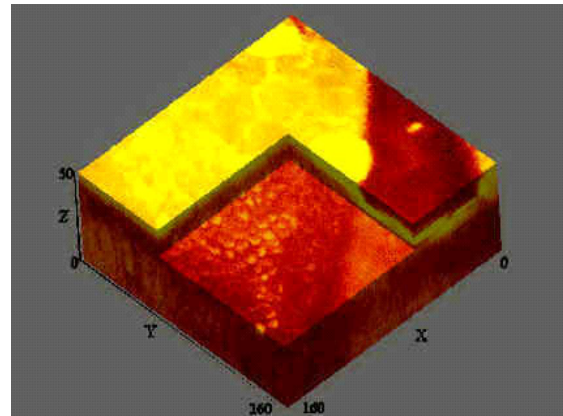
### **1.5.1 Two-photon excitation microscopy**

Two-photon excitation (TPE) microscopy was introduced by Denk et al in 1990 [82]. It is a 3D imaging technology that is based upon non-linear excitation of fluorophores. This multi-photon excitation phenomenon was first predicted by Maria Göppert-Mayer in 1931 within her doctoral thesis [83], but it was not confirmed until after the advent of laser technology. The non-linear phenomenon that makes TPE possible may be achieved through specimens that have a nonlinear optical cross-section with sufficiently intense illumination, for example, a femtosecond Ti-Sapphire pulsed laser. A second order nonlinear susceptibility exists in specimens that have non-centrosymmetric geometry, such as  $\text{LiNbO}_3$ .

Figure 1-4A shows the configuration of a common macro-scale two-photon microscope. An infrared excitation signal is first sent to the sample through two lenses (4F system) for beam expansion and spatial filtering. The returning emission light is then collected through the objective lens and filtered through a frequency selective dichroic mirror. The data are then processed by a computer that regenerates a volumetric image, for example, the reconstructed 3D representation of human skin that is shown in Figure 1-4B.



A: Schematic of a typical two-photon microscope



B: A 3D volumetric view of human skin structures demonstrating the non-invasive visualization of the stratum corneum and the epidermal-dermal junction from a volunteer

**Figure 1-4 Schematic of a typical two-photon microscope and a 3D sample image of human skin tissue (Courtesy of Professor Peter So)**

A single-photon microscope, *e.g.* a confocal microscope, provides increased lateral and axial resolution that is on the order of 0.16 and 0.65 microns respectively. A TPE microscope possesses resolution characteristics that are less fine – lateral and axial resolution of 0.28 and 1.07 microns. Even so, the use of TPE microscopy is often desired because of the following advantages that make it more suitable for live tissue imaging and clinical diagnosis [84, 85]:

1. TPE generates fine depth ( $\sim 1 \mu\text{m}$ ) discrimination based on highly localized fluorescence at the focal point and therefore greatly reduces photo-bleaching and photo-damaging, in contrast to a confocal microscope.
2. TPE has the ability to image biological specimens to a depth of 200~500 micrometers because of the reduced scattering and absorption of near infrared light in comparison to UV and visible wavelengths.
3. TPE allows high sensitivity imaging by eliminating the contamination of fluorescence signal by the excitation light.

4. TPE has the ability to initiate photochemical reactions within a sub-femto liter volume inside cells and tissues. This capability enables the study of photochemical reactions and other biological phenomena within live cells.

### 1.5.2 Confocal microscopy

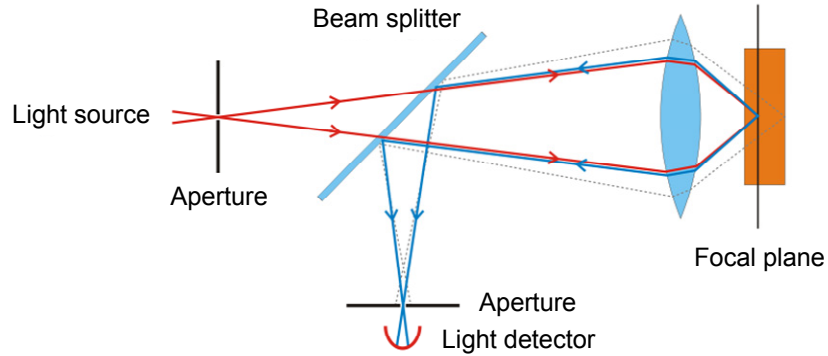
Confocal microscopy, which was created and patented by Marvin Minsky in 1961, is a technique that is capable of collecting non-invasive images of tissues with sub-cellular resolution. It has been extensively used as a tool for live cell microscopy as its commercial introduction in the 1980s [85–87]. Depth discrimination in confocal microscopy is achieved by placing a pinhole in front of a photodetector to exclude out-of-focus light.

Figure 1–5 contains an illustration of the configuration for a typical confocal microscope, where the returning light is redirected to the light detection apparatus by a beam splitter. The out-of-focus image is blocked by a pinhole in front of the light detector, and therefore depth discrimination may be achieved. Figure 1–6 compares the excitation profiles of a one-photon confocal microscope and a TPE microscope. This may be used to understand why a TPE microscope generates less photo-bleaching and photo-damaging in comparison to a confocal microscope. In Figure 1–6A, fluorescence excitation is observed throughout the path of the laser beam while fluorescein solution is excited by one-photon (top arrow) via a 0.1 NA objective. For a TPE microscope that uses a second objective with same NA (bottom arrow), fluorescence excitation occurs only within a 3D localized spot. The schematic diagram in Figure 1–6B explains what happens in Figure 1–6A.

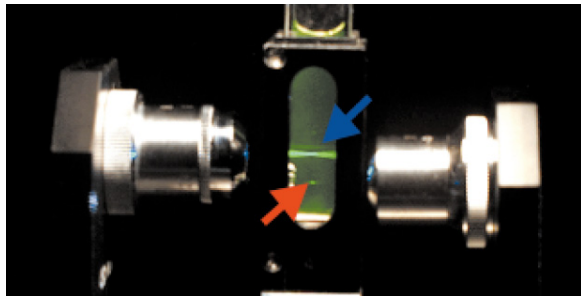
Confocal microscopy may also be operated in fluorescence mode but has several disadvantages in comparison to TPE:

1. Confocal microscopy has a shallower depth penetration (less than 200  $\mu\text{m}$ ) because of absorption of excitation energy throughout the beam path.
2. The use of a detection aperture in confocal microscopy yields significant rejection of scattered photons that may be retained in a TPE endomicroscopes. As a result, a confocal microscope has a lower signal to noise ratio than TPE.

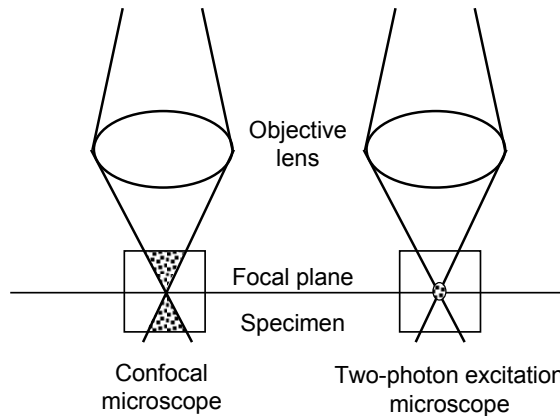
- TPE endomicroscopy produces less photo-damage to tissues than the fluorescence confocal endomicroscope because of the inherent localization of the excitation volume.



**Figure 1-5 Schematic and working principle of a typical confocal microscope**



A: Excitation profiles of a one-photon microscope (top arrow) and a TPE microscope (bottom arrow)



B: A schematic that explains the difference in excitation profiles between a confocal and TPE microscope

**Figure 1-6 A comparison of a one-photon confocal microscope and TPE microscope excitation profiles (Courtesy of Professor Peter So)**

### 1.5.3 Optical coherence tomography (OCT)

OCT is a low coherence interferometry technique that is capable of providing non-invasive optical tomographic imaging and millimeter penetration with axial and lateral resolution that is on the order of tens of microns. The technique was first introduced in 1991 by Professor Fujimoto's group at MIT [88]. OCT systems based on single point or operated in time domain must scan the sample in two lateral dimensions and reconstruct a three-dimensional image using depth information that is obtained via coherence-gating through an axially scanning reference arm [89, 90].

In comparison to TPE and confocal microscopes, an OCT system typically works in a different range for different purposes, *e.g.* ophthalmic applications. A TPE endomicroscope possesses the following advantages over a miniaturized OCT system:

1. An OCT system has lower resolution ( $\sim 10\ \mu\text{m}$ ) than a TPE or confocal microscope although the OCT system provides deeper tissue penetration capability ( $\sim 1\text{mm}$ ).
2. An OCT system only provides morphological tissue images. In contrast, a TPE or confocal system allows selective imaging by placing specific fluorescent labels on the desired target.

## **1.6 Case study: Scanner for a two-photon endomicroscope**

### **1.6.1 Overview of device function and prior art**

The case study for this research was based upon the design and fabrication of a three-axis millimeter-scale optical scanner for a two-photon endomicroscope<sup>2</sup>. This endomicroscope would enable numerous benefits over excisional biopsy. For example, (1) non-invasive optical screening may decrease the number of excision biopsies that are required, (2) optical biopsy may provide more informed selection of excisional biopsy sites minimizing incorrect diagnosis that occurs because of random sampling, and (3) optical biopsy may reduce the labor cost and time required for inspection.

Early attempts at two-photon endoscopes have had varying success. Miniature, hand-held two-photon systems that use Lissajous fiber scanners were able to image brain activity in freely-moving rats [91]. Long, rigid, externally-scanned two-photon endoscopes have used single fibers [92], and more recently fiber bundles [93] to demonstrate the capability of 2D surface scanning. An attempt at two-photon endoscopy was demonstrated with limited success by moving the sample around the distal tip [94]. Despite these advances, the integration of a two-photon optical system and a 3D volumetric scanner within the distal tip of an endomicroscope has yet to be achieved because of the specific speed and range requirements and size constraints that must be met. Micro-actuators would be needed and the state-of-the-art in

---

<sup>2</sup> This project is in collaboration with Professor Peter So's group at MIT.

small-scale actuators had not reached a point at which it could make the scanning technology practical.

### 1.6.2 Functional requirements and constraints

A two-photon endomicroscope requires scanning of a focused point of light to acquire tissue images throughout a volume. The scanning process must be completed between heartbeats in order to keep the tissue-scanner registration accurate during the scanning time. Depending upon the number and the size of optical sections, this constraint will set the scanning speed and range. *In vivo* devices also require a low operating voltage (less than 5V) in order to prevent “shocks” to the heart. To satisfy the aforementioned requirements and constraints, the endoscopic scanner should operate at 3 kHz, 30 Hz, and 2 Hz for the X,  $\theta_x$ , and Z (optical) axis respectively. The focused laser should scan 100 microns in all three axes. Meanwhile, the envelope of the scanner should reside within a 7mm  $\varnothing$  endoscope port. These functional requirements were generated based on clinical needs and they are necessary because of the miniaturized optics and the need for a reasonable frame rate. The functional requirements are summarized in Table 1–2.

**Table 1–2 Functional requirements for the endoscopic scanner generated based on the optical design**

Axis	X	$\theta_x$	Z
Range	100 $\mu\text{m}$	2°	100 $\mu\text{m}$
Speed	3 kHz	30 Hz	2 Hz

### 1.6.3 Proposed solutions and technologies

High-performance TMAs were created in a form that would enable a 3D endoscopic scanner to achieve the design goals that were previously discussed. It is important to note that the bandwidth and stroke requirements are about one order of magnitude larger than that which current technologies may achieve. The 3D endoscopic scanner design consists of (1) an active silicon optical platform that constrains, aligns, and actuates the small optics and (2) a fiber resonator. Both of these sub-systems operate at less than 5V. In depth design procedures and discussions of the two-photon endomicroscope will be presented in Chapter 5.

### 1.6.4 Potential impact of the case study

The scanner was designed to provide a critical component of a TPE endomicroscope. Once all other pieces fall into place, a TPE endomicroscope will be able to provide real-time

sub-cellular resolution volumetric images of live tissues that may be as deep as 200–500 microns. This type of high resolution optical imaging has the potential to be a powerful new tool for clinicians and pathologists to improve their diagnostic accuracy and efficiency. The creation of a TPE endomicroscope may have significant impact on the diagnosis, staging, and treatment of a number of prevalent cancers. In particular, this technique may be used in diagnosis and treatment of early epithelial cancers where tissue imaging to a depth of a few hundred microns may be sufficient. Some important cancer types that fall within this category include colorectal, esophageal, and cervical cancers. Information regarding several cancer types is summarized in Table 1–3. Table 1–3 lists (1) the current U.S. overall mortality rates, (2) mortality rates that occur even after early detection of a cancer, and (3) the percentage of patients that have cancer detected at early stages.

**Table 1–3 Internal cancers that would be impacted via TPE endomicroscopy [95]**

Type	New cases per year	Mortality rates	Mortality rates for early detection	Percentage of patients with cancers detected at early stages
– Colorectal	150,000	53%	10%	39%
– Esophageal	15,000	90%	52%	1%
– Cervical	12,000	36%	5%	N/A

Table 1–3 shows that (a) there is room to increase the percentage of patients that have their conditions detected early and (b) early detection prevents mortality in a significant percentage of those afflicted. The combination of items (a), (b), and the number of new cases per year shows the potential impact that early cancer screening tools may have on human health and well-being.

*This page is intentionally left blank*



# Geometric Contouring of TMAs

---

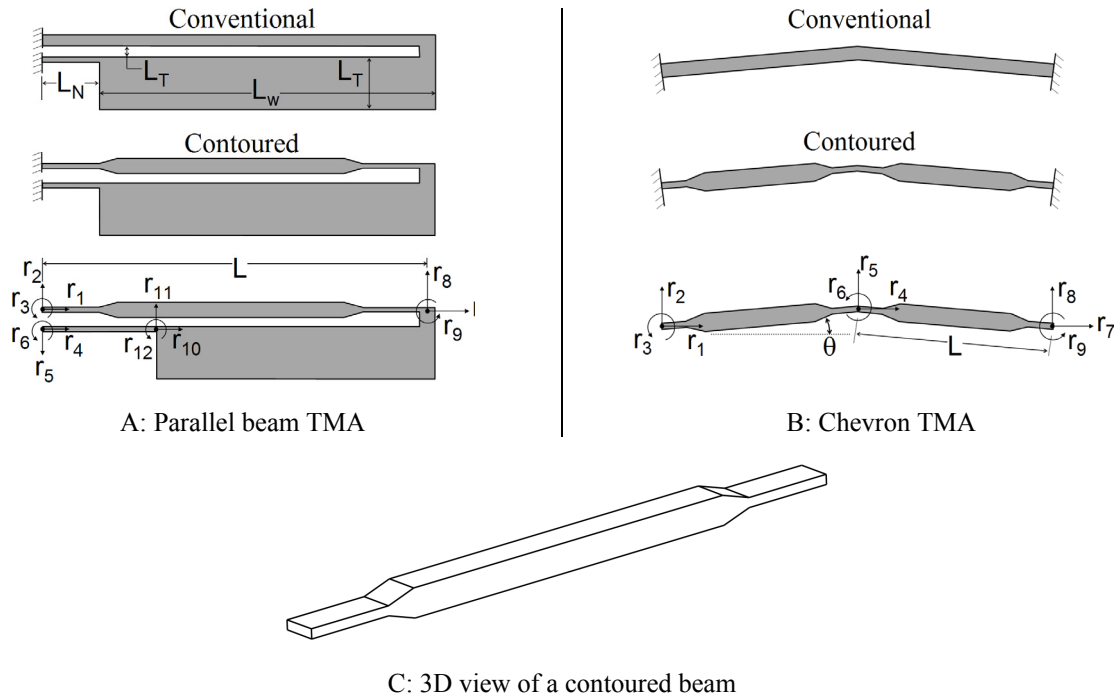
This chapter presents the theory and models of the geometric contouring method that enhances the static and dynamic performance of TMAs. Parametric models were constructed to create a deterministic link between the actuator's design parameters and the actuator's performance characteristics. This chapter also introduces the concept of high-bandwidth pulsing, *i.e.* the use of a transient temperature profile to extend the bandwidth of a contoured TMA.

This chapter aims to teach designers how a conventional TMA may be contoured in order to optimize its static and dynamic performance to satisfy specific functional requirements. The theory and models were combined within a design tool that shows less than 5% error from non-linear Finite Element Analysis (FEA) simulations. The design tool has been used to generate plots that enable designers to (1) understand the qualitative relationships between design parameters and performance and (2) select first-pass design parameters. Designers will be able to use the contents of this chapter to optimize TMAs for desired level of performance enhancement.

## 2.1 Introduction: Concepts and design parameters

Conventional TMAs contain slender, constant cross-section beams. When a current is passed through these beams, the Joule heating causes the beams to strain in a way that enables them to exert force and/or impose a displacement. Figure 2-1A and Figure 2-1B show common TMAs: the parallel beam TMA [9-11] and the chevron TMA [12-14]. TMAs may be designed to exert several mN of force [69], possess bandwidths of thousands of Hz [4], and provide nanometer-level resolution over several micrometers of range [4]. These characteristics, in addition to their ease-of-fabrication, lead to their frequent use in a variety of meso-/micro-scale

devices and positioning systems [4, 54–57]. For instance, they have been used in in-package active fiber alignment devices [96], micro-scanners that were used in endoscopes, and meso-/micro-scale nanositioners [4, 97–99]. The performance of the TMAs that were used in the aforementioned applications could have been improved by 2–10 times if the TMAs were contoured [100].



**Figure 2–1 Commonly used TMAs and relevant design parameters**

Numerous approaches, such as adjusting the length and width of the TMA’s beams [73–76], have been undertaken in order to optimize the performance of TMAs. The benefits of contouring a TMA’s beam cross-section along the beam’s length have not been investigated. A contoured beam is shown in Figure 2–1C. An optimally contoured TMA may simultaneously produce more than twice the force and stroke of a TMA with a constant cross-section. This is because of a constant cross-section beam does not:

- (1) maximize the amount of thermal strain that may be transformed into useful work;
- (2) minimize the strain energy that is stored within the driving beam.

By contouring a beam, *i.e.* optimizing the thermal profile of a beam, one may increase the thermal strain and the elastic range of the beam while decreasing the strain energy that is stored

in the beam during actuation. As a result, more energy is available to do useful work. The geometric parameters of the beam shown in Figure 2–2 may be selected so that this piece–wise contour emulates that of many arbitrary continuous beam contours. A full nomenclature of variables that were used in this research may be found in Appendix A. This contour will be described using five parameters,  $w_s$ ,  $w_L$ ,  $L_s$ ,  $L_L$ , and  $L$ .

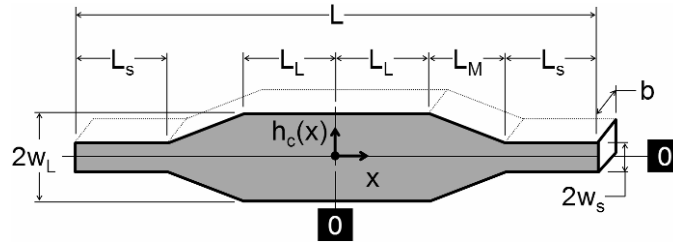


Figure 2–2 Design parameters that are used to describe the contoured beam’s geometry

## 2.2 Thermal modeling

### 2.2.1 Modeling assumptions

It has been shown [73, 96, 101] that conduction is usually the dominant mode of thermal energy transport in slender micro–scale silicon beams that experience Joule heating. For many micro–scale TMAs, it is not uncommon for conduction to account for over 98% of the heat transport while convection and radiation only account for the remaining 2% [96]. Although the design tool that was created in this work may be used to predict radiative and convective heat transfer, the following discussion assumes that their contributions are small compared to transport of heat via conduction.

It is important to note that the Biot number ( $Bi$ ) for micro–scale beams is generally on the order of  $10^{-5}$  to  $10^{-6}$ . A Biot number of this magnitude shows that the heat flow along the beam will be relatively large in comparison to the heat flow in orthogonal directions. As the  $Bi \ll 1$  for the actuators in this research, it was assumed that a 1D thermal conduction model was appropriate. With proper design, the ends of the Joule–heated beam may be maintained at a constant and relatively low, *e.g.*, 350 °K, temperature. As such, it was valid to apply a Dirichlet boundary condition at the end of the beam(s) [96]. In the following discussion of modeling, it is assumed that the electrical, thermal, and mechanical behavior may be modeled via continuum approaches.

### 2.2.2 1D thermal modeling

This section presents a generalized 1D thermal model that is suitable for quasi-static and dynamic modeling of contoured TMAs. This 1D model shows less than 2% error when compared to a 2D FEA model. The steps listed below and the flow chart shown in Figure 2–3 illustrate how the 1D thermal model was established.

Step 1: Construct a piece-wise function,  $A_{CT}(x)$ , for the contoured beam's cross-section area based on the selected design parameters. Then, select and design the driving signal, *i.e.* input current  $i(t)$ , as a function of time that enables specific actuator performance. Different driving signals will be discussed and presented in Section 2.8 and Section 3.4 for various objectives, *e.g.* high-bandwidth pulsing and frequency multiplication.

Step 2: Construct the current density function,  $J(x, t)$ , and convert the 2D contoured beam geometry into 1D by dividing the driving signal,  $i(t)$ , by the contoured beam's cross-section area. Current density,  $J(x, t)$ , was defined as the ratio of input current,  $i(t)$ , over cross-section area,  $A_{CT}(x)$ , of the contour beam. The heat generation per unit volume that was caused by resistive heating,  $\dot{q}$ , was then obtained by multiplying the electrical resistivity,  $\rho$ , of the material (silicon) by the square of current density.

Step 3: Construct and solve the 1D heat equation by substituting the heat generation term into the 1D heat equation with a proper initial condition and boundary conditions. In Figure 2–3, the assumptions that were used include that the system may be modeled as 1D and that heat flow that was caused by convection and radiation are small compared to conduction. The end results relate the temperature characteristics, and the thermal conductivity of the beam, to the material resistivity and current density.

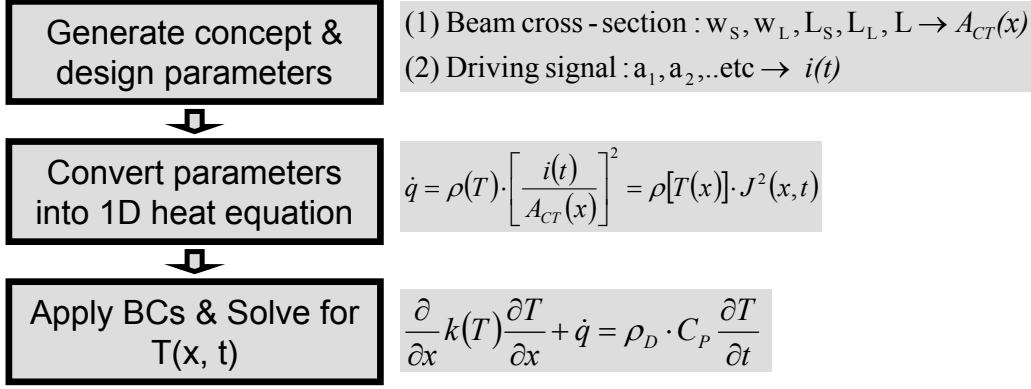


Figure 2–3 Schematics of thermal modeling for contoured TMAs

To use this generalized model for quasi–static modeling:

1. Set the transient term on the right of Equation (1) to zero.
2. Set the input current,  $i(t)$ , to a constant.

Equation (1) and (3) show the governing 1D heat equation that may be used to solve for the transient and the quasi–static thermal behavior of a Joule heated beam respectively.

$$\frac{\partial}{\partial x} k(T) \frac{\partial T}{\partial x} + \dot{q} = \rho_D \cdot C_P \cdot \frac{\partial T}{\partial t} \quad (01)$$

$$\dot{q} = \rho(T) \cdot \left[ \frac{I(t)}{A_{CT}(x)} \right]^2 = \rho[T(x)] \cdot J^2(x, t) \quad (02)$$

$$Static \Rightarrow \frac{d}{dx} k(T) \frac{dT(x)}{dx} = -\rho(T(x)) J^2(x) \quad (03)$$

The values of thermal conductivity,  $k$ , and electrical resistivity,  $\rho$ , may vary by a factor of three or more over the requisite temperature range (room temperature to 1000 °K). As such, Equations (4) and (5) were used to create a curve fit for the electrical resistivity and thermal conductivity as a function of temperature. The units that were used in Equations (4) and (5) are Ohm-m and W/m-°K respectively.

$$\rho(T) = 2.360 \cdot 10^{-12} T^3 - 4.640 \cdot 10^{-9} T^2 + 2.931 \cdot 10^{-6} T - 4.258 \cdot 10^{-4} \quad (04)$$

$$k(T) = 3.12 \cdot 10^{-4} T^2 - 0.55 T + 274.70 \quad (05)$$

Equations that are valid for boron–doped single crystal silicon at a doping level of  $10^{18}$  atoms/cm<sup>3</sup> were used [101].

The increase in beam length,  $\Delta_T$ , which is caused by thermal strain may then be calculated using Equation (6).

$$\Delta_T = \int_{-\frac{L}{2}}^{\frac{L}{2}} [\alpha(T(x))] \cdot [T(x) - T_0] dx \quad (06)$$

The thermal expansion coefficient, shown in Equation (7), also varies with temperature. Equation (7) shows the results of a curve fit calculation for the boron-doped single crystal silicon.

$$\alpha(T) = -4.16 \cdot 10^{-6} T^2 + 7.60 \cdot 10^{-3} T + 0.76 \quad (07)$$

The 1D heat equation was solved via a conventional fixed-step Runge-Kutta method. The uni-axial displacement of a single beam results from the solution of Equation (1) shows less than 5% error when compared with the results from a multi-physics (electrical, thermal, mechanical) COMSOL model. The beam design parameters that were used in this comparison (1D model vs. FEA) are listed in Table 2-1.

**Table 2-1 Design parameters that were used for with the thermomechanical modeling of a single beam**

Parameter	Value	Units
$i$	6, 10, 20, 25, 27	mA
$L$	600	$\mu\text{m}$
$L_S$	100	$\mu\text{m}$
$L_L$	200	$\mu\text{m}$
$w_S$	4	$\mu\text{m}$
$w_L$	12	$\mu\text{m}$
$w_e$	8	$\mu\text{m}$
$b$	30	$\mu\text{m}$
$T_0$	293.15	$^{\circ}\text{K}$

### 2.2.3 Effect of contouring on quasi-static thermal performance

Three examples are presented to better illustrate how contouring a beam will affect actuator performance. It was helpful to compare the thermal and mechanical results for constant cross-section and contoured beams. Toward this end, simulation results for contoured beams shall be compared to a constant cross-section beam that possesses the same depth,  $b$ , and length,  $L$ . The constant cross-section beam will possess an equivalent width,  $2w_e$ , that had been selected to ensure that the volume of the contoured beam and volume of the constant cross-section beam were identical. This was necessary as it ensured that an equivalent volume of material was

available to both beams for the purpose of converting electrical energy to useful work. Example 1 is a constant cross-section beam and examples 2 and 3 are contoured beams with different ratios of  $w_S$  to  $w_L$ . The ratio of these widths is defined via Equation (8) as  $w'$ .

$$w' = \frac{w_S}{w_L} \quad (08)$$

The goal of these examples was to provide a better understanding of how the heat generation per unit volume, *i.e.*, the right side of Equation (3), changes with beam geometry. The design parameters that were used in the examples are listed within Table 2–2.

**Table 2–2 Design parameters that were used in examples 1, 2, and 3**

	Example 1	Example 2	Example 3
Type	Constant cross section	Contour 1	Contour 2
$L_S/L_L$	N/A	4/5	4/5
$w'$	1	1/2	1/5.5
$w_e$	8 $\mu\text{m}$	8 $\mu\text{m}$	8 $\mu\text{m}$
$L$	600 $\mu\text{m}$	600 $\mu\text{m}$	600 $\mu\text{m}$
$b$	30 $\mu\text{m}$	30 $\mu\text{m}$	30 $\mu\text{m}$

In example 1, *i.e.*, the constant cross-section beam, the temperature profile is qualitatively similar to a quadratic function. The highest temperature is at the center of the beam. The maximum output of a TMA occurs when the temperature at any point within the driving beam(s) of the TMA is equal to the maximum temperature that may be experienced without failure of the material. The performance of an actuator with a quadratic temperature profile is therefore limited as only a small portion of the material near the centre is close to failure. The rest of the material is at a lower temperature and therefore it is not fully utilized in converting thermal energy to mechanical energy. The beam's performance may be enhanced by increasing the temperatures in the aforementioned locations, *i.e.* the two-ends of the beam. A more uniform temperature profile may be realized by manipulating the value of  $w'$ . To demonstrate this point, one may compare the temperature profile and heat generated per unit volume for a contoured and a constant cross-section beam. Figure 2–4A and Figure 2–4B show a comparison for the heat generation and temperature profiles of examples 1 (constant cross-section, CC) and 2 (contoured, CT).

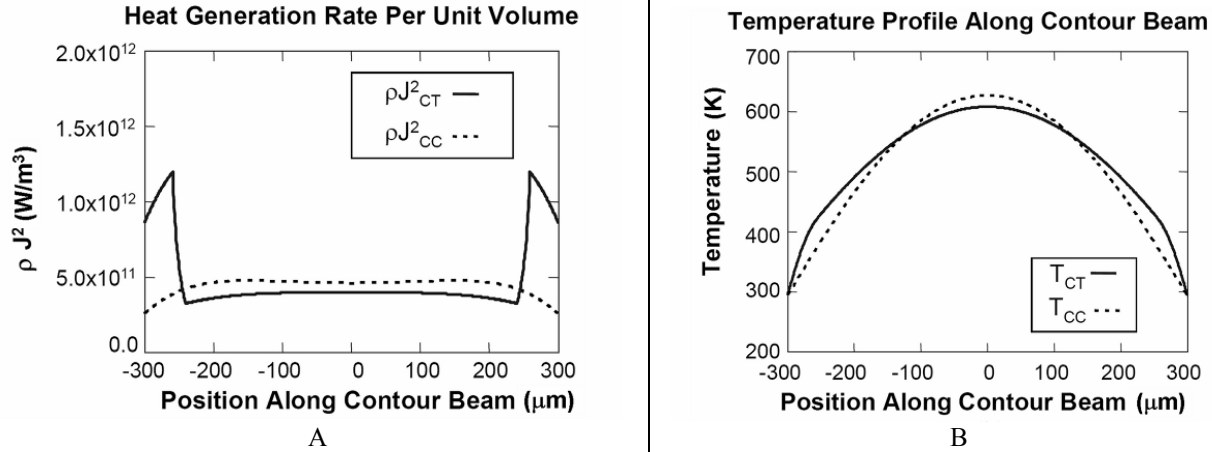


Figure 2-4 Comparison of thermal characteristics between example 1 and example 2

The effect of further reducing  $w'$  may be examined by comparing examples 1 and 3. Figure 2-5A and Figure 2-5B may be used to compare the heat generation and temperature profiles for these examples. The value of  $w'$  is equal to  $\frac{1}{2}$  in example 2 and  $\frac{1}{5.5}$  in example 3. The decrease in  $w'$  leads to a 29% increase in the beam's elongation ( $\Delta T_3/\Delta T_1 = 1.29$ ). Note this occurs when the same actuation current is used. Also note that the temperature increase causes a moderate increase in the electrical resistance and therefore the percentage increase in power required to achieve the additional elongation is only 7%.

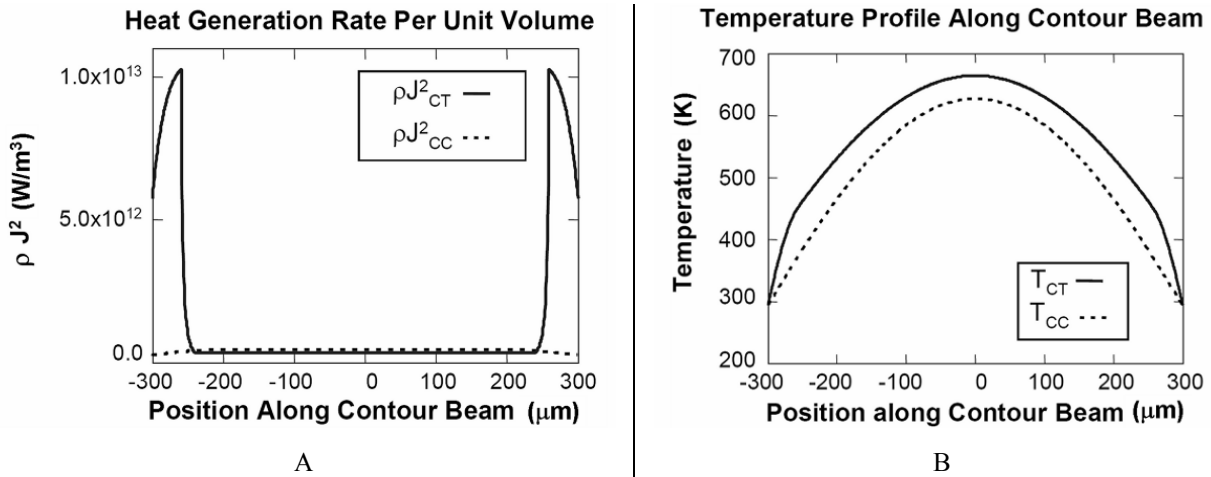


Figure 2-5 Comparison of thermal characteristics between example 1 and example 3

## 2.3 Stiffness and deformation modeling

The preceding comparisons show that beams with narrow ends may be used to obtain increased changes in beam length. This change will also make the beams more compliant in a lateral direction and thereby increase the elastic range. This is fortuitous as a reduction in lateral



bending stiffness reduces the elastic energy stored for a given lateral displacement. In short, this enables a TMA to use less energy to deform itself and thereby use more energy to perform useful work.

It is important to be able to capture the stiffness characteristics of the contoured beam in a way that enables the inclusion of these characteristics within a stiffness matrix representation for the beam. This approach was chosen over a multi-physics (electrical, thermal, and mechanical) or non-linear (nonlinear material properties) FEA because the matrix-based approach enables rapid (a few seconds) calculation and optimization for any type of TMA design. FEA, in comparison, would be slower, design-specific and not as widely available to the community. The beam's stiffness matrix may also be used to generate a device-level stiffness matrix for more complex devices [102], *e.g.*, parallel beam and chevron TMAs. Note the purpose of the stiffness modeling is to allow designers to model different design concepts quickly. Once a concept and critical parameters are selected, FEA is then used to optimize.

The matrix-based stiffness modeling may be simplified by using the parametric form of a stiffness matrix for a constant cross-section beam to describe the behavior of a contoured beam. The stiffness matrix for a constant cross-section beam contains geometry dependant variables such as the second moment of inertia and cross-section of the beam. A stiffness matrix may therefore be adapted for the contoured beam if one assigns an equivalent second moment of inertia,  $I_e$ , and equivalent cross-section area,  $A_e$ , to a contoured beam.

The value of  $I_e$  is obtained by first integrating the beam deflection equations shown in Equations (9) and (10).

$$\frac{dy}{dx} = \int_{-\frac{L}{2}}^{\frac{L}{2}} \frac{(M - P_L x) dx}{E I_{CC}(x) \left[ 1 + \left( \frac{3(1+\nu)}{5} \right) \left( \frac{2w_e}{L} \right)^2 \right]^{-1}} \quad (09)$$

$$\frac{dy}{dx} = \int_{-\frac{L}{2}}^{\frac{L}{2}} \frac{(M - P_L x) dx}{E I_{CT}(x) \left[ 1 + \left( \frac{3 \cdot (1+\nu)}{5} \right) \left( \frac{2h_c(x)}{L} \right)^2 \right]^{-1}} \quad (10)$$

This is done for the contour beam's inertia,  $I_{CT}$ , and the constant cross-section beam's inertia,  $I_{CC}$ . Note the volume of both beams must remain constant to enable meaningful

comparisons. Volume normalization ensures that the same amount of material is available to convert electrical energy to useful work. The results of the two integrands were then compared to obtain the equivalent moment of inertia. Equations (9) and (10) differ from the classical beam bending equations in that they capture shear deflections. Shear-induced deformations start to become significant when  $w_s/L_s$  exceeds approximately 0.2. The inclusion of shear effects ensures the general applicability of the model as a design tool for many different values of  $w_s/L_s$ .

The shear-related terms in the denominator of Equations (9) and (10) were obtained using strain energy methods. Equations (11) and (12) may be used to calculate the contributions of shear and bending toward the strain energy in the beam. The force-displacement relationship, *i.e.*, stiffness, is then calculated from the strain energy relationship.

$$U = \iiint \left( \frac{\sigma_{11}^2}{2E} + \frac{\sigma_{12}^2}{2G} \right) dx_1 dx_2 dx_3 \quad (11)$$

$$U = \frac{P_L^2 L^3}{6EI} \left[ 1 + \left( \frac{3(1+\nu)}{5} \right) \left( \frac{h}{L} \right)^2 \right] \quad (12)$$

The equivalent inertia may be calculated with Equation (13).

$$I_e = \frac{L}{\int_{-\frac{L}{2}}^{\frac{L}{2}} \left\{ \frac{1}{I_{CT}(x)} \left[ 1 + 0.6(1+\nu) \left( \frac{2h_c(x)}{L} \right)^2 \right] \right\} dx} \quad (13)$$

The value of  $A_e$  is obtained via Equation (14).

$$\delta_A = \int_{-\frac{L}{2}}^{\frac{L}{2}} \frac{P_A dx}{E A_{CT}(x)} \quad (14)$$

The same axial stiffness is obtained if the cross-sectional area of the contoured beam is defined via Equation (15).

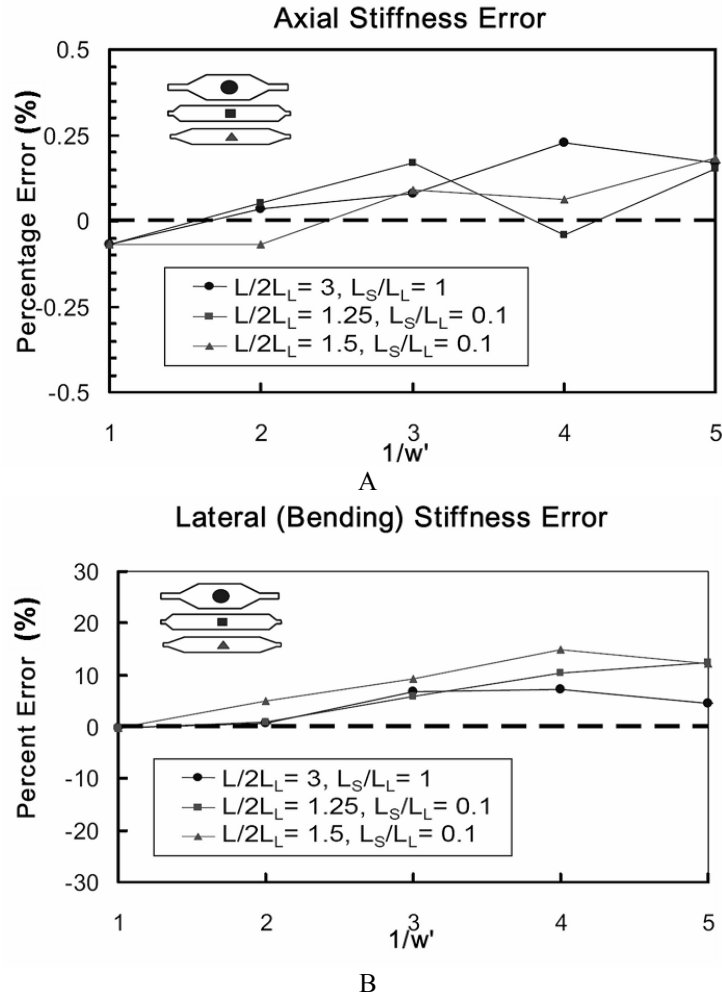
$$A_e = \frac{L}{\int_{-\frac{L}{2}}^{\frac{L}{2}} [A_{CT}(x)]^{-1} dx} \quad (15)$$

A non-linear ADINA FEA model was used to ascertain the accuracy of the stiffness modeling approach. The design parameters that were used in this comparison (stiffness matrix model vs. FEA) are listed in Table 2-3.

**Table 2-3 Values that were used in comparison of stiffness results from the theory and FEA**

Parameter	Value	Units
$L$	600	$\mu\text{m}$
$w_e$	8	$\mu\text{m}$
$b$	30	$\mu\text{m}$
$E$	$1.25 \times 10^{11}$	Pa
$\nu$	0.22	---

The errors between the stiffness model's results and the FEA simulation results are shown in Figure 2-6.



**Figure 2-6 Error observed when calculating (a) the axial stiffness and (b) lateral bending stiffness of a single contoured beam using equivalent inertial and area**

The axial stiffness results exhibit errors less than 0.3% and the lateral stiffness results exhibit errors less than 14%. The 14% is larger than ideal for engineering design purposes; however, it is tolerated here for two reasons: (1) the percent error in stiffness is positive, therefore the model predicts conservative values for actuator output displacements; and (2) the equivalent stiffness is required to perform rapid, matrix-based stiffness modeling. The lateral stiffness errors, *i.e.*, bending stiffness errors, occur because the stiffness of the beam changes as it is deformed. The direct stiffness model must use constant stiffness parameters; therefore the model shows moderate errors. The model is best used to rapidly produce a near finalized design by investigating many design possibilities and the performance sensitivity of each design. If improved accuracy is required for large deformations, the near finalized design may be further refined via a slower, more time- and effort-intensive simulation tool such as FEA.

There are limits on reducing the width of the beam ends, *i.e.*,  $w_S$ . For example, buckling must be avoided. Various buckling loads for contoured beams exist [103, 104] and may be applied here without complication. The reductions in lateral and axial stiffness values of a single beam are shown as functions of  $w'$ ,  $L_S/L_L$ , and  $L_L/L$  in Figure 2–7.

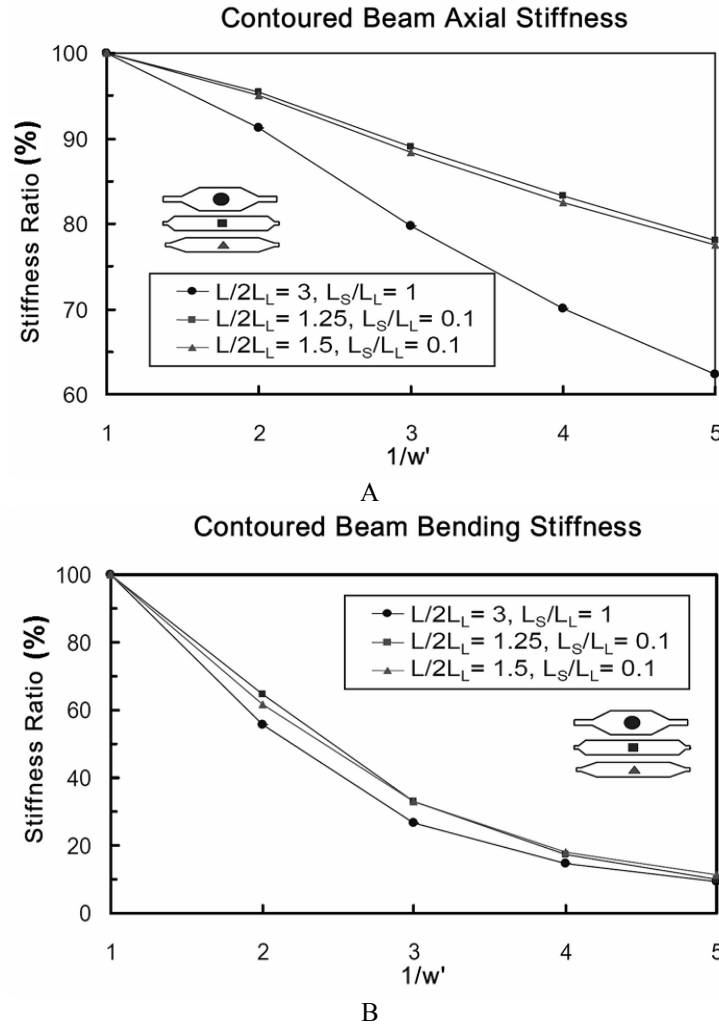


Figure 2–7 Relationship between design parameters and the (a) axial stiffness reduction and (b) lateral bending stiffness reduction of a single contoured beam

## 2.4 Displacement, stiffness and force characteristics

### 2.4.1 Summary of actuator–level modeling

The direct stiffness method was used to model the displacement, stiffness, and force characteristics of chevron TMAs and parallel TMAs for quasi–static state and transient state responses. In regards to dynamic behavior, it has been found that the speed of the thermally

induced strain wave that is caused by Joule heating is orders of magnitude faster than the speed of a TMA. Based upon this result, it is assumed that any temperature–induced displacement of a TMA is an instant response. In other words, the temperature profile at any evolution of time in the simulation is to be directly calculated for the actuator performance, *e.g.* displacement, velocity, and force.

The direct stiffness method is well–known in structural mechanics [102]; therefore only a summary of the model creation is provided. Figure 2–1 shows the design parameters and local coordinate systems that were used to model the individual compliant elements of the TMAs. The compliant elements were connected at their endpoints, *i.e.*, nodes, and variables  $r_i$  were assigned to represent the in–plane rotation and translation displacements of the nodes. The local stiffness of all elements is then combined to form a global stiffness matrix,  $\mathbf{K}$ , for the actuator. The external loads applied to the actuator,  $\mathbf{F}$ , and the displacements,  $\mathbf{X}$ , of the actuator were related by Equation (16).

$$\vec{F} = K\vec{X} \quad (16)$$

Equation (16) may be modified to use the extension,  $\Delta_T$ , of the contoured beams. The extension may be converted into an equivalent nodal force,  $F_N$ , that the beam exerts on a node. The equivalent nodal force is given in Equation (17).

$$F_N = E \cdot A_e \frac{\Delta_T}{L} \quad (17)$$

The equivalent nodal force may then be decomposed into X and Y forces that act upon the corresponding node. The displacement of the actuator may be obtained by decomposing  $F_N$  into the x and y components [102] of  $\mathbf{F}$  for Equation (16). Table 2–4 lists the parameters that were held constant during the modeling and simulation of the TMAs throughout Chapter 2.

**Table 2–4 Parameters that were used for modeling of the example TMAs**

Parameter	Value	Units
$P$	10	mW
$L$	600	$\mu\text{m}$
$w_e$	8	$\mu\text{m}$
$b$	30	$\mu\text{m}$
$\theta$	1	Degree
$L_T$	100	$\mu\text{m}$
$L_G$	12	$\mu\text{m}$
$L_W$	550	$\mu\text{m}$
$L_N$	50	$\mu\text{m}$

### 2.4.2 The effect of contouring on a chevron TMA

This section uses simulation results from the preceding models in order to compare the simulated behavior of 24 contoured actuator geometries to a topologically similar actuator with constant cross-section beam. The behaviors that were examined include (1) the static displacement per unit power input, (2), actuator stiffness, and (3) transmission ratio, *i.e.*, the actuator output displacement over the input displacement,  $\Delta_T$ , from the heated beam(s). These comparisons were constrained by an equal driving power, 10 mW, that the actuators with smaller values of  $w_s$  could tolerate without “burning out”.

Next, a metric that enables the assessment of the enhancement in actuator displacement per unit power was defined. The enhancement ratio for displacement per unit power,  $\Delta'$ , is defined in Equation (18).

$$\Delta' = \frac{\left. \frac{\Delta_A}{P} \right|_{CT}}{\left. \frac{\Delta_A}{P} \right|_{CC}} \quad (18)$$

Equations (19) and (20) provide enhancement ratios for the transmission ratio,  $\zeta'$ , and actuator stiffness,  $K'_A$ .

$$\zeta' = \frac{\zeta_{CT}}{\zeta_{CC}} \quad (19)$$

$$K'_A = \frac{K_{A-CT}}{K_{A-CC}} \quad (20)$$

Figure 2–8 and Figure 2–9 show how  $\Delta'$ ,  $\zeta'$ , and  $K'_A$  vary as a function of contoured beam geometry for the chevron and parallel TMAs. Through the inspection of the figures, it is possible to see how the comparative metrics change between the 24 chevron and the 24 parallel TMA designs. Figure 2–8A and Figure 2–9A show how the actuator output displacement may be increased by (1) increasing  $L_S/L$ , (2) decreasing  $w'$ , or (3) increasing  $L_I/L$ . Figure 2–8B and Figure 2–9B show how the transmission ratio of the actuator may be increased by (1) increasing  $L_S/L$ , (2) increasing  $I/w'$ , or (3) increasing  $L_I/L$ . Figure 2–8C and Figure 2–9C show how the ratio of TMA stiffness (collinear with the output displacements) decreases when (1)  $L_S/L$ , (2)  $I/w'$ , or (3)  $L_I/L$  increases.

It is important to note that although the stroke is increased by more than a factor of 20 at  $I/w'=5$ , the contoured TMA is still within its elastic range. This is counter–intuitive, but more easily believed if one considers that the elastic range of a contoured beam increases roughly in proportion to the  $I/w'$  value. This is because (1) the maximum strain of a bending beam is equal to the distance between the beam's surface to its neutral surface over the beam's radius of curvature, and (2) this maximum strain always occurs at the two narrow ends of a contoured beam/TMA where the narrow ends were connected and constrained to the ground. A detailed discussion of the mechanical failure limits of contoured TMAs will be presented in Section 2.8.5.



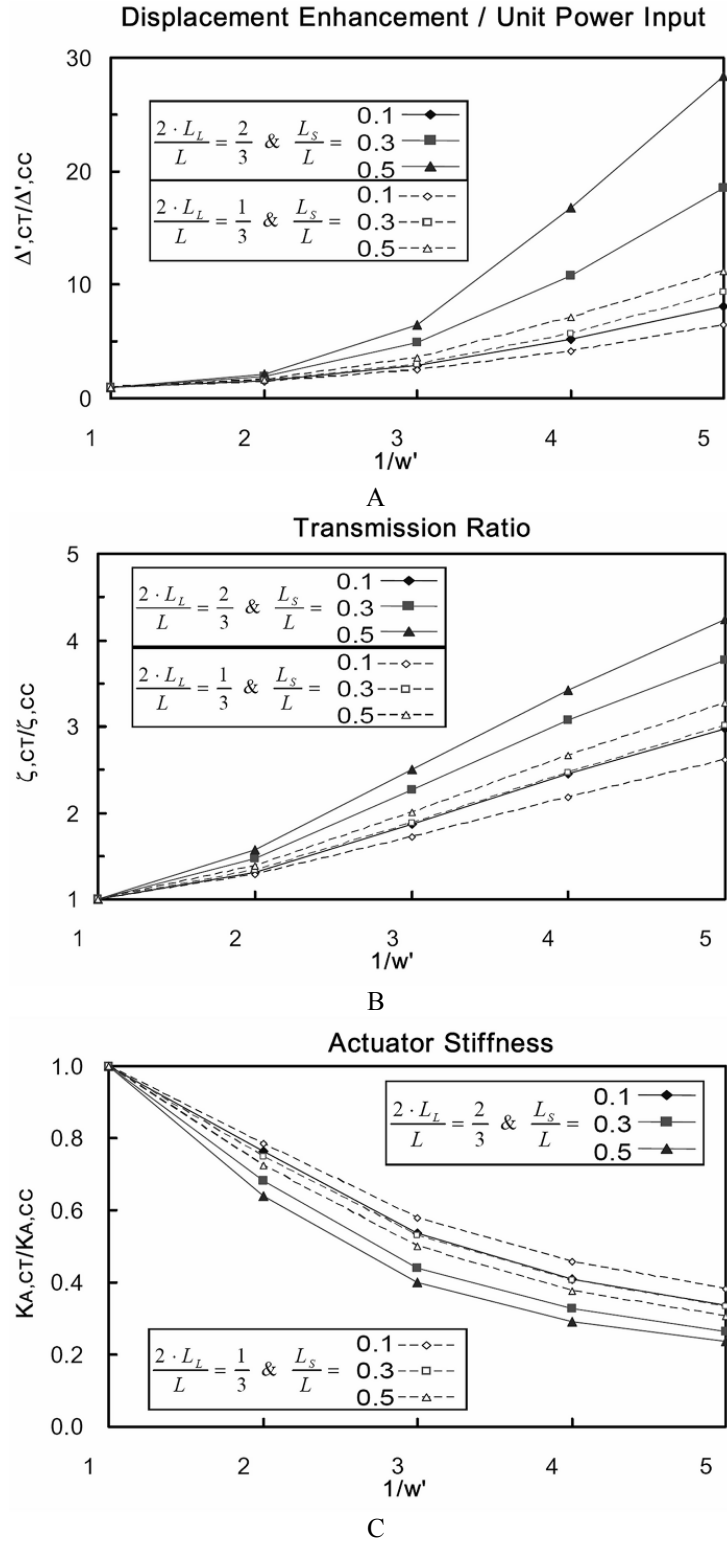
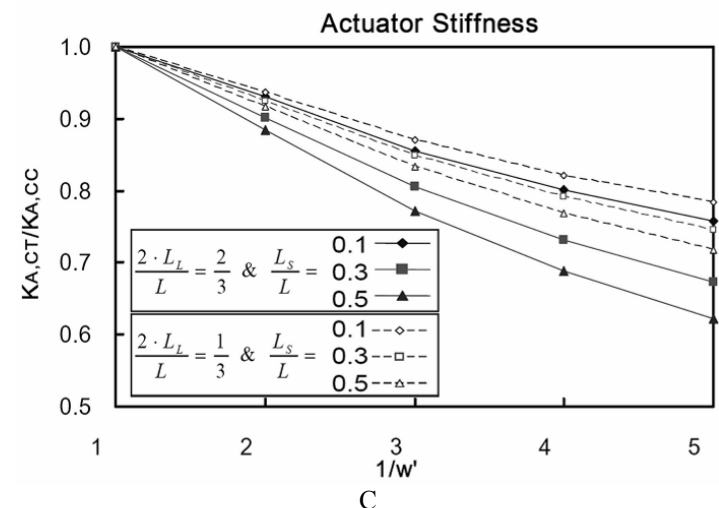
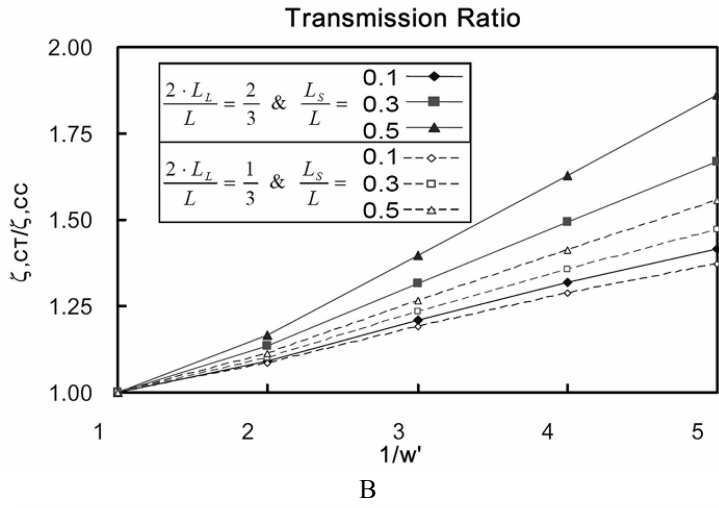
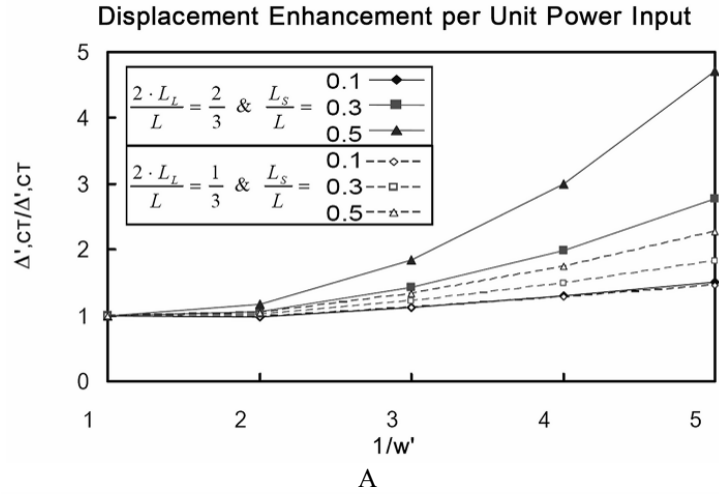


Figure 2–8 Non–dimensional parameters for a chevron TMA vs. enhancement ratios for (a) displacement per unit power, (b) transmission ratio, and (c) actuator stiffness



**Figure 2-9 Non-dimensional design parameters for a parallel TMA vs. enhancement ratios for (a) displacement per unit power, (b) transmission ratio, and (c) actuator stiffness**

### **2.4.3 The effect of contouring on the performance of a parallel TMA**

The trends of the relationships for a parallel TMA are similar to the trends that are exhibited by a chevron beam TMA. As such, the reader may refer to the preceding section.

## **2.5 Implications of quasi–static results for device design**

The accuracy of micro–scale precision actuation stages, *e.g.*, nanopositioners, is sensitive to thermal growth errors. As a result, it is important to reduce the temperature and power requirements of the actuators that drive these devices. Ideally this should be accomplished without reducing the stroke of the positioner. Contouring may be used to simultaneously achieve lower actuation power and lower temperatures without sacrificing stroke at quasi–static state. To understand how to obtain these advantages, the following sub–sections investigate the power reduction ratio and maximum temperature reduction ratio under two conditions: (1) equal displacement, and (2) maximum displacement.

### **2.5.1 Effect of contouring on performance with equal displacement constraint**

This section compares the 24 contoured chevron TMA designs from Section 2.4 to a constant cross–section chevron TMA that is undergoing a constant 3.0 micrometer displacement. The results of the comparison are provided in Figure 2–10 and Figure 2–11.

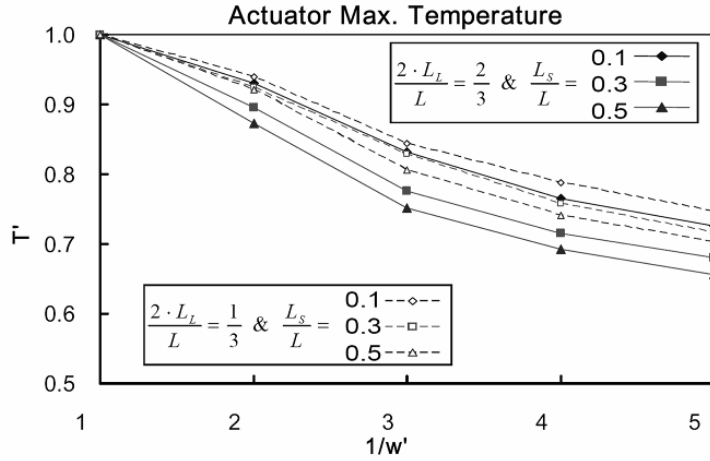


Figure 2-10 Relationship between design parameter changes and decrease in maximum temperature for chevron beam TMAs

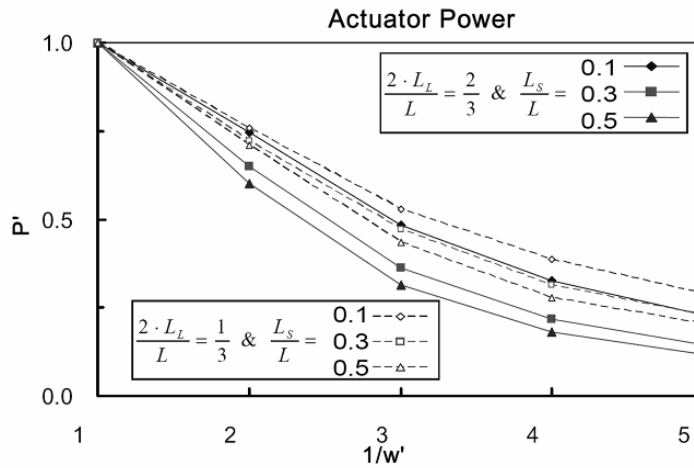


Figure 2-11 Relationship between design parameter changes and the decrease in actuator power consumption for chevron beam TMAs.

The maximum temperature ( $T_{max}$ ) reduction ratio,  $T'$ , and the corresponding power reduction ratio,  $P'$ , are defined in Equations (21) and (22) respectively.

$$T' = \frac{T \max_{CT}}{T \max_{CC}} \quad (21)$$

$$P' = \frac{P_{CT}}{P_{CC}} \quad (22)$$

Table 2-5 lists the parameters that were used in this analysis.

**Table 2–5 Parameters that were used for the designs shown in Figure 2–10 to Figure 2–12**

Parameter	Value	Units
$P$	83	mW
$T_{max}$	565	°K
$w_e$	8	μm
$L$	600	μm
$\theta$	1	Degree
$b$	30	μm
$\Delta_A$	3.0	μm

From Figure 2–10 and Figure 2–11, it is concluded that (1) an equal displacement is obtained at a lower maximum beam temperature, (2) the power required to achieve an equal displacement decreases when  $L_S/L_L$ ,  $l/w'$ , or  $L_L/L$  increases, and (3)  $l/w'$  is the dominant parameter among the three variables. This shows that the value of  $w_S$  will generally be the limiting factor in fabricating practical designs because  $w_S$  is limited by the resolution of the fabrication processes. Figure 2–10 and Figure 2–11 also show that for  $l/w' = 5$ , a 3.0 micrometer displacement may be achieved at 10% of the power required by a constant cross-section beam. In addition, the maximum temperature required to achieve a 3.0 micrometer displacement is reduce by 36%. It is important to note that the transmission ratio and stiffness are a function of geometry only and therefore the results of Figure 2–8B and Figure 2–8C may be applied to Figure 2–10 and Figure 2–11.

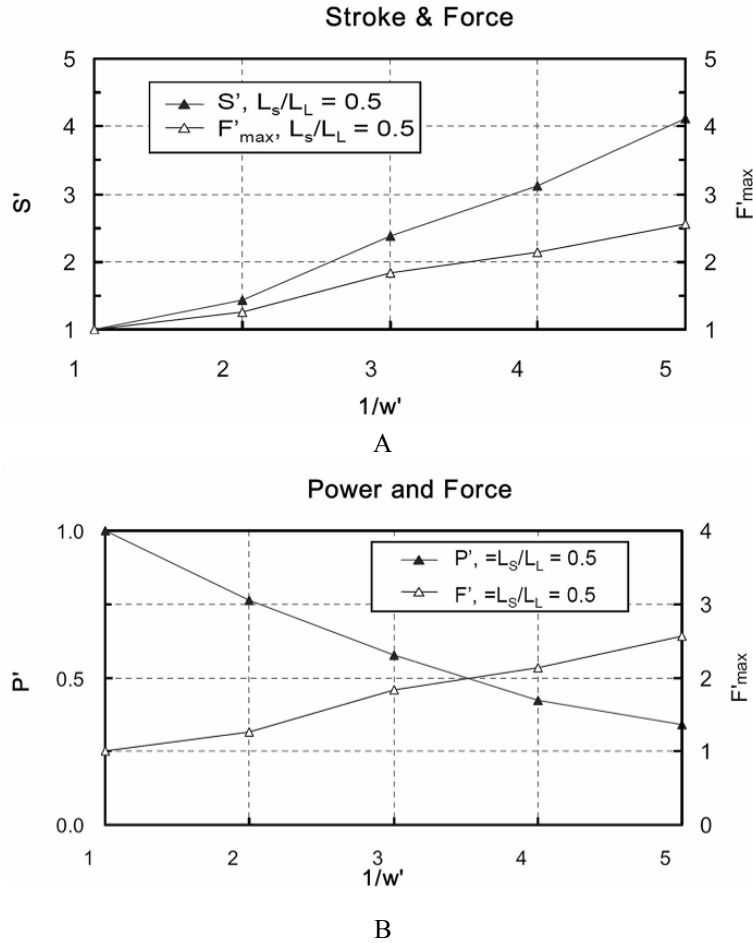
### 2.5.2 Enhancement in stroke and maximum force output

The enhancement in stroke is attributed to the increased transmission ratio and the increased change in beam length,  $\Delta_T$ . The enhancements in stroke and maximum force are measured via the stroke enhancement ratio,  $S'$ , and the maximum force enhancement ratio,  $F'_{max}$ . These metrics are defined in Equations (23) and (24).

$$S' = \frac{S \max_{CT}}{S \max_{CC}} \rightarrow \frac{\zeta_{CT} \Delta_{T CT}}{\zeta_{CC} \Delta_{T CC}} \quad (23)$$

$$F'_{max} = \frac{F \max_{CT}}{F \max_{CC}} \quad (24)$$

The data shown in Figure 2–12 were generated using the parameters that are shown in Table 2–5. Figure 2–12 may be used to ascertain how  $S'$  and  $F'_{max}$  change with design parameters.



**Figure 2–12 Relationship between design parameter changes and (a) actuator stroke and (b) power reduction ratio**

Figure 2–12 shows that for  $1/w' = 5$ , the following may be achieved simultaneously:

1. Increase in stroke and elastic range by a factor of four
2. Reduction in required driving power by 65%
3. Increase in maximum output force by a factor of 2.5

## 2.6 Dynamic characteristics of contoured TMAs

This section will discuss the transient effects of contouring a Joule–heated beam. Note the results of the transient modeling in the following examples/sections were obtained using the 1D thermal model described in Section 2.2 and will not be repeated here.

In Section 2.6.1, two examples (A and B) will be discussed in order to illustrate the transient heating process of a contoured beam. In Section 2.6.2, three examples (C, D and E) are

discussed in order to study the step response and square-wave response characteristics of contoured chevron TMAs for (1) constant current input and (2) for constant displacement. In Section 2.6.3, 24 different chevron TMA designs, the same as those that were used in the previous quasi-static studies, will be discussed. Important implications on TMA design for enhancing transient performance will then be discussed in subsequent sub-sections.

### 2.6.1 Effects of contouring on transient thermal behavior of a beam

This section presents two simulated examples that illustrate the different transient heating processes between a contoured beam (example A) and a straight beam (example B) wherein there is inhomogeneous distribution of heat generation along the contoured beam. This may be observed in Figure 2-4. In example A and B, a constant current of 25mA was supplied to both beams and the change in the temperature profiles with time was recorded from the simulation. The model parameters that were used in the examples are listed in Table 2-6 and the results are presented in Figure 2-13A and Figure 2-13B.

**Table 2-6 Design parameters that were used in examples A and B**

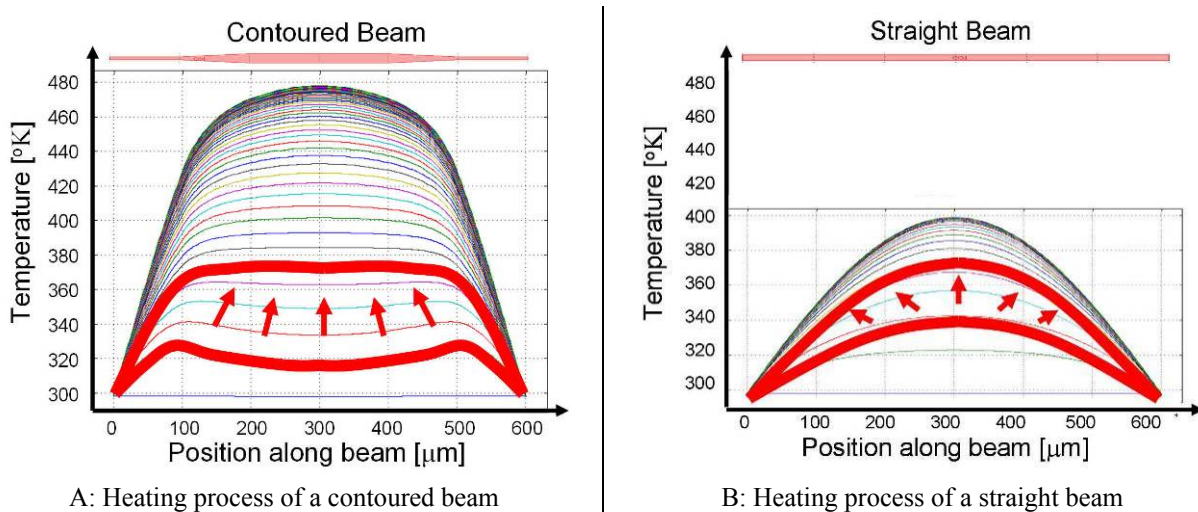
	Example A	Example B
Type	Contour	Constant cross-section
$L_s/L_L$	1	N/A
$L/2L_L$	3	N/A
$w'$	$1/2$	1
$w_e$	8 $\mu\text{m}$	8 $\mu\text{m}$
$L$	600 $\mu\text{m}$	600 $\mu\text{m}$
$b$	30 $\mu\text{m}$	30 $\mu\text{m}$
Driving current	25mA	
Time steps in solver	0.0002second	

In Figure 2-13A and Figure 2-13B, the X-axis and Y-axis represent the position and the temperature along a contoured beam and a straight beam respectively. In both cases, the two ends of the beams were assumed to be attached to a heat sink and maintained at room temperature. Starting from  $T = 300 \text{ }^\circ\text{K}$  (room temperature), each temperature profile is offset by a 0.2 ms time interval. By comparing examples A and B, it was found that the contoured beam has a slightly larger thermal time constant. This is expected because the heat generated at both ends of the contoured beam would require some time to reach thermal equilibrium. The rise time difference between a contoured and straight beam may also be quantitatively estimated by comparing the ratio of each beam's thermal time constant,  $\tau_{\text{Thermal}}$ . When compared to FEA

results, this ratio is accurate within 5% error when  $l/w'$  is less than three. As the width ratio increase, more 2D effects must be taken into account and the errors tend to increase, e.g. 10% error when  $l/w' = 5$ . Note that Equation (25) is only suitable for estimating rise time for constant input.

$$\tau_{Thermal} = R_{Thermal} \cdot C_P = \int_0^L \frac{C_P \cdot dx}{k(T(x)) \cdot A_{CT}(x)} \quad (25)$$

It was also found that the average temperature on the contoured beam rises faster than the straight beam, and this shows that for identical input power, the contoured TMA has a higher forward stroke speed. To understand this phenomenon, quantitative observation and calculations may be done, based upon Figure 2–13A and Figure 2–13B, for the temperature profiles. For example, the fifth temperature profile is the profile at 0.001 second.



**Figure 2–13 Comparison of transient heating process between a contoured and straight beam**

Another important property for a contoured beam is that its temperature profile goes through three different stages/shapes as time progresses. At stage 1, the temperature on both ends of the contoured beam rises faster than in the central region and forms a concave-up profile (as more heat is generated on both ends.). At stage 2, heat diffuses to the central region, and there is a moment in time where the temperature profile becomes nearly “flat” over a wide portion of the contoured beam. At stage 3, the system gradually reaches steady state and forms a bell-shape temperature profile. It is important to note that the heating and cooling temperature profiles are different for a contoured beam. In the cooling process, the temperature will decrease



faster at both ends of the beam, where the temperature gradient is larger. This issue will be revisited in Section 2.8, where temperature gradient as a function of time at the end of a contoured beam and straight beam will be compared under different driving signal conditions.

In contrast to a contoured beam, the temperature profile of a straight beam approaches a quadratic shape during the heating and cooling processes if the time scale of observation is sufficiently long (*e.g.*  $\sim 1/50$  of the heating time for all the examples that were used in this chapter) and constant values for thermal conductivity and electrical resistivity are used. This point becomes clear if thermal conductivity is assumed to be constant, and the heat source term in the 1D heat equation (1) is moved to the right hand side. The solution of this equation then includes a double integral of the heat source term on the right. In practical situations, when thermal conductivity and electrical resistivity are functions of temperature, heating a straight beam usually yields a less uniform temperature profile than parabolic, *e.g.* temperature profiles in Figure 2–24. Consequently, this temperature profile yields reduced thermal strain in the actuator, *i.e.* reduced actuator stroke. This will be demonstrated in Section 2.8.2 when the “pulsing technique” for a contoured beam is presented. The distinct heating and cooling processes for a contoured beam enables the concept of the “high–speed pulsing” that is presented in Section 2.8.

### **2.6.2 Effects of contouring on a specific contoured chevron TMA performance**

This section covers the transient heating and cooling process of a specific contoured TMA in order for designers to understand the general properties that contoured TMAs possess. Three examples (C, D, and E) were used to compare the transient performance between a contoured TMA and a constant cross–section TMA that were formed by the contoured/straight beams in the example A and B respectively. The examples were compared under two different constraints: (1) constant current input for example C and D, and (2) constant displacement for example C and E. In these examples, C is a contoured chevron TMA; D and E are same the constant cross–section chevron TMA with different input constraints. The model parameters and command inputs are listed in Table 2–7.

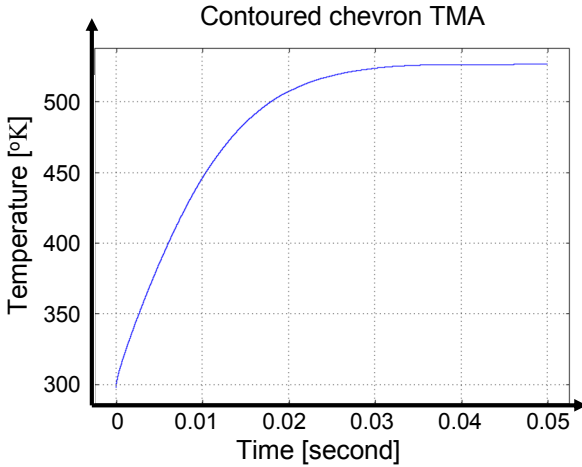
**Table 2–7 Design parameters that were used in examples C, D and E**

	Example C	Example D	Example E
Type	Contoured chevron	Constant cross–section chevron	
$L_S/L_L$	1	N/A	
$L/2L_L$	3	N/A	
$w'$	$\frac{1}{2}$	1	
$w_e$	8 $\mu\text{m}$	8 $\mu\text{m}$	
$L$	1200 $\mu\text{m}$	1200 $\mu\text{m}$	
$b$	30 $\mu\text{m}$	30 $\mu\text{m}$	
Driving current	8.0mA	8.0mA	11.8mA
Time steps in solver	0.0002second		

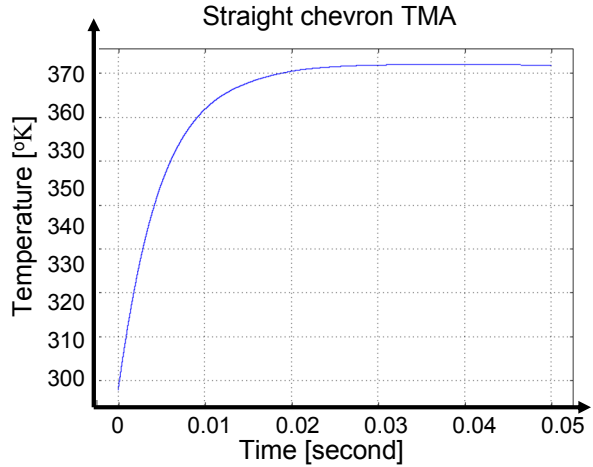
**Contoured chevron TMA performance with constant current input constraint**

As a contoured TMA possesses better quasi–static performance than a constant cross–section TMA, this section uses a specific contoured TMA to demonstrate how contouring also changes the transient performance of a constant cross–section chevron TMA if constant current input is used. In examples C and D, a constant current of 8mA is supplied to the contoured (C) and constant cross–section (D) chevron TMAs. The maximum temperature and displacement at the tip of the chevron TMAs are presented in Figure 2–14 as a function of time. Results from Figure 2–14 are summarized in Table 2–8.

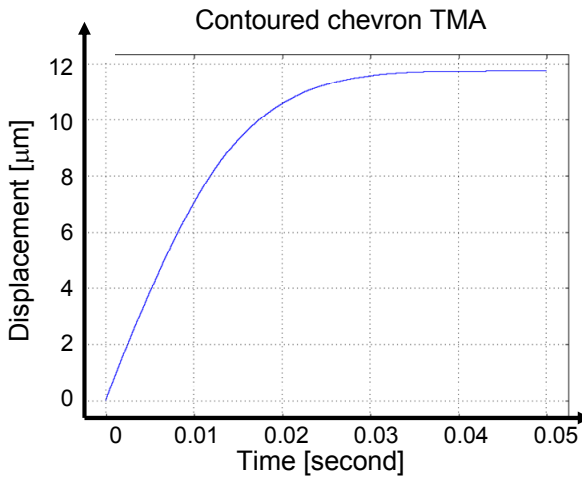
From the constant current input examples C and D, that are shown in Figure 2–14, it was found that the contoured chevron TMA has a 4.7 times faster forward stroke speed and a slightly larger time constant (0.025 vs. 0.02 second) than a straight chevron TMA. The 5.9X enhancement in displacement is a consequence of the contoured TMA’s increased transmission ratio and the increased change in beam length,  $\Delta l_T$ . In general, any contoured TMA possesses better stroke and speed than a constant cross–section TMA if the same driving current is supplied. Note that different levels of contouring, *i.e.* different values of  $l/w'$ , enable tradeoffs between: (1) actuator stiffness and bandwidth, or (2) stroke and speed. These tradeoffs and ways to model/take advantage of them will be discussed in Section 2.6.3.



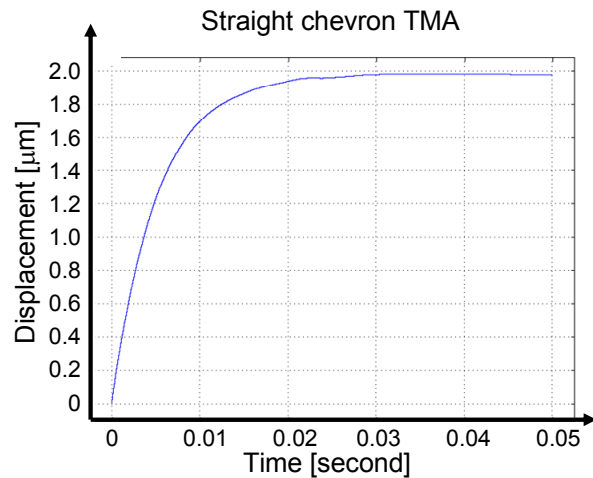
A: Max. temperature response of example C



B: Max. temperature response of example D



C: Displacement response of example C



D: Displacement response of example D

**Figure 2–14 Step responses of example C and D with constant input current constraint**

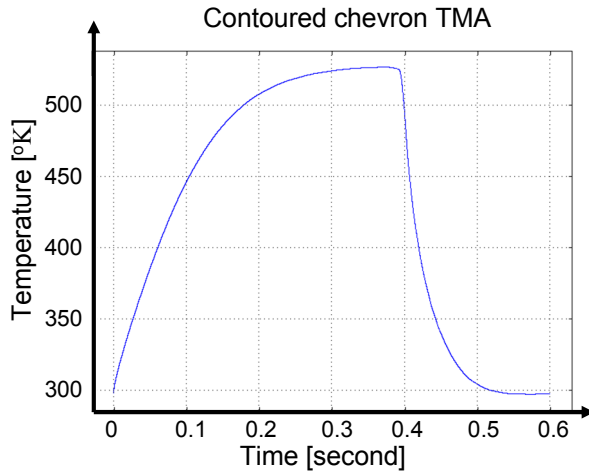
**Table 2–8 Summary of performance of example C, D, and E**

	Example C	Example D	Example E
Type	Contour	Constant cross-section	
Driving current	8.0mA	8.0mA	11.8mA
Displacement	11.64 μm	1.96 μm	11.64 μm
Rise time	0.025 second	0.02 second	0.015 second
Fall time	0.065 second	N/A	0.061 second
Forward stroke speed	465.6 μm/s	98 μm/s	776.0 μm/s
Return stroke speed	179.1 μm/s	N/A	190.8 μm/s
Max. temp. on TMA	526.7K	371.9K	668.4K
Note	C and D for identical current input; C and E for equal commanded displacement		

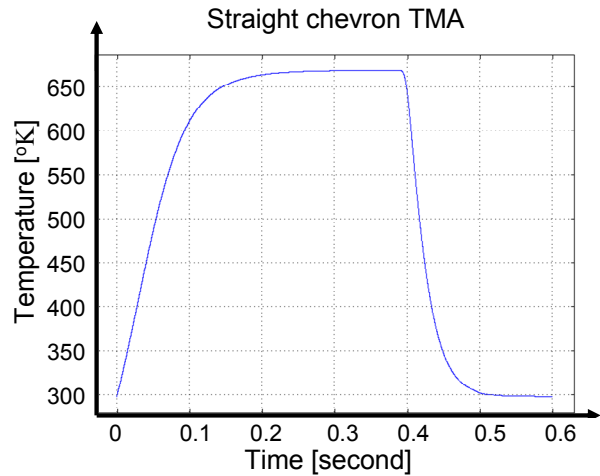
### **Contoured chevron TMA performance with equal displacement constraint**

This section covers the details that explain how power may be saved and how a contoured TMA's transient performance will in general be different, if the displacement is set to be equal. The designs in C and E, the contoured (C) and constant cross-section (E) chevron TMAs were supplied with a square wave input with an 11.6 $\mu$ m constant displacement constraint. The temperature and displacement of the chevron TMAs are plotted in Figure 2–15 as a function of time respectively. Results from Figure 2–15 are summarized in Table 2–8.

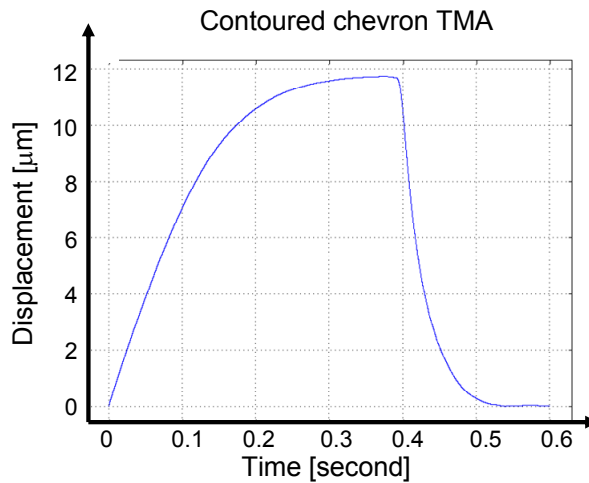
From the constant displacement examples C and E that are shown in and Figure 2–15, it was found that the rise time of a contoured chevron TMA is 66% more than a straight chevron TMA (0.025 vs. 0.015 second). This result is expected because the required power for a straight chevron TMA to achieve constant displacement is 1.7 times more than a contoured chevron and for a Joule heated beam. A faster rise time may always be achieved by supplying more power. The fall time and return stroke speed of the contoured beam chevron TMAs is 6% longer than a straight beam. This difference occurs because, for equal displacement, the straight beam chevron TMA requires a 37.8% higher maximum temperature than the contoured chevron TMA requires, and a large temperature difference generates a larger temperature gradient, and this leads to more rapid heat dissipation. This finding, however, doesn't imply that a contoured TMA must cool down slower than a constant cross-section TMA under equal displacement constraint. Section 2.8 will present a "pulsing technique" that utilizes a contoured TMA's unique transient heating and cooling processes to achieve faster heating and cooling speeds. The pulsing technique further increases a contoured TMA's stroke and speed (30% and 10% respectively) and reduces its power consumption (70%). Recall from Section 2.6.1 that the unique heating/cooling processes refer to a contoured TMA's transient temperature profiles that may be categorized in three types: concave up, flat and concave down.



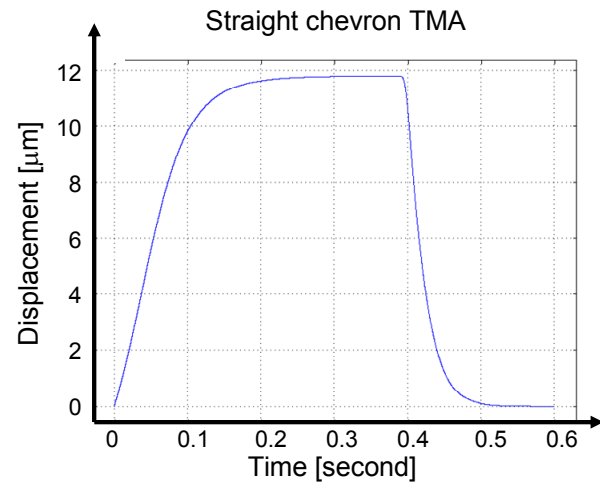
A: Max. temperature response to of example C



B: Max. temperature response of example E



C: Displacement response of example C



D: Displacement response of example E

Figure 2–15 Square–wave responses of example C and with equal displacement constraint

### 2.6.3 Step responses and velocity characteristics of contoured chevron TMAs

In order to demonstrate how different levels of contouring generate different TMA characteristics, *i.e.* tradeoffs between an actuator’s stroke and speed, this section extends the preceding examples and investigates/compares the simulated transient behavior of the 24 contoured chevron TMA geometries of constant power input to a topologically similar actuator with a constant cross–section beam. The rise time, fall time, the forward stroke speed and the return stroke speed, *i.e.*, the actuator displacement over the required time, were compared. These comparisons were done with an equal driving power, 10 mW, that the actuators with smaller values of  $w_s$  could tolerate without failing, *i.e.* “burning out”.

Figure 2–16 and Figure 2–17 show how rise/fall times and normalized forward/return stroke speeds vary as a function of contoured beam geometry for the chevron TMAs. Inspection of the figures reveals how the characteristics time and speed change among the 24 chevron TMA designs. Figure 2–16 shows how the rise time and fall time would increase by either (1) increasing  $L_S/L$ , (2) decreasing  $w'$ , or (3) increasing  $L_L/L$ . Forward and return speeds were obtained by dividing the strokes by the rise and fall times. The speeds were then normalized and plotted in Figure 2–17.

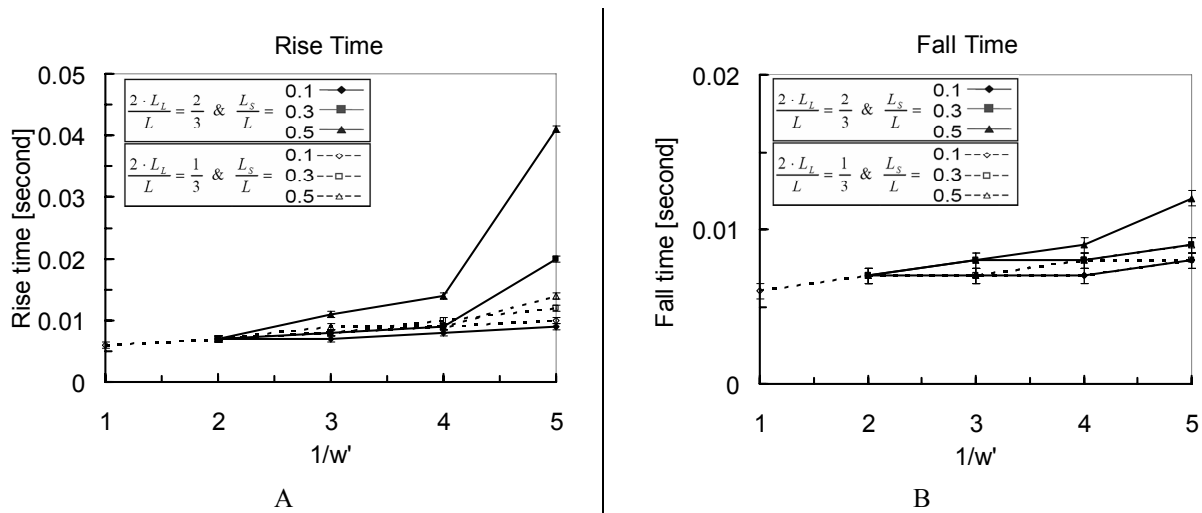


Figure 2–16 Rise time and fall time for 24 chevron beam TMAs

The normalized speeds change by (1) increasing  $L_S/L$ , (2) increasing  $1/w'$ , or (3) increasing  $L_L/L$ . It was found that the benefits of increasing forward speed disappear when  $1/w'$  is larger than four. This result is expected because, as  $1/w'$  increases, the gradual reduction of the cross-section areas at two ends of a contoured beam reduces the amount of heat that may transfer to the center of the contoured beam within a given time. This finding shows that with geometric contouring, a designer may trade-off a TMA's forward and return stroke speed. Note that there is no way in which one may adjust the forward/return speed ratio of a constant cross-section beam TMA. This is a consequence of the fixed cooling time for a specific temperature profile on a cross-section beam TMA. Heating time, however, may be reduced by supplying more power.

The ability to control the ratio of forward/return stroke speed will make TMAs more efficient and easier to control. This technique will also be implemented to design the mechanical frequency multiplier system in Chapter 3.

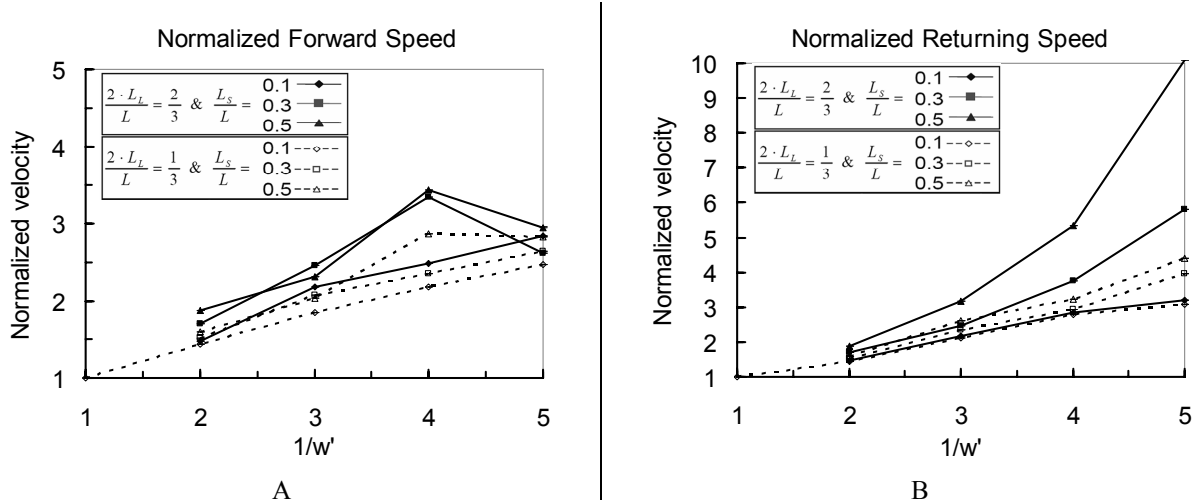
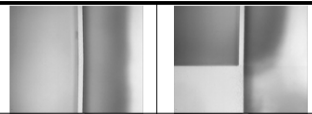




Figure 2-17 Normalized forward and return speed for 24 chevron beam TMAs

## 2.7 Characterization of contouring enhanced performance

Three chevron TMAs were micro-fabricated with the purpose of supplying prototypes for static and dynamic experiments that assess performance improvement. The design parameters, driving conditions, measured displacements, and predicted displacements are summarized in Table 2-9. The predicted stroke is accurate within -6% for small  $1/w'$ . When  $1/w'$  equals 5, the measured displacement is 25% larger than the predicted value. This result may be attributed to (1) the conservative estimation of a contoured beam's lateral stiffness (14% higher than FEA model when  $1/w' = 5$  as shown in Section 2.3), and (2) the increased sensitivity to fabrication errors when  $w_s$  becomes small. Note that all in-plane dimensions of a micro-device were less than the ones drawn on the mask when positive photoresist is used. As a result, adjustments of mask dimensions must be made in order to compensate for unintended geometry variations that occur during lithography. The impact of fabrication errors will be revisited in detail in Chapter 4.

**Table 2–9 Static results of three chevron TMAs with constant current input**

Contoured TMA top views	Measured Disp [ $\mu\text{m}$ ]	Predicted Disp [ $\mu\text{m}$ ]	Error [%]
	0.054 +/-0.005 ( $W_s/W_L=1$ )	0.057 (11.1mA)	5.5%
	0.078 +/-0.005 ( $W_s/W_L=2$ )	0.073 (11.1mA)	6.4%
	0.62 +/-0.005 ( $W_s/W_L=5$ )	0.46 (11.1mA)	25%

The static and dynamic data were obtained with a Micro–Motion Analyzer (MMA)<sup>3</sup>. MMA has the ability to measure transient response with nanometer translational resolution and milli–degree rotational resolution. The measuring procedure is shown in Figure 2–18. Magnified image data are collected through a microscope and recorded by the CCD camera. Stroboscopic illumination is used to take temporal sequence of images at multiple planes of focus. At each point of focus, images were taken at multiple stimulus phases that were in synchronization with the source signal that was generated by the computer. This process was repeated at different frequencies and then the images were analyzed by the Computer Microvision’s algorithms. The output of the algorithm is the motion in three axes as a function of frequency. Using this algorithm, Bode plots may be generated and the dynamics of the system may be obtained.

---

<sup>3</sup> The MMA, a commercial version of the Computer Microvision system, was kindly provided by Professor Dennis Freeman.



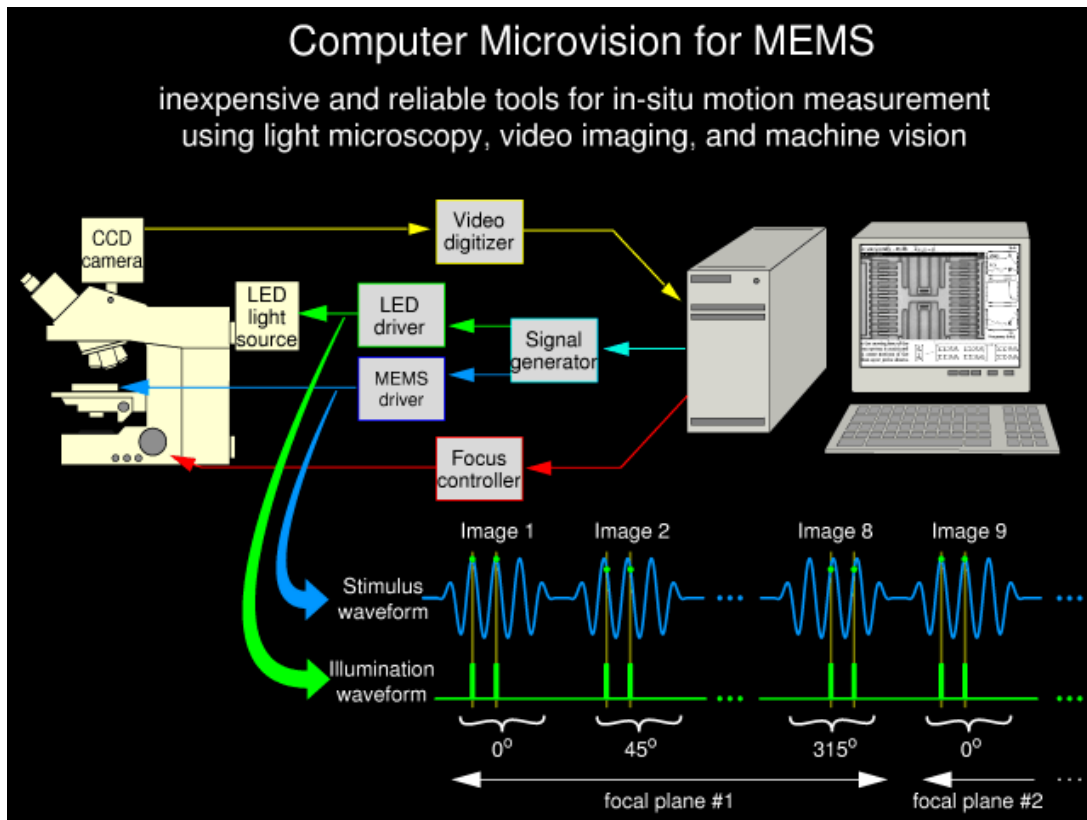
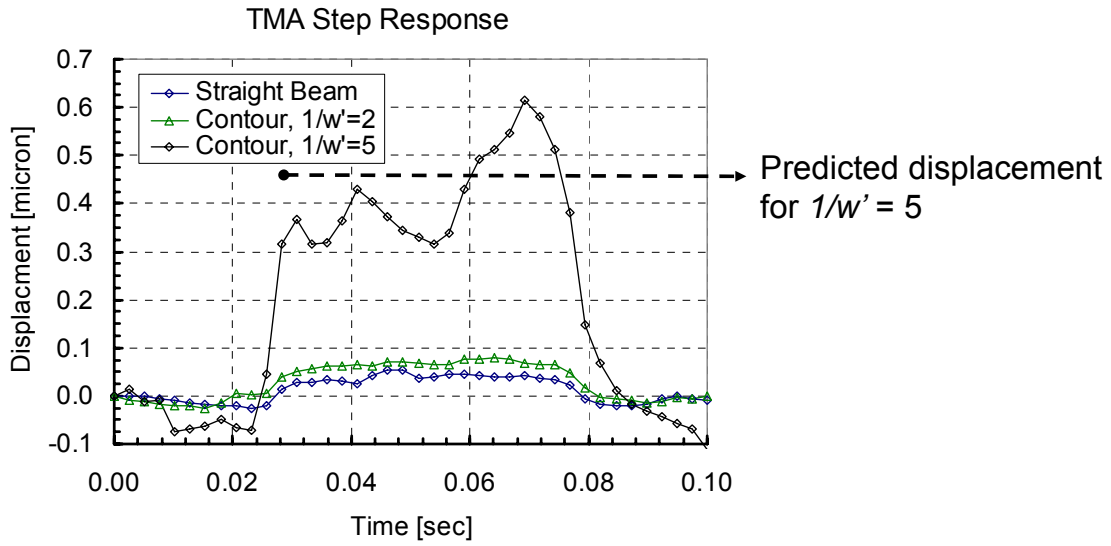


Figure 2–18 Schematics of Computer Microvision system (Courtesy of Professor Dennis Freeman)

The step responses and frequency spectrum of three chevron TMAs are shown in Figure 2–19 and Figure 2–20 respectively. Figure 2–19 shows (1) that the chevron TMA with  $l/w' = 5$  displaces 11.5 times further than the straight beam chevron TMA and (2) that the chevron TMA has a slightly larger time constant (0.06 vs. 0.04 second) than the straight beam chevron TMA. The sawtooth–like patterns observed on the square–wave response were unexpected. It is believed that they were artifacts that were generated by the experimental setup, but this is not certain. A hypothesis is that during the measurement process, the moving part of the device may have wandered partially or completely out of the region of interest. When an object is moving out of the region of interest and the MMA algorithm tries to minimize the error, the MMA system may, at times, generate unexpected results, *e.g.* the sawtooth–like pattern. While objects under study were within regions of interests, the characteristic time constants and ranges all corresponded to the model fairly well. Although the device was, unfortunately, burned out before more experiments could be repeated, the measurements support the case that the device was functioning as desired.



**Figure 2–19 Responses to a square wave input of three chevron TMAs**

Figure 2–20 show that at low frequencies, the bandwidth of a constant cross–section beam TMA is similar to that of a contoured TMA. The MMA system is not able to determine the resonant peaks of different TMAs because of the limited motions (~few nanometers) that TMAs generate at high frequencies. The noise level also increases at higher frequencies when the TMA displacements were approaching the resolution of the MMA system.

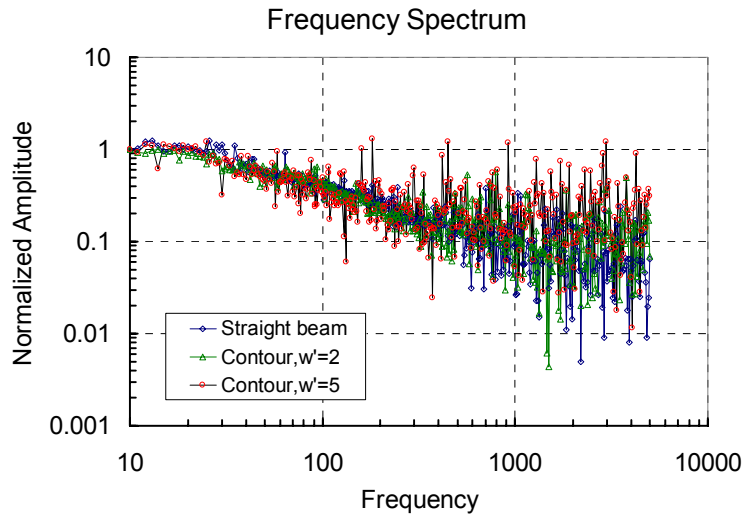


Figure 2–20 Frequency spectrum of three chevron TMAs

## 2.8 A pulsing technique for high–bandwidth positioning

This section covers a method for applying short pulses to a contoured TMA—or any thermal actuator system that is subject to non–uniform heat generation during operation—to accurately control its temperature profile and level at a specific time. The effect that occurs is an increase in thermal actuator stroke and speed of 30% and 10% respectively, and a 70% reduction in power consumption.

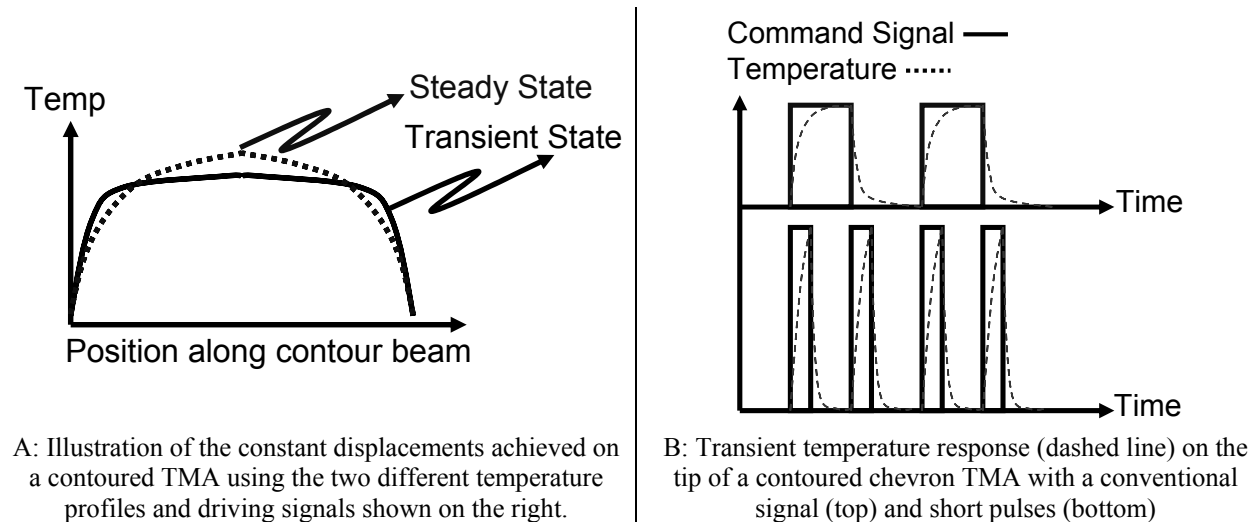
### 2.8.1 Concept of pulsing

The concept of the pulsing technique is to utilize the non–uniform generation of heat along a Joule heated beam to create a flat temperature distribution profile along the beam as shown in Figure 2–21. This technique leads to (1) a high temperature gradient on the two ends of a beam that increases cooling speed, (2) a flat temperature profile that increases thermal strain, and (3) a reduced time for displacing a thermal actuator that decreases the power consumption. Note that the flat temperature profile is a transient state of a thermal actuator for a given voltage/current input. Iterative computations are required to determine the driving signal and the pulse width that are needed to achieve a specified flat temperature.

Conventional scanning techniques commonly drive a thermal actuator to its quasi–static state. Then the actuator slowly cools down until it reaches its original position [4, 98]. A 50% duty cycle signal is common in constant cross–section TMAs because the temperature profile is

always similar to a parabola at any given time during the heating and cooling processes. If the profile is not restricted to parabolic shapes, different duty cycles could be used to improve performance.

Figure 2–21 demonstrates the effects of the pulsing technique upon a contoured TMA. Recall that in Section 2.6.1, Figure 2–13A and Figure 2–13B, it was shown that a contoured beam’s transient temperature profile goes through a sequence: (1) concave up, (2) flat, and (3) concave down. Figure 2–21A demonstrates an identical displacement of a contoured beam that was achieved by using two different temperature profiles. The corresponding signals are presented in Figure 2–21B. Note the transient state temperature profile is steeper at the ends of the beam. This steep profile, *i.e.* high temperature gradient, enables heat energy per unit time to be removed from the contoured beam to the heat sink, and this reduces the overall cooling time of the beam. This transient temperature profile may therefore be used to achieve a desired displacement in less time.



**Figure 2–21 Concepts and principles for pulsing technique for a contoured Joule heated beam**

### 2.8.2 The effects of high–bandwidth pulsing on a contoured chevron TMA

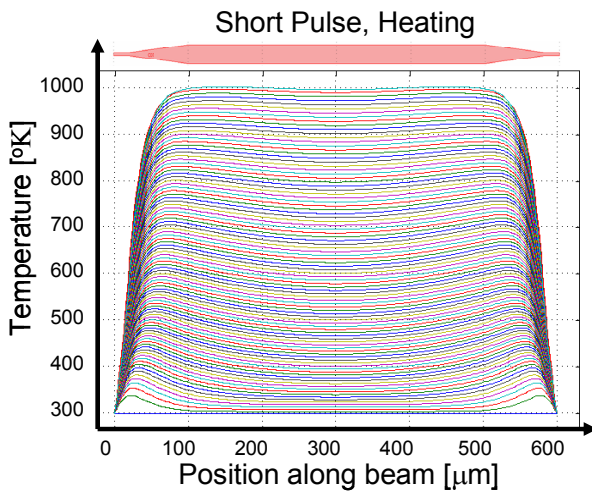
A multi–physics FEA program (COMSOL) was used to study a Joule heated contoured beam that was driven by a pulse signal (example F) and a conventional signal (example G) in order to quantify the benefits that may be obtained with pulsing. In example H, a straight beam that was driven by a conventional signal was simulated and the results of that simulation are listed to provide a baseline for examples F and G. The design parameters of the TMAs are listed

in Table 2–10, and the simulated results are summarized in Table 2–11. The heating and cooling processes of example F, G, and H are shown in Figure 2–22, Figure 2–23, and Figure 2–24 respectively.

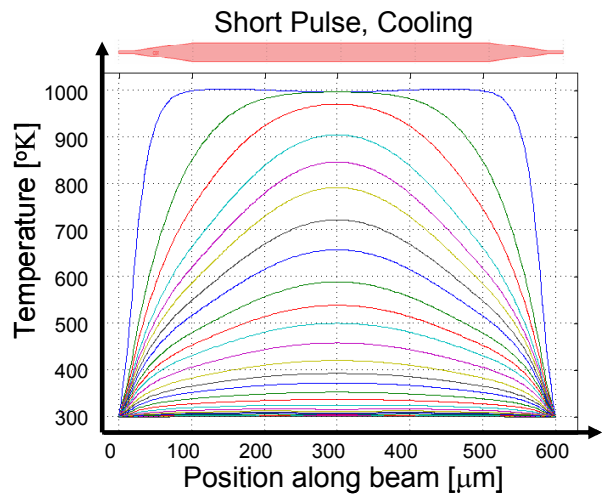
**Table 2–10 Design parameters that were used in examples F, G and H**

	Example F	Example G	Example H
Type	Contour beam		Straight beam
$L_s/L_L$	1/10		N/A
$L/2L_L$	3/2		N/A
$1/w'$	5		1
$w_e$	8 $\mu\text{m}$		8 $\mu\text{m}$
L	600 $\mu\text{m}$		600 $\mu\text{m}$
b	30 $\mu\text{m}$		30 $\mu\text{m}$
Signal type	Short pulse	Conventional	Conventional
Signal value ( $I_p$ )	54 mA	27 mA	35 mA
Pulse width ( $t_p$ )	0.94 ms	30 ms	30 ms
Command max. temp.	1000 °K	1000 °K	1000 °K
Note	Time increment = 10 $\mu\text{s}$		

The TMAs were driven to the limit for a safe operating temperature, 1000 °K. Figure 2–22A and Figure 2–22B illustrate the heating and cooling processes of the contoured beam. In Figure 2–22A, the flat temperature profile was achieved at 1000 °K. Note that almost 80% of the Joule–heated contoured beam may be maintained at 1000 °K (example F) in contrast to a single point at 1000 °K for the contoured beam and straight beam that were driven with conventional signals (example G and H). Through inspection of Figure 2–22B, one may see that the temperature at the ends of the contoured beam will decrease more rapidly because of the larger temperature gradient.



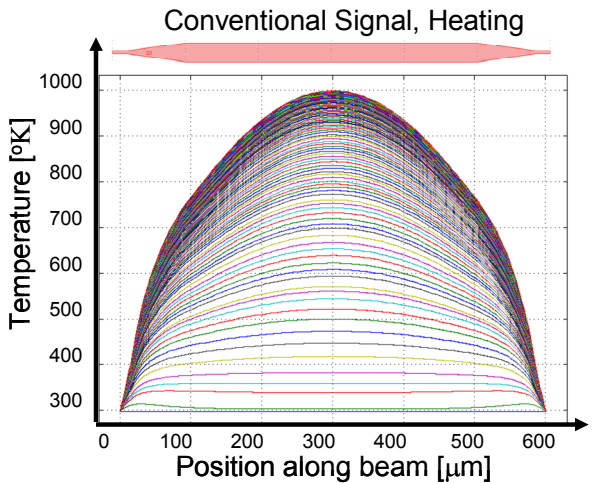
A: Heating process of a contoured beam driven with short pulse



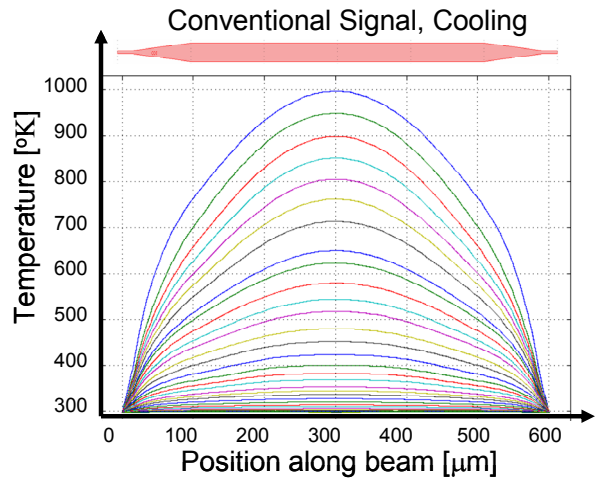
B: Cooling process of a contoured beam driven with short pulse

**Figure 2–22 Example F: Heating/cooling processes of a contoured beam in response to a single short pulse**

Figure 2–23A and Figure 2–23B illustrate the heating and cooling processes of the contoured beam that was driven by a conventional signal.



A: Heating process of a contoured beam driven with conventional signal

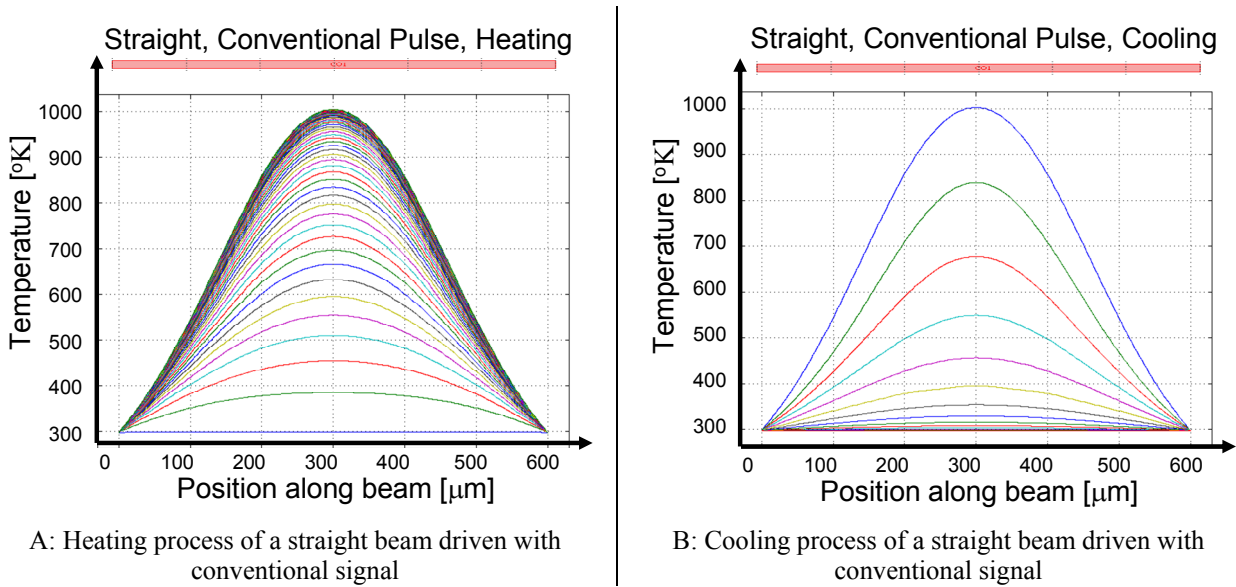


B: Cooling process of a contoured beam driven with conventional signal

**Figure 2–23 Example G: Heating/cooling processes of a contoured beam in response to a conventional signal**

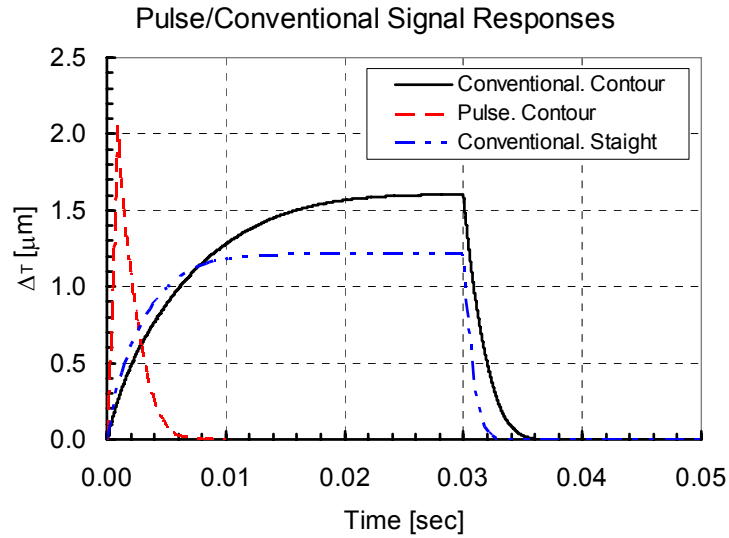
Note in Figure 2–24, the temperature profiles deviate from a parabolic shape. The most important thing to note is the low temperature gradient at the beam’s ends. This effect is attributed to the fact that the thermal conductivity and electrical resistivity for silicon are functions of temperature. Thermal conductivity and electrical resistivity decrease rapidly in silicon as the temperature increases. For example, the straight beam TMA yields worse

transducing performance because the value of silicon's coefficient of thermal expansion at 1000 °K is two times higher than at room temperature. The combined effects of contouring and pulsing yield 70% more change in beam length ( $\Delta l$ ) if both beam types experience a  $T_{max} = 1000$  °K.



**Figure 2–24 Example H: Heating/cooling process of a straight beam in response to a conventional signal**

The beam elongation for different combinations of signals and beam types are plotted as a function of time in Figure 2–25. These plots were obtained by integrating all the temperature profiles using Equation (6) and Equation (7). As expected, the pulsed profile generates almost twice the thermal strain and possesses only half the cycling time compared to a straight beam.



**Figure 2–25 Elongation of the contoured beam and straight beam under different driving conditions with maximum temperature at 1000 °K**

The results from Figure 2–22 through Figure 2–25 are summarized and compared in Table 2–11. A 28% enhancement in stroke, 11% reduction in cooling time, and 70.9% reduction in power consumption were obtained by using the same contoured beam with pulsing. If the pulsing technique is applied to the same contoured beam that was driven with a conventional signal, the same displacement may be achieved at 850 °K by using the flat temperature profile. Also, the time required for cooling and the reduction in power are further enhanced by 23% and 73% respectively.

**Table 2–11 Summary of performance of example F, G, and H**

	Example F	Example G	Example H
Type	Contour		Straight
Signal type	Short pulse	Conventional	Conventional
Rise time	0.85 ms	13.80 ms	6.66 ms
Fall time	3.02 ms	3.40 ms	1.60 ms
Elongation	2.06 μm	1.60 μm	1.21 μm
Stroke enhancement	+0.28	1	-0.24
Normalized forward speed enhancement	+19.8	1	+0.56
Normalized returning speed enhancement	+0.45	1	+0.59
Normalized power consumption	-0.71	1	+0.68
Note	Time increment = 10 μs		



### 2.8.3 Determination of driving signal

This section presents a systematic approach that may be used to determine the proper pulse characteristics for a given contoured beam and at a desired temperature profile. If too much power is supplied during a short time interval, the beam will fail. If too little power is supplied, the temperature profile will become flat at too low of a temperature, and the beam will not achieve its best performance.

Two parameters, driving current ( $I_p$ ) and pulse width ( $t_p$ ), need to be determined. Example F will be used in the following discussion to demonstrate how  $I_p$  and  $t_p$  may be found. In Figure 2–26, the maximum temperature is set at 1000 °K, and the objective is to find the current,  $I_p$ , and  $t_p$  so that the temperature at  $X_1$  (or  $X_3$ ) on the contoured beam is equal to the temperature at  $X_2$  at time  $t_p$ . The variables  $I_p$  and  $t_p$  may be found using Equation (1) with the described objective, a proper initial condition (I.C.) and boundary conditions (B.C.).

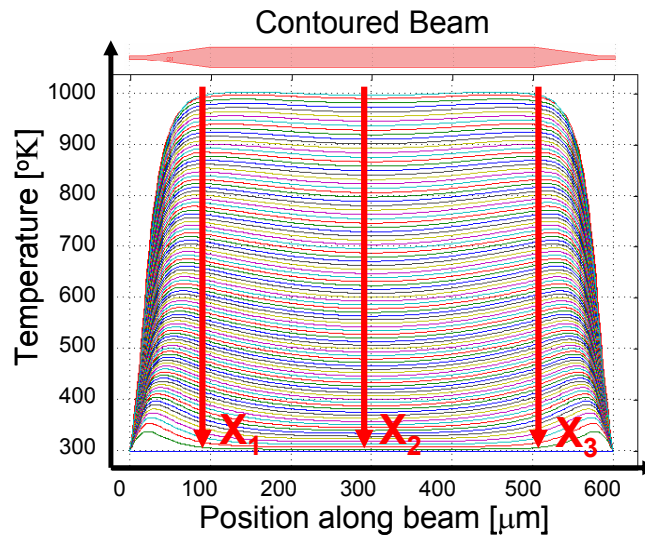


Figure 2–26 Determination of the proper current ( $I_p$ ) and pulse width ( $t_p$ ) so that  $T(X_1, t_p)$  equals to  $T(X_2, t_p)$

Equations (26) to (29) list the design objective, the modified Equation (1), the boundary conditions, and the initial condition that are required to iteratively solve for  $I_p$  and  $t_p$ . Once the position  $X_1$  is selected ( $X_2$  is at the center of the beam), Equation (26) to (29) will yield unique solutions for  $I_p$  and  $t_p$ . Note that  $X_1$  is usually recommended to be at the end of the wide beam section on a contoured beam (in example F,  $X_1 = 100 \mu\text{m}$ ). Choosing an  $X_1$  that is too close to the ground will result in a higher driving current/voltage and small pulse width ( $\sim 10\text{s}$  to  $100\text{s}$  ns).

This may lead to technical difficulties and often does not help to further improve TMA performance.

$$\text{Objective: } T(x_1, t_p) = T(x_2, t_p) = 1000K \quad (26)$$

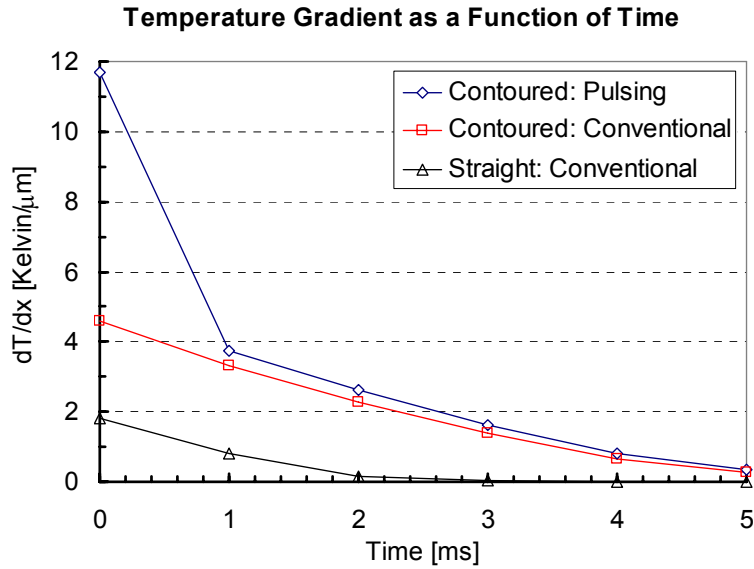
$$\frac{\partial}{\partial x} k(T) \frac{\partial T}{\partial x} + r(x) \cdot \frac{I_p}{A(x)} = \rho \cdot C_p \frac{\partial T}{\partial t} \quad (27)$$

$$\text{B.C. } T(x = L, t_0 = 0) = T(x = 0, t_0 = 0) = 300K \quad (28)$$

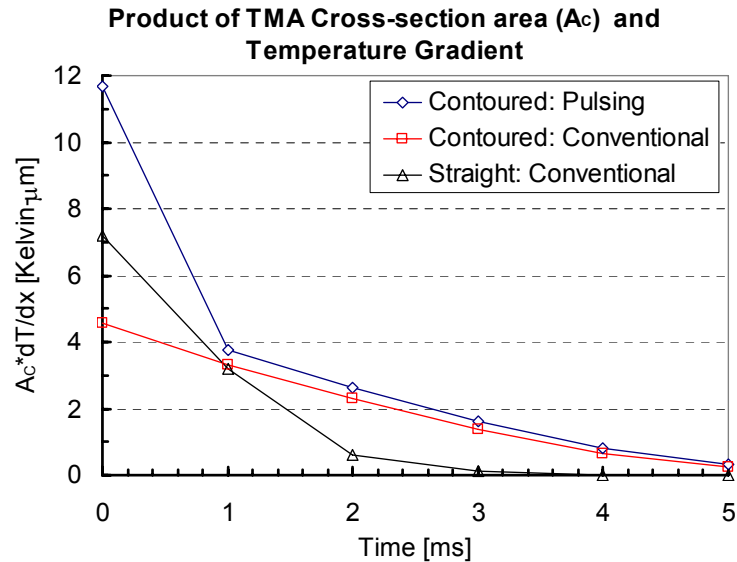
$$\text{I.C. } T(x, t_0 = 0) = 300K \quad (29)$$

#### 2.8.4 The reason for increased heat transfer rate at beam ends during pulsing

As shown in Figure 2–27A, the temperature gradients at the ends of a contoured beam are always larger than the ones for a straight beam. As shown in Figure 2–27A, the pulsed contoured beam initially has a high temperature gradient. This gradient gradually approaches the gradient of a contoured beam that is driven by a conventional signal. Figure 2–27B plots the product of the temperature gradient and the cross-sectional area at the end of the beams. This product is important because it is proportional to the heat transfer rate at the ends of the beam during the cooling process. As in example F and G,  $w_L/w_S = 4$ . This limits the overall heat transfer rate because there is a four-times-smaller cross-section area at the ends of the contoured beam. When pulsing is applied to a contoured beam, a smaller width ratio usually provides better speed, but reduced stroke enhancement. In practice, this is a decision made by the designer depending on the actuator requirements. For example, the contoured TMAs that were used in the prototype scanner within Chapter 3 and Chapter 5 were designed to optimize their speed and stroke performance respectively.



A



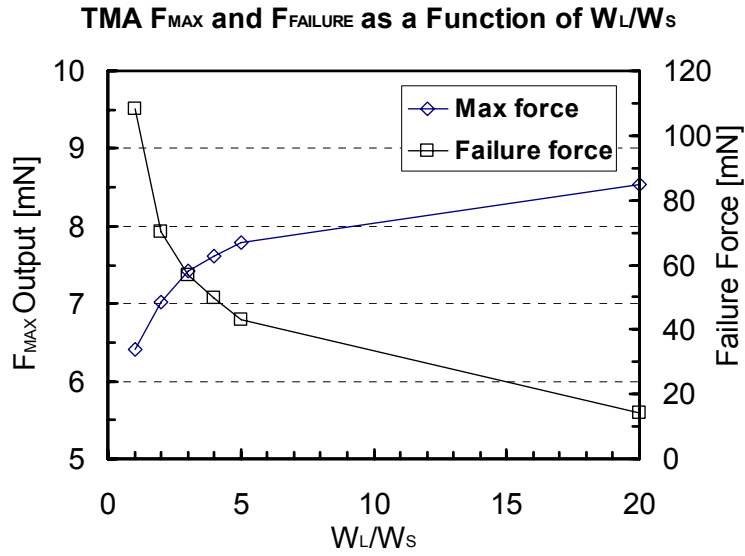
B

Figure 2–27 Temperature gradient and product of temperature gradient and cross–section area at the end of a beam as a function of time for example F, G, and H

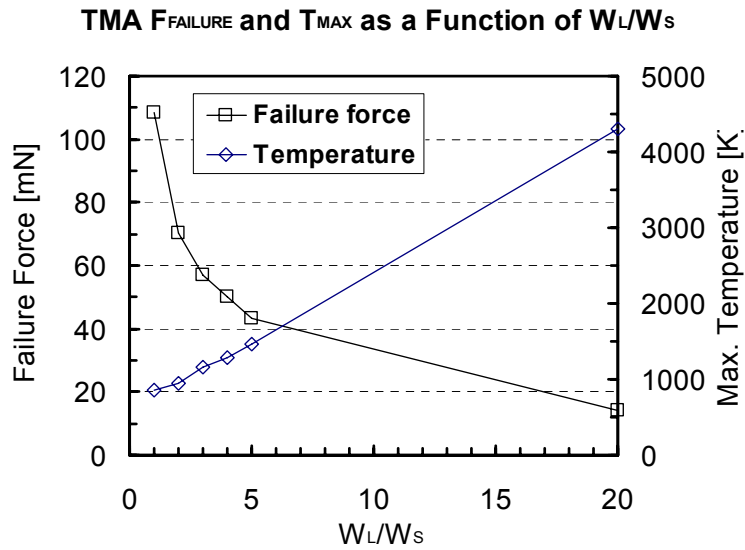
### 2.8.5 Mechanical failure limits

In Figure 2–28A, the maximum force outputs (for actuator displacement = 0) for a chevron TMA and the TMA failure force loads are plotted vs. width ratio. From Figure 2–28A, one may see that as contouring decreases the force required to induce a failure, a TMA’s failure force is much larger than the TMA’s maximum force output for practical width ratios, *e.g.*  $w_L/w_S < 5$ . Figure 2–28B presents the TMA failure force and maximum temperature for a constant

power input. The area under the two curves represents the limiting design condition for a contoured TMA. As the maximum temperature, *i.e.* TMA efficiency, rises when  $w_L/w_S$  increases, the practical operating limit for a specific TMA is limited by the failure temperature of the material.



A



B

Figure 2–28 Limiting conditions for contoured TMAs

## 2.9 SUMMARY

This chapter has demonstrated the principles of geometric contouring and its effects on quasi-static and transient performance via several simulated examples. Through geometric contouring, the quasi-static and the dynamic performance of TMAs may be improved by an order of magnitude. Although contouring micro-devices may enhance their speeds by orders of magnitude, a mismatch between the operating frequency and the mechanical resonant frequency of the micro-device still exists, *e.g.* 500 Hz vs. 10 kHz. In the next chapter, this bandwidth mismatch problem will be resolved via the introduction of a MFM concept that enables tradeoffs between the cycling speed and resonant frequency.

*This page is intentionally left blank*

# Mechanical Frequency Multiplier

---

This chapter introduces the concepts, modeling techniques and design guidelines that are needed to create a mechanical frequency multiplier (MFM) system. These concepts, techniques, and guidelines will be elucidated via the design of a fiber resonator for the endoscopic scanner. The MFM concept provides a way to increase the cycling speed of the TMAs by a factor of 20 or more.

## 3.1 Introduction

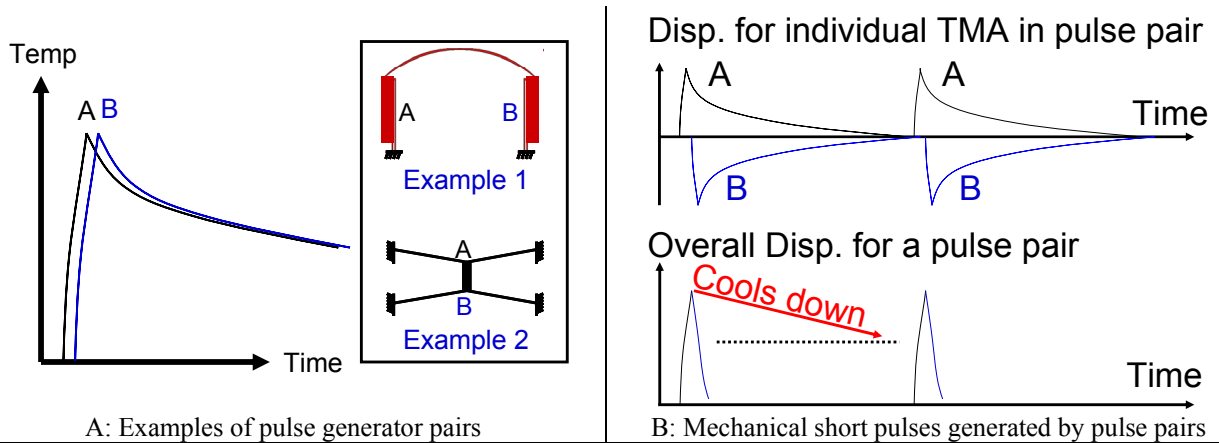
An MFM is a flexure–actuator system that is arranged so that it is possible to use only the constituent actuators’ highest frequency content. The opposed actuators possess different forward and return stroke speeds. The idea of MFM is to use the high–speed portion of the one actuator to rapidly achieve half–cycle motion and then use the opposed actuator to rapidly return the last half cycle. If  $N$  actuator pairs are placed in parallel, time delayed signals may be used to drive each set with a delay, thereby increasing the cycling frequency by  $N$ .

The MFM concept may be used with any type of actuators that possess different forward and return stroke speeds. A TMA provides an excellent example. The bandwidth of a TMA is limited by heat diffusion. A TMA may be quickly heated when a large amount of power is supplied in a short period of time. This characteristic heating time scale is related to microscopic energy transport mechanisms that include (1) electron collision and scattering and (2) phonon scattering. Both are on the scale of  $10^{-15}$  and  $10^{-13}$  second respectively [105]. Cooling is a much slower process, by a factor of 10 orders of magnitude on the micro–scale. This means that cooling (returning stroke) limits the bandwidth of TMAs.

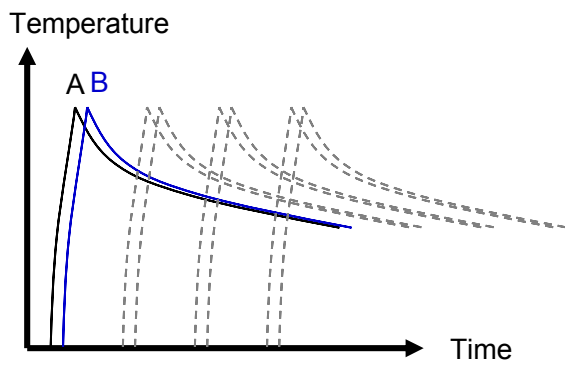
### 3.2 Concepts and design

A high frequency mechanical pulse output may be generated by pairing two TMAs, “A” and “B”, in opposing directions and supplying them with time–delayed power input A and B respectively. This is shown in Figure 3–1A. Although A and B cool down slowly, the resultant motion for the TMA pair is a sharp pulse, as shown in Figure 3–1B. Here, the mechanical pulse width is not limited by cooling time/process. It is only limited by the dynamic characteristics of the actuator pair that is the pair’s resonant frequency.

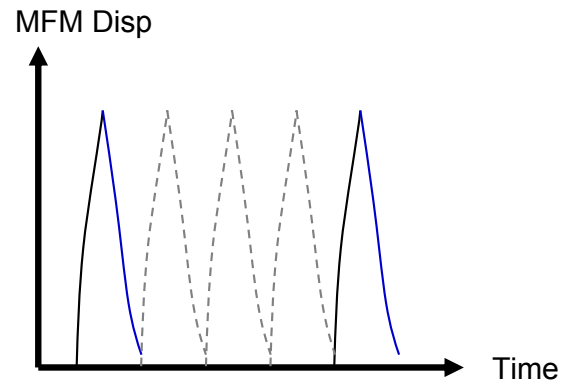
An actuator system with high bandwidth may be constructed if many of the TMA pairs act in parallel to drive a common stage with time delays in their pulses. This concept is illustrated in Figure 3–1 C and D.







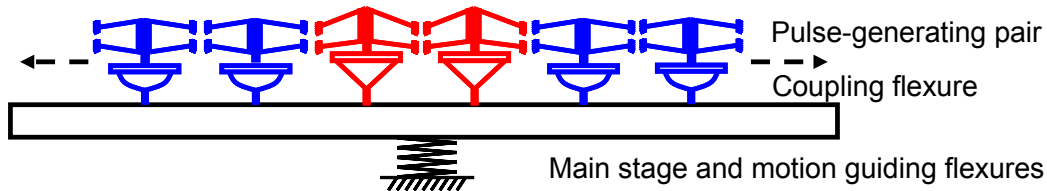
C: Max. temperature on individual pulse pair



D: Multiple pulse pairs are combined to form an MFM

**Figure 3–1 : Schematics of a MFM system. A, B: Pulse generator TMA pair concept; C, D: Ideal case for pulse pairs to run in time–delayed fashion**

A mechanical frequency multiplier consists of three components: (1) a pulse–generating TMA pair, (2) a decoupling flexure, and (3) a main stage that is guided by flexures. Figure 3–2 presents an example that yields linear motion. When the number of TMA pairs is more than two, the decoupling flexure design becomes important. Figure 3–2 shows a decoupling flexure design concept that works like a “mechanical diode”. This design only transmits the motions of the TMA pairs that are in action, *i.e.* the two TMA pairs in the center of the stage, so that the stiffness of all other TMA pairs will not impede the cycling motion of the MMA system.



**Figure 3–2 Schematics for a mechanical frequency multiplier**

### 3.3 Pulse generation

In this section, the results of FEA simulations of MFM–enabled contoured chevron TMA pairs are demonstrated to (1) better understand the physics/phenomenon of the TMA pairs and (2) obtain a reasonable set of design parameters. Figure 3–3A shows a TMA pair and relevant design parameters. Figure 3–3B presents the driving voltages/signals for TMA A and B. The temperature versus time and displacement versus time plots are presented in Figure 3–3C and Figure 3–3D, respectively. As shown in Figure 3–3D, the displacements at point A and B during pulsing are slightly different because the beam that connects TMAs A and B also heats up and

expands during the pulsing process. The small bumps seen after the mechanical pulse are the overshoots that occur when TMA B pushes back on TMA A. These bumps may be avoided via use of better-tuned signal shape and proportion for TMAs A and B.

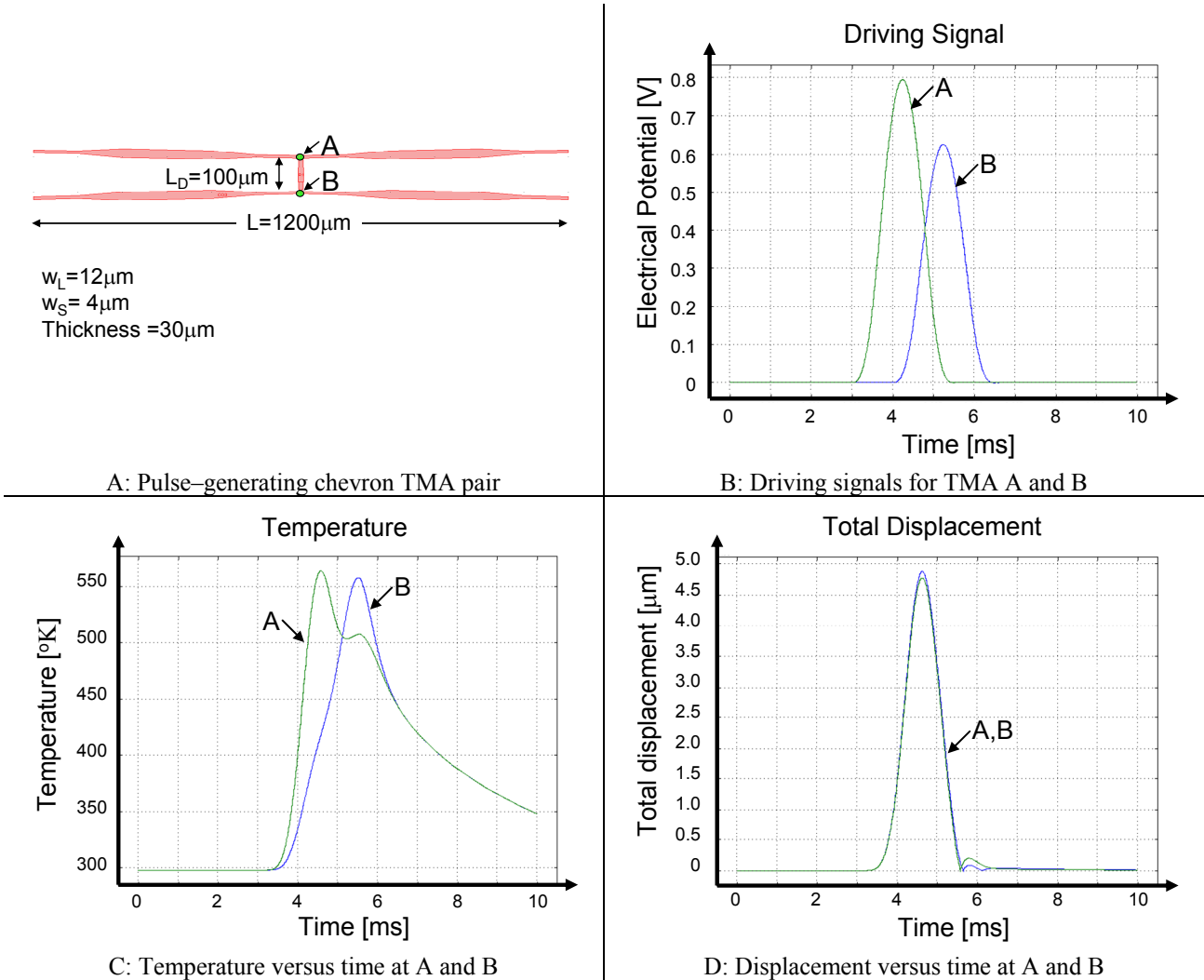


Figure 3-3 A FEA (COMSOL) simulated example of pulse-generating pair design

It is important to note that as the temperature at the points A and B are coupled, the driving signals for actuators A and B must be time-delayed and possess different amplitudes. This is a challenging and interesting problem to tackle, but an alternate solution would be to thermally decouple actuator A and B. A thermally decoupled system simplifies the control, modeling and design of the MFM resonator. If the two were thermally decoupled, the methods in Chapter 2 could be used without change to model the pairs' thermal behavior. From here on, it shall be assumed that the decoupling exists and therefore there is no need to discuss modeling

beyond what was described in Chapter 2. Section 3.4.4 provides metrics and procedures that may be used to determine whether a suitable amount of decoupling exists for one to use the results of Chapter 2 without modification.

### 3.4 MFM fiber resonator

Use of MFM is demonstrated via the design of an MFM fiber resonator that drives one axis of the scanner. A detailed discussion of this case study, including problem definition, functional requirements, experimental results, and an alternative meso-scale fiber resonator design may be found in Chapter 1 and 5.

#### 3.4.1 Functional requirements and constraints

Table 3–1 lists the functional requirements and design constraints of the resonator. These values were generated based on the requirements of a 2 fps and 30 fps scan rate and 100 x 100 x 100  $\mu\text{m}^3$  scan volume. The envelope constraints were necessary as the resonator must fit inside of a standard endoscope port. As the current goal of this endoscopic scanning system is to obtain *ex vivo* high-resolution images, microscopic images of relatively immobile tissues, most optical scanning will be performed at a rather low frame rate, *i.e.* 2–5 fps. As such, the goal in the following design example will be to design a MFM that operates at 1.6 kHz with a fiber loaded upon the device. The maximum cycling frequency was designed to be at 3.0 kHz. The MFM should be able to operate at 3.0 kHz with the easy adjustment of fiber insertion length if this were to be needed.

**Table 3–1 Functional requirements and design constraints for the resonator**

Degree of freedom	1
Maximum cycling frequency	700 Hz for 2D high resolution scanning, frame rate = 2fps 3.0 kHz for high-speed scanning, frame rate = 30fps
Resonator stroke	+/- 1.5 $\mu\text{m}$
Fiber tip displacement	+/- 50 $\mu\text{m}$
Footprint	7x7 $\text{mm}^2$
Voltage	less than 5V

#### 3.4.2 Fiber resonator concept

The concept for the resonator is shown in Figure 3–4. Two pulse-generation chevron TMA pairs are located at either side of the main stage. This is the most basic form of an MFM system. In this design, four TMAs also function as (1) the motion guiding flexures and (2) the

coupling flexures that transmit their motions to the stage. This is an elegant flexure concept that provides the MFM with a high mechanical resonance frequency (17.7 kHz). The device was designed to fit within a 2x2 mm<sup>2</sup> envelope. The four-channel design was able to achieve 4 times the cycling frequency of one of its constituent TMAs.

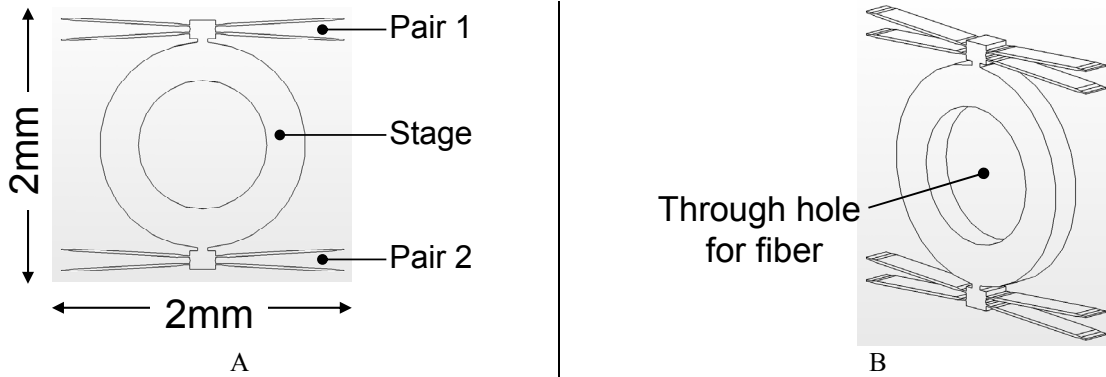
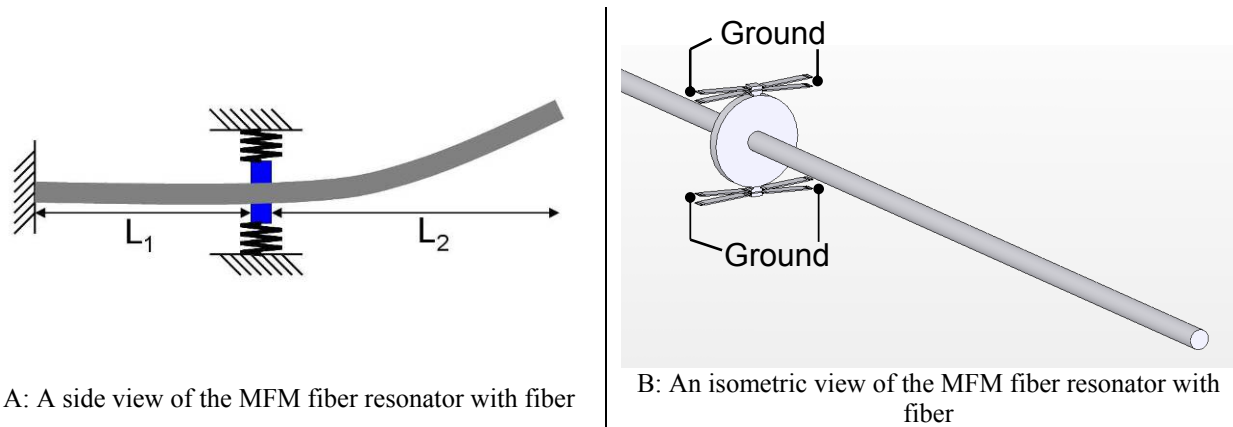


Figure 3-4 Concept of resonator stage

Figure 3-5 demonstrates how the fiber may be attached to the resonator. The length ( $L_1$ ) between the resonator stage and the wall constraint, and the length ( $L_2$ ) from the resonator stage to the fiber's free end, should be determined so that the fiber will resonate at the desired frequency with respect to the resonator stage.



A: A side view of the MFM fiber resonator with fiber

B: An isometric view of the MFM fiber resonator with fiber

Figure 3-5 Schematic for a MFM fiber resonator system

### 3.4.3 Design concerns

A moderately detailed discussion of the hardware design is presented in the following sub-sections.

### Decoupled TMA behavior

In Section 3.3, it was shown that the temperature profiles of each TMA could be coupled. This complicates the modeling of TMA response. As shown in Figure 3–6, this problem, coupling, may be resolved by inserting a heat sink between each beam. Depending upon the heat sink design, one of three different types of behavior will be observed. They are shown in Figure 3–6. In case I (without heat sink), the thin Joule–heated beams that are close to the central region will operate at high temperature while most other regions on the Joule–heated beam will remain at a lower temperature. This design leads to a reduced average thermal strain, *i.e.*, stroke, and so it is avoided. In case II, a flat temperature profile throughout the central region and the TMAs is achieved. In this design the thermal strain is maximized. The temperatures are, unfortunately, coupled, so the system becomes difficult to model and control. In case III, the heat sink is maintained at low temperature so that each beam becomes decoupled from the others. In this case, the modeling results from Chapter 2 are immediately useful. A good way to determine whether each chevron TMA may be considered to be well–decoupled, and to quantify the degree of decoupling, is to compare the temperature rise at the heat sink ( $\Delta T_{SINK}$ ) and the maximum temperature on the TMA ( $T_{MAX}$ ). In general, if  $\Delta T_{SINK}/T_{MAX}$  is less than 15%, the 1D contoured beam model will yield less than 5% error compared to the FEA result. From here on, it will be assumed that MFM TMA pairs are suitably decoupled as in case III.

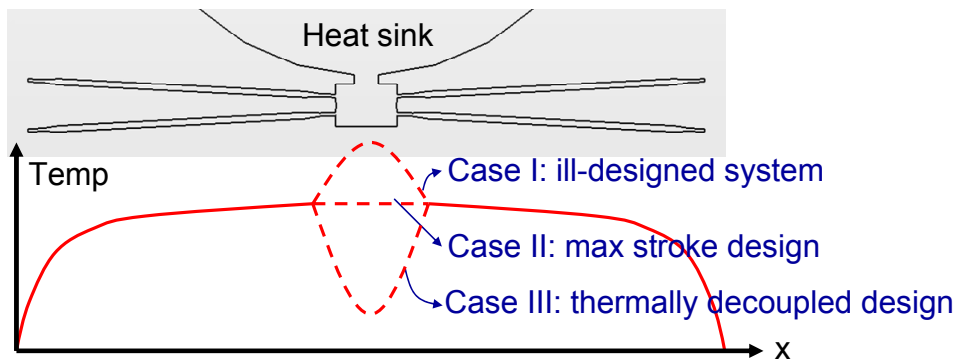
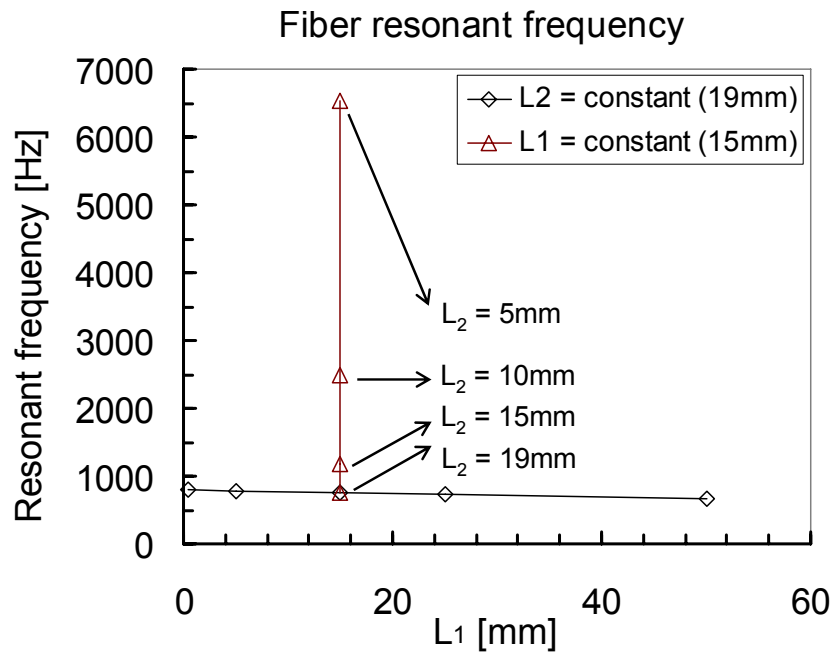


Figure 3–6 Temperature distributions along the chevron TMAs of the MFM resonator. The dashed lines are possible temperature profiles with different design objectives (case I, II and III).

### Determining the traverse resonant frequency of the fiber

FEA simulations were used to determine the relationship between the fiber’s resonant frequency and the fiber resonator design parameters. Note that FEA was used here to help the

designer quickly understand the properties of the resonant fiber. More information about the double cladding photonic crystal fiber [106] and a parametric model that predicts the transverse resonant frequency of the DCPCF will be presented in Section 5.4. The results are summarized in Figure 3–7A and B. From Figure 3–7A, it was found that  $L_2$  is the dominant parameter that controls the resonant frequency and, from Figure 3–7B,  $L_1$  is the dominant parameter that determines the stiffness in the lateral direction. By varying the length of  $L_1$ , the fiber’s lateral stiffness may be changed by as much as 5 orders of magnitude, *i.e.* for  $L_1 = 0$  to 15 mm, the change in stiffness ratio varies from  $5.8 \times 10^{-3}$  to 120. It is therefore possible to precisely control the resonant frequency with the proper values of  $L_1$  and  $L_2$ . These values are also subject to the desires to (1) minimize the device envelope (smallest possible  $L_1$ ), and (2) deliver the proper stroke with optimized energy transfer, *e.g.* matched mechanical impedance of the fiber’s lateral stiffness and MFM stage’s stiffness.



A

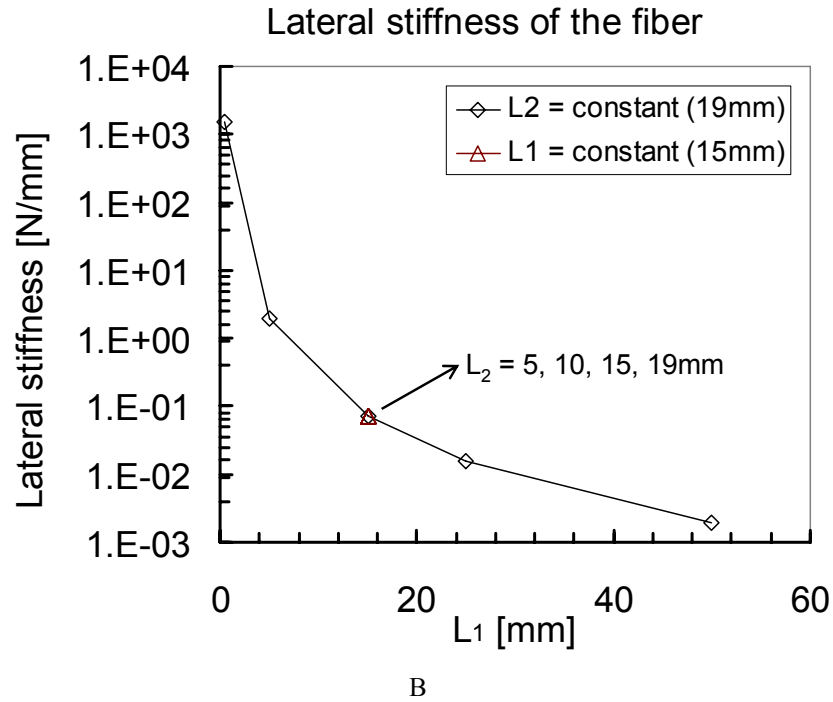


Figure 3-7 Fiber resonant frequency and fiber lateral stiffness variation as a function of  $L_1$  and  $L_2$

### Offset lateral & longitudinal resonant modes

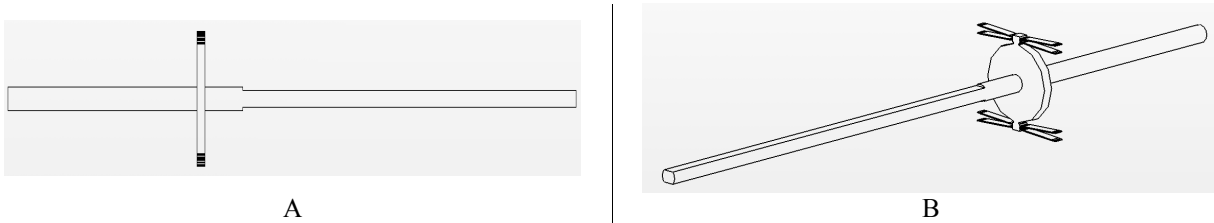
For a uniformly constrained fiber, the lateral and longitudinal resonant frequencies are equal. The fiber resonator for the case study is intended to perform line scanning and therefore, it is important to offset the longitudinal and lateral resonant frequencies in order to prevent undesired resonant modes, *e.g.*, a Lissajous pattern. Experiments show that the modes of vibration for the double cladding photonic crystal fiber (DCPCF) could be resolved if a 10Hz separation in frequency is introduced. This is because of the high Q factor of the silica DCPCF. A more in-depth discussion and property characterization of the DCPCF may be found in Chapter 5. For now, the discussion only needs to acknowledge the aforementioned characteristics.

There are two ways to effectively offset the longitudinal and lateral resonant frequencies:

(1) Offset the axial and lateral stiffness ratio of the MFM fiber resonator stage. This approach was used in this design, or

(2) Partially remove the jacket layer of the DCPCF so that the fiber possesses different stiffness characteristics in the longitudinal and lateral directions.

This could be done as shown in Figure 3–8. The simulated performance of these methods is summarized in Table 3–2. Both methods are feasible ways to induce tens to hundreds of Hertz frequency offset and thereby resolve the issue.



**Figure 3–8 Offset longitudinal and lateral modes by partially removing materials from fiber**

Although removing materials from fiber will offset the resonant modes, it is not recommended unless necessary.

**Table 3–2 Adjusting longitudinal and lateral resonant frequencies of the DCPCF**

Method	Longitudinal mode	Lateral mode	$\Delta\omega$
Offset stiffness ratio of MFM resonator	1577 Hz	1851 Hz	274 Hz
Removing material from fiber	1559 Hz	2053 Hz	494 Hz
This was simulated based on a DCPCF with its jacket layer removed.			

**TMA selection and design: contoured vs. straight**

Geometric contouring designs were applied to the TMAs in the MFM fiber resonator to enhance stroke, efficiency and power consumption. From Chapter 2, it is known that the forward and return speed ratio of a contoured TMA may be controlled by either the input command or the design parameters for a contoured beam ( $L_L$ ,  $L_S$ ,  $W_S$ ,  $W_L$ , and  $L$ ). It is therefore important to design each constituent contoured TMA of the four–TMA MFM system so that its fall time (cooling time) is equal to, or larger than, four times its rise time (heating time). The MFM system will not perform efficiently if this requirement is not met. The contoured TMAs of the MFM system were then designed and optimized based on this objective and the static/dynamic TMA performance charts provided in Chapter 2. The finalized design parameters of TMAs are listed in Table 3–3. The performance enhancements compared to conventional straight beam chevron TMAs are also listed in Table 3–3 for reference. Note that the high–speed pulsing may be applied to the contoured TMAs in the MFM resonator.



**Table 3–3 Design parameters and improved performances of contoured TMAs in comparison to conventional constant cross–section TMAs**

Contoured TMA design parameters for MFM fiber resonator			
$L_S/L_L$	1/8	$w_e$	9.25 $\mu\text{m}$
$L/2L_L$	5/4	$L$	1000 $\mu\text{m}$
$w'$	1/2	$b$	200 $\mu\text{m}$
Contoured TMA performance enhancements vs. constant cross–section TMA			
Constant power		Constant displacement	
Speed	$\uparrow 1.8\text{X}$	Power	$\downarrow 19\%$
Stroke	$\uparrow 1.3\text{X}$	Temperature	$\downarrow 12\%$
Force	$\uparrow 1.3\text{X}$	Efficiency	$\uparrow 2\text{X}$

### **Minimize thermal drift**

In all electromechanical systems, as long as there is heat generated while in actuation, heat will gradually be accumulated within the structure. As the heat capacity is usually related to the total mass of the system, it is not uncommon for a system’s thermal equilibrium time constant to be few orders of magnitude larger than the time constant, *i.e.*, rise/fall time, of its actuators, *e.g.*, TMAs or coils in the electromagnetic actuators.

A thermal–centric design is therefore often applied in precision mechanisms or machines, *e.g.*, the HexFlex mechanism or micro–HexFlex [4], to reduce the magnitude of a system’s thermal drift that may exacerbated by a large system’s thermal time constant. Based upon this concept, a symmetric MFM design was used, and the reduction in thermal drift that occurs will be shown within the next section.

### **Power source selection**

An MFM resonator with four TMAs would be made of one piece of electrically conductive silicon (resistivity = 0.001 Ohm–cm). As such, special attention must be paid in order to direct the current into its desired flow path, *i.e.* current from each channel flows only through the designated TMA as shown in Figure 3–9A. This may be achieved by using four independent current sources as for each current source,  $i_{IN}$  should equal to  $i_{OUT}$ , and this constraint forces the current only to flow in the designated TMA.

As shown in Figure 3–9B, if a voltage source were used, the current would just spread out into all TMAs and the MFM would not function properly. This, however, may be rectified by applying the input voltage at both ends of a TMA and providing two additional grounds at the

middle of the resonator stage as shown in Figure 3–9C. In practice, the additional grounds would be two flexures that are compliant in the stage’s desired direction of motion. As additional compliant flexures added onto the stage may introduce potential problems such as wobbling flexures, the concept in Figure 3–9A was used with a custom–made current supply.

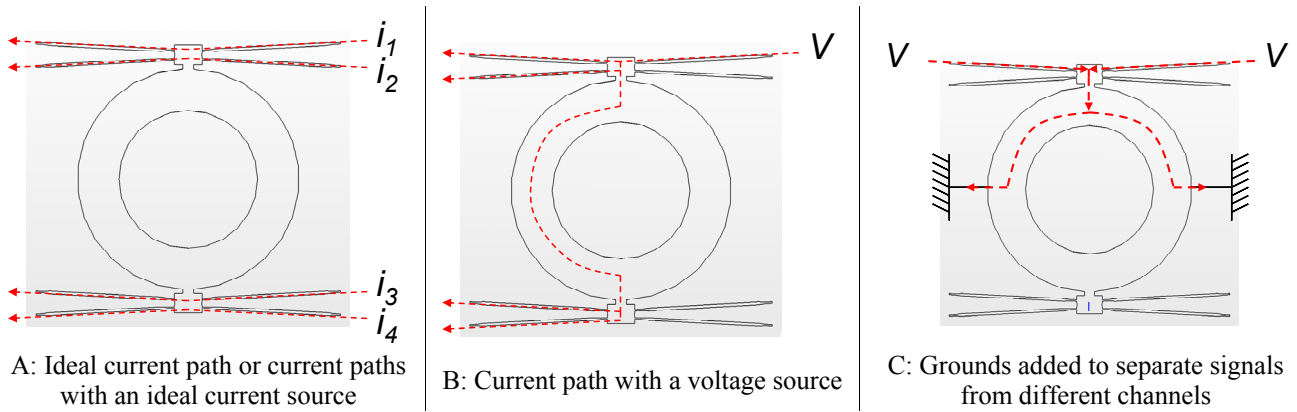


Figure 3–9 Current paths at the MFM resonator with different sources

### 3.4.4 Driving signal for system level model

A parametric signal model was created to drive the MFM system. This equation, shown in Equation (30), is a special case of the driving signal,  $i(t)$ , that was used in the models of Section 2.2.2. The models that were created for thermal and stiffness matrix modeling were not changed and the details regarding them will not be repeated here.

In Equation (30),  $I_0$  is the signal amplitude,  $f$  is the desired operating frequency,  $m$  is the total number of pulse–pairs or channels,  $p$  specifies the time delay on the  $p^{\text{th}}$  channel or TMA ( $p = 0$  to  $2m-1$ ), and  $n$  is the overlay signal index that controls the signal overlay level. Its effects are shown in Figure 3–10.

$$i(t)_{m,p} = I_0 \cdot \left[ \frac{1}{2} \left| \sin \left( 2\pi \cdot f \cdot t - \frac{p\pi}{m} \right) \right| + \frac{1}{2} \sin \left( 2\pi \cdot f \cdot t - \frac{p\pi}{m} \right) \right]^n \quad (30)$$

Figure 3–10 shows an example of how changing the value of the overlay index,  $n$ , will modify the signal. When  $n$  is small, the parametric model yields a square–wave–like signal; when  $n$  is large, the parametric model yields an impulse–like signal.

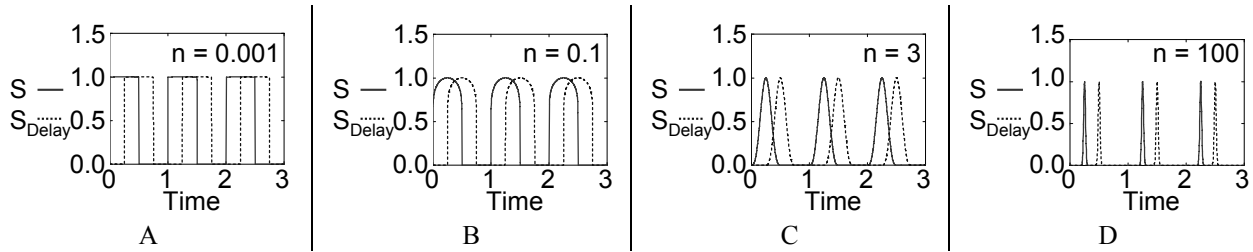


Figure 3-10 Examples of the parametric signal model with  $n=0.001, 0.1, 3,$  and  $100; p=0, 1; m=2; f=1$

### RC time delay circuit

For an MFM system of  $n$  channels, it may be impractical to drive the system with  $n$  independent digital to analog output channels from a data acquisition system. A practical way to drive a multi-channel MFM system is to drive a single channel signal and a high-bandwidth time delay circuit that is coupled with a multi-channel voltage controlled current amplifier.

A four-channel analog RC delay circuit was built for the MFM resonator. The schematic of the circuit is shown in Figure 3-11. The time delay is twice the product of the electrical resistance and capacitance. A broad band op-amp was used to preserve the high frequency content in the command signal. The time delay may be tuned by changing the resistance value of the potentiometer.

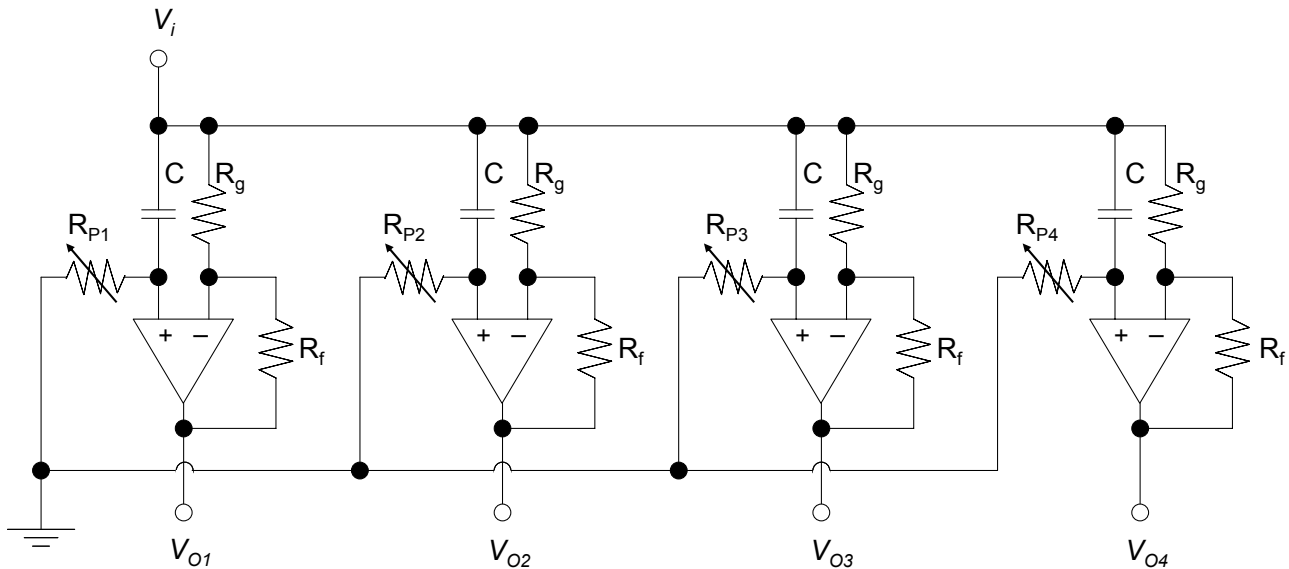


Figure 3-11 A four-channel analog RC delay circuit that was used to drive the MFM fiber resonator

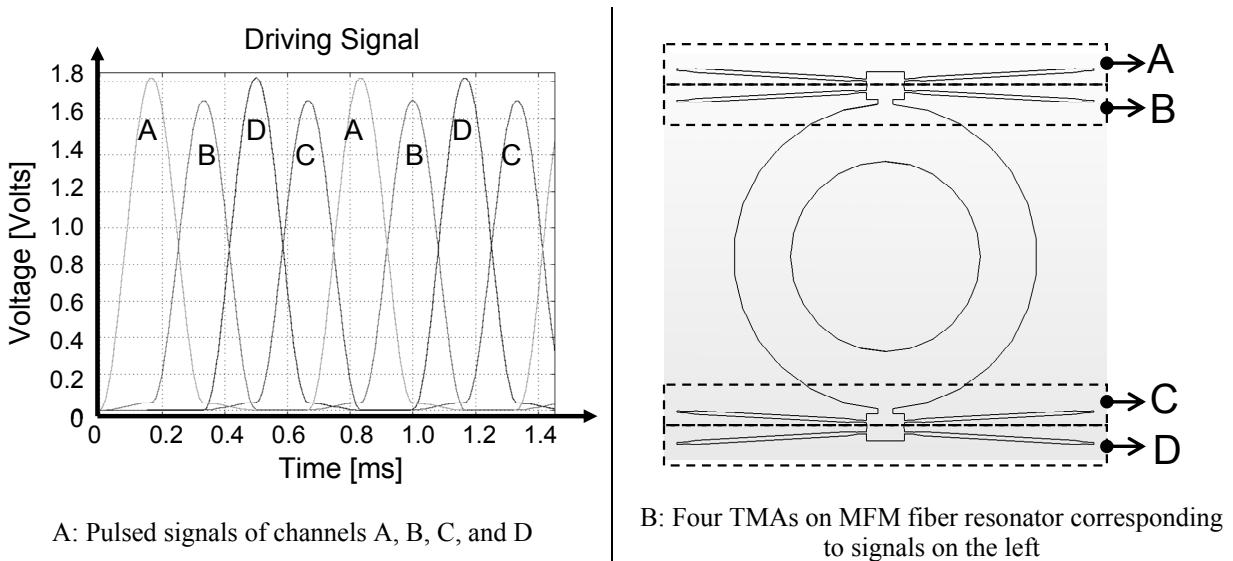
### 3.4.5 Simulation results

The final design was optimized with respect to the design issues that were presented in the previous sections. Simulated results of the resonator's stroke, cycling frequency, transient temperature profiles, etc., are covered within the following. The results are summarized in Table 3–4.

**Table 3–4 Summary of MFM fiber resonator modeling and design**

Device envelope	2x2 mm <sup>2</sup>
Resonant frequency (unload)	17.7 kHz (1 <sup>st</sup> mode)
	28.6 kHz (2 <sup>nd</sup> mode)
Resonant frequency with fiber loaded	1.6 kHz (1 <sup>st</sup> mode)
	1.8 kHz (2 <sup>nd</sup> mode)
Stroke at 1.6 kHz (unload)	8.2 μm (± 4.1 μm)
Maximum cycling frequency	4.0 kHz
Lateral stiffness of the MFM stage	8.69 N/mm
Lateral stiffness of the fiber	0.64 N/mm

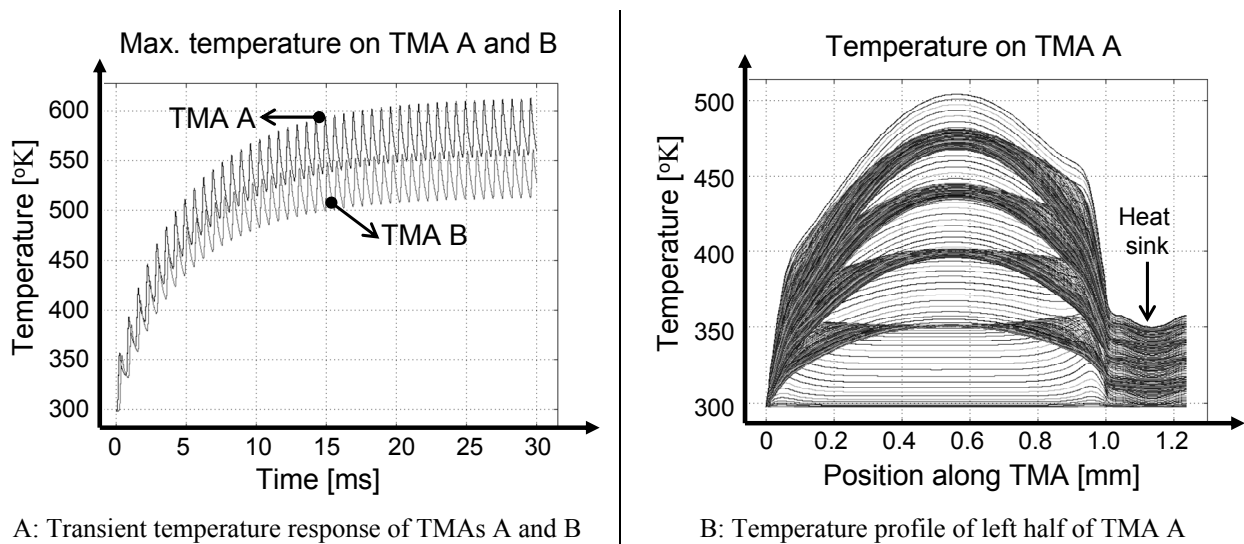
Figure 3–12A shows the time–delayed command signals that were used to drive the TMAs. Figure 3–12B provides a legend for the different TMAs. The command signals were generated using Equation (30). The following values were used:  $f = 1600$  Hz,  $m = 2$ ,  $n = 2$ ,  $I_0 = 45$  mA and 42 mA for  $p = 0, 2$  and 1, 3 respectively.



**Figure 3–12 Time–delayed short pulses for four TMAs: A, B, C, and D**

Figure 3–13 shows the simulated transient temperature evolution along the resonator's TMAs. Figure 3–13A shows transient maximum temperature change at the center of the left most beam in TMAs A and B. From Figure 3–13A, it was found that the resonator has a 12 ms

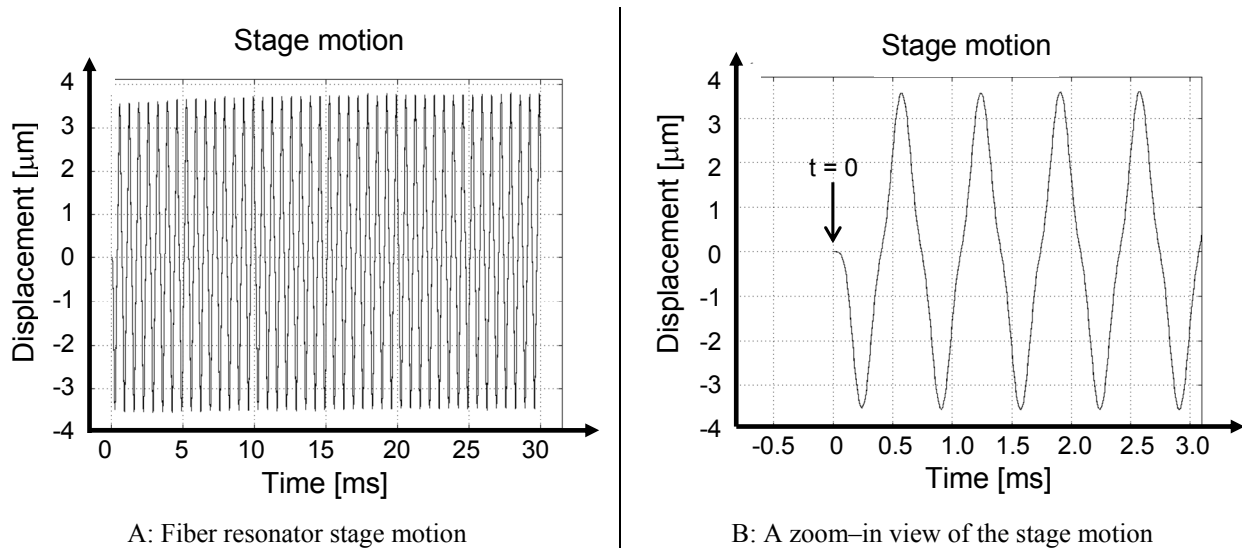
thermal time constant (90% of steady state value). Figure 3–13B plots the transient temperature evolution of the left most part of TMA A, from the ground (left) to the center of the heat sink mass block (right). From Figure 3–13B, it may be seen that with the heat sink the temperatures on the individual TMA were decoupled, such that  $\Delta T_{SINK}/T_{MAX}$  is less than 14% and the difference between the 1D model and FEA results is less than 5%. It should also be noted that the driving current for TMA B and C (channel 1, 3) were designed to be slightly less than the current for TMA A and D (channel 0, 2), in order to compensate for the temperature rise of the heat sink during each half cycle. This was done so that the TMA pulse pairs always generate equal forward and returning strokes. A fully decoupled system would have used the same signals for all channels. In the simulation, different values for  $I_0$  were iteratively determined by setting the forward and returning strokes to be equal. In practice, optimal signal ratio for a TMA pulse generation pair may be obtained through current adjustments via a function generator.



**Figure 3–13 Transient thermal modeling of the MFM fiber resonator**

Figure 3–14 shows the simulated resonator stage motion for resonance at 1600 Hz with an 8.2–micron stroke. Although each individual TMA takes about 12 ms to reach thermal equilibrium state, this thermal drift is not seen in the resonator position. The symmetric design mitigates the effect of the thermal drift. The first three milli–second of the MFM stage motion is shown in Figure 3–14B. The motion is seen to be linear with  $R^2$  value of 0.993 and maximum deviation from linearity of 0.1  $\mu\text{m}$ . More importantly, the MFM stage provides its full stroke almost immediately, well before the 12 ms time required to reach its thermally stable state. This

was achieved via the pulsed signal, as may be seen in the first three heating/cooling cycles in Figure 3–13B.



**Figure 3–14 Simulated MFM resonator stage motion. The MFM fiber resonator’s thermal settling time may be neglected due to the symmetric design.**

The simulated characteristics of the MFM resonator are summarized in Table 3–4. Figure 3–15 shows the simulated results of the MFM resonator’s surface temperature as well as displacement at 1.6 kHz. From Figure 3–15, it may be seen that the MFM stage functions as a heat sink, maintaining approximately room temperature. When the stage is assembled with the fiber, the fiber acts as an extension of the heat sink and provides increased surface area for cooling. During resonance, the fiber and the stage will help to improve the forced convection and the heat sink should be in a thermal equilibrium state at approximately 350 °K. Even if the heat convection and radiation were not considered, the heat sink will still take approximately 2 minutes to rise to 350 °K, *i.e.*  $\Delta T = 50$  degree. This is about two orders of magnitude longer than the scanning time (1~5 seconds) required for obtaining images in a desired volume.

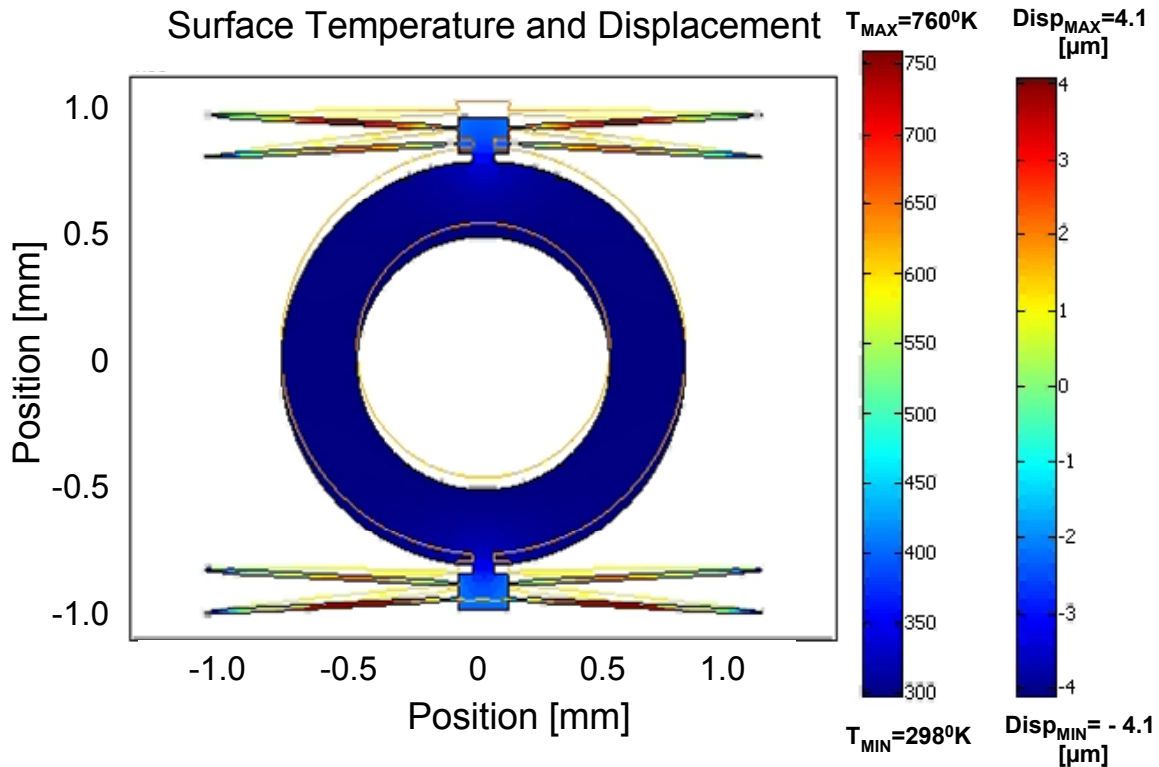


Figure 3–15 Simulated MFM resonator displacement and temperature distribution at 1.6 kHz

### 3.5 Summary

This chapter has presented the concept, modeling, and design approach for MFM systems. The design that was implemented in the resonator used the most basic form of an MFM system that consists of two pulse generation pairs where the TMAs act as coupling flexures. The MFM resonator was optimized by implementing the principle of geometric contouring and high-speed pulsing. A comparison with experimental results and the fiber assembly procedure will be presented in Chapter 5.

*This page is intentionally left blank*



## Device Fabrication

---

The micro-fabrication for this project was carried out in Micro System Laboratory (MTL) at MIT. The MTL houses three clean room facilities: the Integrated Circuits Laboratory – ICL, the Technology Research Laboratory – TRL, and the Nano Structures Laboratory – NSL. Most of the facilities for MEMS and micro-fabrication were located in TRL and ICL.

The fabrication processes were based on micro-fabrication technology that is used in integrated circuits (IC). Figure 4–1 presents an overview of the micro-fabrication processes that were created for the silicon optical endoscopic scanner and MFM fiber resonator. Following are the steps in Figure 4–1:

1. The process starts with a silicon-on-insulator (SOI) wafer.
2. Deposit and pattern the metal contacts for the device.
3. Pattern the device structure with deep reactive ion etching (DRIE).
4. Target-mount the device wafer onto another silicon wafer via photoresist.
5. Release the device with a backside through-etch using DRIE.
6. Release the mounted device wafer and clean the photoresist/residues.

### 4.1 Overview of micro-fabrication and packaging

The steps here only provide a brief idea of how the processes were designed. More detailed discussions on the process introduction and selection will appear in the following sections.

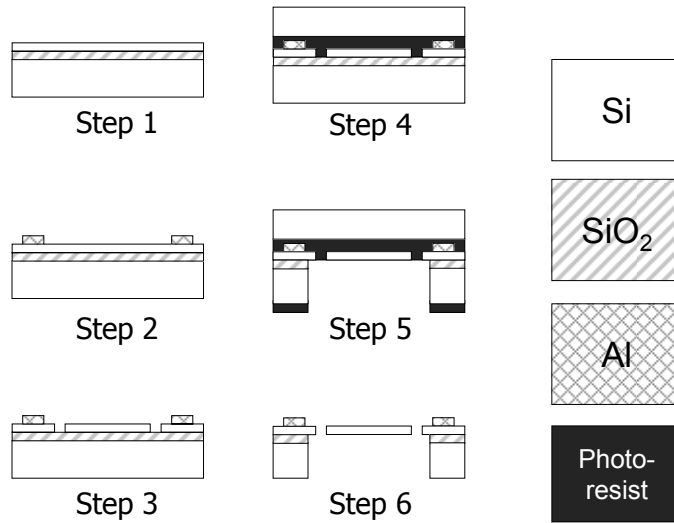


Figure 4-1 Micro-fabrication platform for active silicon optical bench

In this section, all the fabrication processes and methods for building the devices are briefly introduced and discussed with emphasis on process design knowledge and basic micro-fabrication principles. Detailed information, *i.e.* recipes for specific machines, that needs to repeat the micro-fabrication process will be presented in Section 4.2.

#### 4.1.1 Wafers

The silicon bench scanner scans two optical components: a gradient index (GRIN) lens and a prism. An SOI wafer with a 200-micron thick single crystalline device layer was used in order to provide structural integrity and prevent out-of-plane parasitic motion because of component gravity or fabrication errors. The resistivity of the device layer was set to be 0.001 Ohm-cm for low voltage operation of the TMAs (0-3 Volts).

The SOI wafers have three layers: a device layer with silicon, an underlying layer of insulating material, *i.e.* SiO<sub>2</sub>, and a support or “handle” silicon layer [107]. The wafers are made by growing thermal oxide at the specified thickness on the handle layer and subsequently bonding another wafer to the oxide layer. Chemical-mechanical polish is then used to grind the device and handle layers to the desired thickness. The SOI wafers possess excellent structural and electrical uniformity, and also the oxide layer may serve as the insulator between different layers.

### 4.1.2 Lithography

Lithography is the process of transferring patterns from a master mask onto a silicon substrate. Photolithography is the most common method in IC and MEMS fabrication. The combination of accurate registration in exposing a series of successive patterns enables complex multi-layer ICs. The lithography process occupies approximately 50% of the total time of device fabrication and requires some explanation. Lithography generally consists of five major steps: as illustrated in Figure 4-2:

1. Apply photoresist
2. Pre-bake
3. Align and expose
4. Develop
5. Post-bake

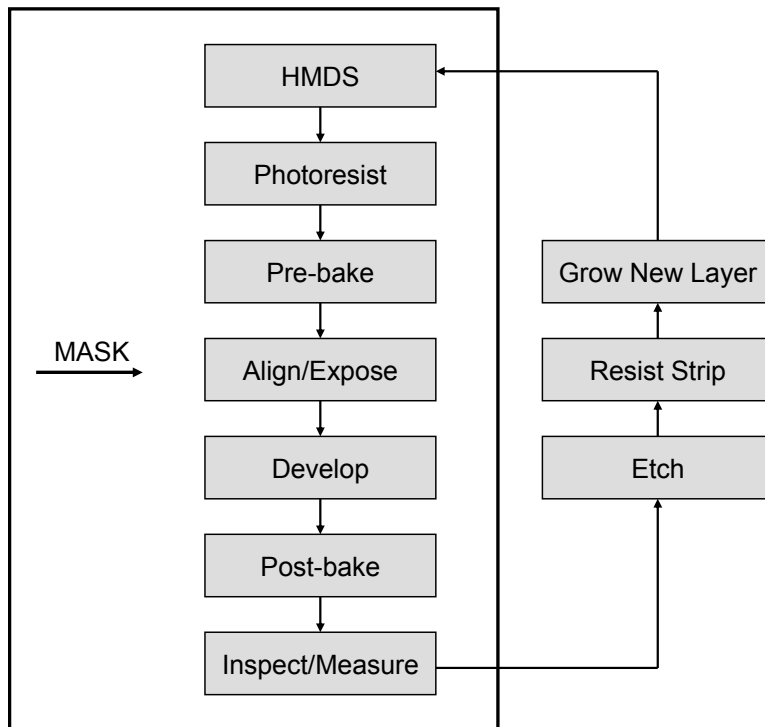


Figure 4-2 Typical lithography procedures

The following explains the typical lithographic procedures in Figure 4–2:

Prior to the application of photoresist, the wafers are first sent to the Hexamethyldisilazane (HMDS) oven in order to dehydrate the surface and promote the adhesion between the photoresist and the surface of the wafer.

The photoresist is dispensed on a wafer that sits on a vacuum wafer chuck. Then, the photoresist is spin coated on the wafer. The thickness of photoresist is generally a function of the spin speed that may be varied between 100–6000 rpm. The choice of thickness for the photoresist depends on the etching requirement.

After the photoresist is uniformly distributed on the wafer, the wafer is sent to the pre-bake oven at 90°C. The soft-bake is to drive off the unnecessary solvents in the photoresist.

The photoresist is then exposed with appropriate energy source. For most quartz/chrome plates, ultra violet (UV) light or deep UV lights should be appropriate. Bright sources are usually required for high throughput. For this process, the exposure time should be determined by experimental data. The mask aligner has three types/modes: contact, proximity, and projection. The contact mode was used in this process. Although the contact mode in general provides better resolution, during exposure the mask and the wafer were in contact, thereby damaging each other by undesired scratching and particles through repeated alignment procedures. The resolution of optical lithography is in fact limited by the diffraction of optics and so the only solution to define a nano-scale pattern is to use the light source with a shorter wavelength, for example X-ray, or electron beam. The Electronic Visions Model EV620 Mask Aligner (EV1) in the TRL that uses an exposure system of 350-Watt high pressure mercury lamp (the wavelengths are 365–405nm), may achieve a sub-micron resolution on devices with appropriate masks. For these reasons, EV1 was chosen to be used in the device fabrication.

After exposure, the pattern is developed in the appropriate developer (Hydroxide). Puddle or spray in temperature controlled environment. Finally, the wafer was rinsed and dried with a spin dryer or nitrogen gun.

Post-bake, also called hard-bake, is used to “bake” the wafers in a higher temperature at 120°C so as to harden the photoresist.

The pattern is then inspected under the microscope to see if the desired patterns are properly formed. Also, the thickness of the photoresist is measured before sending the wafer for etching. If the pattern or thickness is not as desired/designed, the photoresist should be removed (by Piranha or Asher) and the process of lithography should be repeated.

#### **4.1.3 Metal Evaporation**

In metal evaporation, the substrates/wafers are placed in a high vacuum chamber at room temperature with a crucible containing the material to be deposited. A source is used to heat the crucible causing the material to evaporate and condense on all exposed cool surfaces of the wafers in the vacuum chamber. The process is typically performed on one side of the substrate at a time. The metal contacts for the device were evaporated in ICL with E-beam. This process yields the purest grade of metal that is currently possible.

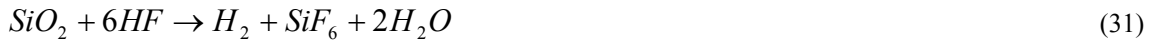
#### **4.1.4 Etching**

Etching is the process of removing the undesired material that is uncovered by the photoresist. Several important parameters, specifically etch rate, selectivity, isotropic etching (undercut), and anisotropic etching, are most critical when designing the etching process. A high etch rate, e.g. 5  $\mu\text{m/s}$ , is generally desirable in a manufacturing environment; however, too high an etch rate may cause difficulties in process control. Selectivity is the ratio of the etch rates over various materials, such as silicon (structure layer) over photoresist or substrate material (sacrificial layer). Undercut is the lateral extent of the etch under photoresist mask. It usually results from the isotropic etching.

#### **Wet etching**

Wet etching is a purely chemical process that has unavoidable drawbacks that include a lack of anisotropy, poor process control, and excessive particle contamination. It is, however, usually highly selective and does not damage the substrate. As a result, it continues to be used for a wide range of tasks. A comprehensive review of wet etching may be found elsewhere [108]. During the fabrication processes of the device, the removal of silicon dioxide ( $\text{SiO}_2$ ) was

accomplished via wet etching with hydrofluoric acid (HF). HF solutions are selective of oxide over silicon. Selectivities are usually better than 100 [109]. Common HF etchants are 6:1, 10:1, or 20:1, meaning 6, 10, or 20 parts water to one part HF. A 6:1 HF solution will etch thermal dioxide at about 1200 Angstrom/min. The exact pathway is complex and depends on the ionic strength, the solution pH, and the etchant solution [110]. The overall reaction for etching SiO<sub>2</sub> is



As the reaction consumes HF, the reaction rate will decrease with time. To avoid this, it is common to use HF with a buffering agent (Buffered Oxide Etch, BOE), such as ammonium fluoride (NH<sub>4</sub>F), that maintains a constant concentration of HF through the dissolution reaction:



Buffering also controls the pH of the etchant and this minimizes the photoresist attack. The concentrated HF has a 49% proportion of HF, and the etch rate is from 18000 to 23000 angstrom/min to SiO<sub>2</sub>.

Wet etching of oxide in HF solution is completely isotropic, and this means that attention must be paid to the undercut effect when designing the fabrication process. An example is presented here to calculate how much time the wafer should be immersed in BOE solution to remove the thermal oxide in step 5 in Figure 4–1 or Table 4–1. The thermal oxide is 2 microns thick, and the etch rate for the BOE solution to oxide is 1000 Angstrom/min. The time required during the etching process is therefore:

$$\text{Time} = \frac{2[\mu\text{m}]}{0.1[\mu\text{m}/\text{min}]} = 20\text{min} \quad (33)$$

As small amount of over etching will not damage the device, it is recommended to use a 25 to 30 minutes total to ensure that the oxide is removed thoroughly. An ultrasonic agitator bath often accompanies the BOE etch (or other wet etch processes) to remove the air bubbles that tend to form/trap in the corners or various locations on wafers when they are placed in etchants.

### **Dry etching**

Dry etching, also called physical etching, removes material from the wafer as it sits in the gas or vapor phase. Dry etching includes ion bombardment (like sputtering, or ion etching),

chemically by a chemical reaction through a reactive species at the surface (like reactive ion etching), or by combined physical or chemical mechanisms. Usually, the dry etching has better anisotropy than wet etching.

The basic idea of silicon deep reactive ion etching (DRIE) is an alternating etch and surface passivation step. This was created and patented by Robert Bosch GmbH. [111–114]. The dry etching of silicon according to this principle is also called High Aspect Ratio Silicon Etching (HARSE), Bosch Deep Silicon Etching, or Advanced Silicon Etching (ASE; Trademark of Surface Technology Systems Ltd.). The etch rate may be over 10  $\mu\text{m}/\text{min}$ , the surface roughness of the sidewall as low as 10nm, or the homogeneity of the etch depth less than  $\pm 3\%$  (on a 4" wafer). The final etch result is a compromise. With a high etch rate, the surface roughness increases; with a large etched silicon area the homogeneity will increase to above  $\pm 10\%$ .

Deep reactive ion etching (DRIE) was used to create the flexures and structures. It enables the bulk micromachining of silicon with aspect ratios (ratio depth to width) up to 30:1 and sidewall angles of  $90^\circ \pm 2^\circ$ . Compared to other bulk micromachining methods, DRIE is anisotropic and independent of the crystal orientation. DRIE allows a high degree of design freedom and therefore it was the main dry etching process that was used to fabricate the scanners.


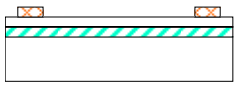



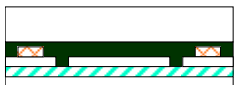
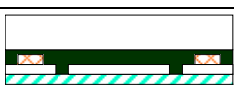
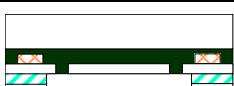
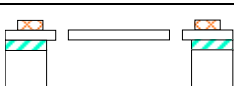
SOI wafers are commonly used for the fabrication of movable structures. The oxide beneath the silicon acts as an etch stop layer for DRIE. By a subsequent removal of the oxide, the structures that were defined via DRIE are released.

## **4.2 Design of micro–fabrication processes**

### **4.2.1 Micro–fabrication platform**

A micro–fabrication platform has been created that may be used for the scanner and fiber resonator. The details of the processes are listed in Table 4–1. SOI wafers with specified electrical properties were used for minimizing the device’s fabrication error (depth) and optimizing the device’s structural integrity.

**Table 4–1 Micro–fabrication platform for silicon endoscopic scanner**

		Si	SiO <sub>2</sub>	Al	Photo-resist
Step	Lab	Machine (Coral)	Recipe/Description		
	TRL		Start with 6” SOI wafer. Device layer: 200 ± 2µm, N–type/Arsine, <100>; buried oxide layer: 2 ± 5%µm; handle layer: 400 ± 10µm, N–type/Phosphorus, <100>.		
	ICL	Endura	Deposit 3000Å aluminum with 2% Si. Pattern the aluminum using aluminum etchant.		
	TRL	HMDS/ Coater/ Prebake/ EV1/ Photowet/ Postbake			
	TRL	Acidhood			
	TRL	HMDS/ Coater/ Prebake/ EV1/ Photowet/ Postbake	Apply and pattern 10µm thick photoresist for deep etch.		
	TRL	STS2	Pattern the device layer via DRIE (Recipe: OLE 37).		
	TRL	Asher	Remove the photoresist and clean the wafer via oxygen plasma for 30min.		
	TRL	Coater/ Prebake	Spray coat photoresist onto wafer. Wafer–mount the SOI wafer to a blank silicon wafer and then bake for 25 minutes at 90°C.		
	TRL	Coater/ Prebake/ EV1/ Photowet/ Postbake	Apply and pattern 20µm thick photoresist onto the backside of the mounting wafer. (Note the mounted wafers did not go into HMDS oven as the high temperatures in the oven may melt the photoresist.)		
	TRL	STS2	Pattern the handle layer via DRIE (Recipe: MIT 37/59).		
		Acidhood	Remove oxide layer by using BOE for 25min.		
	TRL	Acidhood	Separate the SOI wafer from the mounting wafer by a 24–hour acetone bath. Clean the final device with oxygen plasma. Process finished.		

#### 4.2.2 Cursory inspection

Inspections of devices were performed via an optical microscope or optical profilometer at the end of each fabrication step. These inspections were important because during each fabrication step, misalignments may occur and also particles/contaminations may adhere to the



wafers/masks and cause the fabricated device to fail. The preceding errors may be corrected by repeating the (lithographic) step or add an additional cleaning process, *e.g.* Pirahna clean.

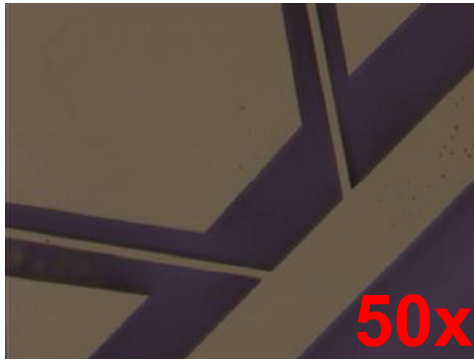
The optical images of the silicon endoscopic scanner and fiber resonator are shown in Figure 4–3A to F and Figure 4–4A and B respectively. Images of the motion amplification flexures, motion–guiding flexures, and chevron TMAs of the prism shuttle are shown in Figure 4–3A, C, and E. Images of the motion amplification flexures and the chevron TMAs of the GRIN lens shuttle are shown in Figure 4–3B, D, and F. Through inspections of the images, there were no obvious flaws or misalignments found on the micro–fabricated scanners and resonators.



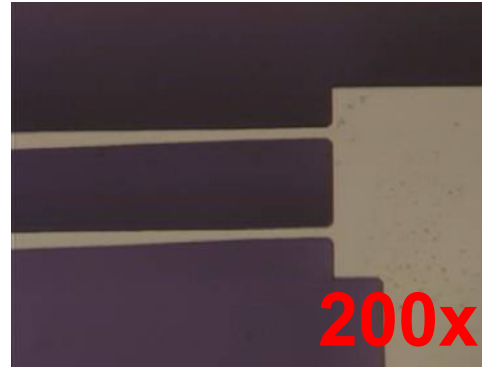
A: Prism shuttle amplification flexure



B: GRIN lens shuttle amplification flexure



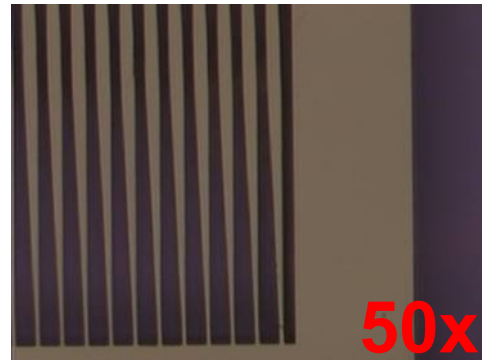
C: Prism shuttle motion-guiding flexure



D: A zoom-in view of GRIN lens shuttle amplification flexure



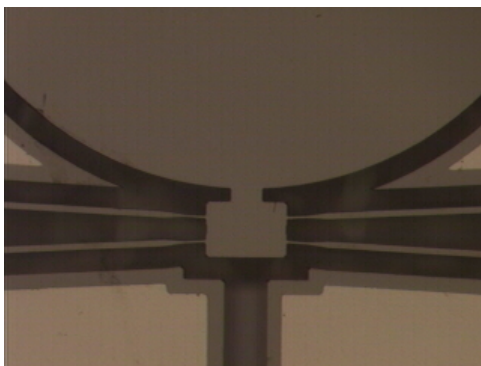
E: Chevron TMAAs of prism shuttle



F: Chevron TMAAs of GRIN lens shuttle

**Figure 4-3 Images from an optical microscope of the silicon endoscopic scanner**

Figure 4-4 shows the images of the MFM fiber resonator that were taken with an optical microscope; chevron TMAAs are shown in Figure 4-4A and the motion stage of fiber is shown in Figure 4-4B.



A: Chevron TMAAs on the MFM resonator (Magnification: 50x)

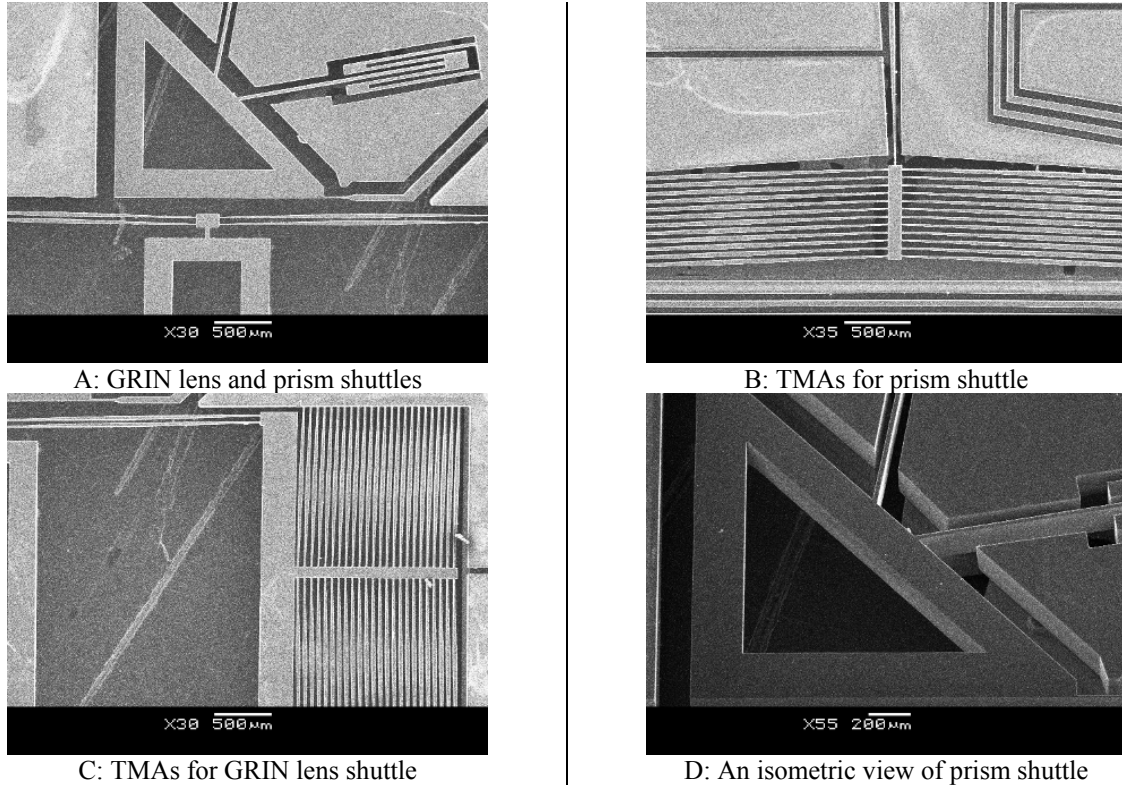


B: Motion stage of the MFM fiber resonator (Magnification: 50x)

**Figure 4-4 Images from an optical microscope of MFM fiber resonator**

Figure 4-5 shows the images acquired through the scanning electron microscope (SEM). Fractures, defects, sidewall properties, and device dimensions on the order of 10s – 100s of nm

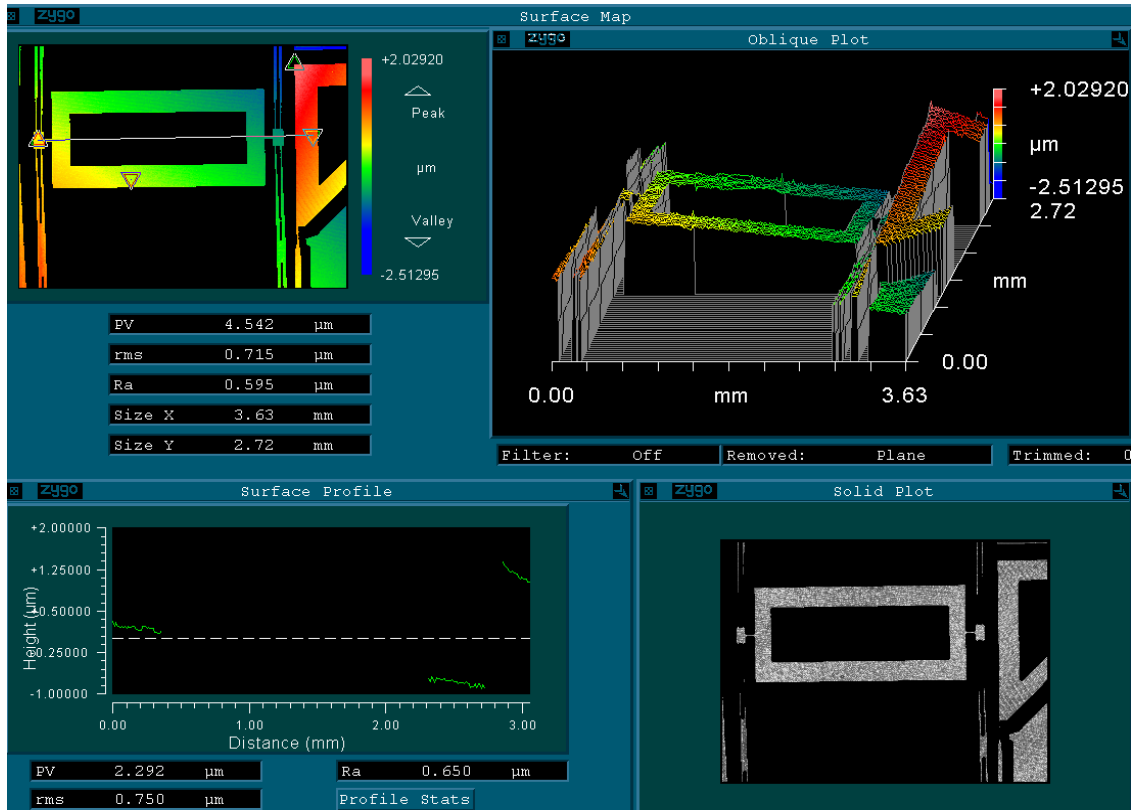
may be observed via the SEM. The magnified SEM images of critical flexures and sidewalls are to be shown in Section 4.3.2. In this section, variations that were caused by deep etch are to be covered.



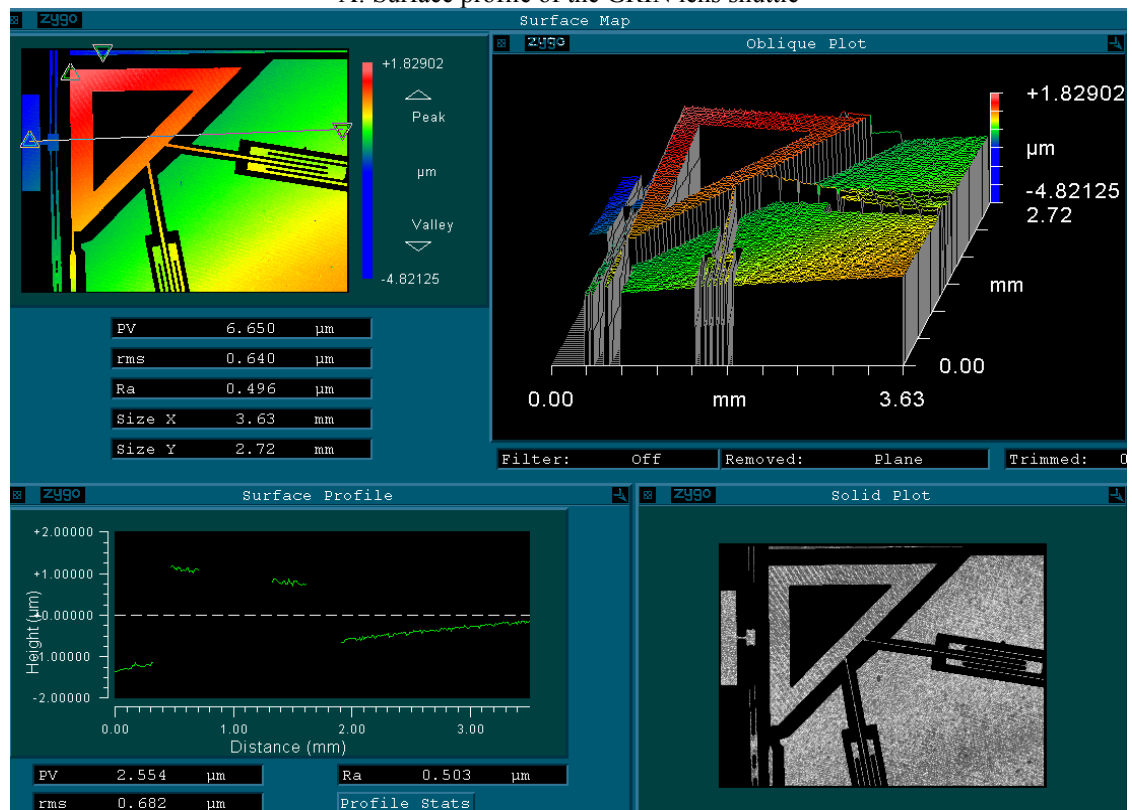
**Figure 4-5 SEM images of the micro-fabricated endoscopic scanner**

The flatness of the silicon endoscopic scanner will affect the alignment between the GRIN lens and prism, *i.e.*, the system optical performance, and is therefore important to measure. A Zygo white light interferometer was used to obtain the surface profile, *e.g.*, flatness and tilt, of the devices.

Figure 4-6A and Figure 4-6B show the surface profiles of the GRIN lens shuttle and the triangular prism shuttle, respectively. It was found that a  $\sim 1/1000$  rad tilt in X- and Y-axis for the prism shuttle as well as a  $\sim 1/20,000$  rad tilt in X-axis for the GRIN lens shuttle. Based upon the optical analysis results, these tilts will cause the focus to shift less than 0.1 micron laterally and they were therefore not deemed critical to the engineering of the prototype.



A: Surface profile of the GRIN lens shuttle



B: Surface profile of the prism shuttle

Figure 4-6 Surface profile of the silicon endoscopic scanner

## 4.3 FAB considerations

This section presents the important fabrication concerns and selections of fabrication processes that may affect the results and performance.

### 4.3.1 Stiction effect

Stiction occurs when the capillary forces are larger than the structure stiffness and they “pull down” the structure during a rinsing or drying process. van der Waal forces, electrostatic forces, and hydrogen bonding then hold the two structures together permanently.

To prevent stiction effect from occurring, the devices were released via deep-etched through-holes from the backside of the wafer.

### 4.3.2 Variations

Small geometric variations of the micro-structures will affect the performance of the device. For example, a flexure’s width will affect its stiffness and range of motion. As such, it is important to understand the sensitivity of the device dimensions/performance with respect to fabrication errors that lead to non-nominal device geometry. If one considers the mask to be perfectly aligned with the wafer, there are two other sources of errors that occur during the lithography process,

1. Transferring the pattern from the mask to photoresist
2. Patterning the device from photoresist

#### **Variations that were caused by pattern transfer during lithography**

In the process of lithography, the variables that most critically affect the geometry/resolution are: exposure time, developing time, pre-bake/post-bake time, types of photoresists, and the humidity level in the room. Figure 4-7A shows an ideal case of photoresist geometry that is protecting the geometry below it. The thick line on top of the photoresist represents the mask location. In the overexposure case, shown in Figure 4-7B, the attenuated power (light) source, because of the diffraction effect, will be able to modulate the photoresist underneath the mask. In the underexposure case, shown in Figure 4-7C, the photoresist will not be thoroughly removed. In the worst case, if the exposure is too short, the photoresist will not

develop at all. In any case, the photoresist profile will not be perfectly straight as shown in Figure 4–7A. The slope on the edge is not avoidable because of a finite contrast of photoresist. A better photoresist profile may be achieved by experimentally determining the appropriate exposure/developing/baking time.

Thin resist typically has a higher resolution than thick resist because of the slope on the edge of photoresist. For example, the positive thin resist, OCG 825, that was used in the TRL at MIT may easily achieve a sub–micron resolution. For a 10–micron–thick photoresist, the resolution reduces to around 1–2 microns. Thick photoresist was used in many of the fabrication processes when defining a pattern that is thicker than 10 or more microns.

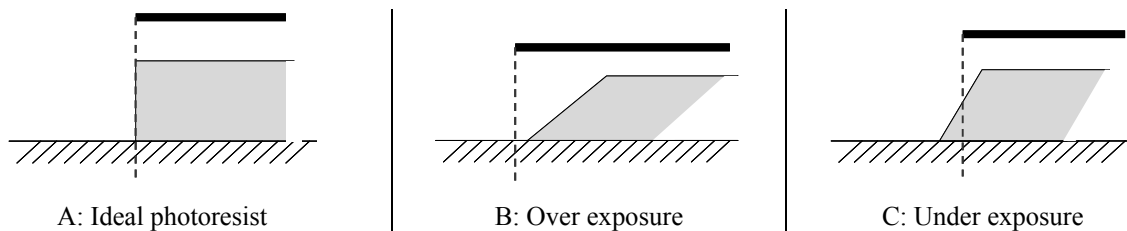


Figure 4–7 Comparison of different exposure time of photoresist

### **Variations that were inherent to DRIE processing**

There were two items that will affect the geometric accuracy of the micro–fabricated devices: (1) the selectivity between the masking material and the material to be etched, *i.e.*, silicon, and (2) the non–uniformity in etch rate across the wafer.

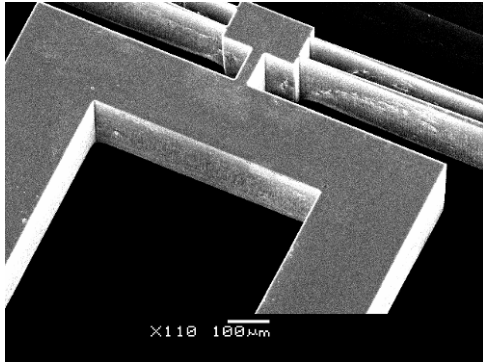
As the photoresist will have a non–vertical sidewall, as shown in Figure 4–7B and C, the photoresist will be gradually etched away starting from the edge during a long/deep etch. This will cause the device to have a non–vertical sidewall as well as inaccurate geometry. As a result, an offset from the mask on the order of a few microns is usually expected. The non–uniform etch rate will also affect this offset and make the actual geometric dimension difficult to control.

For DRIE, the uniformity of etch rate depends on

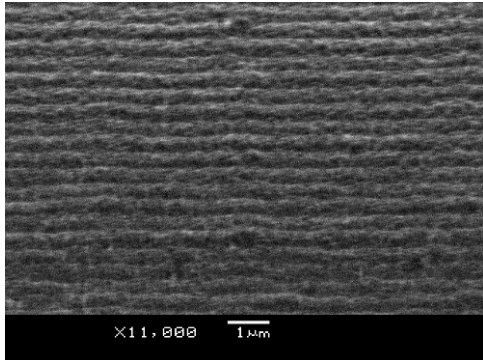
1. The location in the chamber (center region may have a ~10% higher etch rate).
2. The size and aspect ratio of area to be etched; a large open area and/or too narrow a groove will cause the etch rate to be reduced by as much as 20%.
3. Different recipes/chemicals that were used for etching.

There is essentially no remedy for the etch rate variation on different locations in the chamber. As a result, SOI wafers are commonly used to obtain a constant device height. It should also be recognized that a footing effect, which refers to undercut at the bottom of the device layer, may still occur in over-etched regions [115]. Halo-pieces are commonly used to avoid large open areas so that all mask patterns have more uniform width. Their use helps to mitigate the effects of etch rate variation that is experienced in different areas and/or features with different aspect ratios.

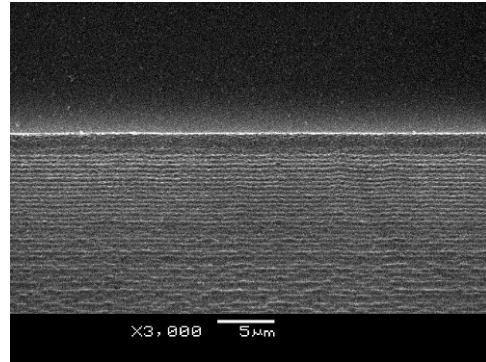
Figure 4-8 shows the DRIE sidewalls at various locations on the GRIN lens shuttle. In these images, typical DRIE scallop patterns were observed. The scallop patterns were uniform in the first 100-micron etch. Towards the bottom of the device, irregular shapes of the scallop patterns were observed. This was caused by gradual removal of the masking layer. The footing effect cannot be seen in these images. As a result, the mechanical characteristics of the scanner and fiber resonator will not be affected by the scallop patterns on the sidewall because the geometry of the scallop pattern is rather small ( $\sim 0.2 \mu\text{m}$ ) when compared to the narrowest width of the flexure ( $\sim 12 \mu\text{m}$ ) and thickness of the device ( $200 \mu\text{m}$ ).



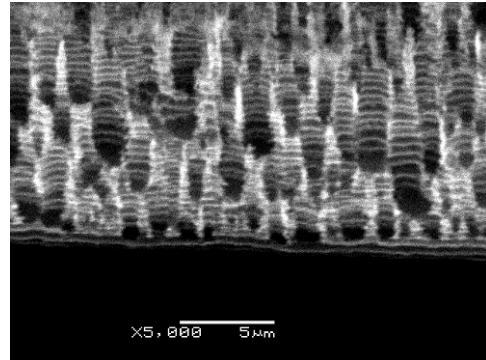
A: An isometric view of GRIN lens shuttle



C: A zoom-in view of the side wall close to the surface of the device layer



B: A zoom-in view of the DRIE sidewall



D: A zoom-in view of the side wall close to the bottom of the device layer

**Figure 4-8 DRIE Sidewalls of the silicon endoscopic scanner**

Measurements of fabricated device dimensions were therefore obtained by measurement of SEM images. For example, Figure 4-9 shows a top view of the chevron TMAs that was used to measure device dimensions. As expected, the dimensions vary by 1.8 to 4 microns from nominal at different locations. The measured values for all critical features in the device were then fed back to the thermal and mechanical models to achieve more accurate performance predictions. Note that although the exact offset is difficult to predict at various locations, one micron offset from the mask were assumed into account when designing the mask for the devices.



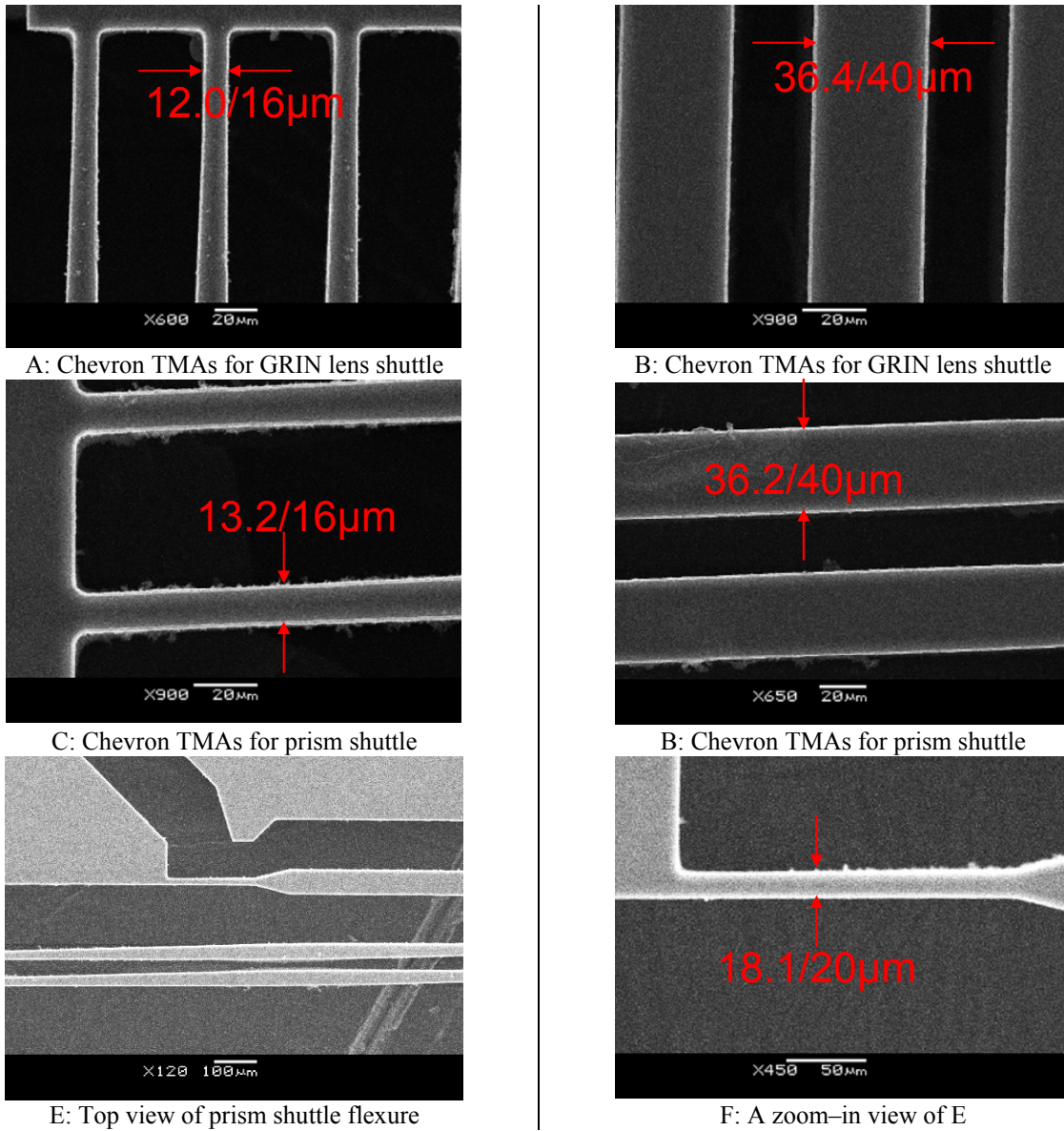


Figure 4-9 SEM images of the silicon endoscopic scanner

#### 4.4 Summary

This chapter contained a summary of the micro-fabrication process that was used to create the scanning system prototype. Design rules and issues of concern for the fabrication processes were discussed. The micro-fabricated prototypes were characterized through an optical profilometer and high resolution SEM to insure that all the dimensions were within the required tolerances.

*This page is intentionally left blank*

## Case Study: A Three–Axis Micro–scanning System

---

### 5.1 Overview

This chapter presents the design, modeling, and experimental characterization of a three–axis micro–optical scanner for a two–photon endomicroscope. The micro–optical scanner consists of two sub–systems: (1) a micro–optical system and (2) a three–axis scanner that moves the optics so that they will raster scan a focal point through a desired volume. The optical sub–system system was modeled, designed, and optimized via ray tracing simulations. An error analysis was conducted in order to ensure that the functional requirements and system constraints were met. Given the design of the micro–optics, the three–axis scanner was initiated. The micro–optical scanner was fabricated, assembled, and then tested to ascertain the match between the predicted and measured results. The scanner was designed to reside within a 7 millimeter  $\emptyset$  tube. It was also designed to operate at 3.0 kHz, 30 Hz, and 2 Hz in the X,  $\theta_x$ , and Z (optical) axis respectively.

#### **Background**

Histological analysis is typically performed for cancer diagnosis. This process requires tissues to be excised, fixated, sectioned, stained and then examined with a microscope. The invasive nature of this process carries cost, risk, and added diagnosis time. A two–photon excitation (TPE) endomicroscope would complement traditional histopathological analysis of cancer and has the potential to reduce cost, risk, and time. More specifically, a TPE endomicroscope would: (1) decrease the number of excisional biopsies required, (2) provide more informed selection of excisional biopsy sites, thereby reducing the number of incorrect

diagnoses that are associated with random sampling, and (3) be used to check for complete surgical removal of malignant cancer tissues, thereby helping to reduce recurrence.

Potential applications exist in treating epithelial cancers where tissue imaging depth of a few hundred microns is sufficient for early diagnosis. Some types of cancer that fall under this category include cervical, colorectal, and esophageal cancers. These cancers occur at a rate of over 12,000, 150,000, and 15,000 new cases per year respectively. The results with additional information were listed within Table 1–3.

## 5.2 Micro-optical system<sup>4</sup>

### 5.2.1 Performance criteria for a two-photon endomicroscope

The performance specifications for the scanner are shown in Table 5–1. These specifications were generated based on clinical needs and comparison to the state-of-the-art confocal endomicroscope. The specifications are listed as a reference [116]. Note that the two-photon endomicroscope possesses specifications that are comparable, or superior, to current commercial systems.

**Table 5–1 Performance criteria of a two-photon endomicroscope**

Criterion	Two-photon endomicroscope	Commercial confocal endomicroscope
Probe diameter	7.5 mm	7.0 mm
Frame size	100 $\mu\text{m}$	320 $\mu\text{m}$
Axial scan range	100 $\mu\text{m}$	250 $\mu\text{m}$
Pixelation	750 x 750	1024 x1024
Resolution (lateral)	0.8 $\mu\text{m}$	0.7 $\mu\text{m}$
Resolution (axial)	4 $\mu\text{m}$	7 $\mu\text{m}$
Frame rate	2 fps	0.8 fps
Excitation light	800 nm, 100 fs	480 nm, CW
Light delivery	Yes, PFC	Yes, SMF, silica core
Detection aperture	8 mm core PF or 500 mm core silica MMF	Confocal pinhole, Aperture size unknown
Detection electronics	Avalanche photodiode, SPC electronics	N/A

The preceding specifications were for the scan method in Figure 5–1. In Figure 5–1, one surface in the X–Y plane refers to “one frame.”

---

<sup>4</sup> The optical design was done in collaboration with Mr. Heejin Choi, a student of Professor Peter So at MIT. The concepts for the scanning mechanism and the error analyses were designed by the author and related simulations were then carried out by Mr. Choi. The optical characterization of the DCPCF was designed and performed by Mr. Choi. The materials are presented together for the reason of continuity and completeness.

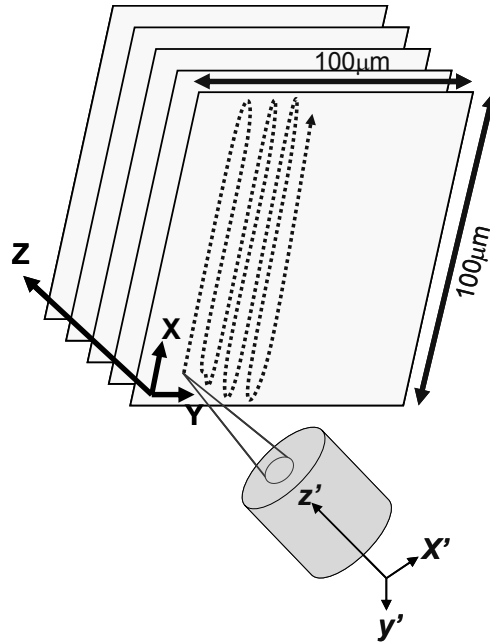


Figure 5–1 Schematics of the Cartesian 3D raster scanning route for the endomicroscope

### 5.2.2 Functional requirements and constraints

Table 5–2 lists the functional requirements that were generated based upon the frame rate and pixilation requirements in Table 5–1. The high scanning speed is required as all scanning processes must be completed between heartbeats in order to keep the tissue–scanner registration accurate. *In vivo* devices also require a low operating voltage (less than 5V) in order to prevent electrical shocks to the heart. The focused laser is required to scan across a distance of at least 100 microns along each of the three axes. Thereby, each optical cross–section would contain approximately 100 cells. This is a suitable number for evaluation of the condition of the precancerous/cancerous cells or tissues. The entire scanner is required to reside within a 7mm Ø endoscope port.

Table 5–2 Functional requirements for the endoscopic scanner generated based on the optical design

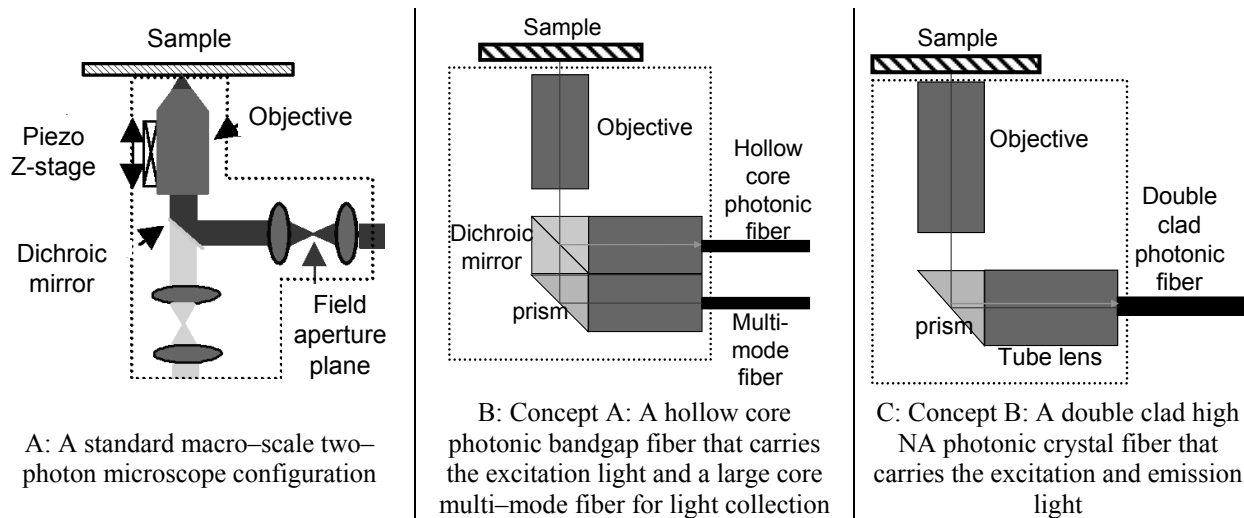
Axis	X	Y	Z
Range	100 μm	100 μm	100 μm
Speed for fine 2D scan (2 fps)	700 Hz	1 Hz	0.02 Hz
Speed for volumetric scan (30 fps)	3 kHz	30 Hz	2 Hz

### 5.2.3 Concepts for the optical system

Figure 5–2A contains a rendering of a common macro–scale two–photon microscope. An infrared excitation signal is first sent to the sample through a two–lens (4F) system that

performs beam expansion/spatial filtering. The excited (scattered) green light is then collected through the objective lens and filtered out by a dichroic mirror (frequency selective).

Two concepts for the distal end optics of the endomicroscope that utilizes the gradient-index (GRIN) lenses<sup>5</sup> have been proposed. They are illustrated in Figure 5–2B (concept A) and Figure 5–2C (concept B). Concept A, as shown in Figure 5–2B, is similar to the macro-scale microscope shown in Figure 5–2A. A dichroic prism is incorporated within the distal end such that the emitted light is separated from the excitation light path, thereby allowing the signal to be collected by a large core (500  $\mu\text{m}$ ) multimode fiber. This design is different from fiber confocal microscopes where a single mode fiber delivers the excitation light and serves as the confocal aperture [116–119]. In multiple scattering media such as tissues, a significant fraction of emitted light is scattered and rejected by the confocal pinhole. For imaging at a depth equal to the scattering length, over 95% of the photons may be lost at a small pinhole aperture. The use of a wide core, broadband multimode fiber should significantly reduce this loss.

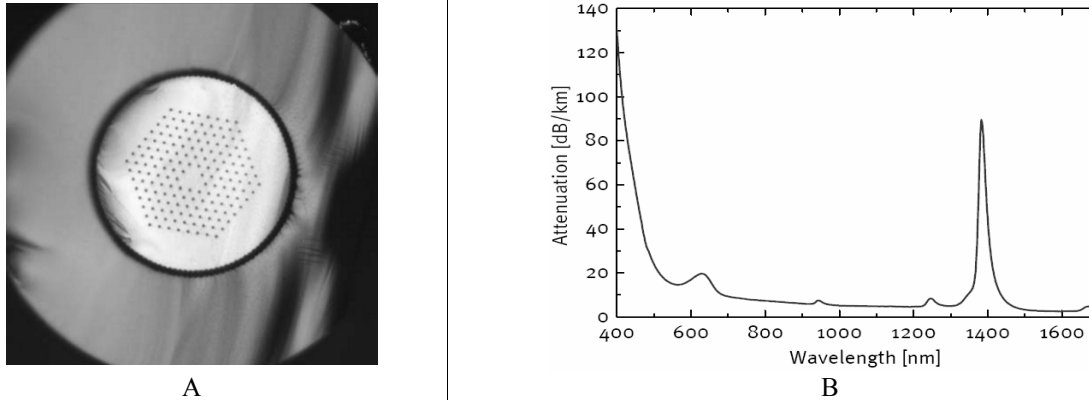


**Figure 5–2 Optical configurations for a macro-scale two-photon microscope (A), and two miniaturized TPE endomicroscopy that utilize GRIN lenses (B and C)**

Concept B, as shown in Figure 5–2C, shows an alternative concept that is similar to conventional fiber confocal microscopy. In this design, one fiber carries the excitation and emission light. The design is largely enabled by the recent introduction of a commercialized

<sup>5</sup> A gradient index lens focuses light through controlled radial variation of the lens' index of refraction. GRIN lenses are commonly used in the fiber optic applications due to their small sizes (~mm) and their flat optical surfaces which greatly simplify the assembly processes.

double clad photonic crystal fiber (DCPCF) [106]. The fiber shown in Figure 5–3 consists of a large mode area, single mode core embedded in a high NA (~0.6 at 600nm) multimode fiber structure. The fiber allows a single mode beam to propagate forward and at the same time allows the scattered light to be collected and propagated backwards. The high NA of the multimode structure has better signal detection efficiency compared to the multi–mode fiber (NA = 0.4) within first concept.



**Figure 5–3 (A) A cross–section view of the DCPCF, where a single mode core is embedded in a high NA (~0.6 at 600nm) multimode fiber structure, and (B) Attenuation of the multimode guide [106]**

The pros and cons of the two concepts are summarized within the Pugh chart in Table 5–3. Concept B was selected as it uses a single fiber for excitation and detection that (1) simplifies the distal optics design, (2) enables decoupling of the three scanning axes, and (3) reduces the required device envelope.

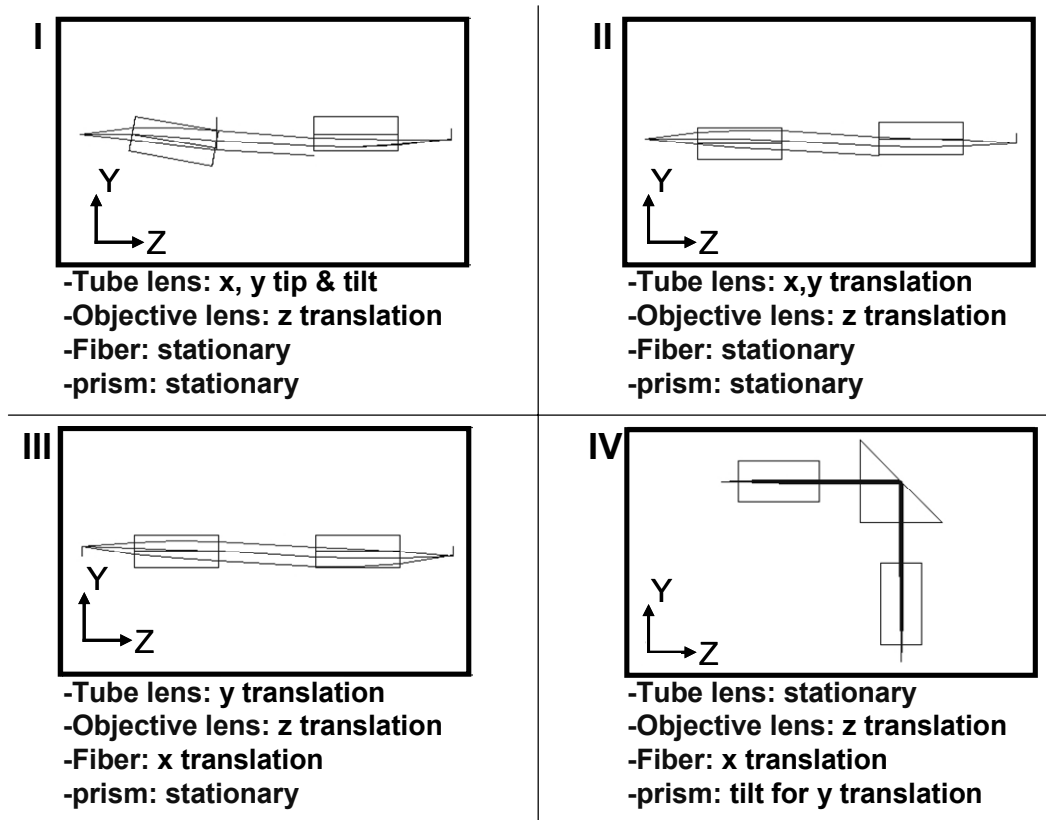
**Table 5–3 Pugh chart of the optical configuration for concept selection**

Concept selection chart		Concept A	Concept B
Metrics	Weight		
Envelope/size	1	0	1
Two–photon efficiency	2	0	–1
Ease of scanning system design	2	0	2
Assembly and manufacturability	1	0	1
Total scores		0	4

### **Design of optics and scanning motions**

One may choose any three out of the four elements (objective lens, tube lens, prism, or fiber that may be seen in Figure 5–2C) to move so as to generate focal spot scanning. The only requirement is that the overall footprint of the scanning optics, the guiding flexures, and the actuators should satisfy the 7mm Ø envelope constraint discussed in Section 5.2.2. Figure 5–4

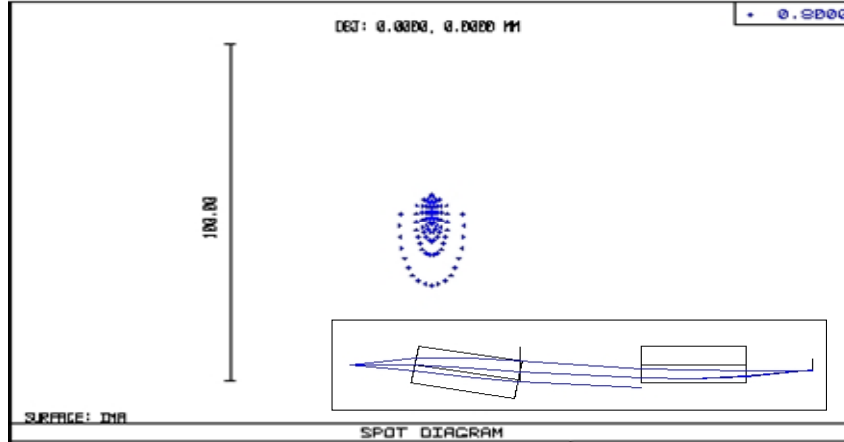
shows four selected concepts for scanning. For each concept, ray tracing and aberration analysis were performed using Zemax. The metrics for the comparisons include the spot size, point spread function, and the intensity of focused light. Note that the full width at half maximum (FWHM) of the cross-section of a point spread function is commonly used as a reference to the best possible spatial resolution that may be achieved by an optical imaging system, such as an optical microscope.



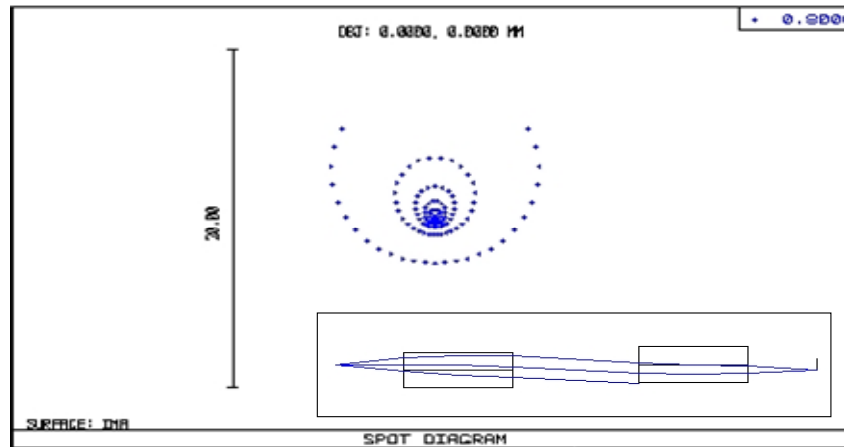
**Figure 5-4 Four different decoupling scanning scenarios, where three out of the four optical elements (objective lens, tube lens, prism, or fiber) were chosen to run simulation**

Figure 5-5A and B show the ray tracing results of tip-and-tilt scanning and translational scanning. For each of these scanning modes, the tube lens was commanded to move so that the focal point on the image plane would scan 150 microns. This required (1) the tube lens to rotate by  $10^\circ$  for the tip-and-tilt scanning and (2) the tube lens to translate 150 microns for the translational scanning. The results in Figure 5-5 show that translational scanning will in general provide better optical performance in terms of a smaller spot size and better light intensity than tip-and-tilt scanning.





A: Spot diagram for tip-and-tilt scanning: scan 150  $\mu\text{m}$  by rotating the tube lens for 10 degree



B: Spot diagram for translational scanning: scan 150  $\mu\text{m}$  by moving the tube lens downward for 150  $\mu\text{m}$

**Figure 5–5 Spot diagram comparison for tip-and-tilt and translational scanning**

The pros and cons of the four concepts are summarized in the Pugh chart in Table 5–4. The fourth concept involving displacement of the fiber, prism, and objective in X,  $\theta_x$ , and Z axis respectively, was selected. This was because (1) it places the least stroke requirement on the actuators, and (2) it possesses the best optical performance among all scenarios.

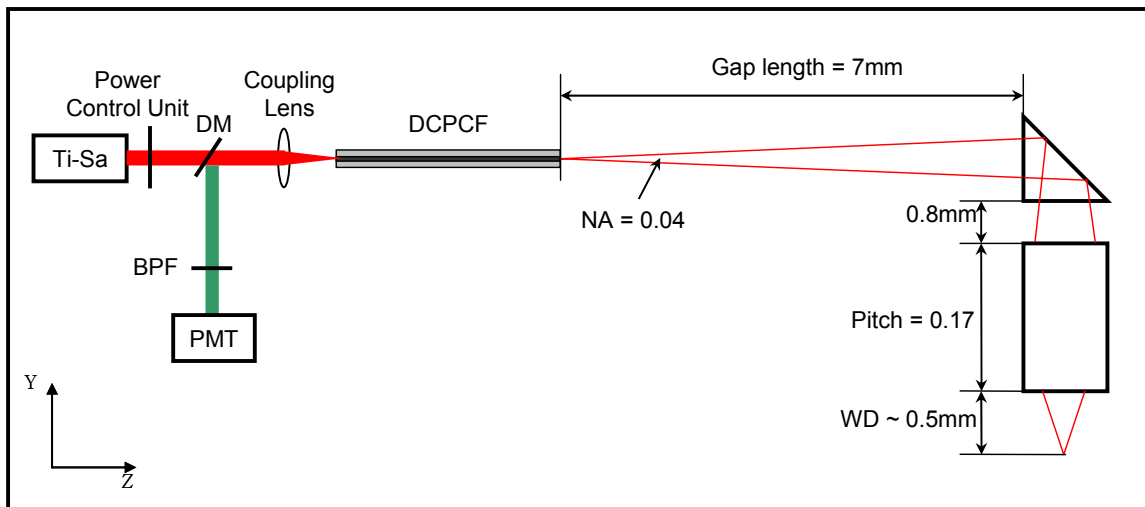
**Table 5–4 Pugh chart of the scanning scenarios for concept selection**

Concept selection chart		Concept I	Concept II	Concept III	Concept IV
Metrics	Weight				
Spot size (PSF)	1	0	1	1	1
Light intensity	1	0	1	1	2
Ease of scanning system design	1	0	1	2	3
Assembly	1	0	1	1	1
Total scores		0	4	5	7

Figure 5–6 shows the finalized design. In this design, the stationary tube lens was removed without reducing the efficiency and point spread function as shown in Figure 5–7.

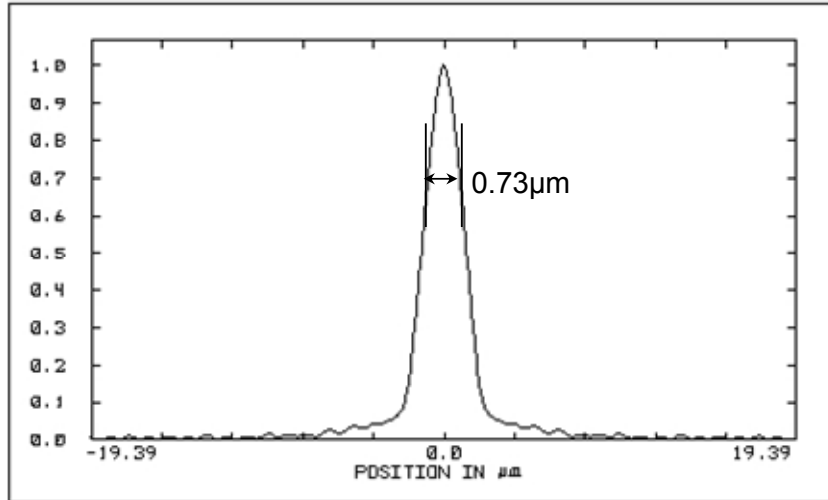
Removing the tube lens, however, requires a larger gap (gap length = 7mm) between the tip of the DCPCF and the prism for beam expansion. The resolution will be optimized if the beam is fully expanded in the objective GRIN lens. The increased gap length is permitted because (1) fewer optical components yield reduced misalignments/errors and (2) the system will possess a smaller envelope and therefore provide more room for actuator/flexure placement, or for further device miniaturization.

In Figure 5–6, the gap length (7 mm) affects the filling area on the back aperture of the GRIN lens and therefore affects the effective NA of the GRIN lens. The pitch ( $p = 0.17$ ) determines the working distance. Pitch is equivalent to the light traversing one sinusoidal cycle. The optical system has been designed to increase the working distance (0.5 mm) in order to maintain a reasonable/workable distance (less than 0.3mm) between the objective lens and the sample.



**Figure 5–6 Finalized optical design and relative locations/dimensions of optical components**

As shown in Figure 5–7, the ray tracing results show that the optical design possesses a 0.73 micron resolution without the consideration of chromatic aberration and misalignment between optical components that will be presented/discussed in the next section. Note that throughout this thesis, the Y-axis of the PSF cross-section plots represent the normalized intensity of the PSF.



**Figure 5-7 Resolution and normalized point spread function without misalignment and aberration, FWHM = 0.73  $\mu\text{m}$ . Note the Y-axis represents the normalized intensity of the PSF.**

Based on the optical configuration and the ray tracing results, the fiber would be required to scan 100 microns in X-axis, the prism would need to rotate about the center of the flat (the center point of the hypotenuse in Figure 5-6) through  $2^\circ$ , and the objective GRIN lens would need to scan 100 microns in the Z-axis in order to maneuver the focal point over a  $100 \times 100 \times 100 \mu\text{m}^3$  volume. The functional requirements for each optical component are summarized in Table 5-5.

**Table 5-5 Functional requirements for each optical components generated based on the optical system characteristics**

Axis	X	$\theta_x$	Z
Component	DCPCF	Prism	GRIN lens
Range	100 $\mu\text{m}$	$2^\circ$	100 $\mu\text{m}$
Speed for volumetric scan	3000 Hz	30 Hz	2 Hz
Speed for fine 2D scan	700 Hz	1 Hz	0.02 Hz

Table 5-6 lists the specifications for the prism and for three candidate GRIN lenses. A custom made GRINTECH lens (design III) with a specified pitch of 0.17 was selected for the final optical design. This GRINTECH lens was chosen based upon its (1) larger numerical aperture (NA) that yielded better resolution and (2) its pitch that in effect extended the working distance.

**Table 5–6 Specifications of the selected prism and three final candidates of GRIN lenses**

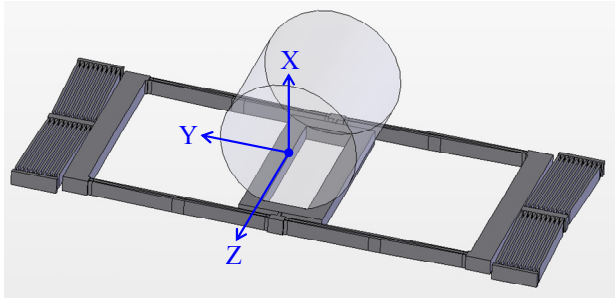
GRIN lens candidates	Design I	Design II	Design III
Grin lens part number	SLW 100 017 156 NC0 (NSG)	SLW-1.0-Z=1.96-A2-0.83 (anti-reflection coated at 830nm) (NSG)	GT-LFRL-100-017-50(810) (GRINTECH)
Length	1.823mm	1.960mm	1.646 mm
Diameter	1.0mm	1.0mm	1.0mm
Length tolerance	+0.0/-0.040mm	±0.02mm	±5µm/ ±0.5µm
Diameter tolerance	+0.005/- 0.010mm	+0.005/- 0.010mm	+/- 0.01mm
Mass	1.43g	1.54g	1.29g
<b>Prism</b>			
Prism part number	Edmund optics		Best NA/custom made Pitch: 0.17
Angle/length	900/ 1mm		
Length tolerance	+0/-0.1mm		
Angle tolerance	±2arc minutes		
Mass of prism	1.20g		

#### **5.2.4 Sensitivity analysis of the optical assembly**

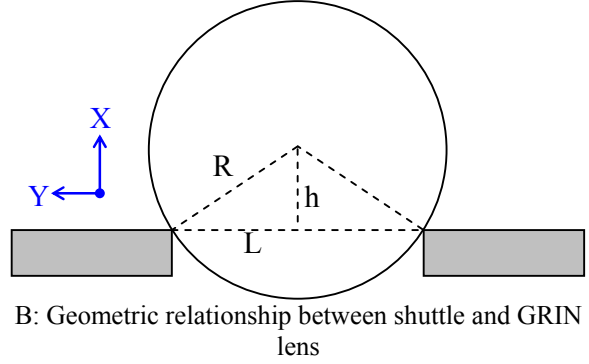
In this section, the sensitivity analysis was performed via ray tracing models. This model was used to simulate and analyze specific circumstances that may affect the optical efficiency and optical system performance. These circumstances include the (1) effect of a partial blocking of the beam by the shuttle as shown in Figure 5–8, (2) effect of misaligned optics manifest as a result of fabrication errors in the scanner/shuttle, (3) effect of chromatic aberration that is caused by the frequency/wavelength differences of the excitation and emission light, and (4) effect of deformed shuttle/lenses that is caused by elevated temperature.

#### **The effect of light blocked by SOB shuttle**

As shown in Figure 5–8A, the GRIN lens’ interface to the shuttle was designed to allow precise registration between the lens and the shuttle. The alignment was made possible by the accurately micro-fabricated sidewalls of the shuttle. When the GRIN lens is positioned in the groove of the shuttle, a portion of the light beam will be blocked by the shuttle, thereby reducing the optical performance, *i.e.*, resolution. The deeper the GRIN lens sits within the groove, the more the lens’s center of gravity approaches the shuttle’s center of stiffness. This will yield improved dynamic performance. In consideration of the preceding, it was important to find a position that optimizes the optical and mechanical performance.



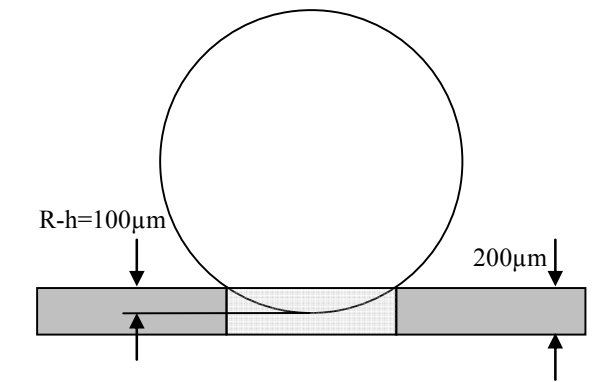
A: An isometric view that illustrates how the GRIN lens is constrained on the shuttle



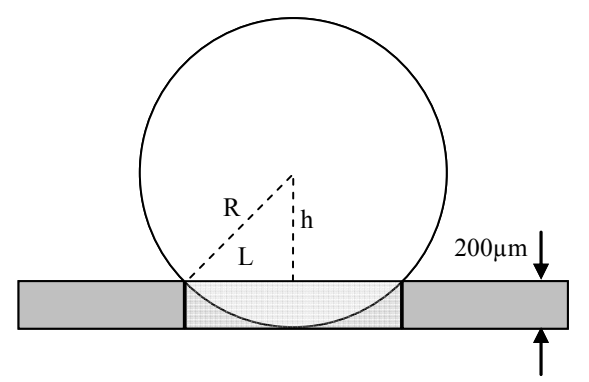
B: Geometric relationship between shuttle and GRIN lens

**Figure 5-8 Geometric relationship between the GRIN lens and shuttle (front view)**

The models in Figure 5-9 were used to investigate the change in optical performance that was caused by a partially blocked beam and the maximum misalignment in X-axis ( $\Delta h$ ) that was the result of fabrication errors in the GRIN lens and the shuttle registration. In example 1 and 2, the beams from the GRIN lenses were blocked by 100 microns and 200 microns respectively.



A: Example 1 (the shuttle blocks the beam for 100  $\mu\text{m}$ ), where  $R = 0.5 \text{ mm}$ ,  $h = 0.4 \text{ mm}$ ,  $L = 0.3 \text{ mm}$



B: Example 2 (the shuttle blocks the beam for 200  $\mu\text{m}$ ), where  $R = 0.5 \text{ mm}$ ,  $h = 0.3 \text{ mm}$ ,  $L = 0.4 \text{ mm}$

**Figure 5-9 Example 1 and 2 for investigating the effects of (1) partially blocked beam, and (2) misalignments that are caused by fabrication errors in GRIN lens and shuttle geometries**

Figure 5-8B shows the geometric relationship between the GRIN lens and the shuttle, where  $h$  is the distance from the center of the GRIN lens to the surface of the shuttle,  $R$  is the radius of the GRIN lens, and  $L$  is half the shuttle width. Equation (34) may be used to determine the required mask dimension for the specified GRIN lens position.

The sensitivity equation, Equation (35), may be obtained by differentiating Equation (34). By applying Equation (35), the variation of the GRIN lens position ( $\Delta h$ ) that is caused by the fabrication errors in the GRIN lens ( $\Delta R$ ) and shuttle ( $\Delta L$ ) may be estimated. The expected errors that were related to the fabrication errors in the GRIN lens diameter may be found in Table 5-6.

The errors in the shuttle geometry may be controlled within  $\pm 0.5$  micron by using careful machine and recipe calibration. The results of the sensitivity analysis are summarized in Table 5–7. The results show that the deeper the GRIN lens is seated within the shuttle, the more sensitive the GRIN lens position,  $\Delta h$ , will become.

$$R^2 = h^2 + L^2 \quad (34)$$

$$2R\Delta R = 2h\Delta h + 2L\Delta L \Leftrightarrow \Delta h = \frac{R}{h}\Delta R - \frac{L}{h}\Delta L \quad (35)$$

**Table 5–7 Summary of fabrication error sensitivity analysis and its affects on  $\Delta h$  (X-axis)**

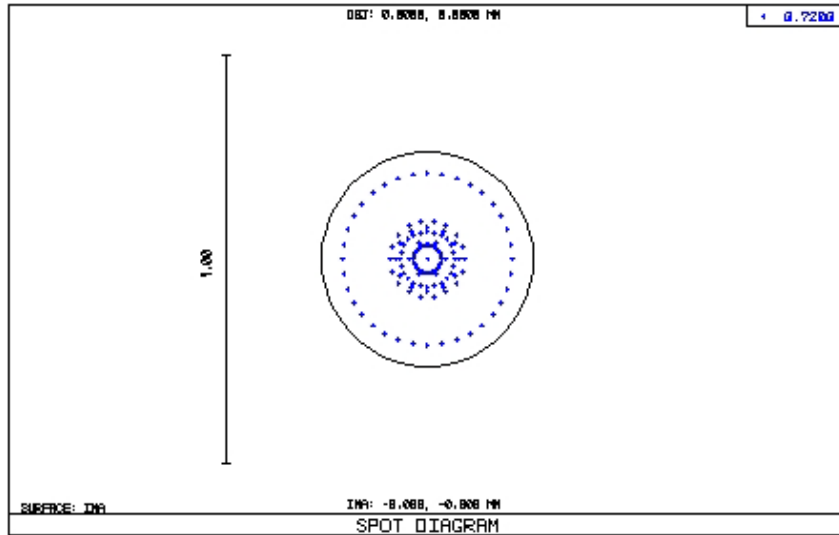
Example 1 (the shuttle blocks the beam for 100 $\mu\text{m}$ )		Example 2 (the shuttle blocks the beam for 200 $\mu\text{m}$ )	
$R$	0.5mm	$R$	0.5mm
$h$	0.4mm	$h$	0.3mm
$L$	0.3mm	$L$	0.4mm
$\Delta R$	$\pm 5.0\mu\text{m}$	$\Delta R$	$\pm 5.0\mu\text{m}$
$\Delta L$	$0.5\mu\text{m}$	$\Delta L$	$0.5\mu\text{m}$
$\Delta h$	$\pm 6.6\mu\text{m}$	$\Delta h$	$\pm 9.0\mu\text{m}$

This section discusses how the blocking of the beam would affect the system optical performance via a comparison of the point spread function (PSF) and the spot diagram of (1) an unblocked beam, (2) a beam blocked by 100 microns (example 1), and (3) a beam blocked by 200 microns (example 2). In these scenarios, no misalignment is assumed in the analyses. The results are shown in Figure 5–10, Figure 5–11, and Figure 5–12 respectively. The optical components and parameters that were used in the models are listed in Table 5–8.

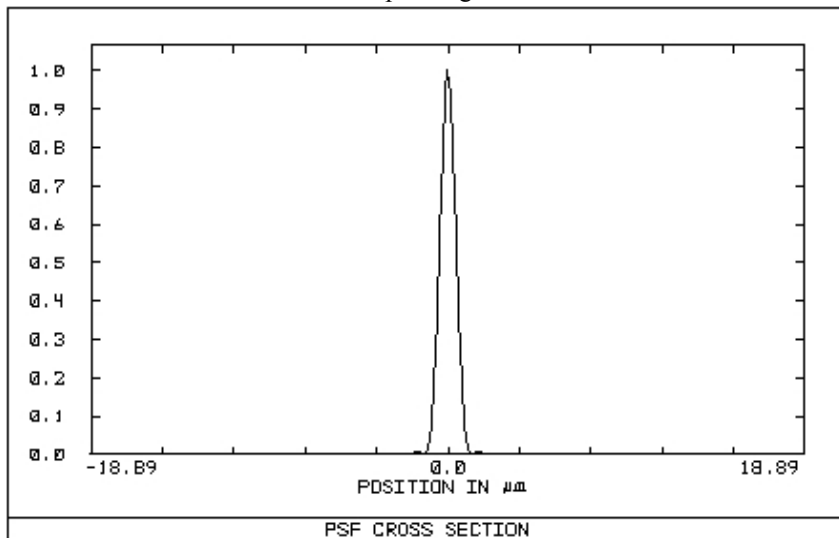
**Table 5–8 GRIN lens and parameters that were used for ray tracing model**

Objective lens	GRINTECH: GT-LFRL-100-017-50(670), $Z = 1.633$ mm
Wavelength	$\lambda = 720\text{nm}$ , Gaussian profile beam with apodization factor $\sigma = 1$
Working distance	WD = 0.616mm
Gap length	11mm (designed for 100% filling of the GRIN lens' back aperture)

Figure 5–10 shows the spot diagram and the PSF of the ray tracing results of an unblocked beam, where the FWHM = 0.730 micron was observed.



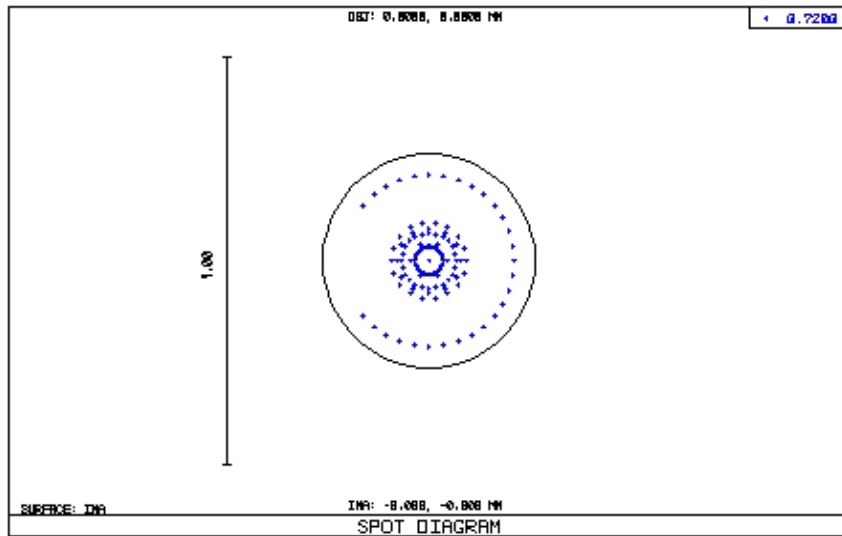
A: Spot diagram



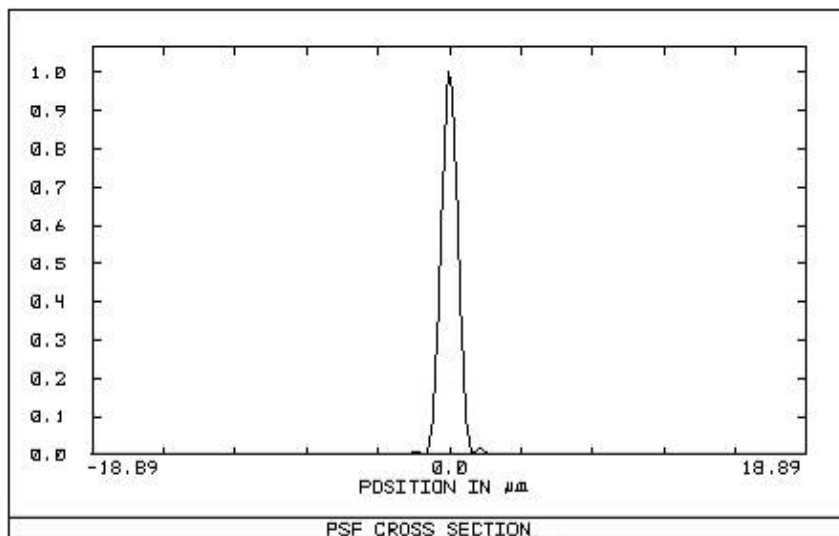
B: Normalized PSF cross-section

**Figure 5–10 Spot diagram and PSF of the unblocked beam**

Figure 5–11 shows the spot diagram and PSF of the ray tracing results of a beam blocked by 100 microns, where the FWHM = 0.732 micron was observed.



A: Spot diagram

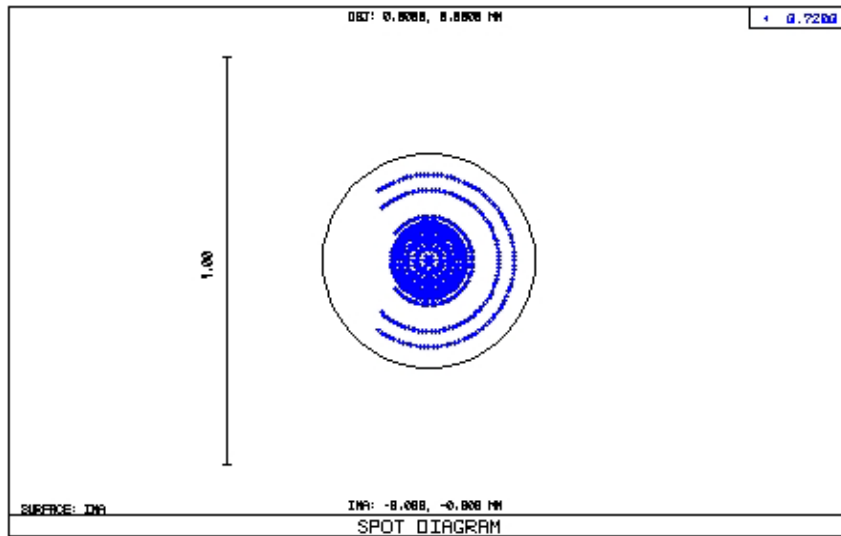


B: Normalized PSF cross-section

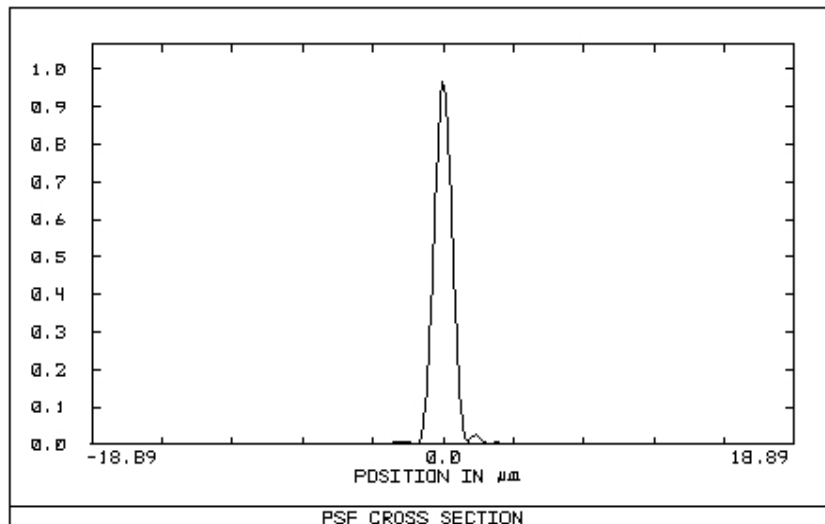
**Figure 5–11 Spot diagram and PSF of the beam blocked by 100 microns**

Figure 5–12 shows the spot diagram and PSF of the ray tracing results of a beam blocked by 200 microns, where the FWHM = 0.763 micron was observed.





A: Spot diagram



B: Normalized PSF cross-section

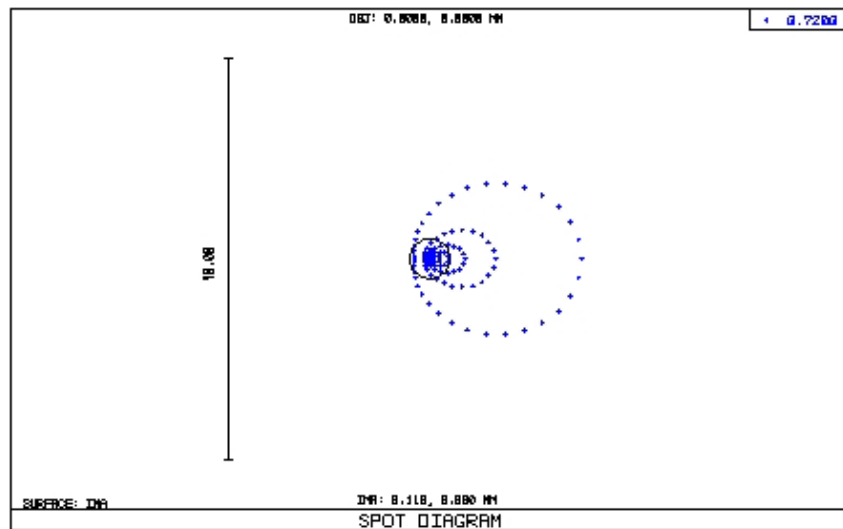
Figure 5–12 Spot diagram and PSF of the beam blocked by 200 microns

### The effect of GRIN lens misalignment

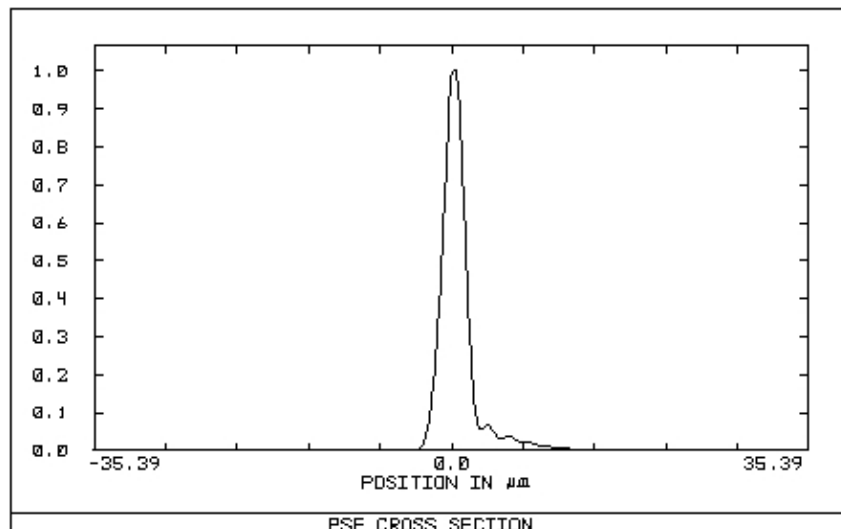
In this section, misalignments from different axes were modeled and compared. Figure 5–13 and Figure 5–14 illustrate the performance deterioration that was caused by misalignments of the Y-axis and X-axis ( $\Delta h$ ) respectively. As the GRIN lens was desired to scan in Z-axis (optical axis), its misalignment in the Z-direction is not discussed because this will only shift the focal point in Z-direction and therefore the optical performance will remain workable within the designed scan range. Note that the modeling results in Figure 5–13 and Figure 5–14 were completed before the optical assembly design was finalized. The resolution is lower than the optimized value shown in the previous section ( $0.73 \mu\text{m}$  vs.  $1.46 \mu\text{m}$ ); however, as the

dimensions and fabrication errors for different lenses were on the same scale, the results were presented to illustrate the relationship and sensitivity of optical performance.

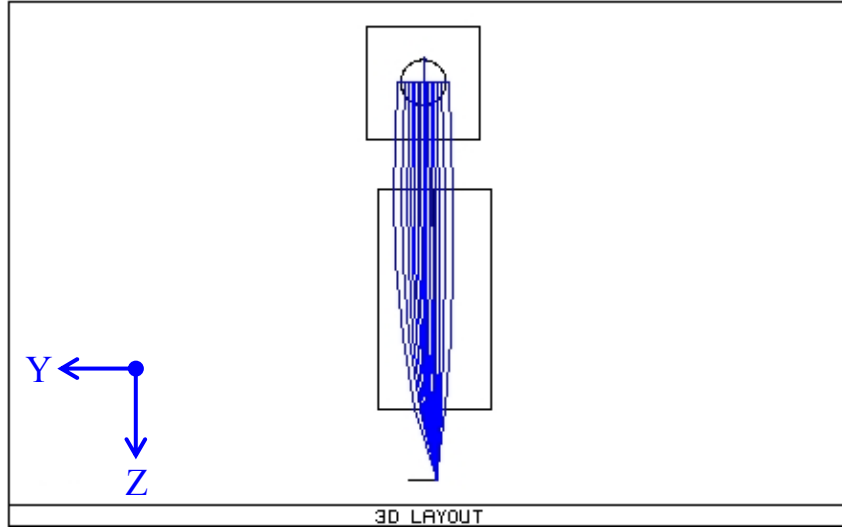
Figure 5–13 modeled the effects of misalignment in the Y-axis from a value of 0 to 50 microns. In Figure 5–13D, one may observe linear performance deterioration before a 30 micron misalignment. From the sensitivity analysis, it was known that the worst misalignment in the Y-axis, 10 to 15 microns, causes a 15% increase in FWHM, *i.e.* FWHM worsens from 1.55 to 1.77 microns. As a result, a GRIN lens with tighter design tolerances was used to better control the optical performance within 1.5% of its optimal value. For the final design,  $\text{FWHM} = 0.73 \pm 0.01$  micron.



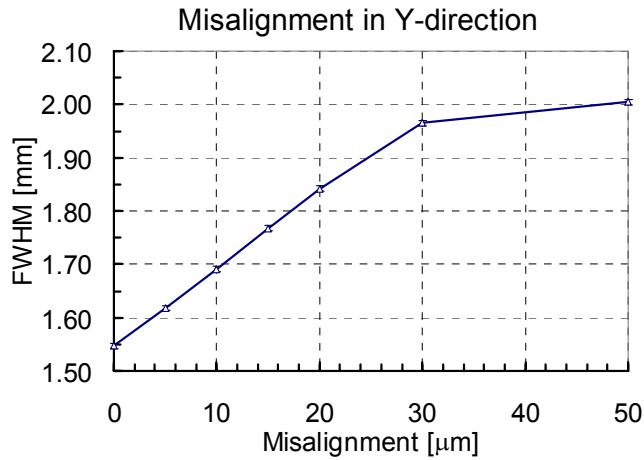
A: Spot diagram



B: Normalized PSF cross-section



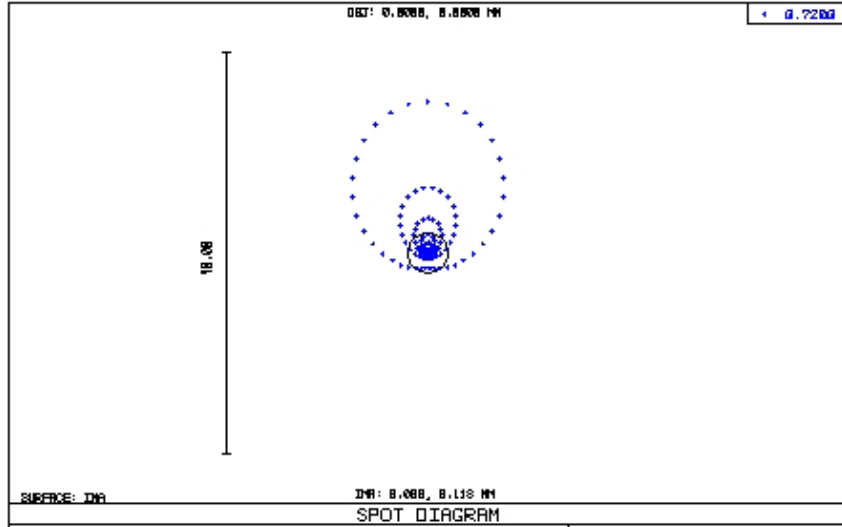
C: Layout of prism, GRIN lens: The beam coming out of the plane from the fiber is first reflected by the prism, and then goes down through the GRIN lens, focusing at the bottom of the figure



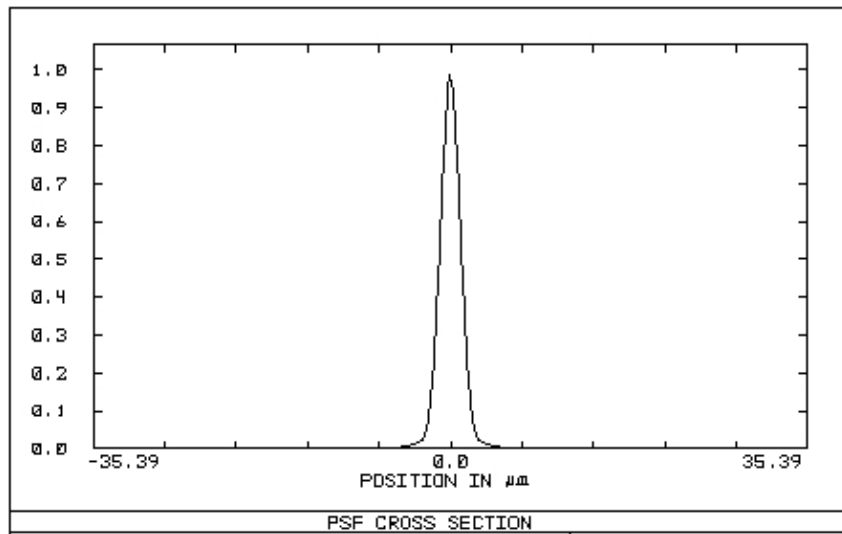
D: FWHM as a function of misalignment in X-axis

**Figure 5–13 Effects of misalignment in Y-axis from 0 to 50 microns**

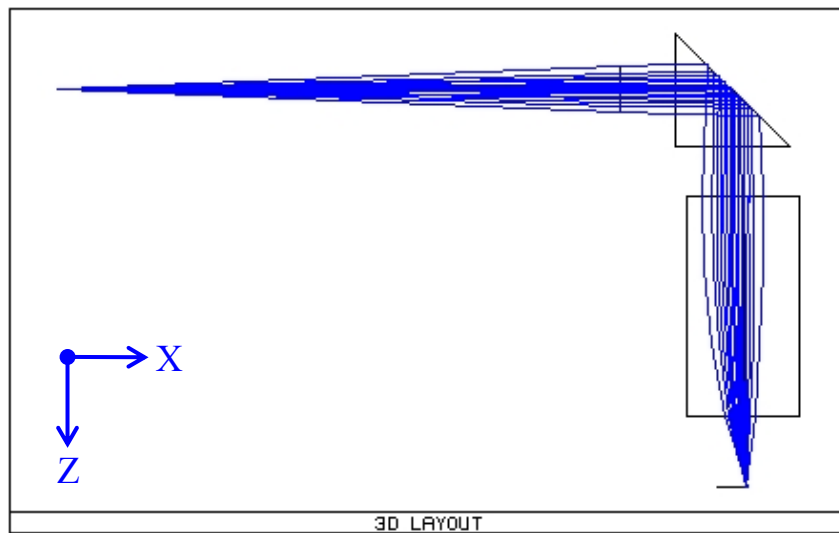
Figure 5–14 shows the effects of misalignment in X-axis from 0 to 50 microns. The results show that the optical performance was less sensitive to misalignments in the Y-axis than in the X-axis. Only a 2.5% variation in FWHM was found with a 20–micron misalignment. The alignment in the X-axis was easily achieved within a few microns via standard micro-fabrication processes.



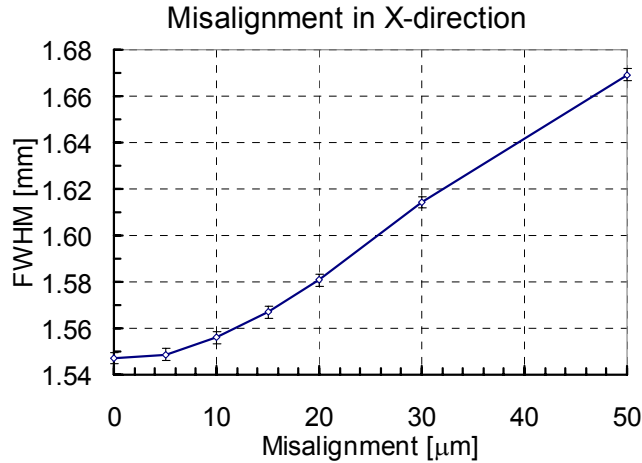
A: Spot diagram



B: Normalized PSF cross-section



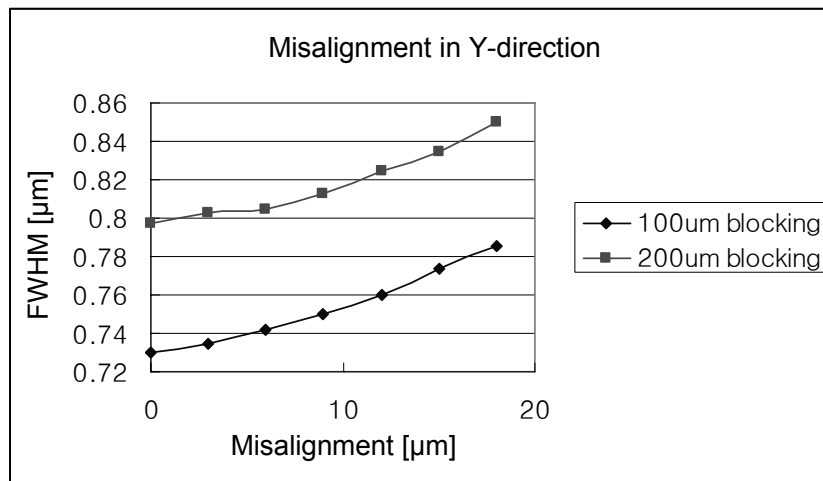
C: Layout of prism, GRIN lens: The beam leaves the fiber as a point source from the upper left corner



D: FWHM as a function of misalignment in X-axis

**Figure 5-14 Effects of misalignment in X-axis from 0 to 50 microns**

Figure 5-15 shows the simulated results of the combined effects of a blocked beam and misalignments in the Y-axis. The X-axis was not included because its effects on optical performance were shown to be small. The results show that the final optical design with a 100 micron blocked beam and a 1 micron misalignment yielded FWHM = 0.73 micron. Figure 5-15 and the results in this section are important as they allow optical designers, who are in general not familiar with precision system design, to consider and rapidly identify various misalignment mechanisms so that they may better understand their effect on optical performance.



**Figure 5-15 The effect on system resolution as a function of (1) misalignment of the optical components and (2) the blocking of light**

The pros and cons of the two GRIN lens shuttle concepts, *i.e.* 100-micron and 200-micron blocked beam, are summarized in the Pugh chart in Table 5-9. The 100-micron blocked

beam example was selected because it (1) provides better resolution (FWHM = 0.73  $\mu\text{m}$  vs. 0.76  $\mu\text{m}$ ) and intensity, and (2) possesses lower sensitivity to fabrication errors.

**Table 5–9 Pugh chart of the GRIN lens shuttle for concept selection**

Concept selection chart		100 $\mu\text{m}$ blocked beam	200 $\mu\text{m}$ blocked beam
Metrics	Weight		
Assembly	1	0	-1
Sensitivity to fabrication error	2	0	-1
Dynamic performance	2	0	1
Optical performance (PSF)	2	0	-1
Total scores		0	-3

**The effect of chromatic aberration**

Chromatic aberration cannot be avoided. In this design, the infrared excitation beam leaves the tip of the fiber as a point source. It should be noted, however, the second harmonic generated emission beam from the sample has a different wavelength (green light) as shown in Figure 5–16. As the index of refraction is a function of wavelength, it causes the emission beam to focus in front of the tip of the fiber (instead of at the fiber tip) when it travels back to the fiber from the sample. Accordingly, a coupling loss of approximately 50% is expected to occur because of the mismatch between the focal points. Recall from Section 5.2.3, the use of a DCPCF enables the scanning axes to be decoupled, but this comes at the cost of reduced optical efficiency. The only way to avoid a 50% coupling loss is to use an alternative multi-mode fiber to collect the emission light. Unfortunately, this was not possible.

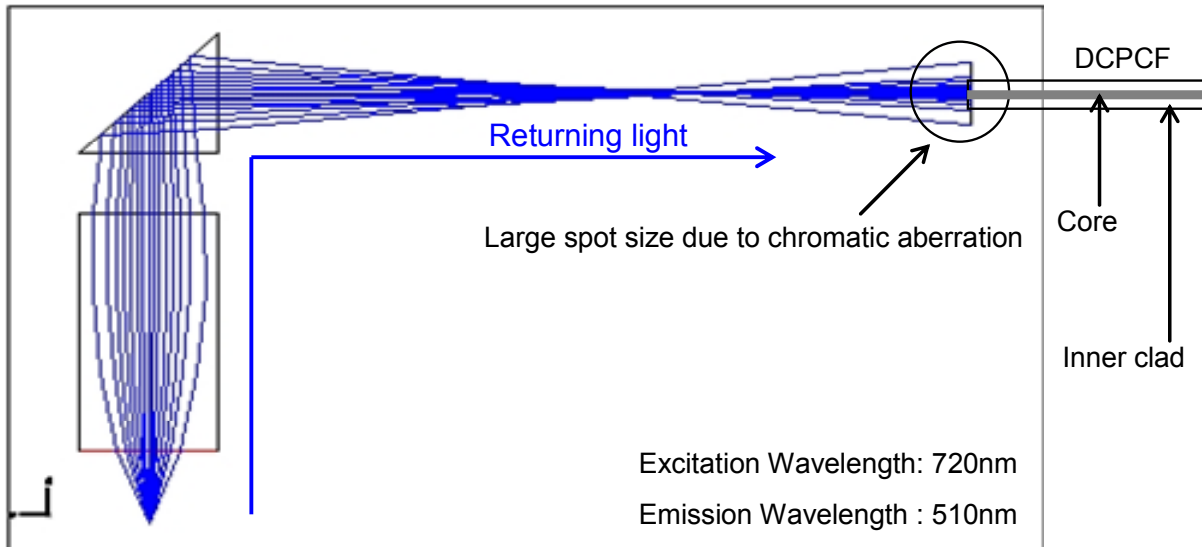


Figure 5-16 Simulated excitation/emission ray tracing results of chromatic aberration, where in simulation excitation wavelength = 720 nm and emission wavelength = 510 nm were used

### **The effect of temperature change on the GRIN lens and the GRIN lens shuttle**

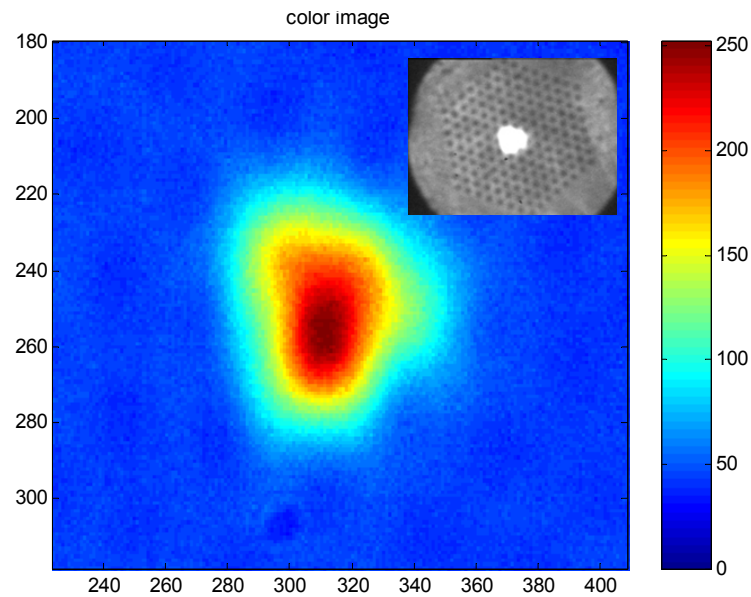
This section covers the effects of thermal changes upon optical performance. This analysis was performed because the GRIN lens and prism shuttles were actuated by TMAs and when the TMAs were driven at full stroke, the shuttle's temperature may rise by as much as 100 °K. The design check was performed to determine whether a thin thermal isolation layer, *e.g.*, silicon dioxide, was required to avoid temperature changes that would adversely affect performance.

In this case study, a 300 °K temperature increase was assumed for the shuttle and the lenses. A  $\Delta T = 300$  °K was used as this leads to the maximum operating temperature of the TMAs, *i.e.* the maximum possible temperature on the optical bench. The simulated result shows the optical system exhibits a 0.027% change in FWHM and a 0.0021% change in working distance at 600 °K versus 300 °K (room temperature) as a result of thermal strain. It was therefore concluded that the temperature effect is not critical when compared to other errors and therefore a thermal isolation layer on the shuttle was not required.

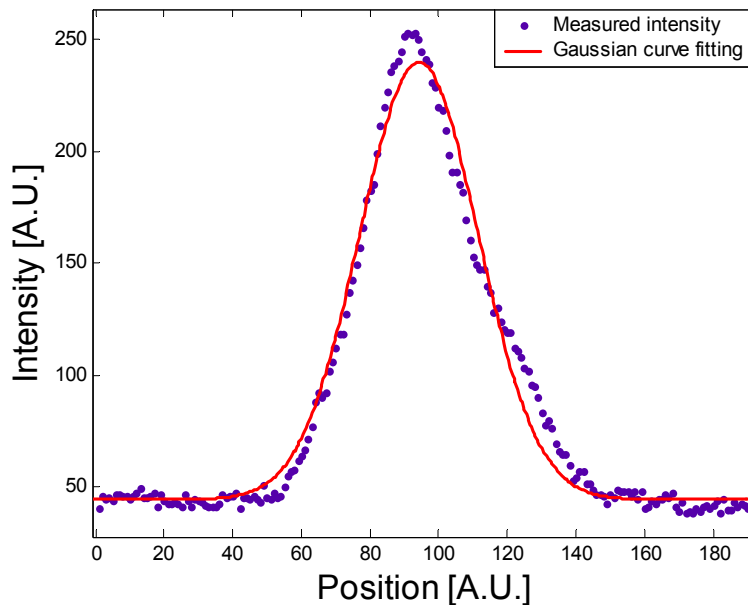
### **Characterization of DCPCF's optical behavior**

The performance of the DCPCF had to be characterized and optimized before the design of the scanner could proceed. Figure 5-17 presents the results of the intensity and PSF profile

characterization of the DCPCF. The measured laser intensity profile in the DCPCF shows a good agreement with the theoretical Gaussian beam profile with less than 5% error.



A: Measured intensity distribution of single mode beam



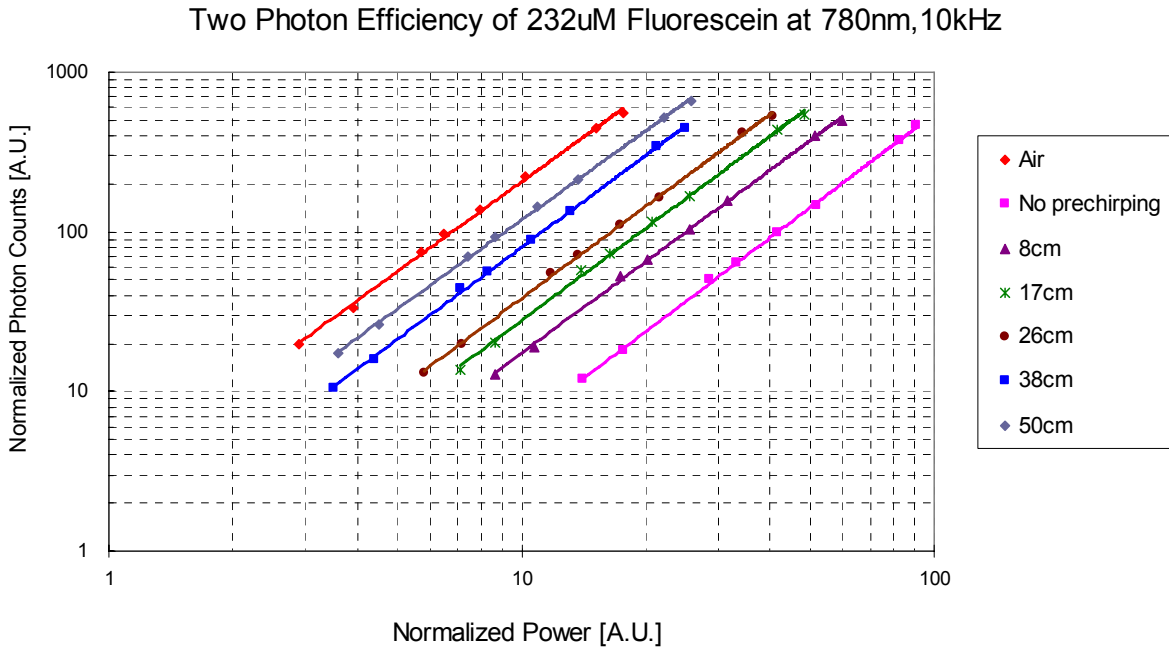
B: Gaussian intensity profile of single mode beam

**Figure 5–17 Intensity and laser profile characterization of DCPCF (Courtesy of Mr. Heejin Choi)**

In order to optimize the two-photon efficiency, a signal pre-chirping unit was used to characterize and minimize the linear dispersion—pulse widening effect—when the pulse laser traveled in the DCPCF. Experiments were devised to obtain the optimal two-photon efficiency versus various lengths of the pre-chirping unit. The experimental results are summarized in



Figure 5–18. In Figure 5–18, normalized photon counts of different gate lengths (from 8 cm to 53 cm) are plotted with respect to the normalized power input. As expected, the two–photon efficiency is proportional to intensity squared because of the non–linear second harmonic generation. The two–photon efficiencies of the pulse laser that (1) travels in free air and (2) travels in the DCPCF, but without the pre–chirping unit, were also experimentally determined and used as reference baselines.



**Figure 5–18 Two–photon efficiency measurement for different signal pre–chirping lengths**

Table 5–10 lists the detailed experimental results of the pulse–widening experiment on the DCPCF. For the experiment, the length of the distance between the two gratings of the pre–chirping unit was set at 50 centimeters for optimal FWHM. The length of the DCPCF that were used for this experiment was 172 centimeters. Figure 5–18 and Table 5–10 will be useful for optical scientists/designers who intend to use the DCPCF. This will allow them to rapidly identify the optimal gate length for the signal pre–chirping unit.

**Table 5–10 Effects of pulse widening on the DCPCF**

	Pulse width [fs]	Photon Count at $x = 15$	Photon Ratio	FWHM/FWHM <sub>AIR</sub>
Air	84.8	439.4	Air/DCPCF	1.0
DCPCF no pre-chirping	2026.9	13.5	32.5	23.9
DCPCF grating at 8cm	1171	37.6	11.7	13.8
DCPCF grating at 17cm	781.3	60.7	7.2	9.2
DCPCF grating at 26cm	518.8	83.3	5.3	6.1
DCPCF grating at 38cm	257.3	173.7	2.5	3.0
DCPCF grating at 50cm	180.9	252.2	1.7	2.1
DCPCF grating at 53cm	197,4	184.7	2.4	2.3

### 5.3 Endoscopic scanner design

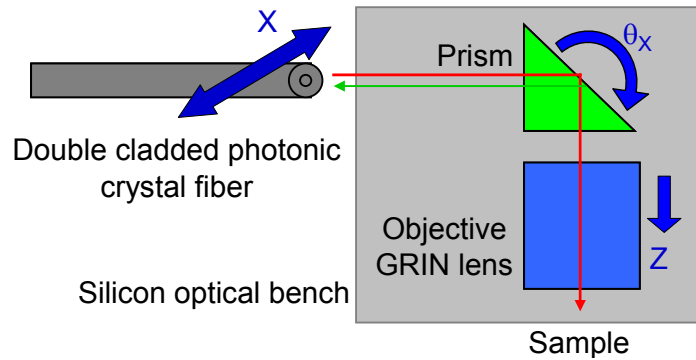
This section presents the concepts, modeling, design, assembling, and experimental characterization of the two-axis endoscopic scanner with an integrated GRIN lens and a micro-prism. From the optical assembly design, three independent axes are required to perform a volumetric scan. The GRIN lens and micro-prism should be aligned and scanned in-plane with respect to the Z-axis and the  $\theta_x$ -axis respectively at moderate speeds, and the DCPCF should be scanned along the X-axis at high-speed. The functional requirements for the scanner are listed in Table 5–11.

**Table 5–11 Functional requirements for the endoscopic scanner**

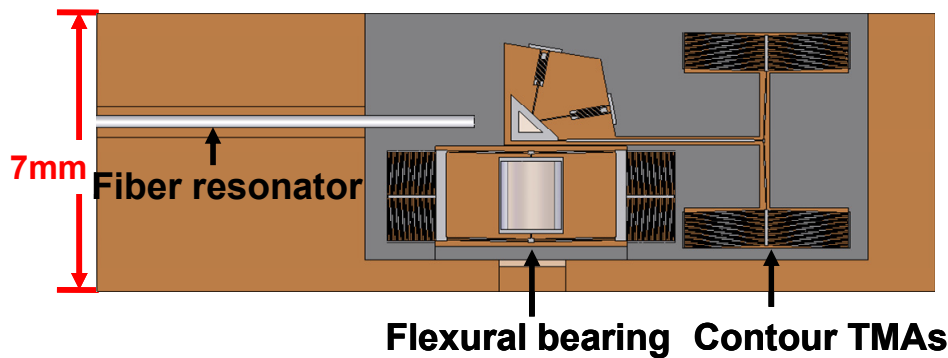
Axis	X	$\theta_x$	Z
Component	DCPCF	Prism	GRIN lens
Range	100 $\mu\text{m}$	2°	100 $\mu\text{m}$
Speed for volumetric scan	3000 Hz	30 Hz	2 Hz
Speed for fine 2D scan	700 Hz	1 Hz	0.02 Hz

Figure 5–19 shows the optical system on scanner. The scanner is comprised of the guiding flexures and actuation system. In this design, the GRIN lens and the micro-prism were of millimeter scale and were integrated with the in-plane TMAs on a micro-fabricated silicon optical bench (SOB). The SOB provides micrometer-level precision alignment for the lenses. The performance of the chevron TMAs were optimized through a geometric contouring technique. High-speed operation may be achieved through the application of the high-speed pulsing technique that was presented in Chapter 2.

The most salient issues surrounding SOB design include: (1) actuation selection and design, (2) guiding flexure mechanism design, (3) assembly of the optical components, and (4) device characterization. They will be presented and discussed in the following sub-sections.



A



B

Figure 5–19 Schematics of the endoscopic micro–scanner and micro–optical bench design, where the femtosecond laser beam is guided to the optical platform through the resonating fiber. On the optical platform, the collimated laser goes to the objective GRIN lens through the reflection off of a millimeter–scale prism.

### 5.3.1 Actuation system design

#### Selection of micro–actuation technology

An extensive literature review of micro–actuation technologies was summarized in Table 1–1 in Chapter 1. The results conclude that TMAs were the most suitable actuator species for the following reasons:

1. Reliability and repeatability of micro–fabrication
2. Small device envelope
3. High force and stroke
4. Low–voltage operating condition (typically less than 5V) that makes it specifically suitable for in vivo procedures.

Note that most other micro–actuation technologies operate at a higher voltage, *e.g.*, electrostatic actuator, piezoelectric actuator. Although a TMA may run at high temperature (800

°K), it would introduce no harm as long as the power level was low, *e.g.* 100 mW. In case of unexpected exposure during *in vivo* operation, a high temperature, low power micro–device will only damage a highly localized region of cells/tissue. In contrast, high voltage devices could cause a potentially dangerous current flow through the heart.

### Design and optimization of TMAs

Figure 5–20 shows the layout of the SOB that consists of two sets of flexural bearings with chevron TMA trains. The chevron TMAs were selected over parallel TMAs because for a given footprint they were able to run in parallel and generate larger force output without sacrificing the stroke as shown in Figure 5–20.

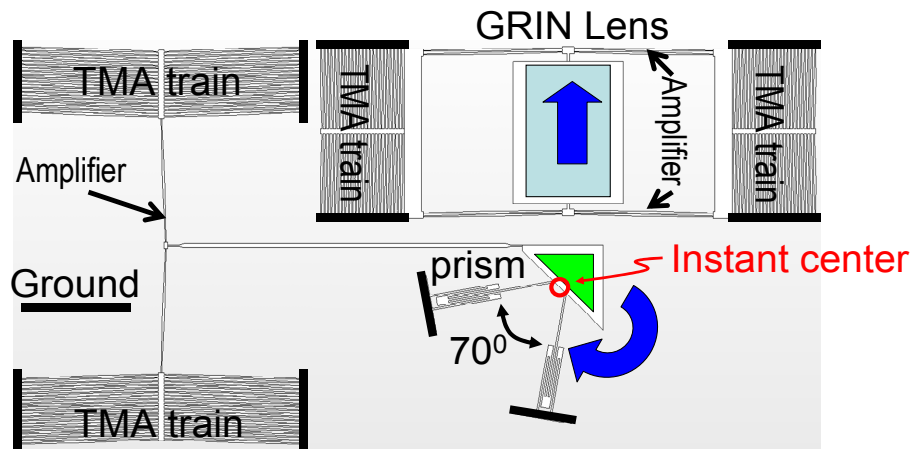


Figure 5–20 A SOB with integrated TMAs and flexural bearings that generate linear and rotary motions

In contrast to the contoured TMAs that were optimized for speed and force in Chapter 3, the design objectives for the contoured TMAs were to (1) minimize the power consumption and (2) maximize the stroke. This was desired because the TMA trains on the SOB operate at a moderate speed of 30Hz and 2Hz, but require a rather large stroke of 100 microns. The speed is not critical here because with the pulsing technique the TMA train is able to achieve a 10X cycling speed. As the flexure mechanism may easily provide more than 10X motion amplification, the required stroke for individual TMA was set to be 10 micron. The amplifier design and optimization shall be described in Section 5.3.2. The functional requirements and the constraints for the contoured TMAs are summarized in Table 5–12.

**Table 5–12 Functional requirements and constraints for the TMAs that were used in the SOB**

Stroke	larger than 10 $\mu\text{m}$
TMA bandwidth for the Prism shuttle	larger than 30 Hz
TMA bandwidth for the GRIN lens shuttle	larger than 2 Hz
Envelope	less than 7 mm
Operating voltage	less than 5 V
Number of chevron TMAs for the train	To be determined

The optimal design parameters were selected by using the contoured chevron TMA performance charts provided in Chapter 2, *i.e.* Figure 2–8, Figure 2–10, Figure 2–11, and Figure 2–17. The TMA performance for the GRIN lens shuttle and the prism shuttle was modeled and is summarized in Table 5–13. The results showed that the TMAs would satisfy the speed and stroke requirements. With the pulsing technique, the TMA cycling speed would in fact be 3 times better than the requirements, *i.e.* 100 Hz vs. 30 Hz. The experimental results of these TMAs are presented in Section 5.3.4.

**Table 5–13 Simulated performance of contoured TMA for the SOB**

TMA for th GRIN lens shuttle	
Stroke	10 $\mu\text{m}$
Operating voltage	2.8 V
Operating temperature	580 °K
TMA bandwidth	8 Hz (before pulsing)
Max. force output	10 mN
TMA for the prism shuttle	
Stroke	14 $\mu\text{m}$
Operating voltage	2.8 V
Operating temperature	580 °K
TMA bandwidth	16 Hz (before pulsing)
Max. force output	8 mN

Table 5–14 lists the design parameters of the individual contoured TMA that were used in GRIN lens and prism shuttles and their performance improvements in comparison to conventional constant cross–section TMAs as a reference. Note the speed enhancements in Table 5–14 represent the performance before the pulsing technique was applied.

**Table 5–14 Design parameters and performance enhancements of contoured TMAs that were used in GRIN lens shuttle and prism shuttle**

Contoured TMA design parameters			
GRIN Lens shuttle		Prism shuttle	
$L_S/L_L$	5/8	$L_S/L_L$	5/8
$L/2L_L$	35/4	$L/2L_L$	15
$w'$	2/5	$1/w'$	2/5
$w_e$	14.3 $\mu\text{m}$	$w_e$	14.2 $\mu\text{m}$
$L$	1400 $\mu\text{m}$	$L$	2400 $\mu\text{m}$
$b$	200 $\mu\text{m}$	$B$	200 $\mu\text{m}$
Contoured TMAs performance enhancements compared to constant cross–section TMAs			
Constant power		Constant power	
Speed	$\uparrow 2.5\text{X}$	Speed	$\uparrow 2.2\text{X}$
Stroke	$\uparrow 5.3\text{X}$	Stroke	$\uparrow 3.4\text{X}$
Force	$\uparrow 1.7\text{X}$	Force	$\uparrow 1.4\text{X}$
Constant displacement		Constant displacement	
Power	$\downarrow 80\%$	Power	$\downarrow 69\%$
Temperature	$\downarrow 58\%$	Temperature	$\downarrow 44\%$
Efficiency	$\uparrow 45\text{X}$	Efficiency	$\uparrow 15\text{X}$

### 5.3.2 Choice of bearings and concepts

Flexural bearings were used for precision motion guidance within the scanner components that are contained within Figure 5–20. Flexure bearings are easily fabricated via standard MEMS processes and they provide smooth, sub–micron resolution; however, they usually possess parasitic motions and they require a large bearing footprint in comparison to the motion they must provide. The success of the scanner relies upon leveraging the good characteristics while minimizing the negative characteristics. The following sub–sections describe how this was accomplished.

#### **Translation flexural bearing concept**

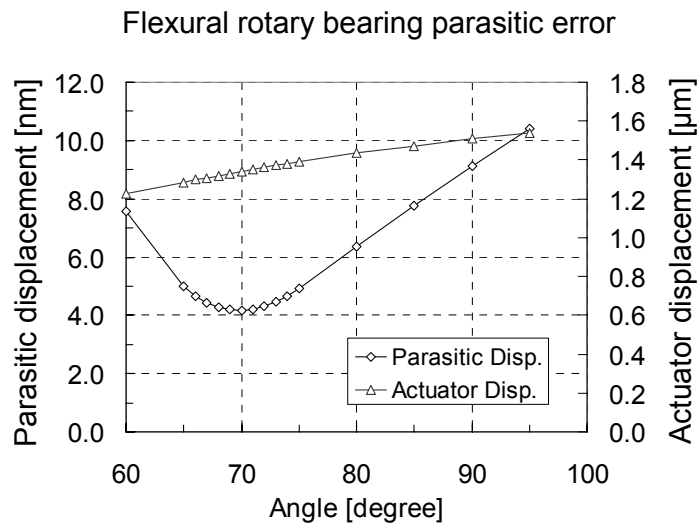
The flexural bearing that was actuated by the TMA trains provides precision guidance and reduced parasitic motion for active optical components. As shown in Figure 5–20, the flexural bearing that carries the objective GRIN lens generates linear motion and travels 100 microns. This flexural bearing consists of a two–stage chevron amplification mechanism that was driven by two sets of chevron TMA trains. The symmetric design is well–known to prevent lateral parasitic motion. Note that only the chevron TMA train was used as an actuator. The interlinking chevron flexure was for transmitting/amplifying mechanical motion, and did not experience internal heat generation.

**Rotary flexural bearing concept**

The second flexural bearing carried the micro-prism and generated rotary motion about the instant center over  $+2.50^\circ$ . This rotary bearing was driven by the two-stage chevron amplification mechanism and chevron TMA train that is shown in Figure 5–20. The shuttle that carries the prism was part of a flexure-based four-bar mechanism. The instant center of this four-bar mechanism was designed to be on the reflecting point of the prism’s inner surface. Parasitic translational motion should therefore be minimized during the rotation. The optimization result of the four-bar mechanism, shown in Figure 5–21, shows that the two supporting flexures of the four-bar mechanism should intersect at  $70^\circ$ . This only yields 6 nm of parasitic motion at the full stroke ( $2.5^\circ$ ) of this rotary bearing. As the GRIN lens and prism weigh 1.5 and 1.2 grams respectively, the gravity effects on both shuttles were modeled and proven to be below a level that would cause practical concern. Simulated performance characteristics of the translational and rotary bearing are presented in Table 5–15.

**Table 5–15 Simulated performance of translational and rotary bearing with integrated TMA train**

	Translational bearing	Rotary bearing
Range	120 $\mu\text{m}$	$2.5^\circ$
Gravity deflection	0.04 $\mu\text{m}$	0.30 $\mu\text{m}$
1 <sup>st</sup> Resonant frequency (unload)	1,527 Hz	3,205 Hz
2 <sup>nd</sup> Resonant frequency (unload)	7,121 Hz	7,096 Hz



**Figure 5–21 A flexural rotary bearing optimization. The results show that at  $70^\circ$  the bearing will have an optimal transmission ratio (defined as parasitic displacement over actuator displacement) equal to  $2.9 \times 10^{-3}$  [mm/mm].**

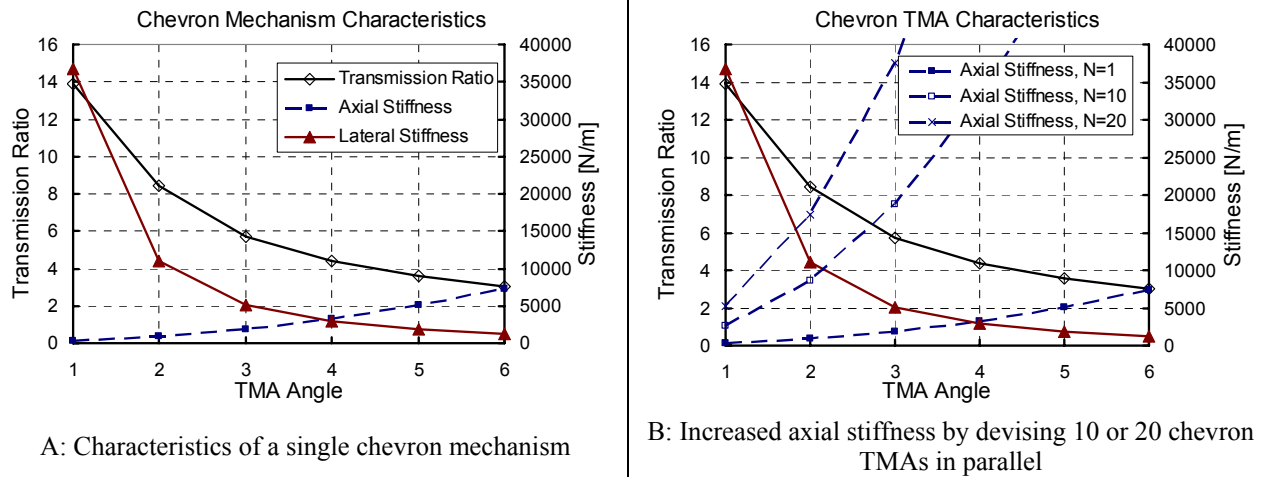
### **Transmission ratio optimization**

In the previous section, the four-bar mechanism topology for the prism shuttle was optimized. The cascaded chevron flexure was then modeled in order to optimize its performance and transmission ratio. The transmission ratio for the chevron mechanism is defined as the ratio of its output displacement to its input displacement.

The transmission ratio, axial stiffness and lateral stiffness of a chevron flexure, are functions of the angle between the chevron beam and the horizontal line shown that is shown in Figure 5–22A and Figure 5–23. In Figure 5–22A, the transmission ratio and the lateral stiffness of a chevron mechanism drop sharply, while the axial stiffness increases gradually, as the angle increases. It is not uncommon for designers to attempt to cascade two chevron mechanisms at small angles in order to receive a large transmission ratio. In fact, this design will result in a low transmission ratio because of the mismatch between the axial and lateral stiffness of the first (TMA) and second (amplification flexure) chevron mechanisms that are shown in Figure 5–23.

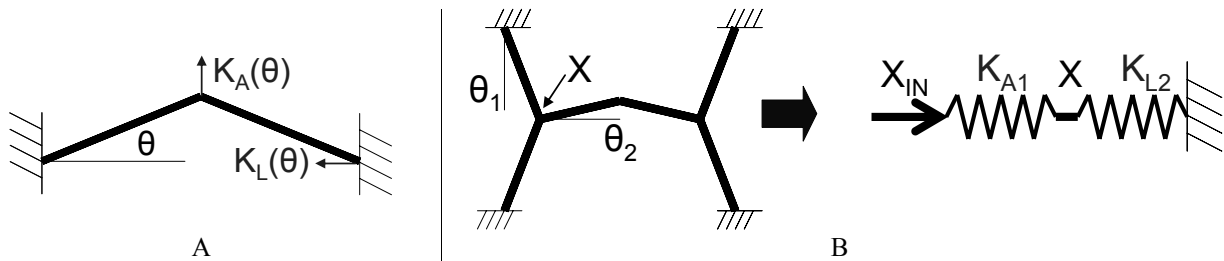
A basic concept that may be used for optimizing the energy transfer from the first chevron TMA to the second chevron mechanism is to match their mechanical impedance, *i.e.* design the chevron flexures so that the axial stiffness ( $K_{A1}$ ) and lateral stiffness ( $K_{L2}$ ) of the first and second chevrons are equal. There are two ways to adjust the relative values of  $K_{A1}$  and  $K_{L2}$  for mechanism optimization: (1) adjust  $\theta_1$  and  $\theta_2$  as shown in Figure 5–22A, or (2) run many chevron TMAs in parallel, where the effect of increased axial stiffness helps to increase the transmission ratio as shown in Figure 5–22B. Although a large transmission ratio may be obtained through applying the second option, this may result in a large power requirement to ensure that all TMAs may be run simultaneously.





**Figure 5–22 Transmission ratio, axial, lateral stiffness of a chevron mechanism as a function of angle**

As shown in Figure 5–23, the cascaded chevron mechanism may be modeled as a two–spring system, where spring constants  $K_{A1}(\theta_1)$  and  $K_{L2}(\theta_2)$  represent the axial stiffness and the lateral stiffness of the first and second chevron mechanism respectively. The variable  $X_{IN}$  represents the displacement of a chevron TMA (first chevron mechanism), and  $X$  is the output displacement of the cascaded system. The relationship between  $X$  and  $X_{IN}$  is shown in Equation (36). The overall transmission ratio of the cascaded mechanism is shown in Equation (37). The stroke of cascaded system is the product of the input displacement and the transmission ratio, as shown in Equation (38).



**Figure 5–23 A two–spring model for the cascaded chevron mechanism**

$$X = \frac{1}{1 + K_{L2}(\theta_2)/K_{A1}(\theta_1)} \cdot X_{IN} \quad (36)$$

$$\text{Transmission Ratio} = T_{R1}(\theta_1) \cdot \left[ \frac{1}{1 + K_{L2}(\theta_2)/K_{A1}(\theta_1)} \right] \cdot T_{R2}(\theta_2) \quad (37)$$

$$\text{Stroke} = T_{R1}(\theta_1) \cdot \left[ \frac{1}{1 + K_{L2}(\theta_2)/K_{A1}(\theta_1)} \right] \cdot T_{R2}(\theta_2) \cdot X_{IN} \quad (38)$$

Equation (37) was used to set a transmission ratio as a function of  $\theta_1$  and  $\theta_2$ . A plot of the optimal transmission ratio for a given number of the TMAs was also obtained. Figure 5–24A presents the optimal transmission ratios as a function of the number of TMAs. The normalized mechanism stroke, *i.e.*, power efficiency, as a function of number of TMAs, may be obtained by dividing the optimal transmission ratio by the number of TMAs. Figure 5–24 shows that more parallel TMAs lead to a larger transmission ratio. Unfortunately, there is a corresponding decrease in power efficiency. A minimum number of TMAs should be used if the optimization objective is to minimize the power consumption.

An approach that may be used to obtain an efficient design is to:

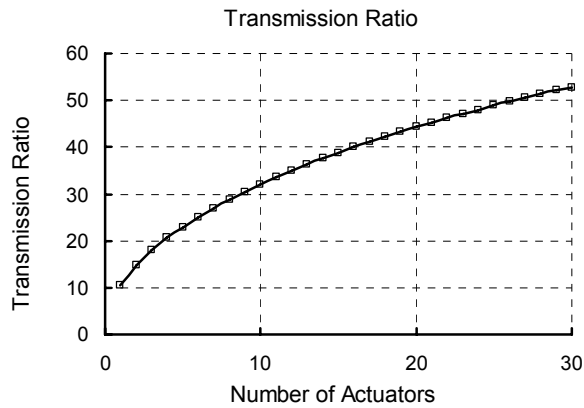
Step 1: Determine the required stroke ( $S$ ) from functional requirements.

Step 2: Determine the required displacement ( $d$ ) of an individual TMA.

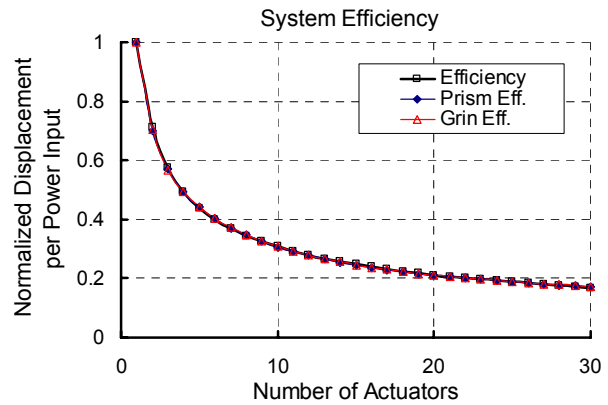
Step 3: Determine the required optimal transmission ratio ( $T_R$ ) by dividing the system stroke by the individual TMA's displacement ( $T_R = S/d$ ).

Step 4: Obtain the corresponding values for  $\theta_1$  and  $\theta_2$  for the optimal transmission ratio from the transmission equation.

Note that this is a general approach and it is applicable for different design/optimization objectives. The following sections demonstrate the design and optimization procedures of the GRIN lens shuttle for three different objectives: (1) temperature minimization design, (2) power minimization design, and (3) design for a specified number of parallel TMAs. The design processes for the prism shuttle is identical and will not be described in detail.



A: Optimal transmission ratio as a function of number of TMAs



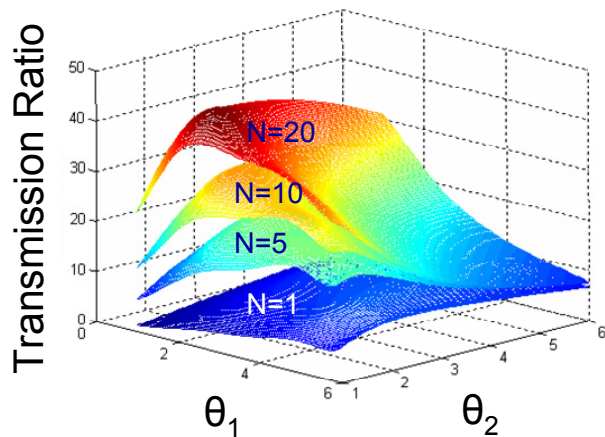
B: Power efficiency as a function of number of TMAs

**Figure 5–24 Optimal transmission ratio and power efficiency as a function of number of actuators**

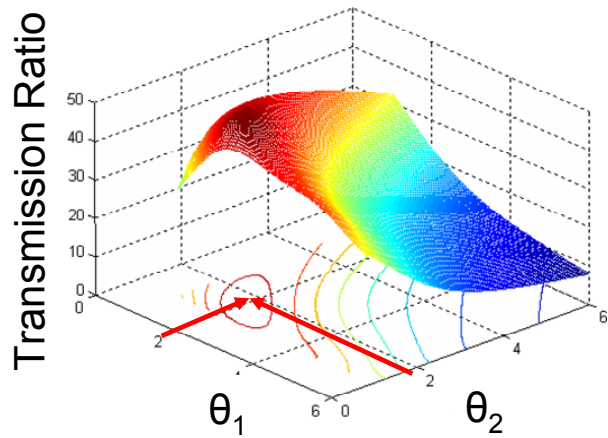
### **Temperature minimization**

As the scanner is designed for *in vivo* operation, a reduced operating temperature was preferred. The design process is then: (1) determine the TMA’s maximum operating temperature from functional requirements, *e.g.*, 150°C, (2) optimize the TMA’s performance, *e.g.* stroke, at the specified temperature by the geometric contouring method, and (3) obtain the required number of TMAs and the relative optimal transmission ratio from the surface plots that are shown in Figure 5–25A and Figure 5–25B. Note that these surface plots were obtained using Equation (37). In Figure 5–25A, one may find that the optimal transmission ratio will increase as the number of TMAs increases, and as the values of  $\theta_1$  and  $\theta_2$  decrease.

This example uses 20 parallel TMAs to achieve a 100 micron output displacement at 150°C operating temperature, where the optimal transmission ratio is 45.10, for  $\theta_1 = 2.0^\circ$ , and  $\theta_2 = 1.98^\circ$ .



A: Transmission ratio surface plots for different number of TMAs



B: Transmission ratio surface plot for N=20

Figure 5–25 A transmission ratio surface plot as a function of  $\theta_1$ ,  $\theta_2$ , and  $N$

### **Power minimization**

As TMAs operate more efficiently at high temperature, the required displacement is achieved when most of a TMA's material operates at 1200 °K—the highest safe operating temperature for silicon. Once the maximum operating temperature had been set, the rest of the design procedures were the same as the previous section (temperature minimization) and will not be repeated here.

This example uses only two parallel TMAs to achieve a 100 micron output displacement with 125 mW power consumption, where the optimal transmission ratio is 28.1, for  $\theta_1 = 2.5^\circ$ , and  $\theta_2 = 3.6^\circ$ . The transmission ratio surface plots of the GRIN lens shuttle design, as well as the prism shuttle design, are presented in Figure 5–26 and Figure 5–27 respectively. These surface plots were obtained using Equation (37). In the contour maps of Figure 5–26 and Figure 5–27, the flat region corresponds to the optimal angles of the transmission ratio. This means the optimal transmission ratio is insensitive to moderate variation in  $\theta_1$  and  $\theta_2$ .

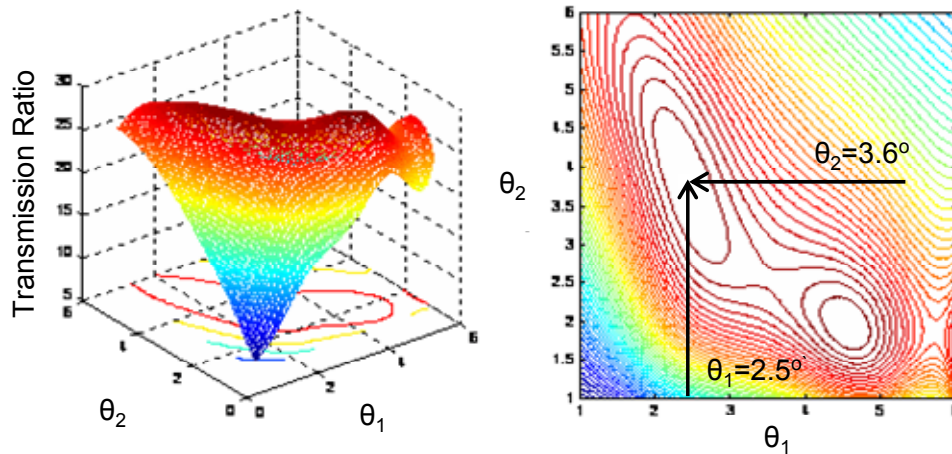


Figure 5–26 A transmission ratio plot for the GRIN lens shuttle with the low power objective

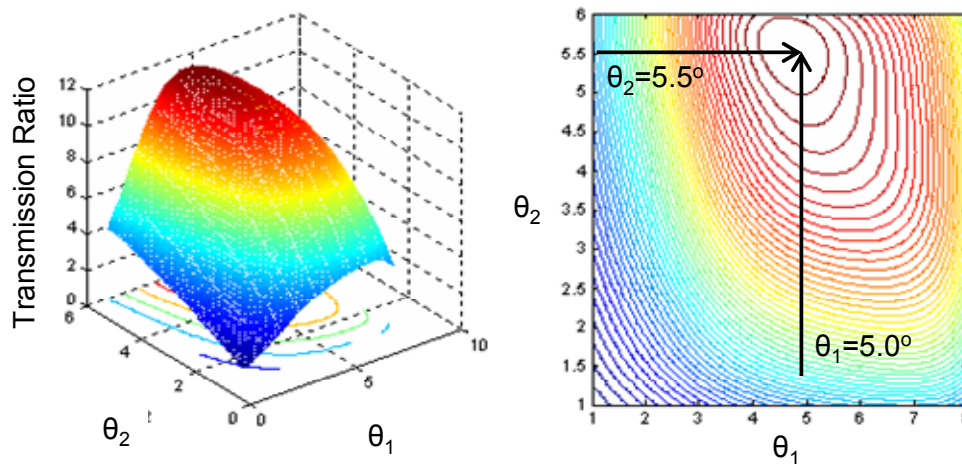


Figure 5–27 A transmission ratio plot for the prism shuttle with the low power objective

### Optimal design for specified number of parallel TMAs

Each of the previous examples may have drawbacks. For the low temperature design, the combined power consumption of the GRIN lens and prism shuttle on a single chip sum up to 1.2W. This may heat up the die and cause damage to tissues. For the low power design, the maximum stroke at 100 micron will be reached at 1200 °K. This device has no room for providing additional displacement if this were to be required. Additionally, the use of more parallel TMAs increases the shuttle’s structural integrity.

The design steps were conducted again to optimize the transmission ratio for 5 parallel TMAs. For  $N = 5$ , the functional requirements may easily be satisfied and the TMAs may

achieve a 100 micron output displacement with 160 mW power consumption. The optimal transmission ratio was 43.8, for  $\theta_1 = 2.2^\circ$ , and  $\theta_2 = 2.8^\circ$ . The transmission ratio surface plots that were generated via Equation (37) for the GRIN lens shuttle and the prism shuttle are shown in Figure 5–28 and Figure 5–29 respectively. In this design, the GRIN lens shuttle easily fulfills the required functional requirements with a full stroke of 400 microns. The scanner also operates at a much lower power, 160 mW.

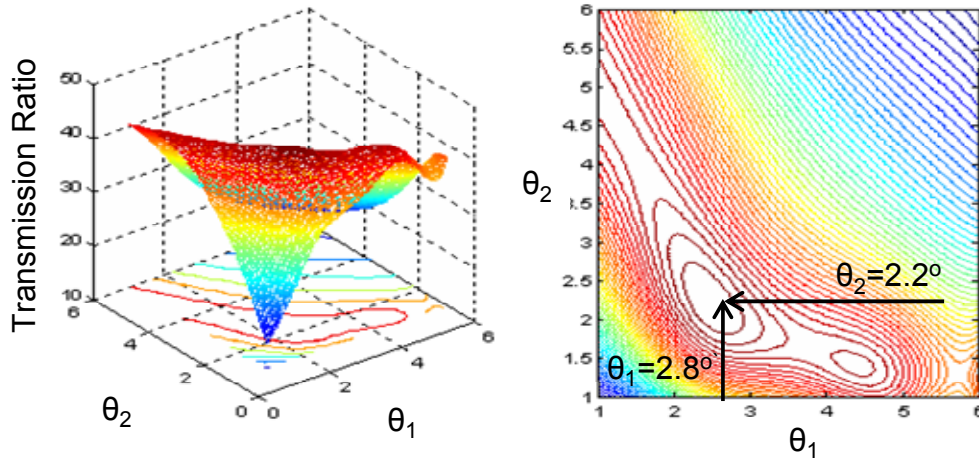


Figure 5–28 A transmission ratio plot for the GRIN lens shuttle for  $N = 5$

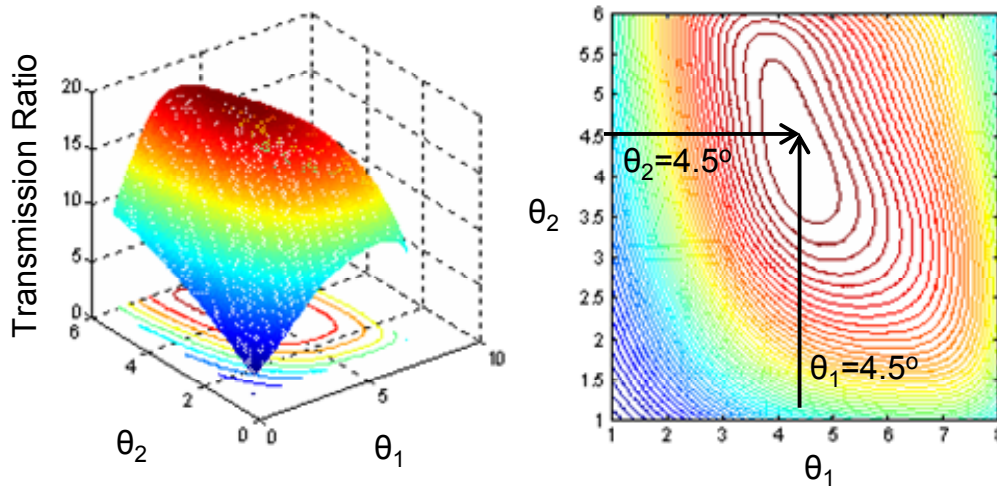


Figure 5–29 A transmission ratio plot for the prism shuttle for  $N = 5$

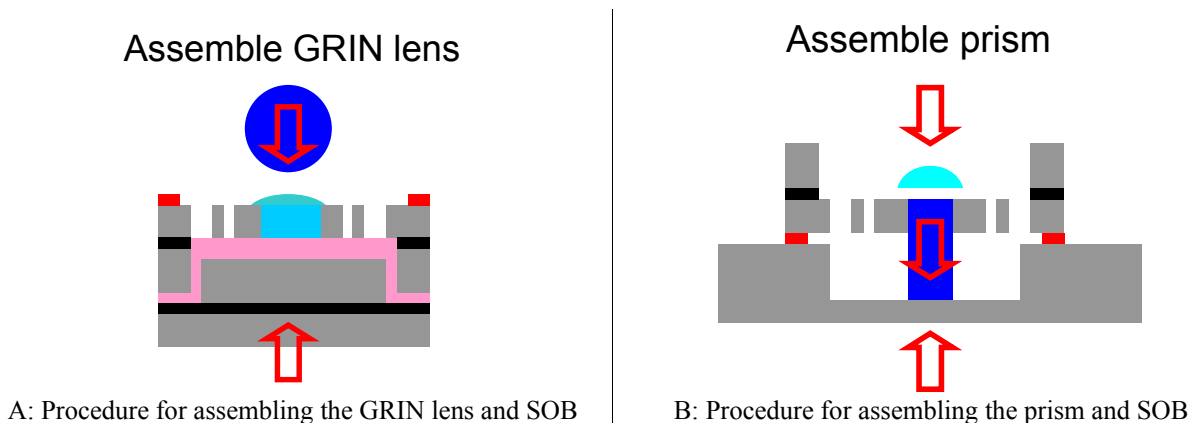
The design parameters and simulated performance of the GRIN lens shuttle and the prism shuttle for three different design objectives are summarized in Table 5–16.

**Table 5–16 Summary of three scanner designs for different objectives**

	Design I	Design II	Design III
	Low temperature	Low power	Optimal design
Parameters			
Transmission for GRIN shuttle	45.10	23.83	43.83
$\theta_1$	2.00°	2.5°	2.8°
$\theta_2$	1.98°	3.6°	2.2°
Stroke	100 $\mu\text{m}$	100 $\mu\text{m}$	100 $\mu\text{m}$
Power (at full stroke)	700 mW	125 mW	160 mW
Transmission for prism shuttle	42.50	11.46	18.81
$\theta_1$	2.0°	5.0°	4.5°
$\theta_2$	2.5°	5.5°	4.5°
Stroke	2°	4°	8°
Power (at full stroke)	500 mW	50 mW	125 mW

### 5.3.3 Assembling and packaging

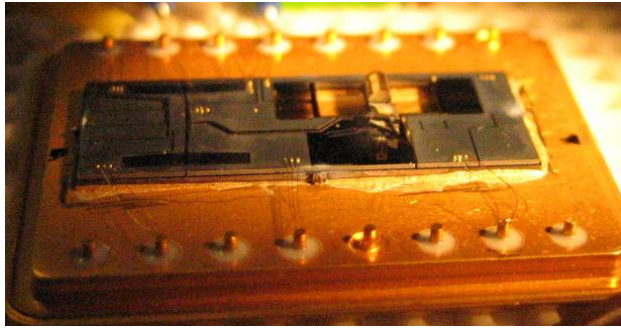
Figure 5–30 shows the assembly procedures for GRIN lens and prism. In Figure 5–30A, the scanner was positioned on an assembly die that was coated with photoresist or oil. After a UV securing glue was applied to the GRIN lens shuttle, the GRIN lens was placed onto the shuttle. The glue was cured after 30 seconds of exposure of UV light. In Figure 5–30B, the endoscopic scanner was flipped upside down and then aligned with the micro–prism that was positioned in the assembling die with the appropriate depth. The UV securing glue was subsequently applied from the backside of the prism shuttle. The prism was securely fixed onto the shuttle after 30 seconds of exposure under UV light. This procedure is fortunately amenable to automated mass production.



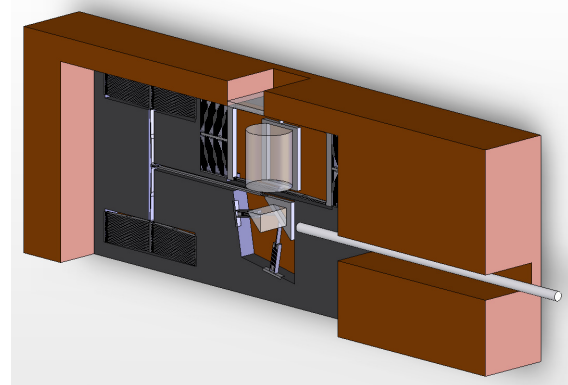
**Figure 5–30 Assembling procedures for GRIN lens and prism**

Figure 5–31A shows the image of a packaged SOB with a GRIN lens and a prism that were securely affixed onto the shuttle. Note that the gold package does not have a sounding wall

so that the laser may be aligned with the optical components without obstruction. Figure 5–31B shows a concept for a production package for the scanner. The SOB resides within a plastic housing and it allows the resonating fiber to be inserted from the right side. The glass cover on top of the plastic housing protects the objective lens from direct contact with specimen tissues. The SOB and its housing were designed to be a low–cost, disposable component that could be replaced after every *in vivo* scan procedure.



A: A wire–bonded SOI package with GRIN lens and prism glued to the shuttle



B: An isometric view of the proposed package for production

**Figure 5–31 A packaged SOB for experimentation and a concept package for production**

### 5.3.4 Device characterization

This section presents the characterization of the device’s static and dynamic behavior and compares this with modeling results. The data were obtained via a Micro–Motion Analyzer (MMA). The working principle of the MMA was explained in Section 2.7. To characterize the MMA’s in–plane repeatability and resolution, a sample device was tested at 50 different frequencies by capturing 8 motion phases at each frequency. The measurement was repeated 100 times. Based upon the data, the average standard deviation of 50 different frequencies for in–plane measurements is 7.1 nm [120]. The MMA has the ability to resolve images much smaller than the pixel size, by using the modulation of the brightness of relevant pixels. The MMA system has a resolution of 10 nm for motion measurement [120]. Note that most error bars in the plots of the MMA measurements are too small to be observed over the data point symbols.



### GRIN lens shuttle

Figure 5–32 shows the frequency spectrum of the GRIN lens shuttle and its simulated mode shapes. The first and second mode of the GRIN lens shuttle generates in–plane and out–of–plane motion at 1,527 Hz and 7,121 Hz respectively. The measured in–plane resonant peak is at 1,508 Hz. This matches the simulated value within 1.3%. The accuracy of the frequency modeling is attributed to the accurate geometry values that were obtained via measurement within the SEM. The frequency result also indirectly shows that there were no hidden cracks or broken flexures in the device.

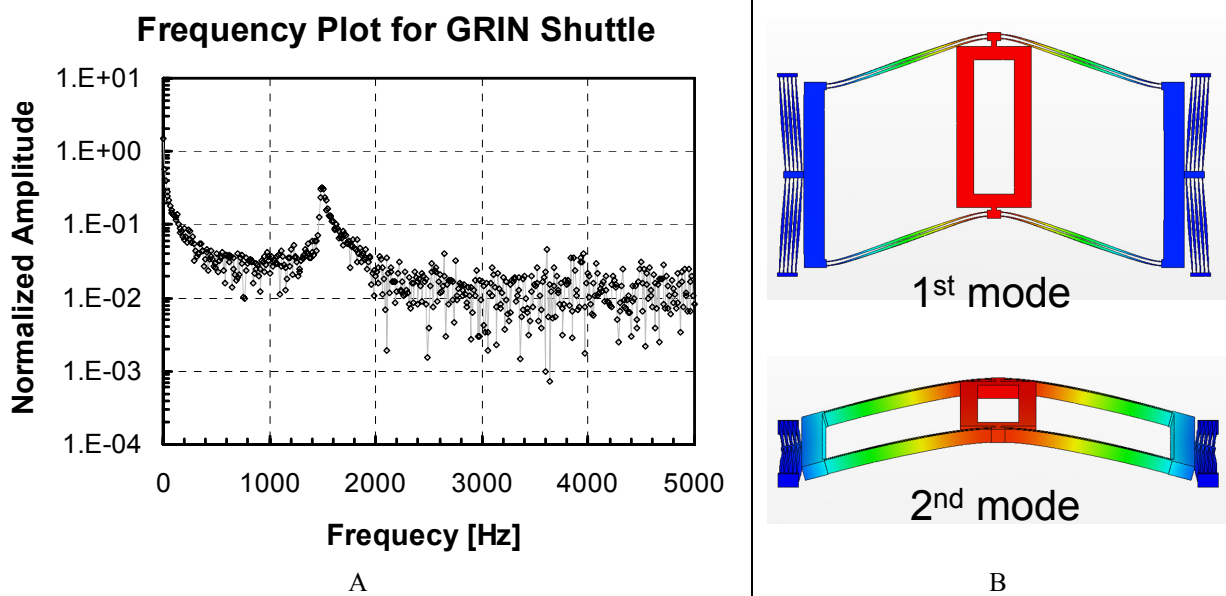


Figure 5–32 Measured frequency spectrum and simulated mode shapes for GRIN lens shuttle

Figure 5–33 shows the step response of the GRIN lens shuttle. The measured rise time and fall time for the GRIN lens shuttle were 0.46 and 0.38 second respectively. These values show an error of –6.5%.

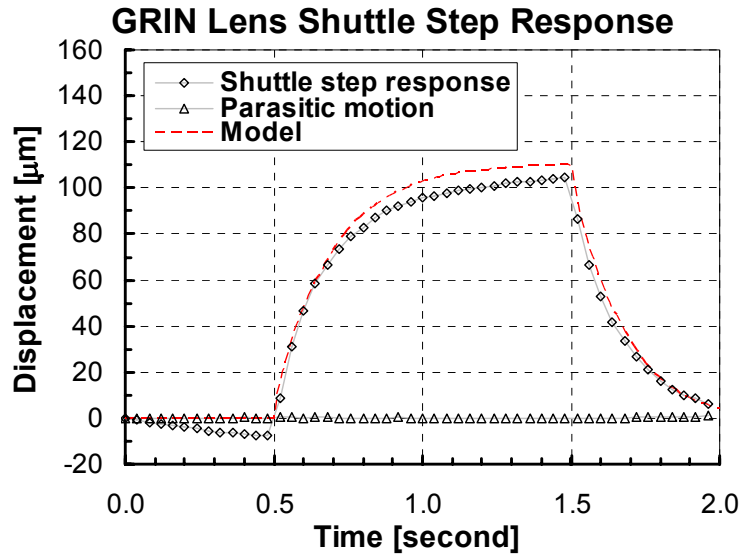


Figure 5–33 Step response of GRIN lens shuttle

The dynamic test results for the GRIN lens shuttle are summarized in Table 5–17. From the measured results, it was found that the cycling speed of the GRIN lens shuttle fulfills the requirements, *i.e.* to scan at 2 Hz, before the pulsing technique was applied.

Table 5–17 Summary of GRIN lens dynamic test

GRIN lens shuttle	Measured value	Simulated value	Error [%]
Frequency Test			
1 <sup>st</sup> Resonant frequency (in-plane)	1,508 Hz	1,527 Hz	+1.26%
2 <sup>nd</sup> Resonant frequency (out-of-plane)	N/A	7,121 Hz	N/A
Step response			
Rise time [sec]	0.46	0.43	-6.5%
Fall time [sec]	0.38	0.37	-2.6%

The accuracy of the dynamic modeling results may be used to assess bounds upon the accuracy of the electrical resistivity, coefficient of thermal expansion (CTE), and thermal conductivity (both functions of temperature) in comparison to the values that were used in the models. From Equation (1), it is known that in the heating process, the resistivity, CTE, and conductivity are coupled. In the cooling process, however, only the thermal conductivity and CTE are coupled in the equation because the heat generation term is zero. For practical purposes, the thermal conductivity and CTE have been shown to be independent of dopant type and doping level. A more accurate modeling result may therefore be expected for the cooling process. This has already been observed and proven via the dynamic data that were presented within this section.

As the value of thermal conductivity that was used is accurate within  $\pm 0.1$  W/m-°K throughout the actuation temperature range, the accuracy of electrical resistivity may then be assessed by examining the simulation results for the rise time. The value of electrical resistivity is usually given with the SOI wafer, or it is easily measurable in the clean room at room temperature. Values for elevated temperatures are not available from the manufacturer and these values were not well-documented in the literature. An accurate value of resistivity at increased temperature was difficult to obtain in this case.

The resistivity variation depends upon the type of dopant as well as the doping level. For these arsine-doped SOI wafers, the material properties (resistivity, conductivity, and CTE) for silicon with phosphorous [101] were used to generate curve fits that capture the property-temperature relationships. The properties of arsine-doped silicon were suitable for use as phosphorous and arsine reside in the same column of the periodic table and therefore should possess a temperature dependant electrical resistivity that is more appropriate to use than the constant temperature resistivity of arsine-doped silicon.

Figure 5-34 shows the results for static displacement of the GRIN lens shuttle. Measured positions were plotted as a function of command current in Figure 5-34A, and as a function of command position in Figure 5-34B. In Figure 5-34, the measured displacements show a gradual divergence from commanded values at elevated temperature, where a +6.7% error was observed at full stroke. This divergence was due in part to the temperature dependence of electrical resistivity and the differences in the manner in which electrical properties of phosphorous and arsine change with temperature. Assuming the thermal conductivity and CTE of the arsine-doped wafer were accurate, the resistivity would have a 7% error at elevated temperatures. Note that the fabrication errors were not included in the error analysis as all critical dimensions of the devices were measured in the SEM after they were fabricated.

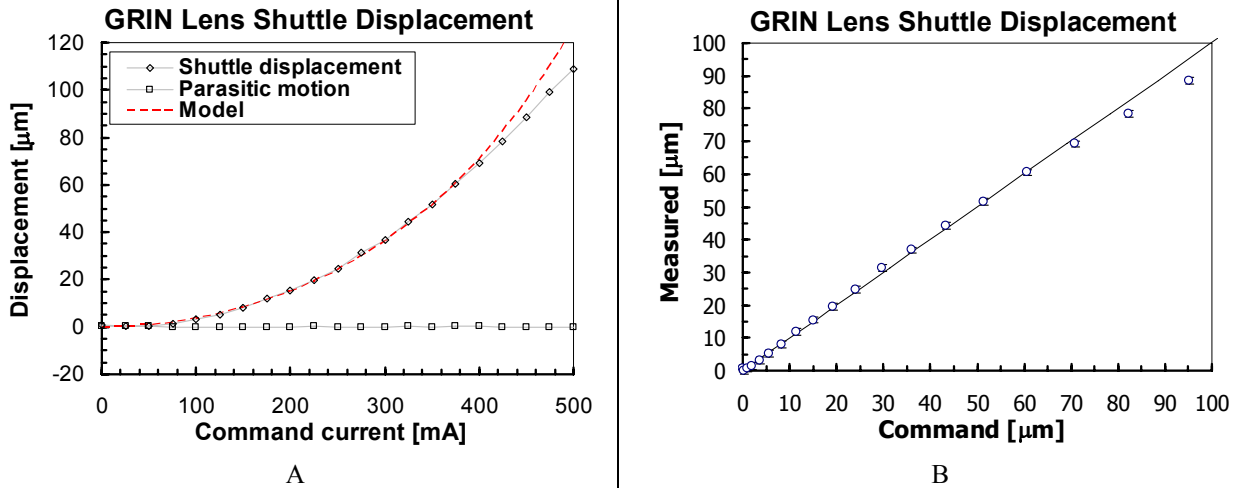


Figure 5-34 Displacement vs. input command plot for GRIN lens shuttle

**High-speed pulsing on GRIN lens shuttle**

Figure 5-35 shows the results of pulsing experiments. In this experiment, the GRIN lens shuttle was first driven by the conventional signal and then by the pulsed signal. A shorter rise time and fall time were observed for identical command displacement (8.5 μm). The forward speed and return speed were improved by factors of 20 and 9 respectively. A simulated step response of a constant cross-section TMA GRIN lens shuttle is shown alongside the corresponding response for a contoured TMA within Figure 5-35.

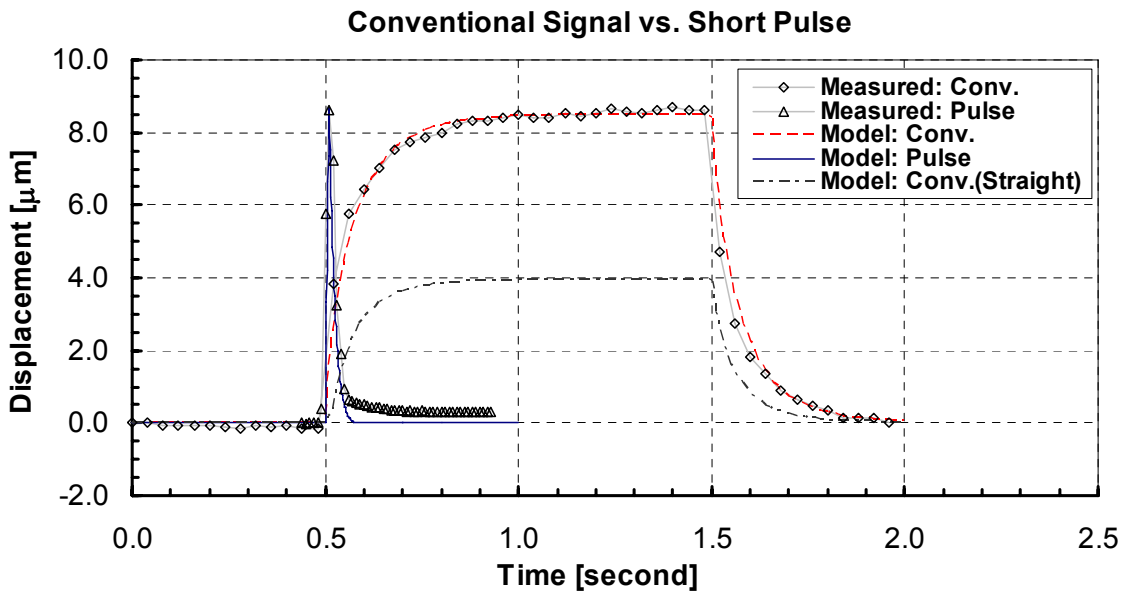


Figure 5-35 Demonstration of pulsing technique on the GRIN lens shuttle with contour chevron TMAs

The signal parameters and experimental results of the pulsing experiment are summarized in Table 5–18. The errors in the pulsing experiment were larger, *i.e.* –10% and +10% for rise time and fall time respectively. This is expected because for non–periodic measurements on the MMA system, the time resolution is determined by the maximum number of motion phases ( $N_P$ ,  $N_P = 50$ ). The time resolution =  $\Delta t_{PULSE}/N_P$ . Accordingly, the time resolution for the pulsing experiment is  $\pm 5$  milli–second.

**Table 5–18 Summary of high–speed pulsing technique applied on GRIN lens shuttle**

GRIN lens shuttle	Measured value	Simulated value	Error [%]
Pulsed signal	Square wave, 0.5Hz, 125mA, duty cycle = 50%.		
Rise time [s]	0.010	0.009	–10%
Fall time [s]	0.020	0.022	+10%
Conventional signal	Square wave, 2Hz, 250mA, duty cycle = 5%.		
Rise time [s]	0.200	0.190	–5.00%
Fall time [s]	0.180	0.185	+2.78%
Enhancement of forward speed	↑ 20.0X		
Enhancement of return speed	↑ 9.0X		

Table 5–19 summarizes the performance improvements of the contoured TMAs that were used in the GRIN lens shuttle. With the pulsing technique, a contoured TMA may exhibit a 28.6 faster cycling speed as predicted by the model. This result is important as it shows that a TMA’s speed may be improved by more than an order of magnitude with geometric contouring and pulsing. A broad range of conventional TMAs [4, 9–14, 16, 17] were found within the literature with strokes on the order of tens of microns and possessing kHz bandwidth. These could operate at bandwidth greater than 10 kHz with improved the stroke and power efficiency with contouring and pulsing.

**Table 5–19 Performance enhancements of contoured TMAs that were used in GRIN lens shuttle**

Constant power	
Speed	↑ 2.2X
Speed (pulsing)	↑ 28.6X
Stroke	↑ 3.4X
Force	↑ 1.4X
Constant displacement	
Power	↓ 69%
Temperature	↓ 44%
Efficiency	↑ 15X

The errors analyses and dynamic pulsing modeling for the prism shuttle were similar to the preceding and will therefore not be repeated.

### Prism shuttle

Figure 5–36 shows the frequency spectrum of the prism shuttle as well as the simulated mode shapes. The first and second mode of the GRIN lens shuttle generate in–plane motion at simulated values of 3,205Hz and 7,096Hz respectively. The measured corresponding resonant peaks match the simulated values errors of +2.6% and –3.0% respectively.

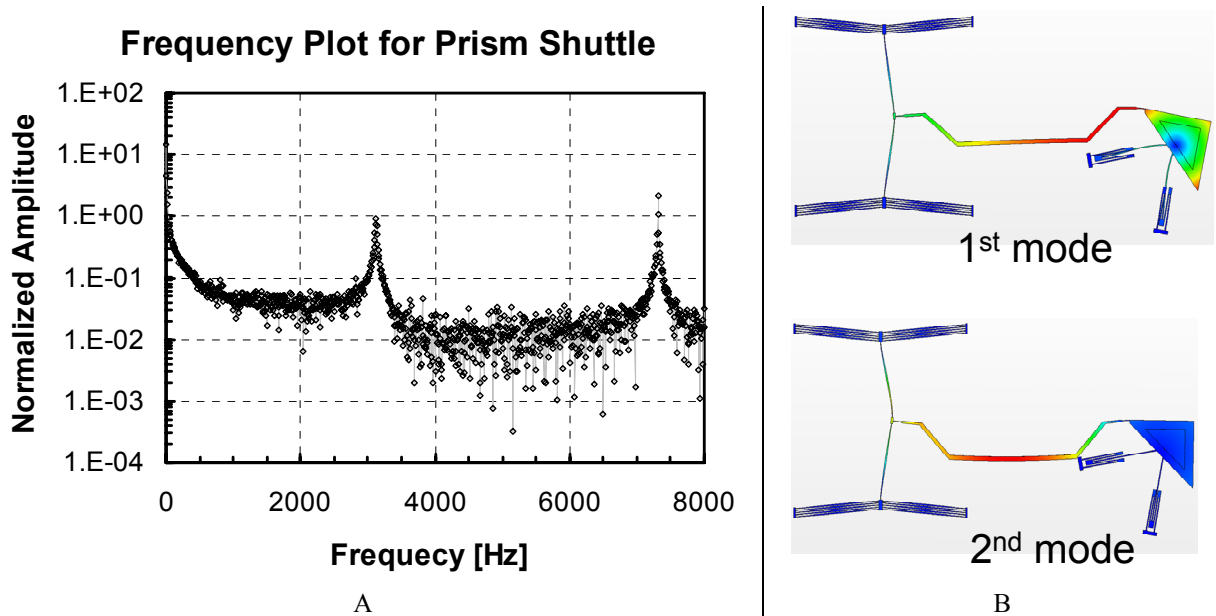


Figure 5–36 Measured frequency spectrum and simulated mode shapes of prism shuttle

Figure 5–37 shows the step response of the GRIN lens shuttle. From the experiment, it was found that the rise time and fall time for the prism shuttle were 0.13 and 0.09 second respectively. The worst case error between these values and the predicted values was +7.7%. The dynamic test results of the prism shuttle are summarized Table 5–20.

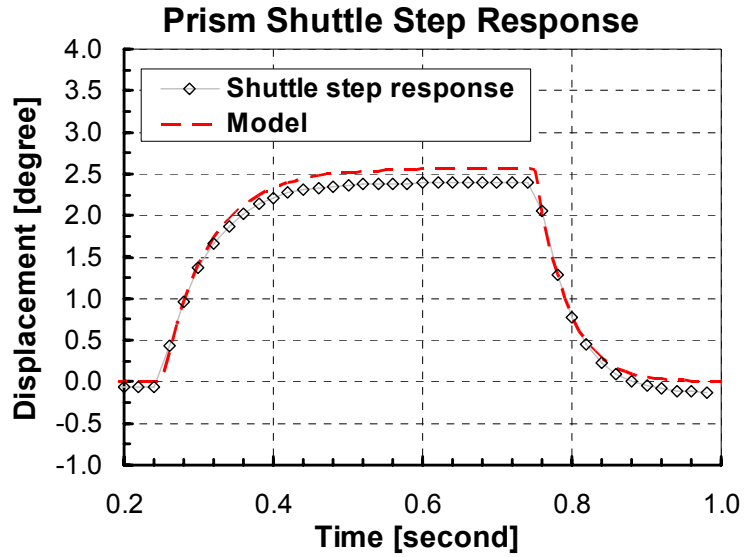


Figure 5–37 Step response of prism shuttle

Table 5–20 Summary prism shuttle dynamic test

Prism shuttle	Measured value	Simulated value	Error [%]
Frequency Test			
1 <sup>st</sup> Resonant frequency (in-plane)	3,124 Hz	3,205 Hz	+2.59%
2 <sup>nd</sup> Resonant frequency (in-plane)	7320 Hz	7,096	-3.06%
Step response			
Rise time [sec]	0.13	0.14	+7.7%
Fall time [sec]	0.09	0.095	+5.5%

Figure 5–38 shows the static results of the prism shuttle. Measured positions were plotted as function of command current in Figure 5–38A and as a function of command position in Figure 5–38B.

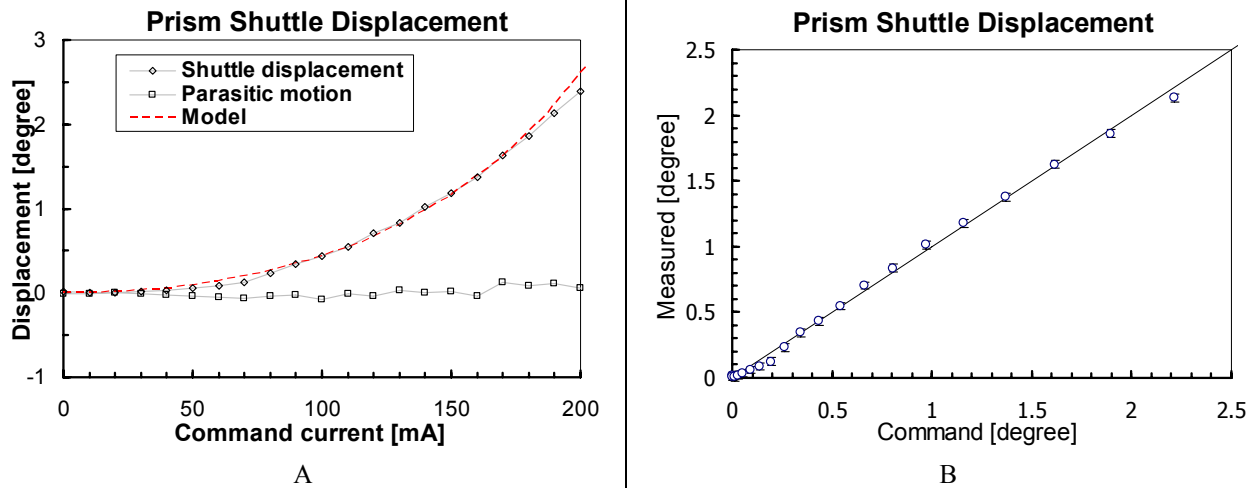


Figure 5-38 Displacement vs. input command plot of prism shuttle

The match between the simulated and experimental results gives confidence that models that were created in this research may be used by designers to predict device performance with less than 8% error and sometimes with as little as 2% error.

## 5.4 Fiber resonator design

The fiber resonator, as mentioned in the previous sections, is responsible for the scan axis that runs from 700Hz to 3 kHz with a minimum  $\pm 50$  micron range of motion. The mechanical properties of the DCPCF were first modeled and characterized on a meso-scale piezo-driven resonator. The results were then used to generate the functional requirements for the final, smaller fiber resonator.

The meso-scale resonator was designed to create a first prototype of the scanner to hold the fiber and the two-photon endomicroscope. The meso-scale resonator fulfills the functional requirements and size constraint of this application. A small-scale MFM resonator was designed (1) to enable the assessment of the TMA performance, and (2) to demonstrate the feasibility of using a low-cost version in a practical application. The cost of the MFM resonator is low enough to make it a disposable component. The MFM resonator has a device envelope that is three times smaller than the functional requirements, presented in Chapter 3. Once the fiber is glued to the MFM stage, the length and the operating frequency may not be adjusted. The experiments were therefore performed primarily using the meso-scale fiber resonator as the resonance frequency could be adjusted by changing the protruding length of the fiber. After the



system characteristics were set, the meso-scale resonator was replaced by the MFM resonator in preparation for the characterization of the final prototype.

#### 5.4.1 Characterization of double clad photonic crystal fiber (DCPCF)

A meso-scale fiber resonator was designed to resonate the fiber at its first mode. The concept for the resonator is shown in Figure 5–39. The DCPCF has a rather complex mechanical structure that consists of a silica core with hollow channels and an acrylic protection layer, as shown in Figure 5–3.

The fiber resonator was actuated by a piezoelectric actuator that was capable of producing an 8-micron stroke at 120V (PI, P–885.20). The actuator was constrained on its ends by two metal cylinders and it was preloaded by screwing down the hex bolt shown on the left in Figure 5–39. A high-speed camera (512x512 resolution, 12,000 fps, Redlake MASD Ektapro Model 1012) was used to record the motion of the resonating fiber and the data were used to calculate the fiber’s resonant frequency. The high-speed camera should provide a  $\pm 0.05$  Hz resolution for the intended fiber operating speed, *i.e.* 1–3 kHz.

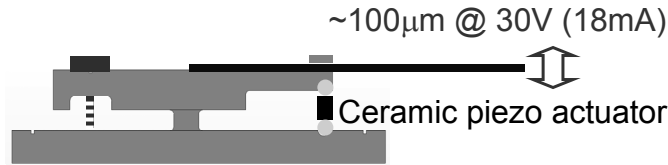
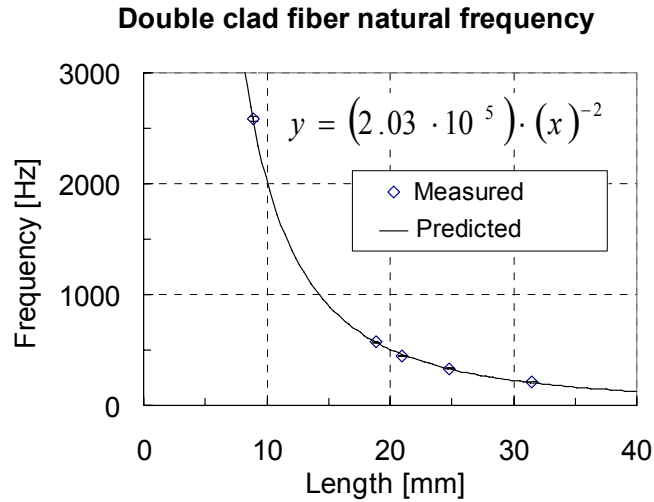


Figure 5–39 Schematics of the fiber resonator design

The experimental results are presented in Figure 5–40, along with predictions of Equation (39). This equation may be used to predict the resonant frequency within  $\pm 3$  Hz. Equation (39) is a modified form of an equation that was used to predict the transverse resonant frequency of a prismatic cantilever beam [121]. The modified equation captures the effect of the complex fiber structure. In this approach, the fiber is modeled as Silica cantilever beam. The equivalent density ( $\rho_{D,eq}$ ) and radius ( $R_{eq}$ ) in Equation (39) were obtained by conserving the total mass and while maintaining the second moment of inertia for the double clad fiber respectively. The variable,  $L$ , in Equation (39) refers the unclamped length of the fiber.

$$Frequency(Hz) = \left( \frac{R_{eq}}{2\pi} \right) \cdot \sqrt{\frac{3E_{Silica}}{\rho_{D,eq}}} \cdot (L)^{-2} \quad (39)$$



**Figure 5-40 Comparison of predicted and measured fiber resonance frequency**

The experiments showed that the DCPCF is able to provide more than  $\pm 50$  microns fiber tip motion at various speeds between 500 Hz to 3 kHz during resonance. Over  $\pm 50$  microns displacement was observed at 900 Hz with 30V supplying to the piezoelectric actuator. This performance will satisfy the functional requirements for range and speed so that the endoscopic scanner may operate at or above the desired speed, *e.g.* up to 30 fps and at a minimum 2fps respectively.

The effect of small errors in all parameters (such as the fiber length, the inner and outer radius of the double clad fiber, etc.) were considered. Errors in the measurement of the length of the fiber extending away from the resonator base were the most critical parameters. This yields 0.3% error in estimating resonant frequency. As a result, it is relatively easy to predict the resonant frequency within  $\pm 5$  Hz.

#### **5.4.2 Meso-scale endoscopic fiber resonator design and characterization**

The meso-scale fiber resonator and the MFM resonator share the same functional requirements and the design constraints that were listed in Table 3-1, and therefore they will not be repeated here. The following subsections present: (1) concept generation, (2) material selection, (3) flexural design/optimization, (4) manufacturing, and (5) device characterization.

**Actuator and flexure concept**

The piezoelectric actuator was selected for the actuation of the fiber resonator because of its high energy density and bandwidth that enabled it to produce the required speed (1–10 kHz) and stroke (10 μm) within the desired envelope. The pros and cons of the piezoelectric actuators in comparison to two other selected meso–scale actuators are summarized in the Pugh chart in Table 5–21. A general actuation system selection review may be found in [122–124].

**Table 5–21 Pugh chart of actuator selection for the meso–scale fiber resonator**

Concept selection chart		Electromagnetic	Piezoelectric	Shape memory alloy (SMA)
Metrics	Weight			
Envelope/size	2	0	1	1
Bandwidth	3	0	1	–1
Force output	2	0	1	1
Assembly/packaging	1	0	1	–1
Total scores		0	8	0

The ceramic piezoelectric actuator possesses high stiffness and natural frequency that enables the overall resonator system to be designed to operate at a resonant frequency that was higher than its desired bandwidth. The specifications of the selected ceramic piezoelectric actuator are listed in Table 5–22.

**Table 5–22 Specifications of the selected piezoelectric actuator (PI, P–882.51)**

Model number	PI, P–882.51 PICMA® Ceramic Encapsulated Piezo Actuator
Actuator envelope	2 x 3 x 18 mm <sup>3</sup>
Stroke	18 μm ± 10% at 100 Volts
Max. driving voltage	120 V
Stiffness	12 N/μm
Minimum preload	90 N (15 MPa)
Natural frequency	70 kHz
Capacitance	0.31
Required current for full stroke operation	31 mA

Three concepts are presented for motion amplification of the piezoelectric actuator as shown in Figure 5–41A, Figure 5–41B and Figure 5–41C. In concept A, a two–stage cascaded chevron mechanism, with a pivoting rod for additional amplification, is shown. Concept B does not use symmetry in order to reduce the length of the resonator. In concept C, two parallel chevron mechanisms provide amplification.

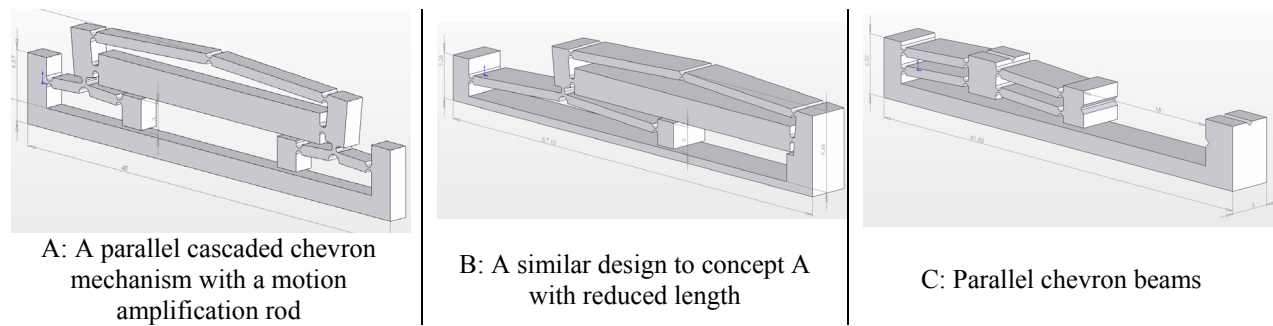


Figure 5-41 Concepts for the meso-scale fiber resonator

The simulation results of the first-pass designs for concept A, B, and C are summarized in Table 5-23.

Table 5-23 Summary of simulated performance for concepts A, B, and C

	Concept A	Concept B	Concept C
Device cross-section	5 x 9 mm <sup>2</sup>	5 x 9 mm <sup>2</sup>	5 x 7 mm <sup>2</sup>
Stiffness	1.50 N/μm	1.53 N/μm	1.60 N/μm
Stroke	90 μm	90 μm	100 μm
Natural frequency	1.0 kHz	1.0 kHz	1.5 kHz

The pros and cons of the three concepts are summarized in the Pugh chart that is shown in Table 5-24. Concept C was selected mostly because of its small envelope and higher natural frequency.

Table 5-24 Pugh chart of the fiber resonator for concept selection

Concept selection chart		Concept A	Concept B	Concept C
Metrics	Weight			
Envelope/size	3	0	1	2
Natural frequency	3	0	0	1
Sensitivity to error	3	0	1	1
Parasitic motion	2	0	-1	-1
Manufacturability	2	0	0	0
Thermal stability	1	0	0	0
Total scores		0	4	10

### Material concern/selection

Table 5-25 lists the normalized material properties for material selection of the flexure mechanism. Three figures of merit were used to compare the static and dynamic characteristics of the flexure design concepts. A high ratio of yield stress to Young's Modulus ( $\sigma_Y/E$ ) shows the ability to achieve higher deformations for a given flexure geometry. A high ratio of Young's Modulus to density ( $E/\rho$ ) denotes a high ratio of stiffness per unit mass and so the natural frequency qualitatively scales with this ratio to some power. A high ratio of thermal diffusivity

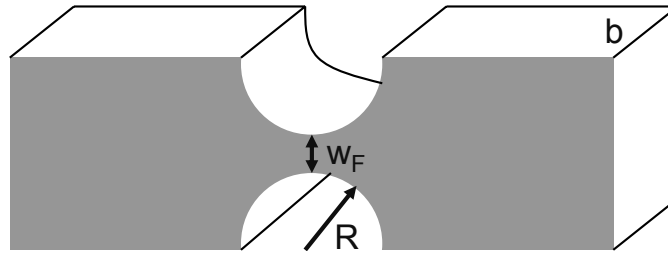
to CTE ( $\alpha_{Diff}/\alpha_{CTE}$ ) shows a shorter time constant for the transient temperature change induced thermal expansion and lower thermal strain per unit temperature. Aluminum 7075 was selected because of relatively favorable values of  $\sigma_Y/E$  ratio,  $E/\rho$  ratio,  $\alpha_{Diff}/\alpha_{CTE}$  ratio, and its low cost.

**Table 5–25 Normalized material property table for material selection**

Material	$\sigma_Y/E$	$\alpha_{Diff}/\alpha_{CTE}$	$E/\rho$	Cost
Titanium V	1.00	0.14	0.92	3.77
Aluminum 7075	0.70	1.00	1.00	1.00
Stainless steel 316	0.09	0.13	0.94	3.50
Invar – Annealed	0.19	0.87	0.70	5.21

### **Flexural joint design**

The design and modeling of the flexural joints that were used in the resonator shall be briefly reviewed. The functional requirements of the fiber resonator were first converted to the corresponding requirements of the flexural bearing such as the stiffness and range of motion for a given factor of safety. These values were then substituted into the governing equation, Equation (40), to obtain the design parameters that are shown in Figure 5–42 [80]. It is important to ensure that the flexural bearing/device possesses the desired performance with the consideration of fabrication errors. As a result, the final design allows 280N force input/output with a safety factor equal to 4.



**Figure 5–42 Design parameters for a flexural bearing**

$$k \cong \frac{dM}{d\theta} = \frac{2E \cdot b \cdot w_F^{5/2}}{9\pi \cdot R^{1/2}}, w_F = \sqrt{\frac{6M}{\sigma_Y \cdot b}} \quad (40)$$

### **Manufacturing**

The fiber resonator was machined from a 5mm thick aluminum 7075 plate. The V-grooves for positioning the fibers and tap holes for the set screw were machined first. The low tolerance ( $\pm 10 \mu\text{m}$ ) flexures and main structure were then machined by the wire-EDM machine. The fiber resonator, with piezoelectric actuator, is shown in Figure 5–43.

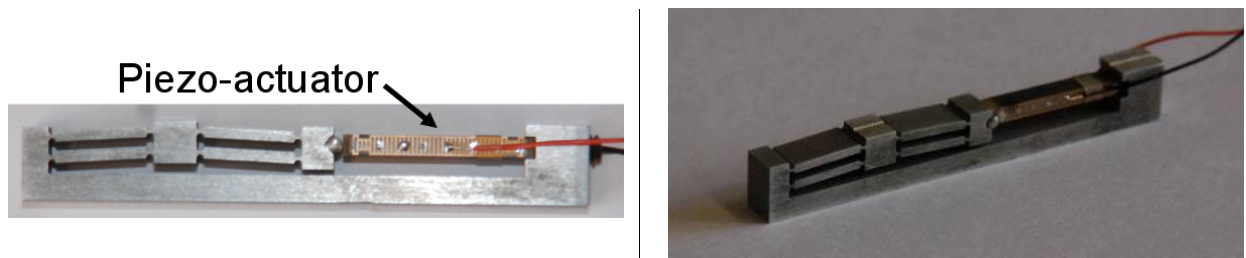


Figure 5-43 Image of the meso-scale fiber resonator made by wire-EDM

### Measured performance

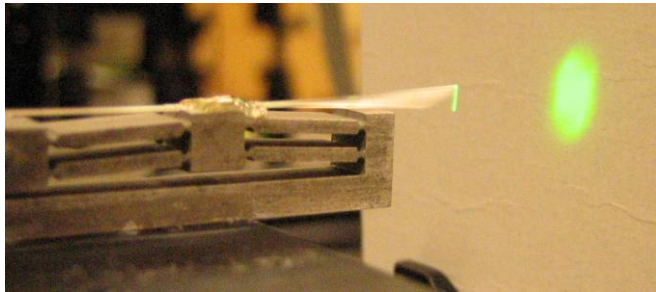
The measured and simulated characteristics of the meso-scale fiber resonator are compared in Table 5-26. The displacement of the fiber resonator stage was measured by a capacitance probe. The resonator's transmission ratio was then calculated by dividing the stage output by the corresponding actuator output that was obtained by analyzing the displacement-voltage chart provided by the vendor. The measured transmission ratio (3.36) is less than the FEA prediction (4.50). This is likely due to imperfections in the alignment between the piezoelectric actuator and the horizontal base of the resonator. It is also important to note that the manufacturer's data were used in this calculation and errors within this data are likely contributors.

Table 5-26 Summary of meso-scale fiber resonator characteristics

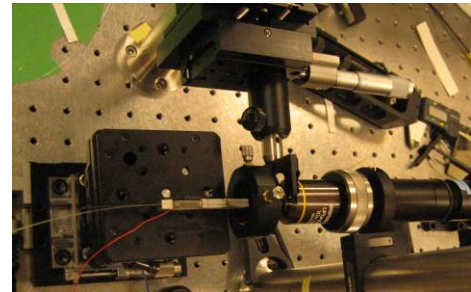
Simulated values	
Natural frequency	1.62 kHz (1 <sup>st</sup> mode)
Resonator stiffness	17.4 N/ $\mu$ m
Factor of safety	4.5
Measured values	
Device envelope	6.8 x 5.0 x 18.0 mm <sup>3</sup>
Fiber resonator stroke	18.9 $\mu$ m at 100V
Transmission ratio of resonator	3.36 (FEA = 4.50)
Transmission ratio of fiber (730Hz resonance)	370

The DCPCF was secured on the V-groove by the use of a crystal bond that melts at elevated temperature and cures quickly when the heat is removed. This allows repeatable readjustments of the fiber position, *i.e.*, resonating frequency. A 2 mm DCPCF tip oscillation at 30 Volts and 730 Hz has been observed from the initial test, as shown in Figure 5-44A. The result shows that (1) the fiber's transmission ratio was 370 and (2) only 1.5V was required to drive the actuator through the required 100-micron scanning range.

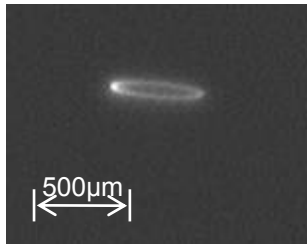
A femtosecond laser was then aligned to the DCPCF. The setup is shown in Figure 5–44B. Fluorescein samples were placed between the fiber tip and a CCD camera that focused on the fluorescein sample. An infrared filter was placed in front of the CCD objective lens so that excited emission two–photon signals could be differentiated, collected, and then imaged. Figure 5–44C and Figure 5–44D show the oval–shaped and straight scan lines that were acquired from the CCD camera. This experiment confirmed that different patterns of specific scan lines may be obtained at different specified frequencies.



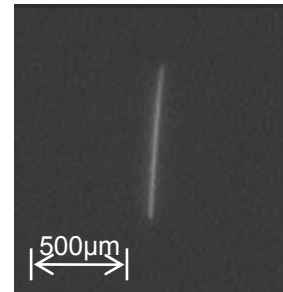
A: Resonating fiber with green laser for 2mm scan range



B: Fiber resonator with objective lens and CCD camera for characterizing scan line



C: Oval scan line imaged at 750Hz



D: Straight scan line imaged at 730Hz

**Figure 5–44 Experiments for fiber resonator characterization**

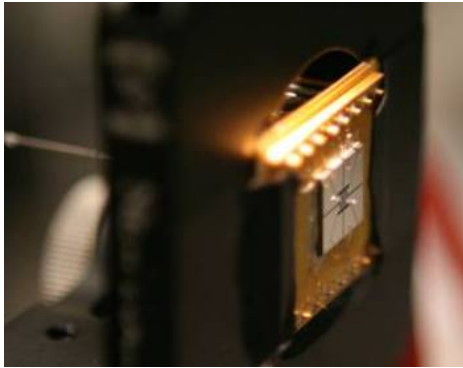
### 5.4.3 Characterization of MFM fiber resonator

This section presents the packaging, assembly and characterization of the four–channel MFM fiber resonator. A multi–mode fiber of 235 micron diameter was used in this experiment because of the limited availability of the DCPCF.

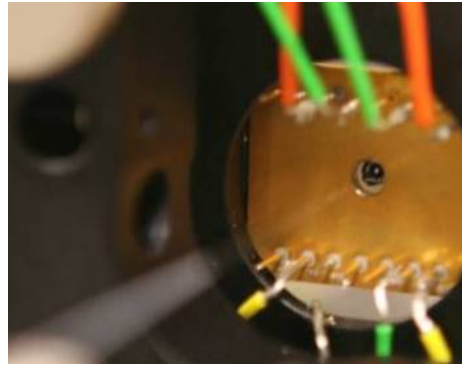
#### **Packaging the MFM fiber resonator for the experimental setup**

The MFM resonator was securely mounted on a gold–plated package that contained a through–hole that guided fiber insertion. The inserted fiber is shown in Figure 5–45A and Figure 5–45B. Silver epoxy was used to mount the resonator to the package. The silver epoxy provides

good thermal conduction and a strong mechanical bond. Lead-out wires for command signals were soldered to the pins on the back of the metal package.



A: MFM package in the process of assembly

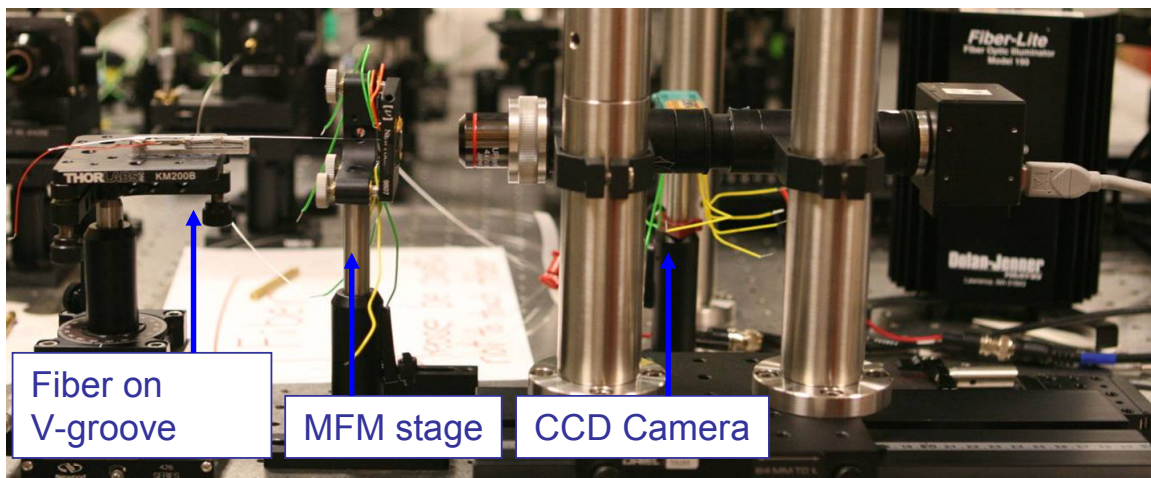


B: Backside of the packaged MFM with wiring soldered to the pins

**Figure 5–45 Wire–bonded MFM resonator package**

### Assembly

Figure 5–46 shows the setup for the assembly and the experiment. The fiber was constrained and fixed onto the V–groove of the meso–scale fiber resonator. The resonator was then mounted on a 5–axis positioning stage. The MFM resonator was mounted on a 4–axis positioning stage and then placed adjacent to the fiber’s tip. A CCD camera was mounted upon a 3–axis stage and then positioned so that it could image the relative position of the MFM stage and the multi–mode fiber throughout the assembly procedure.

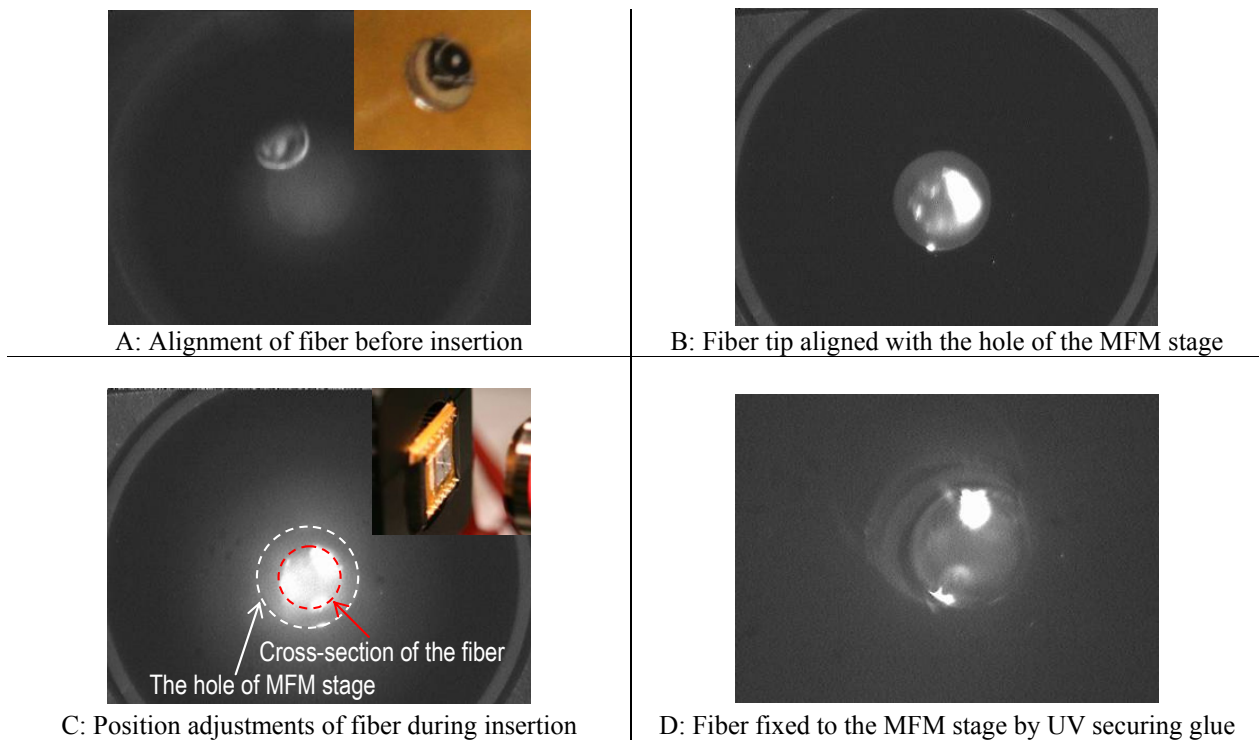


**Figure 5–46 Experimental setup for MFM resonator experiment**

Figure 5–47 shows the fiber assembly procedure in four steps. In Figure 5–47A, the fiber was positioned behind the MFM stage within a few 100s of microns. In Figure 5–47B, the tip of



the fiber was aligned to the hole of the MFM stage. In Figure 5–47C the insertion process started. As the fiber was not perfectly perpendicular to the MFM stage, constant adjustment of the fiber’s tip was required during insertion. During insertion step that is shown in Figure 5–47C, light was directed upon the center of the MFM stage. A magnified cross–section image of the transparent fiber at the surface of the MFM stage was constantly shown in the computer in real-time to aid in accurate alignment. In Figure 5–47D, the fiber was securely glued onto the MFM stage. This procedure was conducted by applying a droplet of UV securing glue to the fiber and then pulling the fiber in, the opposite direction of insertion. When the glue reached the MFM stage, the glue was drawn into the gap between the MFM stage and the fiber by capillary forces. The glue was cured via exposure to UV light.



**Figure 5–47 Fiber assembling procedures for MFM fiber resonator**

The assembled MFM resonator stage, with the multi–mode fiber, is shown in Figure 5–48.

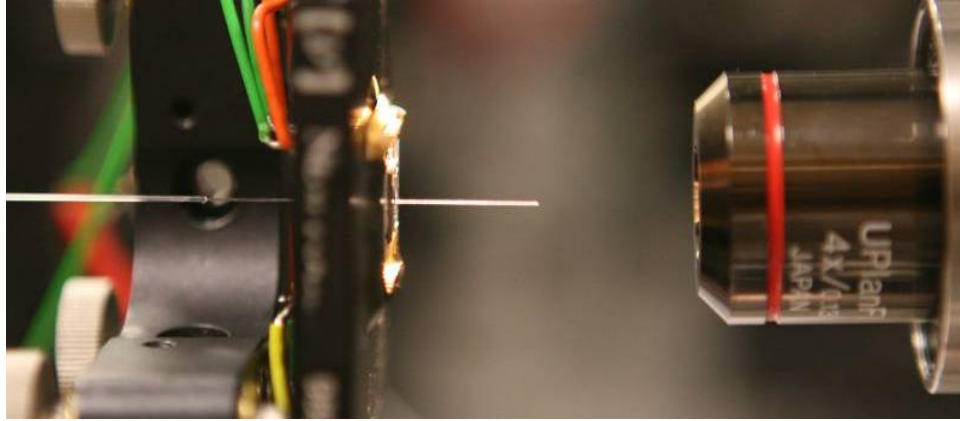
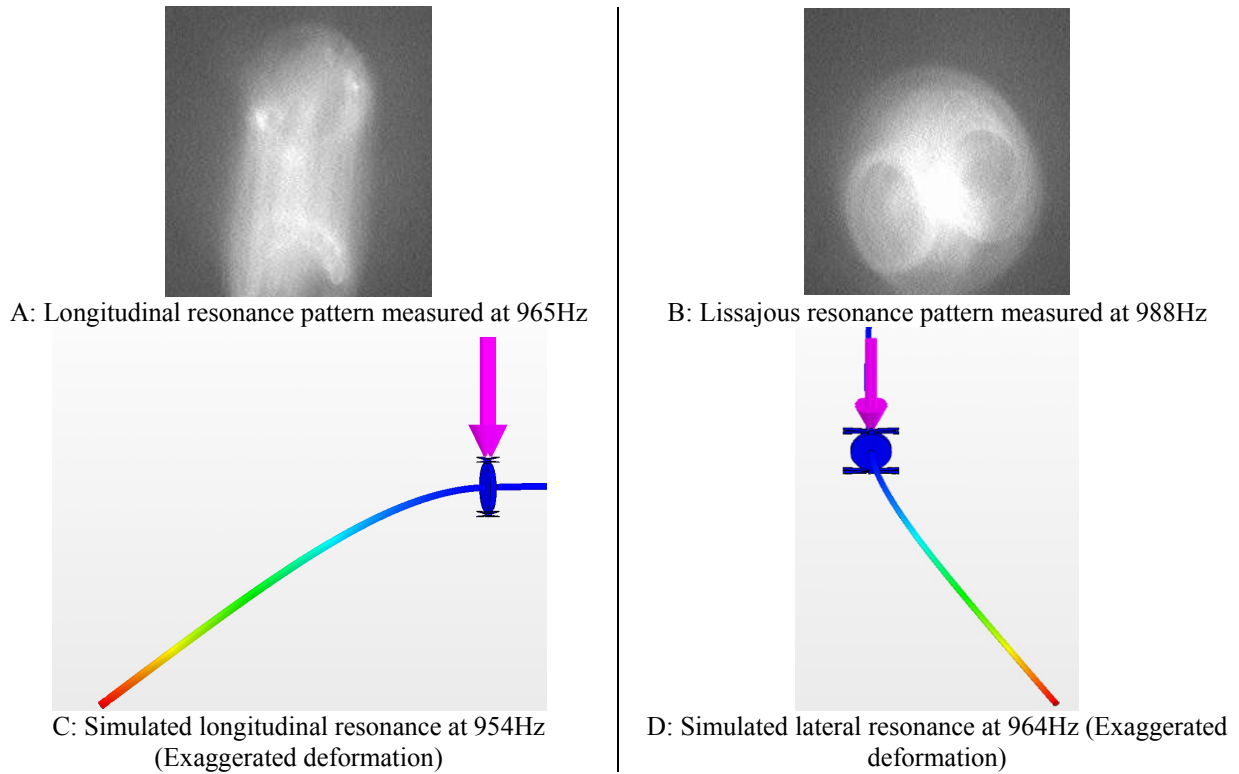


Figure 5–48 Assembled MFM stage with the multi–mode fiber

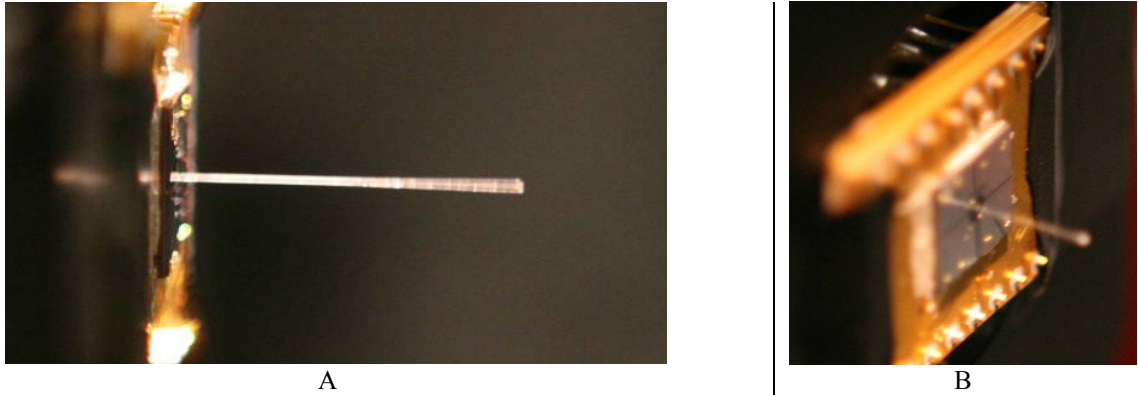
### *Experimental characterization of MFM resonator*

For an MFM to operate at a designated frequency, four command signals must be synchronized by the RC time delay circuit that was presented in Chapter 3. The resonant frequencies and the modes of the fiber were determined before this experiment by exciting the fiber with the fiber resonator that is shown on the left of Figure 5–46. Figure 5–49A and Figure 5–49B show images from the CCD camera. The longitudinal and lateral resonant modes, 965 Hz and 988 Hz respectively, may be seen. Figure 5–49C and Figure 5–49D show the modes that were predicted via FEA. For both modes, there is less than 3% error between the simulated and the experimental frequencies.



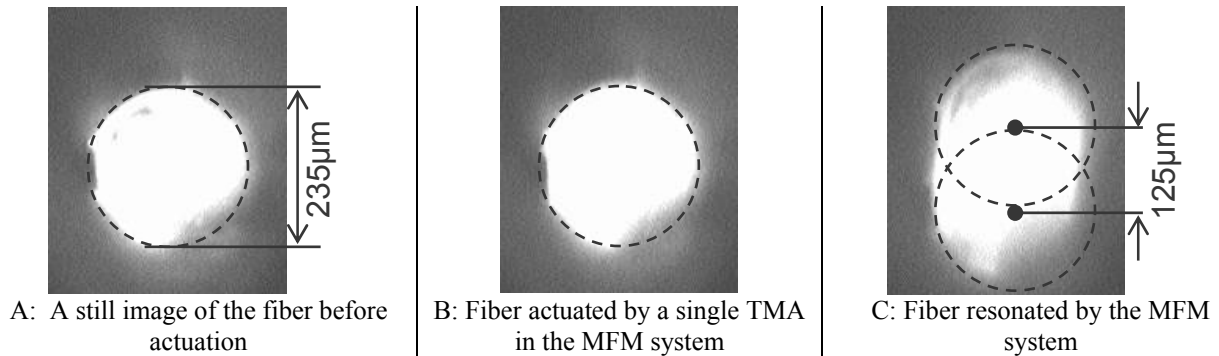
**Figure 5-49 Results of the frequency sweep performed by the meso-scale fiber resonator**

The MFM system was then commanded to drive the multi-mode fiber at 965Hz with four properly time-delayed command signals. The command signal was generated by the waveform generator shown in Equation (30). The signal was split into four channels that were connected to four independent voltage controlled current amplifiers. The amplified command signals from each channel were then connected to the RC circuit to obtain proper time-delay. Each TMA in the MFM system was operated at 241 Hz (a quarter of 965), such that together they provided a 965Hz output frequency. Figure 5-50 shows the fiber in resonance as driven by the MFM resonator.



**Figure 5-50 Fiber in resonance actuated by MFM resonator**

Figure 5-51 shows the results of the resonance on the fiber's tip. The images were acquired via the CCD camera. Figure 5-51A shows a still image of the fiber's tip before the MFM was energized. Figure 5-51B shows the fiber's motion while only one TMA in the MFM resonator was actuated at 965Hz. In this case, it was not possible to discern motion that was caused by the actuation of a single TMA actuation. This is expected because the bandwidth of a single TMA is lower than 965Hz. Figure 5-51C shows the fiber movement patterns that were generated by actuating the MFM with properly coordinated actuation signals. The amplitude of the scanning range was estimated to be  $125 \pm 2$  microns by scaling the motions relative to the diameter of the fiber, 235 microns. The accuracy was ascertained by pixel-counting the image obtained from the CCD camera, where each pixel in the image equals to  $0.5 \mu\text{m}$ .



**Figure 5-51 CCD images of MFM resonator operated at 965 Hz**

The important parameters for the command signals and characteristics of the experimental results are summarized in Table 5-27 and Table 5-28 respectively.

**Table 5–27 Parameters that were used for MFM resonator experiment**

Parameters	
Fiber diameter (multi–mode fiber) [ $\mu\text{m}$ ]	225 $\pm$ 5
$L_1$ [mm]	12.5 $\pm$ 0.05
$L_2$ [mm]	60.0 $\pm$ 0.05
Command Signal	
$I_0$ [mA]	100
$n$	1
$p$	3

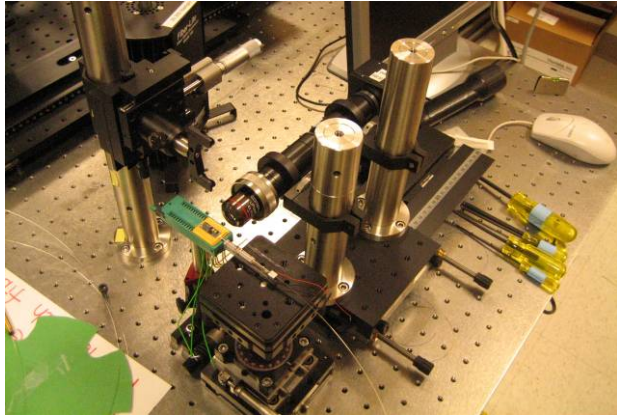
**Table 5–28 Summary of MFM experimental results**

Experimental results	
Amplitude [ $\mu\text{m}$ ]	125 $\pm$ 2
Longitudinal scan mode [Hz]	965 $\pm$ 0.01 (error –1.1%)
Lateral scan mode [Hz]	988 $\pm$ 0.01 (error –2.3%)
Simulated resonant modes	
Linear scan mode [Hz]	954
Lateral scan mode [Hz]	965

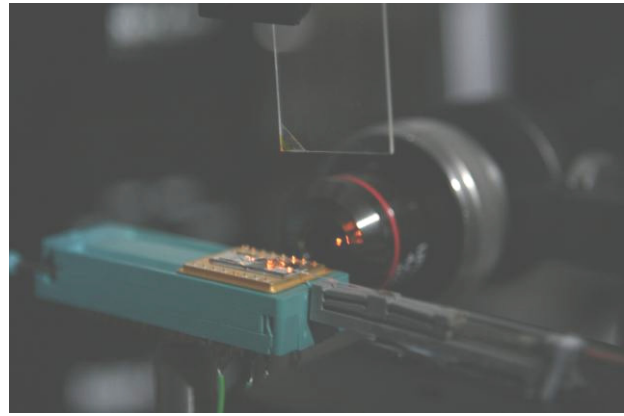
## 5.5 Scanning system integration

The scanning components were assembled and aligned with the femtosecond laser. This setup was used to characterize the scanning of the axes independent from each other. This information was required to enable accurate, volumetric image reconstruction and post data processing.

Figure 5–52A and Figure 5–52B show the overall scanning system setup. In Figure 5–52A, the fiber resonator was securely fixed on a six–axis stage for fine position adjustments. The packaged active SOB chip was constrained on a socket that was affixed to a two–axis ( $Z$  and  $\theta_z$ ) stage for positioning. In Figure 5–52B, the traveling path of the infrared laser could be observed, where the laser first left the DCPCF, then went through the micro–prism and GRIN lens, and eventually focused on the objective lens.



A: Scanning system setup

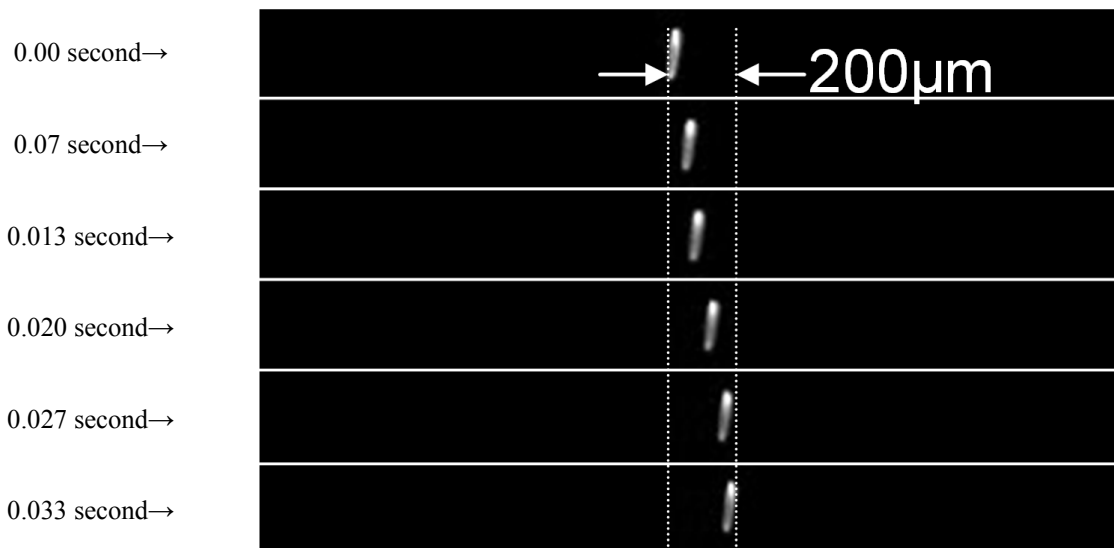


B: The SOB aligned with fiber. Infrared laser light was fed through the optics and then focused on the objective lens.

**Figure 5–52 Experimental setup for two–photon imaging**

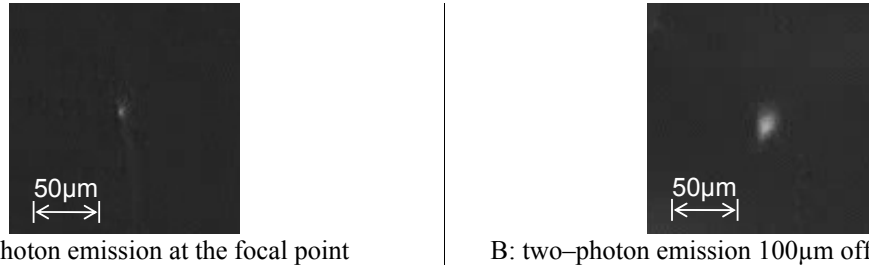
**Line scan characterization**

This section presents the scan line characterization over a specified surface and within a volume that was achieved by driving the fiber resonator and active SOB with a designated command signal. Figure 5–53 shows the compiled line scanning screenshots at 0.07 second time intervals over a  $200 \times 200 \mu\text{m}^2$  surface. Each straight line in the rows is the scan line of the DCPCF as it oscillates at 730Hz. The screenshot show lines, rather than points, because of the limited frame rate of the CCD relative to the frequency of the scanning in the vertical direction.



**Figure 5–53 Screenshots of X–Y scan, where X and Y–axis scan at 730Hz and 1Hz respectively**

The Z-scan distance, unfortunately could not be directly characterized by the CCD camera. As shown in Figure 5-54, when the GRIN lens shuttle moves off the focal plane, it only causes a blurring of the two-photon signal. The range of Z-scan was therefore estimated by the displacement-current relationship obtained from the model and the experimental results, presented in Section 5.3.4. With the preceding, it is assumed that the scanner possesses a  $200 \times 200 \times 125 \mu\text{m}^3$  volumetric scanning range. This is five times larger than the functional requirement.



A: two-photon emission at the focal point

B: two-photon emission 100µm off the focal plane

Figure 5-54 Screenshots of two-photon emission at the focal plane during Z-axis scanning at 2 Hz for 100 µm

## 5.6 Summary

This chapter has presented the design, modeling, and experimental characterization of the prototype scanner that was enabled via the use of (1) geometric contouring, (2) high-bandwidth pulsing, and (3) MFM. Three major parts of an endomicroscope, (1) optical assembly design/characterization, (2) silicon endoscopic scanner design/characterization, and (3) optical and scanning system integration and two-photon signal acquisition, were covered. In the first part, the design, modeling, and error analyses of the optical assembly were presented. Selection and characterization of individual optical components, including the GRIN lens, prism, and DCPCF were carefully performed and presented. The second part covered the modeling, design, and characterization of the three-axis scanner, including the two-axis SOB, the meso-scale fiber resonator, and the MFM fiber resonator. In the third part, a micro-scanning system was assembled and aligned with the optics modules for system characterization, wherein line scans of individual axis were characterized.

*This page is intentionally left blank*



**Conclusions**

---

This chapter concludes the dissertation with an overview of research, a discussion of the original contributions, and future research directions and applications in selected emerging technologies.

**6.1 Summary of research**

The aim of this research was to understand the factors that limit the performance of micro-scale TMAs and to understand how their performance characteristics could be improved via the introduction of (1) geometric contouring and (2) mechanical frequency multiplication. These techniques were shown to simultaneously improve the force, speed, and stroke of a TMA by more than an order of magnitude. As a result, this work has extended the performance envelope of small-scale electromechanical systems to cover the needs of emerging positioning applications that were previously impractical. Two techniques were created in this work to address the preceding limitations of current actuation technology: (1) Geometric contouring and (2) Mechanical frequency multiplication. This thesis uncovered the reasons for, and created models that could predict, behaviors that led to increases in the stroke, force, and operating frequency of micro-scale TMAs by factors of 4, 2.5, and 10 respectively. This also enabled the reduction of driving power by up to 40%.

The utility and practical implementation of these techniques were illustrated via a high-bandwidth, three-axis optical scanner for a two-photon endomicroscope. This scanner design was conceived for minimally invasive optical biopsy of internal tissues during cancer detection/diagnosis. The device consists of three major sub-systems: (1) an optical system (prism, graded index lens, and optical fiber) that was used to deliver/collect photons during imaging, (2) a small-scale electromechanical scanning system that raster scanned the focal point

of the optics through the specimen and (3) a silicon optical bench that was used to combine the electromechanical and optical systems. Experimental results and simulations showed that the micro-scale TMAs concepts enabled the scanner to exceed the design requirements. The device was capable of 3.5kHz x 100Hz x 30Hz scanning throughout a 125 x 200 x 200  $\mu\text{m}^3$  volume. In contrast, preceding micro-scale TMA technology for this application would only have scanned over 12.5% of the required volume at 10% of the required frequency (~100 Hz).

## **6.2 Thesis contributions**

This work forms a body of knowledge, design rules/principles and best practices that may be used to extend this work to realize similar benefits in other small-scale devices that use TMAs. The contributions of this work include the concepts, modeling, and design of micro-scale TMAs and the practical application/implementation of the TMA concepts in the prototype.

### **Geometric contouring**

The most important contribution is the identification of the combined thermal and mechanical benefits that are associated with geometric contouring of TMAs. The geometric contouring was a counter-intuitive discovery that led to new cross-energy domain modeling, optimization that were used to enable improvements in force, speed, and stroke by a factor of 2.5, 20, and 4 respectively.

### **Pulsing technique**

The 20X speed enhancement of the contoured TMAs was largely achieved by the technique of pulsing. This method utilized the non-uniformly distributed heating within a contoured beam to control the transient temperature profile along a TMA for optimized thermal strain, and heating and cooling speeds. This was the first time that the concept of controlling a TMA's transient temperature profile had been performed. Design rules, tools, models, and process for the pulsing technique were created accordingly.

### **Mechanical frequency multiplication**

Another important contribution was the MFM. The use of the MFM will enable designers to systematically construct high-bandwidth actuation systems that are based upon low-speed actuators. This was the first systematic approach that enabled tradeoffs between an

actuator's cycling speed and resonant frequency. The MFM concept is applicable to all actuators that have different forward and return stroke speeds. This work provides the general concept, models, design rules and control signal that are required to realize MFM.

### **Engineering contributions**

Practical engineering contributions include the modeling, design, fabrication, and characterization of a three-axis micro-optical scanning system, and the demonstration of the feasibility and utility of this research. For in-plane scanning, an SOB was designed and constructed with integral optics and contoured TMAs. The scanning speed of the SOB was improved by a factor of 10 after pulsing was applied. Out-of-plane scanning was achieved via a MFM fiber resonator that scanned a multi-mode fiber at kilohertz speed. Experimental results were used to show that the models that were created in this research may be used to design practical devices with accuracy that is satisfactory for engineering purposes. Practical engineering contributions also included the creation of a micro-fabrication process and the assembly processes for the optical components. Although the fabrication processes and assembly methods did not require scientific advances, the micro-fabrication/assembly platform that were created in this research will be useful for practical implementation of the research results within a commercial endoscope scanner.

## **6.3 Extensions and visions for future research**

The technology and knowledge that were generated in this research should be extended to other fields and applications. Some examples that are envisioned to have high economic or scientific impact are discussed in the following sub-sections.

### **6.3.1 Extension of geometric contouring and MFM to other applications**

The principle of geometric contouring and MFM may be directly applied to many micro-scale and meso-scale actuation technologies. Actuators such as shape memory alloys (SMAs), polymer gel actuators, ionic polymer composite (IPC) actuators, or mammalian muscles [125] are good candidates to implement these principles. In summary, geometric contouring may be applied to all thermally triggered actuators/devices, *i.e.* anything that generates motion or volume change based on temperature change or thermal strain, *e.g.* SMAs, MEMS inject printer array [58], and thermally actuated micro-pumps/valves [60, 61]. MFM is applicable to all actuators

that possess different dynamics during forward/return action or contraction/relaxation process. This includes, for example, polymer gel actuators, IPCs and SMAs. It is envisioned that an active vibration control algorithm could be applied to the MFM in order to achieve a desired dynamic behavior via vibration cancellation technology [126–130].

Preliminary estimations show that suitable actuators, *e.g.* SMAs, that implement contouring or MFM should also receive performance improvements that are similar to those which were demonstrated for TMAs in this thesis. Performance improvements of existing actuator technologies are important because these actuators are already being used extensively in many applications/fields and therefore the improvements would have a large impact on these fields. For example, SMAs have a broad spectrum of applications that range from biomedical devices, *e.g.* catheters/endoscopes, to space technology, *e.g.* latch mechanism in spacecrafts [125]. If SMAs' performance may be improved by an order of magnitude, advancements in medical devices and more energy efficient or lightweight actuators for space application could be possible.

### **6.3.2 Miniaturization of next generation scanner**

The current diameter of the scanner is 7 millimeter; it is desirable to reduce the device envelope by 50% in order to facilitate the integration of the scanner in a broader array of endoscopic systems. The minimum system size is, however, not limited by actuator performance, but by the stroke to device envelope ratio for silicon based flexure mechanisms. A proposed solution is to develop an alternative high–deformation material, *e.g.* metallic glasses, as the structural material for micro–scale flexure mechanisms. High–deformation material is the key to increasing the stroke of a compliant mechanism, because the product of a flexure's characteristic size and the material's maximum strain sets the limit on the maximum range of the flexure. This means that metallic glass flexural elements may be made smaller and exhibit larger ranges of motion than their silicon counterparts. Metallic glasses (*e.g.*  $Zr_{41.2}Ti_{13.8}Cu_{12.5}Ni_{10}Be_{22.5}$ ) exhibit material properties that enable them to achieve large elastic deformations/strains. Metallic glasses exhibit a 2% elastic strain limit (compared to 0.1% for silicon), a modulus of elasticity of 96 GPa (similar to aluminum) and a tensile yield strength of 1.90 GPa (similar to high strength steels). It is therefore worthwhile to investigate the possibility of integrating a micro–molded flexure mechanism that is made of metallic glass. This

monolithic mechanism could include micro-optics and micro-actuators through the creation of new modeling and micro-fabrication techniques [131]. The change in material may make it possible to reduce the scanner size to fit within a 3 mm diameter.

### **6.3.3 Confocal and two-photon endomicroscope**

The present work has resolved the actuation bottleneck for developing a TPE endomicroscope. It is reasonable to foresee that a commercially available version of a TPE endomicroscope may appear and be used for cancer screening in ten or twenty years. Proposed following steps to carry on this exciting field of research include:

1. Improve and characterize the optical performance of the prototype TPE endomicroscope. This could start with collection of *ex vivo* images of prepared cancerous tissues or epithelial tissues of melanoma patients. In terms of optical design, the GRIN lens assembly may be modified for increased working distance and numerical aperture, *i.e.* resolution. A device package should be created so that individual micro-fabricated scanning components may be constrained and aligned with proper electrical lead-outs. If done, the current scanner system, fixed on a precision positioner, may be maneuvered around for various experiments.
2. Modify the system for *in vivo* animal experiment. While it requires significant time for any new system to be approved for human clinical trials, animal experiments may be performed after only slight modification. With expected subcellular resolution, real time imaging capability, this research has attracted interest from world leading biologists in using the prototype endomicroscope for experiments designed to study/observe currently unapproachable biological systems/phenomena. Professor Susumu Tonegawa, a Nobel Laureate, world leading immunologist and neuroscientist at MIT, has expressed interests in modifying the scanner current system into a head-mounted endomicroscope for experiments on mice. The goal of this new work would be to image real time neuron activity of mice under different conditions.
3. Intravital microscopy is emerging as a powerful tool for studying cell trafficking (e.g. immune cells and cancer cells) in live animals and provides spatial and temporal resolution that is possible with other imaging modalities such as X ray/CT and MRI. Invasive surgical procedures are, however, currently required to expose organs such

as lymph nodes, spleen, and bone marrow for imaging under an optical microscope. Endomicroscopy will alleviate the need for surgical manipulation, minimize trauma and inflammation, and make it possible to conduct longitudinal imaging of the same animal over extended period of time so that the progression of disease and response to therapy may be observed.

# Appendix A: Nomenclature

$b$	Height or thickness of a beam	m or $\mu\text{m}$
$d$	Displacement of a TMA	m or $\mu\text{m}$
$e$	Subscript that denotes an equivalent variable	—
$f$	Desired operating frequency of a MFM system	Hz
$i$	Current	A or mA
$k$	Thermal conductivity	$\text{W}/\text{m}\cdot\text{K}$
$m$	Number of pulse-pairs/channels of a MFM system	—
$n$	Signal overlay index of a MFM system	—
$p$	Signal on the $p^{\text{th}}$ TMA in a MFM system	—
$t$	Time	Second
$w$	Width of a beam	m or $\mu\text{m}$
$h_c$	Piece-wise height function of beam profile	m or $\mu\text{m}$
$k_A$	Axial stiffness of a beam	N/m
$k_B$	Bending, <i>i.e.</i> lateral, stiffness	N/m
$t_p$	Pulse width for pulsing technique	second
$\dot{q}$	Heat generation per volume that is caused by resistive heating	$\text{W}/\text{m}^3$
$w_e$	Half width of a constant cross-section beam	m or $\mu\text{m}$
$w_F$	Thickness of a flexure bearing	m or $\mu\text{m}$
$w_L$	Width of wide central section of contoured beam	m or $\mu\text{m}$
$w_S$	Width of thin end sections of contoured beam	m or $\mu\text{m}$
$w'$	Ratio of $w_S/w_L$	m or $\mu\text{m}$
$A$	Cross-sectional area of a beam	$\text{m}^2$
$E$	Young's Modulus	Pa
$F$	Load vector applied to TMA; force in general	N
$G$	Shear Modulus	Pa
$I$	2 <sup>nd</sup> moment of inertia	$\text{m}^4$
$J$	Current density	$\text{A}/\text{m}^2$
$K$	Global stiffness matrix of TMA	N/m and N-m/rad
$L$	Length of a contoured beam; length of a fiber	m or $\mu\text{m}$
$M$	Moment applied to beam	N-m
$P$	Power	W
$S$	Stroke of a TMA	m or $\mu\text{m}$
$T$	Temperature	$^{\circ}\text{K}$ and $^{\circ}\text{C}$
$U$	Strain energy	J
$X$	Displacement vector of TMA	m or $\mu\text{m}$
$CC$	Subscript referring to constant cross-section	—
$CT$	Subscript referring to contoured cross-section	—
$F_{max}$	Maximum force output of a TMA	N

$F_N$	Equivalent nodal force in a stiffness matrix	N
$F'_{max}$	Maximum force enhancement ratio	—
$I_0$	Current amplitude for MFM signal	Amps
$I_P$	Current amplitude for pulsing technique	Amps
$C_P$	Heat capacity	J/°K–g
$K_A$	Stiffness of actuator in its working (axial) direction	N/m
$K'_A$	Stiffness enhancement ratio	—
$K_L$	Stiffness of chevron flexure in its lateral direction	N/m
$L_G$	In–plane gap between a wide beam and a thin beam in a parallel TMA	m or $\mu\text{m}$
$L_L$	Length of wide central section of contoured beam	m or $\mu\text{m}$
$L_N$	Length of the short “hinge beam” that connects the wide beam to the ground in a parallel TMA	m or $\mu\text{m}$
$L_S$	Length thin end sections of contoured beam	m or $\mu\text{m}$
$L_T$	Width of the wide beam in a parallel TMA	m or $\mu\text{m}$
$L_W$	Length of the wide beam in a parallel TMA	m or $\mu\text{m}$
$L_1$	Length of fiber: from wall constraint to MFM stage	m or $\mu\text{m}$
$L_2$	Length of fiber: from MFM stage to its free end	m or $\mu\text{m}$
$P_A$	Axial force applied to beam	N or mN
$P_L$	Lateral force applied to beam	N or mN
$P'$	Power reduction ratio	—
$R_{eq}$	Equivalent radius of a fiber	m or $\mu\text{m}$
$R_{Thermal}$	Thermal resistance of a beam	°K/W
$S'$	Stroke enhancement ratio	—
$T_{max}$	Maximum allowable temperature in a TMA	°K
$T_{R1,2}$	Transmission ratio of the 1 <sup>st</sup> and 2 <sup>nd</sup> chevron flexure in a cascaded chevron mechanism	°K
$T_0$	Room temperature	°K
$T'$	Maximum temperature reduction ratio	—
$\alpha$	Thermal expansion coefficient	$\mu\text{m}/\text{m}^{\circ}\text{K}$
$\nu$	Poisson ratio	—
$\rho$	Electrical resistivity	Ohm–m
$\zeta$	Transmission ratio for a contoured TMA	—
$\theta_{1,2}$	1 <sup>st</sup> and 2 <sup>nd</sup> chevron flexure’s angle of a cascaded chevron mechanism	degree
$\rho_D$	Density	$\text{kg}/\text{m}^3$
$\zeta'$	Transmission ratio enhancement ratio	—
$\sigma_{11}$	Stress in 11 direction (tensile/compressive)	Pa
$\sigma_{12}$	Stress in 12 direction (shear)	Pa
$\sigma_Y$	Yield stress	Pa
$\tau_{Thermal}$	Thermal time constant of a Joule heated beam	second
$\Delta_A$	Actuator displacement	m or $\mu\text{m}$
$\Delta_T$	Change in beam length that is caused by thermal strain	m or $\mu\text{m}$
$\Delta'$	Comparative ratio of contoured beam displacement per unit power	—



# Appendix B: Efficiency of TMAs

---

The efficiency of a Joule heated beam that possesses a constant cross-section is given by Equations (A1) and (A2) [132]. Equation (A1) gives the efficiency of a Joule heated, singly-supported beam of length  $L$  that is subject to a step current input of duration  $t$ , with a constant temperature at the support. Equation (A1) is written in terms of the dimensionless quantity  $u$  and the derived quantity  $l(u)$  as defined in Equation (A2) and (A3).

$$\eta = \frac{E_{out}}{E_{in}} = \frac{\frac{1}{2} \frac{EA}{L} dl^2}{E_{in}} = \frac{1}{4} \frac{E \cdot \alpha^2}{\rho \cdot C_p \cdot k} \dot{q} \frac{l(u)^2}{u} \quad (\text{A1})$$

$$u = \frac{k \cdot t}{\rho \cdot C_p \cdot L^2} \quad (\text{A2})$$

$$l(u) = \left\{ \frac{2}{3} - \frac{64}{\pi^4} \sum_{n=0}^{\infty} \frac{1}{(2n+1)^4} \exp\left[ \frac{-u(2n+1)^2 \pi^2}{4} \right] \right\} \quad (\text{A3})$$

Equation (A1) is used to plot the TMA efficiency variations at different length scales and time scales, as shown in Figure A-1. The analysis shows that a TMA will operate most efficiently at small scales with short duration high-power pulses. Figure A-1 also shows the improved efficiency, *i.e.* an order of magnitude, of TMAs when geometric contouring and pulsing are applied. The hatched region represents the possible TMA efficiencies at different design and operating conditions. Given that a practical cycling time for micro-TMAs is  $10^{-2}$  to  $10^{-4}$  seconds, the upper bound of a contoured TMA's efficiency has been extended to 0.5%. This is a marked improvement over the preceding state-of-the-art.

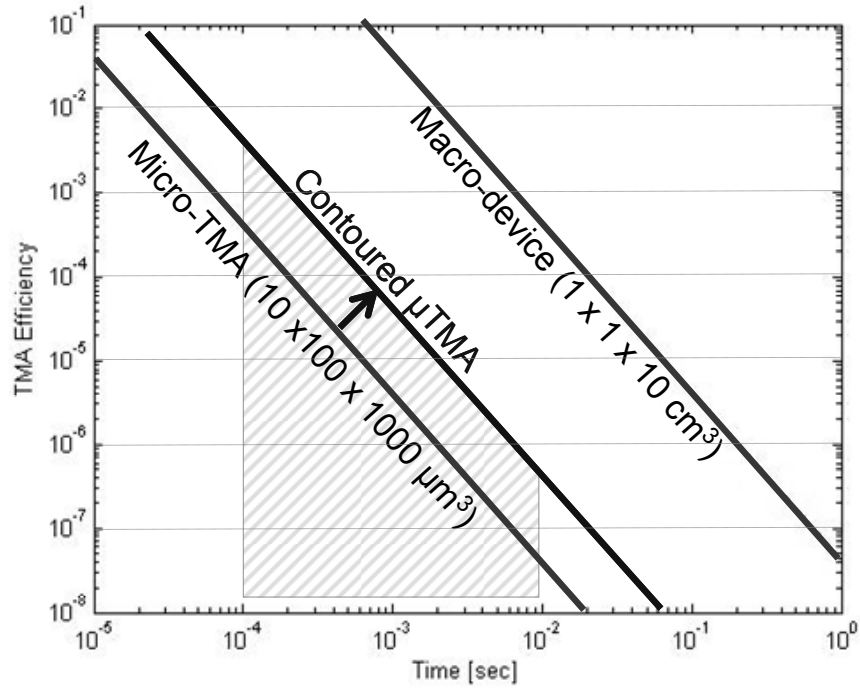


Figure A-1 Efficiency for TMAs at different length scale and operating conditions

# References

---

- [01] Eleftheriou, E., et al., 2003, "Millipede—a MEMS-based Scanning-probe Data-storage System," *IEEE Transactions on Magnetics*, 39(2), pp. 938–45.
- [02] Patazi, A., et al., 2004, "A Servomechanism for a Micro-electromechanical-system-based Scanning Probe Data Storage Device," *Nanotechnology*, 15(10), pp. 612–21.
- [03] Sun, Y., et al., 2002, "A High-aspect-ratio Two-axis Electrostatic Microactuator with Extended Travel Range," *Sensors and Actuators A: Physical*, 102, pp. 49–60.
- [04] Chen, S.-C. and Culpepper, M. L., 2006, "Design of a Six-axis Microscale Nano-positioner –  $\mu$ Hexflex," *J. of Precision Eng.* 30(3), pp. 315–24.
- [05] Pozidis, H., et al., 2004, "Demonstration of Thermomechanical Recording at 641 Gb/in<sup>2</sup>," *IEEE Transactions on Magnetics*, 40(4), pp. 2531–6.
- [06] Mita, M., et al., 2005, "Bulk Micromachined Tunneling Tips Integrated with Positioning Actuators," *J. of Microelectromechanical Systems*, 14(1), pp. 23–28.
- [07] Stoev, K., et al., 2001, "Demonstration and Characterization of Greater than 60 Gb/in<sup>2</sup> Recording Systems," *Eighth Joint Magnetism and Magnetic Materials Intermag Conference*, 37(4, pt.1): pp. 1264–7.
- [08] Rothuizen, H., et al., 2000, "Fabrication of a Micromachined Magnetic X/Y/Z Scanner for Parallel Scanning Probe Applications," *Microelectronic Engineering*, 53:pp. 509–12.
- [09] Guckel, H., Klein, J., Christenson, T., Skrobis, K., Laudon, M., and Lovell, E.G., 1992, "Thermo-magnetic Metal Flexure Actuators," *Solid-State Sensor and Actuator Workshop, 5th Technical Digest.*, IEEE, pp. 73–75.
- [10] Comtois, J., Bright, V., and Phipps, M., 1995, "Thermal Microactuators for Surface-micromachining Processes," *Proc. SPIE*, 2642, pp. 10–21.
- [11] Comtois, J.H. and V.M. Bright, 1997, "Applications for Surface-micromachined Polysilicon Thermal Actuators and Arrays," *Sensors and Actuators a-Physical*, 58(1), pp. 19–25.
- [12] Que, L., Park. J.-S., and Gianchandani, Y.B., 1999, "Bent-beam Electro-thermal Actuators for High Force Applications," *Microelectromechanical Systems*, *IEEE International Conference*, Orlando, FL, pp. 31–36.
- [13] Que, L., Park. J.-S., and Gianchandani, Y.B., 2001, "Bent-beam Electrothermal Actuators: I. Single Beam and Cascaded Devices," *J. Microelectromech. Systems*, 10(2), pp. 247–54.
- [14] Cragun, R. and Howell, L., 1999, "Linear Thermomechanical Microactuators," *ASME IMECE*, Nashville, TN, pp. 181–8.
- [15] Bell, D.J., et al., 2005, "MEMS Actuators and Sensors: Observations on Their Performance and Selection for Purpose," *J. Micromech. Microeng.*, 15, pp. 153–164.
- [16] Carlen, E.T. and Mastrangelo, C. H., 1999, "Simple, High Actuation Power, Thermally Activated Paraffin Microactuator," *Transducers International Conference on Solid-State Sensors and Actuators*, 2, pp.1364–67.
- [17] DeVoe, D. L., 2002, "Thermal Issues in MEMS and Microscale Systems," *IEEE Trans. Compon. Packag. Technol.*, 25(4), pp. 576–583.
- [18] Tang, W.C., Nguyen, T., and Howe, R.T., 1989, "Laterally Driven Polysilicon Resonant Microstructures," *Sensors and Actuators A: Physical*, 20, pp. 25–32.
- [19] Grade, J.D., Jerman, H., and Kenny, T.W., 2003, "Design of Large Deflection Electrostatic Actuators," *J. of Microelectromechanical Systems*, 12(3), pp. 335–343.
- [20] Hirano, T., Furuhashi, T., Gabriel, K.J., and Fujita. H., 1992, "Design, Fabrication, and Operation of Submicron Gap Comb-drive Microactuators," *J. of Microelectromechanical Systems*, 1(1), pp. 52–59.
- [21] Niino, T., Egawa, S., Nishiguchi, N., and Higuchi, T., 1992, "Development of an Electrostatic Actuator Exceeding 10N Propulsive Force," *IEEE Micro Electro Mechanical System*, Germany, pp. 122–127.
- [22] Saif, M.T.A and MacDonald, N. C., 1995, "A Millinewton Microloading Device," *Transducers International Conference on Solid-State Sensors and Actuators*, 2, pp. 60–63.

- [23] Berger, J.D., et al., 2001, "Widely Tunable External Cavity Diode Laser Based on a MEMS Electrostatic Rotary Actuator," Optical Fiber Communication Conference and Exhibition, 2, pp. TUJ21–TUJ23.
- [24] Rodgers, M.S., et al., 2000, "A New Class of High Force, Low-voltage, Compliant Actuation Systems," in Proceedings of the Solid State Sensor and Actuator Workshop, Hilton Head, NC.
- [25] Xie, H., Pan, Y., and Fedder, G.K., 2003, "A CMOS–MEMS Mirror with Curled–hinge Comb–drives," J. of Microelectromechanical Systems, 12(4), pp. 450–57.
- [26] Sniegowski, J.J. and E.J. Garcia, 1996, "Surface–micromachined Gear Trains Driven by an On–chip Electrostatic Microengine," Electron Device Letters, 17, pp. 366–68.
- [27] Tanner, D.M., et al., 2002, "Pin–joint Design Effect on the Reliability of a Polysilicon Microengine," in 40th Annual IEEE International Reliability Physics Symposium Proceedings., Dallas, TX, pp. 122–129.
- [28] Lee, W.C., Jin, Y.–H., and Cho., Y.–H., 2002, "Nonlinearly Modulated Digital Microactuators for Nano–precision Digital Motion Generation," in Proceedings of the 15th International Conference on MEMS, Las Vegas, NV, pp. 594–597.
- [29] Horsley, D.A., Wongkomet, N., Horowitz, R., and Pisano, A.P., 1998, "Design and Feedback Control of Electrostatic Actuators for Magnetic Disk Drives," IEEE Solid–State Sensor and Actuator Workshop, pp. 120–123.
- [30] Lee, K.B. and Cho, Y., 2001, "Laterally Driven Electrostatic Repulsive–force Microactuators Using Asymmetric Field Distribution," J. of Microelectromechanical Systems, 10(1), pp.128–136.
- [31] Legtenberg, R., Berenschot, E., Elwenspoek, M., and Fluitman, J., 1995, "Electrostatic Curved Electrode Actuators," IEEE Solid–State Sensor and Actuator Workshop, pp. 37–42.
- [32] Chen, F., Xie, H., and Fedder, G.K., 2001, "A MEMS–based Monolithic Electrostatic Microactuator for Ultra–low Magnetic Disk Head Fly Height Control," J. of Microelectromechanical Systems, 37(4), pp. 1915–18.
- [33] Deutsch, E.R., et al., 2003, "A Large–travel Vertical Planar Actuator with Improved Stability," Transducers International Conference on Solid State Sensors, Actuators, Microsystems, Boston, MA, 1, pp.352–355.
- [34] Hung, E.S. and Senturia, S.D., 1999, "Extending the Travel Range of Analog–tuned Electrostatic Actuators," J. of Microelectromechanical Systems, 8(4), pp. 497–505.
- [35] Toshiyoshi, H. and Fujita, H., 1996, "Electrostatic Micro Torsion Mirrors for an Optical Switch Matrix," J. of Microelectromechanical Systems, 5(4), pp. 231–237.
- [36] Greywall, D.S., et al., 2003, "Crystalline Silicon Tilting Mirrors for Optical Cross–connect Switches," J. of Microelectromechanical Systems, 12(5), pp. 708–712.
- [37] Shutov, M.V., et al., 2003, "Electrostatic Actuators with Long Range Translation," Transducers International Conference on Solid State Sensors, Actuators, Microsystems, Boston, MA, 1, pp. 356–359.
- [38] Choi, J.–J., et al., 2001, "Electromagnetic Micro X–Y Stage for Probe–based Data Storage," J. of Semiconductor Technology and Science, 1(1): pp. 84–93.
- [39] Kim, K.H., et al., 2005, "Fabrication and Test of a Micro Electromagnetic Actuator," Sensors and Actuators A: Physical, 117, pp. 8–16.
- [40] Verma, S., Kim, W.–j., and Gu, J., 2004, "Six–axis Nanopositioning Device with Precision Magnetic Levitation Technology," IEEE/ASME Transactions on Mechatronics, 9(2), pp. 384–91.
- [41] Ahn, S.–H. and Kim, Y.–K., 2004, "Silicon Scanning Mirror of Two DOF with Compensation Current Routing," J. of Micromechanics and Microengineering, 14, pp. 1455–1461.
- [42] Miyajima, H., et al., 2003, "A MEMS Electromagnetic Optical Scanner for a Commercial Confocal Laser Scanning Microscope," J. of Microelectromechanical Systems, 12(3), pp. 243–251.
- [43] Bernstein, J. J., et al., 2004, "Electromagnetically Actuated Mirror arrays for Use in 3–D optical Switching Applications," J. of Microelectromechanical Systems, 13(3), pp. 526–535.
- [44] Luginbuhl, P., et al., 1996, "Piezoelectric Cantilever Beams Actuated by PZT Sol–gel Thin Film," Sensors and Actuators A: Physical, 54, pp. 530–535.
- [45] DeVoe, D. L., et al., 1997, "Modeling and Optimal Design of Piezoelectric Cantilever Microactuators," J. of Microelectromechanical Systems, 6(3), pp. 266–270.
- [46] Weinberg, M. S., 1999, "Working Equations for Piezoelectric Actuators and Sensors," J. of Microelectromechanical Systems, 8(4), pp. 529–533.

- [47] Ahn, J., et al., 2000, "Fabrication of Piezoelectrically Driven Micro-cantilever using Pb(Zr,Ti)O<sub>3</sub> Films," in Proceedings of the 12th IEEE International Symposium on Applications of Ferroelectrics.
- [48] Wong, C. W., et al., 2003, "Analog Tunable Gratings Driven by Thin-film Piezoelectric Microelectromechanical Actuators," *Applied Optics*, 42(4), pp. 621–626.
- [49] Robbins, W. P., et al., 1991, "Design of Linear-motion Microactuators Using Piezoelectric Thin Films," *J. of Micromechanics and Microengineering*, 1, pp. 247–252.
- [50] Dubois, M.-A., et al., 1998, "PZT Thin Film Actuated Elastic Fin Micromotor," *IEEE Transactions on Ultrasonics, Ferroelectrics, and Frequency Control*, 45(5).
- [51] Cusin, P., et al., 2000, "Compact and Precise Positioner Based on the Inchworm Principle," *J. of Micromechanics and Microengineering*, 10, pp. 516–521.
- [52] Conway, N. J., et al., 2004, "Large-strain, Piezoelectric, In-plane Micro-actuator," in Proceedings of the 17th International Conference on MEMS, Amsterdam.
- [53] Tsauro, J., et al., 2002, "2D Microscanner Actuated by Sol-gel Derived Double Layered PZT," in Proceedings of the 15th IEEE International Conference on MEMS, Las Vegas, NV, pp. 548–51.
- [54] Jokiel, B., Benavides, G.L., Bieg, L.F., and Allen, J.J., 2001, "Planar and Spatial Three-degree-of-freedom Micro-stages in Dilicon MEMS," Annual Meeting of the American Society for Precision Engineering, pp. 32–35.
- [55] Haake, J.M., Beranek, M., 1998, "Integrated Microelectromechanical Alignment and Method for Fiber Optic Module Manufacturing," US Patent No.: 6164837.
- [56] Bamberger, H. and Shoham, M., 2004. "A New Configuration of a Six Degree-of-freedom Parallel Robot for MEMS Fabrication," *Proc. IEEE International Conference on Robotics and Automation*, pp. 4545–50.
- [57] Liu, Z., DeVoe, D.L., 2001, "Micromechanism Fabrication Using Silicon Fusion Bonding," *Robotics and Computer Integrated Manufacturing*, pp. 131–137.
- [58] Bassous, E., Taub, H.H., and Kuhn, L., 1977, "Ink Jet Printing Nozzle Arrays Etched in Silicon," *Appl. Phys. Lett.*, 31(2), pp. 135–7.
- [59] Bassous, E., 1975, "Nozzles Formed in Monocrystalline Silicon," U.S. Patent 3 921 916.
- [60] Yue, Y., et al., 1996, "A Bimetallic Thermally Actuated Micropump," *ASME IMECE, NEW YORK, NY*, 59, pp. 351–4.
- [61] Freygang, M. H. Glosch, H. Haffner, and S. Messner, 1996, "Thermal Actuation Units for Microvalves and Micropumps," in *Proc. Actuator Conf.*, pp. 84–7.
- [62] Kun, T.K. and Kim, C.-J., 1998, "Vaveless Pumping Using Traversing Vapor Bubbles in Microchannels," *J. Appl. Phys.*, 83(11), pp. 5658–64.
- [63] Riethmuller, W. and Benecke, W., 1988, "Thermally Excited Silicon Micro-actuators," *IEEE Transactions on Electron Devices*, 35(6), pp.758–63.
- [64] Yang, Y. -J, and Kim, C.-J., 1995, "Testing and Characterization of a Bistable Snapping Microactuator Based on Thermo-Mechanical Analysis," *Transducer International Conference on Solid-State Sensors and Actuators, Stockholm, Sweden*, 2, pp.337–40.
- [65] Baltzer, M., Kraus, T., and Obermeier, T., 1997, "A Linear Stepping Actuator in Surface Micromachining Technology for Low Voltages and Large Displacements," *IEEE Conf. Solid-State Sensors and Actuators, Chicago, IL*, pp. 781–4.
- [66] Tas N. R., Sonnenberg T., Molenaar R. and Elwenspoek M., 2003, "Design, Fabrication and Testing of Laterally Driven Electrostatic Motors Employing Walking Motion and Mechanical Leverage," *J. Micromech. Microeng.*, 13 N6–15 (1).
- [67] Maloney, J.M., Schreiber, D.S., and DeVoe, D.L., 2001, "Electrothermal Linear Micromotors Fabricated by Deep Reactive Ion Etching of Single Crystal Silicon," *ASME IMECE, New York, NY*.
- [68] Schreiber, D.S., Cheng, W.-J., Maloney, J.M., and DeVoe, D.L., 2001, "Surface Micromachined Electrothermal Microstepper Motors," *ASME IMECE, New York, NY*.
- [69] Sinclair, M.J., 2000, "A High Force Low Area MEMS Thermal Actuator," in *Proc. IEEE Inter Society Conference on Thermal Phenomena*, pp. 127–32.
- [70] Butler, J. T., Bright, V.M., and Cowan, W. D., 1997, "SPICE Modeling of Polysilicon Thermal Actuators," *Proc. SPIE*, 3224, pp. 284–93.

- [71] Mankame, N. D., Anathasuresh, G. K., 2001, "Comprehensive Thermal Modeling and Characterization of an Electro-Thermal-compliant Microactuator," *J. Micromech. Microeng.*, 11, pp. 452–62.
- [72] Yan, D., Khajepour, A., and Mansour, R., 2004, "Design and Modeling of a MEMS Bidirectional Vertical Thermal Actuator," *J. Micromech. Microeng.*, 14(7), pp. 841–50.
- [73] Hickey, R., et al, 2002, "Heat Transfer Analysis and Optimization of Two-beam Microelectromechanical Thermal Actuators," *J. Vac. Sci. Technol. A*, 20(3), pp. 971.
- [74] Huang, Q., Lee, N., 1999, "Analysis and Design of Polysilicon Thermal Flexure Actuator," *J. Micromech. Microeng.*, 9, pp. 64–70.
- [75] Maloney, J. M., DeVoe, D. L., and Schreiber, D. S., 2000, "Analysis and Design of Electrothermal Actuators Fabricated from Single Crystal Silicon," *ASME IMECE*, pp.233–40.
- [76] Cragun, R., Larry, L.H., 1999, "Linear Thermomechanical Microactuators," *Proc. ASME IMECE*, pp. 181–187.
- [77] Jonsmann, J. et al, 1999, "Compliant Electro-thermal Microactuators," in *IEEE Conf. on Micro Electro Mechanical Systems*, Orlando, FL, pp. 588–592.
- [78] Howell, L., 2001, *Compliant Mechanisms*, John Wiley and Sons Inc., NY.
- [79] Culpepper, M. L. and Kim, S., 2004, "Framework and Design Synthesis Tool Used to Generate, Evaluate and Optimize Compliant Mechanism Concepts for Research and Education Activities," *ASME Design Engineering Technical Conference*, Salt Lake City, UT.
- [80] Slocum, A.H., 1992, *Precision Machine Design*, Society of Manufacturing Engineers, Dearborn, MI, pp. 521–38.
- [81] Smith, S.T., 2000, *Flexures: Elements of Elastic Mechanisms*, CRC Press, Ann Arbor, MI.
- [82] Denk W, Strickler JH, Webb WW., 1990, "Two-photon Laser Scanning Fluorescence Microscopy," *Science*, 248, pp. 73–76.
- [83] Göppert-Mayer M., 1931, "Über Elementarakte mit Zwei Quantensprungen," *Ann. Phys., Leipzig*, 5, pp. 273–94.
- [84] So, P.T.C., Dong, C.Y., Masters, B.R., and Berland K.M., 2000, "Two-photon Excitation Fluorescence Microscopy," *Annu. Rev. Biomed. Eng.*, 2, pp. 399–429.
- [85] Diaspro, A. et al., 2002, *Confocal and Two-photon Microscopy: Foundations, Applications, and Advances*, John Wiley and Sons Inc, NY.
- [86] Wilson, T., 1990, *Confocal Microscopy*, Academic Press, London.
- [87] Pawley, J.B., editor, 1995, *Handbook of Confocal Microscopy*, Plenum, New York.
- [88] Huang D, et al., 1991, "Optical Coherence Tomography," *Science*, 22, 254(5035), pp. 1178–81.
- [89] Fercher, A.F, et al., 1995, "Measurement of Intraocular Distances by Backscattering Spectral Interferometry," *Optics Communications*, 117(1), pp. 43–48.
- [90] Yeow, J.T.W., et al., 2004, "Micromachined 2-D Scanner for 3-D Optical Coherence Tomography," *Sensors and Actuators A*, 117(20), pp. 331–340.
- [91] Helmchen, et al., 2001, "A miniature Head-mounted Two-photon Microscope: High-resolution Brain Imaging in Freely Moving Animals," *Neurotechnique*, 31(6), pp.903–12.
- [92] Jung, et al., 2002, "Multiphoton Endoscopy," *Optics Letters*, 28(11), pp. 902–04.
- [93] Gobel, et al., 2004, "Miniaturized Two-photon Microscope Based on a Flexible Coherent Fiber Bundle and a Gradient-index Lens Objective," *Optics Letter*, 29(21), pp. 2521–23.
- [94] Bird, et al., 2003, "Two-photon Fluorescence Endoscopy with Micro-optic Scanning Head" *Optics Letters*, 28(17), pp.1552–54.
- [95] American Cancer Society, 2007, *Cancer Facts & Figures*, <http://www.cancer.org/>.
- [96] Chen, S.-C., 2003, "A Six-degree-of-freedom Compliant Micro-manipulator for Silicon Optical Bench," S.M. thesis, Dept. of Mech. Eng., MIT.
- [97] Carl, P., 2004, "Design of a Thermally Actuated Silicon Optical Bench Mount for Obtaining and Maintaining GRIN Lens Focus in a Two-photon Endoscope," M.S. thesis, Dept. of Mech. Eng., Technischen Universität München.

- [98] Chen, S.-C., et al., 2006, "Design of a High-speed, Micro-scale Fast Scanning Stage for Two-photon Endomicroscopy," Proceedings of the Annual Meeting of the ASPE, Monterey, CA, pp. 279 – 282.
- [99] Choi, H., Chen, S., et al., 2006, "Design of a Non-linear Endomicroscope Biopsy Probe," OSA Biomedical Optics Topical Meeting and Tabletop Exhibit, FL.
- [100] Chen, S.-C. and Culpepper, M.L., 2006, "Design of Contoured Microscale Thermomechanical Actuators," Journal of Microelectromechanical Systems, 15(5), pp. 1226–34.
- [101] Lide, D.R. and Kehiaian, H.V., 1994, *CRC Handbook of Thermophysical and Thermomechanical Data*, CRC Press, Ann Arbor, MI, pp. 878–899.
- [102] Spyarakos, C.C. and Raftoyiannis, J., 1997, *Linear and Nonlinear Finite Element Analysis in Engineering Practice*, Algor Inc, PA.
- [103] Gere, J.M. and Carter, W.O., 1962, "Critical Buckling Loads for Tapered Columns," J. of Struct. Eng., ASCE.
- [104] Young, W.C., and Budynas, R.G., 2002, *Roark's Formulas for Stress and Strain*, 7th edition, McGraw-Hill Inc, New York.
- [105] Tien, Majumdar, and Gerner, 1997, *Microscale Energy Transport*, Taylor & Francis Group, Washington.
- [106] Crystal Fiber, 2007, "Double Cladding Photonic Crystal Fiber," <http://www.crystal-fibre.com/products/active.shtml>.
- [107] Madou, 2002, *Fundamentals of Micro Fabrication*, second edition, CRC. pp. 287–288.
- [108] Kern, W.A., and Deckert, C.A., 1978, *Chemical Etching in Thin Film Processing*, Academic, New York.
- [109] Hu, S.M., and Kerf, D.R., 1967, "Observation of Etching of N-type Silicon in Aqueous HF solutions," J. Electrochem. Soc., 114, pp. 414.
- [110] Campbell, S. A., 2001, *The Science and Engineering of Microelectronic Fabrication*, second edition, Oxford, pp. 258–260.
- [111] Bosch Gmbh R.B., 1994, U.S. Pat. 4855017, U.S. Pat. 4784720, and Germany Pat. 4241 045C1
- [112] J.K. Bhardwaj, H. Ashraf, 1995, "Advanced Silicon Etching Using High Density Plasmas," SPIE Proc. Series, 2639, pp. 224–233.
- [113] .K. Bhardwaj, H. Ashraf, A. McQuarrie, 1997, "Dry Silicon Etching for MEMS," Symp. on Microstructures and Microfabricated Systems at the Annual Meeting of the Electrochem. Soc., Montreal, Quebec, Canada.
- [114] Protron Mikrotechnik, 2003, "Deep RIE," <http://www.protron-mikrotechnik.de/>.
- [115] Zhang, J. et al., 2006, "Simulations for Surface Evolverment and Footing Effect in ICP DRIE Fabrications," Journal of Physics, Conference Series, 34, pp. 522–526.
- [116] Kiesslich, R., et al., 2004, "Confocal Laser Endoscopy for Diagnosing Intraepithelial Neoplasias and Colorectal Cancer *in vivo*," Gastroenterology, 127(3), pp. 706–713.
- [117] Ilyin, S.E., et al., 2001, "Fiber-optic Monitoring Coupled with Confocal Microscopy for Imaging Gene Expression *in vitro* and *in vivo*," J. Neurosci Methods, 108(1), pp. 91–96.
- [118] Krohne, I., T. Pfeifer, M. Zacher, F. Depiereux, and H. Stepp., 2002, "New Concept for the Development of a Confocal Endomicroscope," Biomed Tech (Berl), 47, Suppl 1 Pt 1, pp. 206–208.
- [119] Rouse, A.R., Kano, A., Udovich, J.A., Kroto, S.M., and Gmitro, A.F., 2004, "Design and Demonstration of a Miniature Catheter for a Confocal Endomicroscope," Appl. Opt., 43(31), pp. 5763–71.
- [120] Umech Technologies, 2002, "MMA Principles and Performance: Application Note 0190," <http://www.umech.com/>.
- [121] Timoshenko, S., 1974, *Vibration Problems in Enginerring*, John Wiley & Sons, London.
- [122] Huber, J.E.; Fleck, Z.A.; Ashby, M.F., 1997, "The Selection of Mechanical Actuators Based on Performance Indices," Proc R Soc London Ser A, 453, pp. 2185–2205.
- [123] Zupan, M, et al., 2002, "Actuator Classification and Selection—the Development of a Database," Advanced Eng. Materials, 4(12), pp. 933–939.
- [124] Bell, D.J., et al., 2005, "MEMS Actuators and Sensors: Observations on Their Performance and Selection for Purpose," J. Micromech. Microeng., 15, pp. S153–S164.
- [125] Pons, J.L., 2005, *Emerging Actuator Technologies, a Micromechatronic Approach*, John Wiley & Sons, England.

- [126] Bailey, T., and Hubbard, J. E., 1985, "Distributed Piezoelectric Polymer Active Vibration Control of a Cantilever Beam," *J. of Guidance Control and Dynamics*, 8(5), pp. 605–611.
- [127] Baz, A., Imam, K., and McCoy, J., 1990, "Active Vibration Control of Flexible Beams Using Shape Memory Actuators," *J. of Sound and Vibration*, 140(3), pp. 437–456.
- [128] Chen, S. H., Wang, Z. D., and Liu, X. H., 1997, "Active Vibration Control and Suppression for Intelligent Structures," *J. of Sound and Vibration*, 200(2), pp. 167–177.
- [129] Housner, G., et al., 1997, "Structural Control: Past, Present, and Future," *J. of Engineering Mechanics–Asce*, 123(9), pp. 897–971.
- [130] Olgac, N., et al., 1997, "Active Vibration Control of Distributed Systems Using Delayed Resonator with Acceleration Feedback," *J. of Dynamic Systems Measurement and Control–Transactions of the ASME*, 119(3), pp. 380–389.
- [131] Chen, S., Culpepper, M.L., et al., 2006, "Formation of Micro–scale Precision Flexures via Molding of Metallic Glass," *Annual Meeting of the American Society for Precision Engineering, Monterey, CA*, pp. 283–86.
- [132] Noworolski, J. Mark et al., 1996, "Process for In–plane and Out–of–plane Single–crystal–silicon Thermal Microactuators," *Sensors and Actuators, A55*, pp. 65–69.